From the Institute of Experimental and Clinical Pharmacology and Toxicology
of the University of Lübeck
Director: Prof. Dr. Markus Schwaninger

Investigation of the role of G$\alpha_{q/11}$ signaling in brain endothelial cells

Dissertation
for Fulfillment of
Requirements
for the Doctoral Degree
of the University of Lübeck

from the Department of Natural Sciences

Submitted by

Dimitrios Spyropoulos
from Gavrolimni, Nafpaktos, Greece

Lübeck 2024

First referee: **PD Dr. rer. nat. Jan Wenzel**

Second referee: **Prof. Dr. med. Peter König**

Date of oral examination: **February 6th, 2025**

Approved for printing: **February 18th, 2025**

Table of contents

List of figures

List of supplementary figures

List of tables

Abbreviations

$[Ca^{2+}]_i$	Intracellular Ca^{2+}
ABC (eg ABCB1, ABCG2)	ATP-binding cassette
ABI3	ABI gene family member 3
acetoxymethyl ester	AM (eg Fluo-4 AM)
aCSF	Artificial cerebrospinal fluid
AD	Alzheimer's disease
AD+/- (in Barnes maze)	Adjacent quadrant
ADAM15	A Disintegrin and metalloproteinase domain-containing protein 15
ADGRG6	Adhesion G protein-coupled receptor G6
adj.	adjusted
ADP-β-S	Adenosin-5′-0-(2-thiodiphosphat) trilithiumsalt
Alcam	Activated leukocyte cell adhesion molecule
AMT	Adsorptive-mediated transcytosis
ANGPT2	Angiopoietin-2
ANOVA	Analysis of variance
Apoe	Apolipoprotein E
Asns	Asparagine synthetase
ATP	Adenosine 5'-triphosphate
AUC	Area under the curve
BAC	Bacterial artificial chromosome
BBB	Blood-brain barrier
BCRP	Breast cancer resistance protein
BDNF	Brain derived neurotrophic factor
beKO	Brain endothelial knockout
Bgn	Biglycan
bp	Base pair
BP	Biological process
BSA	Bovine serum albumin
CA (eg CA1)	Cornu ammonis
$CaCl_2$	Calcium chloride
cAMP	Cyclic adenosine monophosphate
Cat. Nr	Catalog number
CC	Cellular component
CD eg.CD31	Cluster of differentiation
CDC42	cell division cycle 42
CDH5	Cadherin-5
Ces2c	Carboxylesterace 2C
Cldn5	Claudin-5
CMT	Carrier-mediated transporter
CNS	Central nervous system
CO_2	Carbon dioxide

Coll IV	Collagen IV
Cre	Cyclisation recombinase
CreER^{T2}	Cre fused to a mutant estrogen ligand-binding domain (ERctT2)
CSC	Cell surface capture
Cxcl12	C-X-C motif chemokine ligand 12
Cy3	Cyanine3
Cyp4b1	Cytochrome P450 4B1
DAG	Diacylglycerol
DAPI	4′,6-diamidino-2-phenylindole
dd	double distilled
DEPC	Diethyl pyrocarbonate
DHA	Docosahexaenoic acid
DMEM/F12	Dulbecco's Modified Eagle Medium/Nutrient Mixture F-12
DMSO	Dimethyl sulfoxide
(g)DNA	(genomic)Deoxyribonucleic acid
DNase I	Deoxyribonuclease I
dNTP	Deoxynucleotide triphosphate
ECGS	Endothelial cell growth supplement
ECs	Endothelial cells
Edn1	Endothelin-1
EDTA	Ethylenediaminetetraacetic acid
EdU	5-ethynyl-2'-deoxyuridine
Eno1	Enolase 1
ENTPD1	Ectonucleoside triphosphate diphosphohydrolase 1
Ephb2	Ephrin type-B receptor 2
EtBr	Ethidium bromide
ETH	Eidgenössische technische hochschule
F	Fluoresence intenstity
F$_0$	Baseline fluoresence intensity
F2RL2	Coagulation factor II (thrombin) receptor-like 2
Fab	Fragment antigen-binding
FBS	Fetal bovine serum
FC	Fold change
FC	Fold change
FcR	Fragment crystallizable receptor
fl (eg Gnaq$^{fl/fl}$)	Floxed
Fmo2	Flavin-containing monooxygenase 2
G protein	Guanine nucleotide-binding protein
GAP	GTPase activating protein
GCaMP8	GFP-calmodulin-M13 peptide fusion protein
GDP	Guanosine diphosphate
GEF	Guanine nucleotide exchange factor
GFAP	Glial fibrillary acidic protein
GFP	Green fluorescent protein
GO	Gene ontology

Gp9	Platelet glycoprotein IX
GPR (eg GPR68) or GPCR	G protein-coupled receptor
Grpel2	Gro-P like protein E protein homolog 2
GTP	Guanosine-5'-triphosphate
GTPases	GTP-binding proteins with hydrolase activity
Gα/β/γ	G protein subunit alpha/beta/gamma
H2-T23	Histocompatibility 2, T region locus 23
HCl	Hydrochloric acid
hCMEC/D3	Human cerebral microvascular endothelial cell line D3
Hmgcs2	Hydroxymethylglutaryl-CoA synthase 2
HMOX1	Heme oxygenase 1
I.U.	International units
IAR	Inverse aspect ratio
Iba1	Ionized calcium-binding adaptor molecule 1
ICAM- 1	Intercellular adhesion molecule 1
Ig (eg IgG)	Immunoglobulin
IKCA	Intermediate conductance Ca^{2+} activated K^+ channel
IKK	IκB kinase
IL	Interleukin
IP_3	Inositol 1,4,5-trisphosphate
IP_3R	Inositol 1,4,5-triphosphate receptor
iPSC	induced pluripotent stem cell
Itgb4	Integrin beta-4
IκBα	Nuclear factor of kappa light polypeptide gene enhancer in B-cells inhibitor alpha
JAK	Janus kinase
JAM	Junctional adhesion molecule
KCl	Potassium chloride
Kdr	Kinase insert domain receptor
KH_2PO_4	Potassium dihydrogen phosphate
KIT	KIT Proto-Oncogene, Receptor Tyrosine Kinase
Kras	Kirsten rat sarcoma virus
L1cam	Neural cell adhesion molecule L1
LB	Labeling buffer
LDL	Low-density lipoprotein
LSR	Lipoprotein stimulated receptor
Ltc4s	Leukotriene C4 synthase
MAP2	Microtubule associated protein 2
MARVELD2	MARVEL domain containing 2
MBP	Myelin basic protein
MF	Molecular function
MFSD2a	Major facilitator superfamily domain-containing protein 2a
$MgCl_2$	Magnesium chloride
MPBECs	Mouse primary brain endothelial cells
MRP	Multidrug Resistance-associated protein

MSigDB	Molecular signature database
MTORC1	mammalian target of rapamycin complex 1
N_2	Nitrogen
$Na_2HPO_4 \times 2H_2O$	Sodium phosphate dibasic dihydrate
NaCl	Sodium chloride
$NaH_2PO_4.H_2O$	Sodium phosphate monobasic monohydrate
$NaHCO_3$	Sodium bicarbonate
$NaIO_4$	Sodium periodate
NaN_3	Sodium azide
NEMO	NF-κB essential modulator
NeuN	Neuronal nuclei
NF-κB	Nuclear factor “kappa-light-chain-enhancer” of activated B-cells
NIK	NF-κB-inducing kinase
NKCC1	Sodium potassium chloride co-transporter 1
NO	Nitric oxide
Npr3	Atrial natriuretic peptide receptor 3
Nqo1	NAD(P)H dehydrogenase [quinone] 1
NVU	Neurovascular unit
O (in Barnes maze)	Opposite quadrant
O_2	Oxygen
OCLN or Ocln	Occludin
OPR	Object place recognition
P (P0)	Passage 0
(D)PBS	(Dulbecco’s) phosphate buffer saline
PCR	Polymerase chain reaction
PDS	Plasma derived bovine serum
PECAM1	Platelet endothelial cell adhesion molecule 1
Pgf	Placenta growth factor
P-gp	P-glycoprotein
PIP_2	Phosphatidylinositol 4,5-bisphosphate
PLC-β	Phospholipase C beta
Plin2	Perilipin-2
PLVAP	Plasmalemma vesicle associated protein
Plxnb1	Plexin-B1
PRR	Pattern-recognition receptor
Prss23	Serine protease 23
RAC	Ras-related C3 botulinum toxin substrate
RAS	Rat sarcoma
RHOA	Ras homolog family member A
RMT	Receptor-mediated transcytosis
ROS	Reactive oxygen species
RRID	Research resource identifier
RT	Room temperature
SD	Standard deviation
SDS	Sodium dodecyl sulphate

SEM	Standard error of mean
SKCA	Small conductance Ca^{2+} activated K^{+} channel
SLC	solute carrier
SMCs	Smooth muscle cells
Stab1	Stabilin-1
STAT (eg STAT5)	Signal transducer and activator of transcription
T (in Barnes maze)	Target quadrant
TAE	Tris-acetate-EDTA buffer
TAK1	TGFβ-activated kinase 1
TEER	Trans-endothelial electrical resistance
Tf	Transferrin
TGFβ	Transforming growth factor beta
Thbd	Thrombomodulin
THBS1	Thrombospondin-1
Thermus aquaticus	Taq
Thsd7a	Thrombospondin type-1 domain-containing protein 7A
TJP1	tight junction protein 1
TJs	Tight junctions
TLCK	N-α-Tosyl-L-lysine chloromethyl ketone hydrochloride
TNF	Tumor necrosis factor
Tris-HCl	Tris-(hydroxymethyl)-aminomethane hydrochloride
TRPC	Transient receptor potential cation channel
VCAM-1	Vascular cell adhesion molecule 1
VEGF	Vascular endothelial growth factor
VEGFR (eg. VEGFR2)	Vascular endothelial growth factor receptor
VwF	Von Willebrand factor
WHO	World Health Organisation
Wnt	Wingless-related integration site
ZO	Zonula occludens

Abstract

The aging population is projected to increase in the next decades posing new challenges for societies. Normal aging can severely affect the cognitive function of individuals even in the absence of overt pathologies but currently, the therapeutic options are limited. Therefore, based on scientific evidence that aging vasculature is linked to the development of age-dependent cognitive decline, deepening our knowledge of the cerebrovascular system could unravel new potential pharmacological targets.

The current study, aimed to understand the role of $G\alpha_{q/11}$ proteins in the brain endothelium. Based on previous work, it was hypothesized that brain endothelial $G\alpha_{q/11}$ proteins affect the cognitive function of aging mice. The hypothesis was tested with behavioral tests during the lifespan of aging mice with specific brain endothelial deletion of the genes that express the $G\alpha_{q/11}$ proteins ($G\alpha_{q/11}^{beKO}$ mice). The results provided evidence that the $G\alpha_{q/11}$ proteins do not affect the memory function of young mice but have a significant effect on the cognitive function of aged mice.

Immunohistological stainings on aged mice revealed increased formation of string vessels in the brains of $G\alpha_{q/11}^{beKO}$ mice compared to control mice. String vessels are structures positive for basement membrane markers and negative for endothelial cell markers presumably resulting from collapsed vessels. Interestingly, no significant differences were found in the other parameters investigated such as neuroinflammation, neuronal and synaptic density, myelination, or blood-brain barrier (BBB) leakage.

Based on literature research and previous findings of our group, shear stress was identified as a possible factor to be involved in the formation of string vessels. Mechanical stimulation of primary mouse brain endothelial cells (MPBECs) was found to induce intracellular calcium ($[Ca^{2+}]_i$) increase and activation of the NF-κB pathway independent from the $G\alpha_{q/11}$ pathway. Furthermore, long-term cultivation of MPBECs under flow was identified to lead to significant morphological and proteomic changes compared to static conditions. Finally, based on the proteomic analysis, which revealed that shear stress induces angiogenic pathways in MPBECs, it was found that thrombomodulin (THBD) as well as $G\alpha_{q/11}$ proteins are involved in *in vitro* migration and proliferation respectively.

All in all, the current study provides evidence that the brain endothelial $G\alpha_{q/11}$ signaling is important for cognitive function in aged mice. Future work could shed light on the exact underlying mechanisms of the observed phenotype, which could probably involve string vessel-induced hypoxia. Finally, we provide a comprehensive proteomic database that could be further exploited to unravel novel mechanosensory targets.

Zusammenfassung

Es wird prognostiziert, dass die alternde Bevölkerung in den nächsten Jahren zunehmen wird, was neue Herausforderungen für die Gesellschaften mit sich bringt. Der normale Alterungsprozess kann die kognitiven Funktionen des Einzelnen stark beeinträchtigen, selbst wenn keine offensichtlichen Erkrankungen vorliegen, doch die therapeutischen Möglichkeiten sind derzeit begrenzt. Da wissenschaftlich erwiesen ist, dass die Alterung der Gefäße mit der Entwicklung des altersabhängigen kognitiven Defizits zusammenhängt, könnte die Vertiefung unseres Wissens über das zerebrovaskuläre System neue potenzielle pharmakologische Angriffspunkte erschließen.

Ziel der aktuellen Studie war es, die Rolle der $G\alpha_{q/11}$-Proteine im Gehirnendothel zu verstehen. Auf der Grundlage früherer Arbeiten, wurde die Hypothese, dass der $G\alpha_{q/11}$-Signalweg im Gehirnendothel die kognitive Funktion alternder Mäuse beeinflusst, aufgestellt. Die Hypothese wurde durch Verhaltenstests während der Lebensspanne alternder Mäuse mit spezifischer gehirnendothelialer Deletion der Gene, die die $G\alpha_{q/11}$-Proteine codieren ($G\alpha_{q/11}^{beKO}$-Mäuse), untersucht. Die Ergebnisse lieferten Hinweise darauf, dass die $G\alpha_{q/11}$-Proteine die Gedächtnisfunktion junger Mäuse nicht beeinträchtigen, aber einen signifikanten Einfluss auf die kognitive Funktion gealterter Mäuse haben.

Immunhistologische Färbungen an gealterten Mäusen zeigten eine stärkere Bildung von sogenannten *String Vessels* im Gehirn von $G\alpha_{q/11}^{beKO}$-Mäusen im Vergleich zu Kontrollmäusen. *String Vessels* sind Strukturen, die positiv für Basalmembranmarker und negativ für Endothelzellmarker sind, was vermutlich auf kollabierte Gefäße zurückzuführen ist. Interessanterweise wurden keine signifikanten Unterschiede bei den anderen untersuchten Parametern wie Neuroinflammation, neuronale und synaptische Dichte, Myelinisierung oder Bluthirnschranken-Dichtigkeit (BBB) gefunden.

Auf der Grundlage von Literaturrecherchen sowie früheren Ergebnissen unserer Gruppe, wurde der durch fließendes Blut verursachte Schubspannung am Endothel als ein möglicher Faktor identifiziert, der an der Bildung von *String Vessels* beteiligt sein könnte. Es wurde festgestellt, dass die mechanische Stimulation von primären Gehirnendothelzellen aus Mäusen (MPBECs) zu einem Anstieg der intrazellulären Calciumkonzentration ($[Ca^{2+}]_i$) und zur Aktivierung des NF-κB-Signalwegs unabhängig vom $G\alpha_{q/11}$-Signalweg führt. Darüber hinaus wurde festgestellt, dass die Langzeitkultivierung von MPBECs unter Strömungsbedingungen im Vergleich zu statischen Bedingungen zu signifikanten Veränderungen der Morphologie und auf Proteinebene führt. Schließlich wurde auf der Grundlage der Proteomanalyse, die ergab, dass Schubspannung angiogene Signalwege in MPBECs induziert, festgestellt, dass sowohl Thrombomodulin (THBD) als auch $G\alpha_{q/11}$-Proteine an der *In vitro*-Migration bzw.- Proliferation beteiligt sind.

Alles in allem, liefert diese Arbeit Beweise dafür, dass der endotheliale G$\alpha_{q/11}$-Signalweg im Gehirn für die kognitive Funktion bei gealterten Mäusen wichtig ist. Zukünftige Arbeiten könnten die genauen Mechanismen, die dem beobachteten Phänotyp zugrunde liegen, aufklären, wobei es sich wahrscheinlich um eine durch die *String Vessels* induzierte Hypoxie handeln könnte. Schließlich stellen wir eine umfassende Proteomdatenbank zur Verfügung, die weiter genutzt werden könnte, um neue mechanosensorische Ziele zu entschlüsseln.

1 Introduction

Medical and technological advancements have significantly enhanced worldwide life expectancy in recent decades. The aged population currently accounts for 10 % of the global population and is projected to rise to 16 % by 2050 (UN, World Population Prospects 2022). This increase in life expectancy has brought new challenges for the socioeconomic and healthcare systems of the countries, as diseases associated with aged individuals, like dementia and stroke, have risen on the list of medical conditions responsible for global deaths (Benjamin et al., 2018; Cortes-Canteli & Iadecola, 2020; UN, World Population Prospects, 2022). According to the World Health Organization's (WHO) Global Health Estimates, stroke and dementias, two pathological disorders that affect the brain vasculature and are associated with aging, ranked in the top 10 leading causes of death for 2019. Together, these diseases were responsible for approximately 14 % of global deaths (WHO Global Health Estimates, 2020).

However, even in the absence of overt pathological conditions, normal aging is accompanied by a decline in cognitive function that affects individuals' quality of life as well as their families and, in the broader view, the healthcare and socioeconomic system (Cortes-Canteli & Iadecola, 2020; Sharma et al., 2010; Toth et al., 2017). Accumulating evidence has shown that normal aging leads to systemic and cerebrovascular changes strongly associated with memory decline (Cooper et al., 2016; Cortes-Canteli & Iadecola, 2020; Ighodaro et al., 2017; Toth et al., 2017). Given the lack of significant therapeutic options to tackle age-dependent cognitive decline and the critical role of the vasculature in its development, our research on understanding brain endothelium's function and identifying new pharmacological targets with an extended therapeutic interest for cerebrovascular and neurological diseases is of utmost importance and urgency.

1.1 Architecture of the brain vasculature

Like every organ in the human body, the brain depends on blood circulation for its function. The circulating blood supplies the brain with necessary nutrients and removes the metabolic byproducts. Although it accounts only for 2 % of body weight, the human brain receives around 15 % of the total cardiac output (Xing et al., 2017) and consumes more oxygen (O_2) and glucose to meet its metabolic demands compared to most of the peripheral organs (Gibbs et al., 1942; Kety, 1957; Reinmuth et al., 1965). However, in contrast to the peripheral organs, the brain has limited energy storage capacity thus making it vulnerable to blood supply disturbances which can lead to neuronal damage.

The brain vasculature comprises a vast network of interconnected vessels that ensure the constant blood flow and removal of metabolic waste. The brain is supplied by four extracranial major arteries arising from the aortic arch or its major branches, the right and left internal carotid arteries and the right and left vertebral arteries (Cipolla, 2009; Schaeffer & Iadecola, 2021). These four arteries distally enter the skull, merging and forming an intracranial completely anastomotic ring, the circle of Willis. From the circle of Willis, three pairs of intracranial main arteries arise that supply blood to the cerebrum: the anterior cerebral arteries, the middle cerebral arteries, and the posterior cerebral arteries (Cipolla, 2009). These arteries divide progressively into smaller diameter vessels that run along the surface of the brain and anatomically, lie in the pial-arachnoid space (or leptomeninges) separated from the brain tissue through pia matter (Engelhardt et al., 2017). The pial arteries divide into smaller arteries and penetrate the brain tissue. Further deeper into the brain parenchyma, the diameters of the vessels become smaller as the vessels branch into arterioles and, finally, into capillaries where nutrients and O_2 exchange mainly occur. From the capillaries, the blood outflow travels through the post-capillary venules to larger diameter veins and then to the larger valveless veins located on the pial surface or in the deeper parts of the brain (Cipolla, 2009).

Interestingly, while the capillary bed is the major site of blood flow resistance (Gould et al., 2017), the extracranial and intracranial arteries contribute significantly to the total cerebrovascular resistance. This feature of the latter is necessary for blood flow maintenance and protection of the downstream arteries and arterioles from blood pressure changes (Faraci & Heistad, 1990).

1.2 Structure of brain vessels

The structure of brain vessels has some common characteristics along the vascular tree but also stark differences, which reflect their role in regulating the blood supply and other functional differences. Similarly to the periphery, the vessels that supply blood to the brain consist of a continuous monolayer of endothelial cells (ECs) surrounded by mural cells (Cipolla, 2009; Engelhardt et al., 2017). In the extracranial arteries, a thick layer of contractile smooth muscle cells (SMCs) surrounds the endothelial monolayer and is separated from it through the internal elastic lamina (Schaeffer & Iadecola, 2021). At the intracranial and pial arteries in the subarachnoid space, the SMC layer becomes progressively thinner, and the perivascular space arises between the external part of the vascular wall, and the glia limitans, the outermost layer of the brain tissue. Both intracranial and extracranial arteries receive extrinsic innervation from cranial autonomic ganglia, which regulate their tone (Cipolla, 2009; Schaeffer & Iadecola, 2021).

In the smaller arteries that dive into the parenchyma, the perivascular space is obliterated as the glia limitans fuse with the external part of the vascular wall (Morris et al., 2016). In this part of the vascular tree, the layer of SMCs becomes a monolayer, and the neuronal output from parenchymal nerve terminals contributes to the regulation of the vascular tone. At the level of the capillaries, the SMCs are replaced by pericytes. Pericytes are embedded in the endothelial basement membrane and covered by the astrocytic end-feet, which separates the vessels from the brain parenchyma (Engelhardt et al., 2017; Schaeffer & Iadecola, 2021). On the venous side, the perivascular space appears again, and the endothelial layer is covered with SMCs, but to a lower extent and with a different shape compared to the arterial side (Hartmann et al., 2021; Vanlandewijck et al., 2018).

Despite the relatively simple structure of the vascular segments, recent advances in next-generation sequencing have revealed a significant heterogeneity of vascular cells along the vascular tree, called zonation, and in different brain areas (Saunders et al., 2018; Vanlandewijck et al., 2018). Interestingly, ECs show higher heterogeneity than mural cells, presumably attributed to specialized functions of ECs from different vascular segments (Profaci et al., 2020; Saunders et al., 2018; Vanlandewijck et al., 2018).

The cellular organization and close interaction between endothelial, mural, glial, and neuronal cells in the microvascular bed of the central nervous system (CNS) is termed the neurovascular unit (NVU) (Schaeffer & Iadecola, 2021). The NVU in the region of the microvasculature plays a crucial role in the regulation of cerebral blood flow as well as in the formation and function of the BBB.

1.3 The BBB

The BBB refers to the barrier, predominantly established by the microvascular brain ECs, which tightly controls molecules' transportation through the vascular wall. The BBB prevents neurotoxic plasma components, blood cells, and pathogens from entering the brain and allows the transport of blood-borne substances essential for proper neuronal function toward the brain parenchyma (Sweeney et al., 2019). Although the properties of the BBB are primarily manifested within the ECs, the interaction of ECs with pericytes and astrocytes is critical for the induction and maintenance of the BBB (Figure 1).

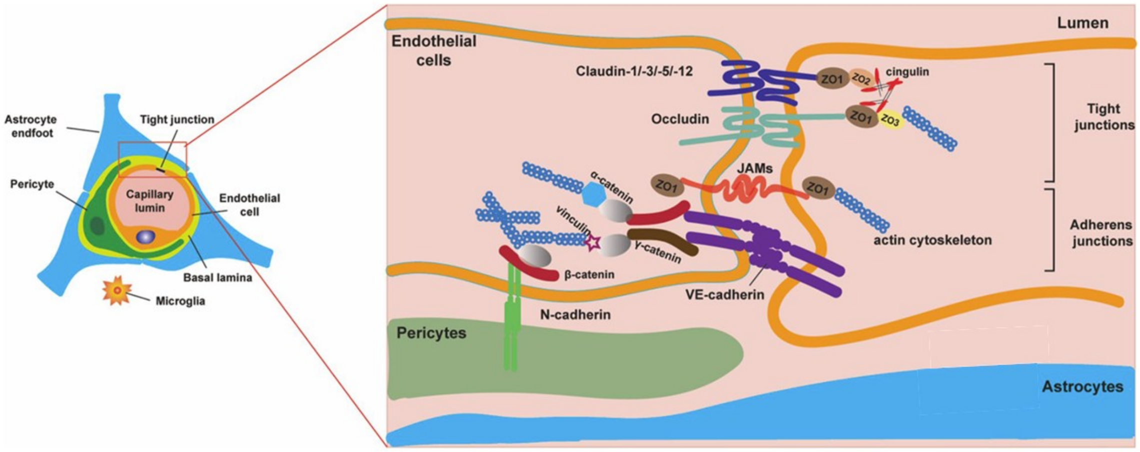

***Figure 1: Cellular organization and molecular structure of the BBB.** Left) The ECs, covered by the basal lamina or else basement membrane, form the vessel wall and control the transportation of molecules from and towards the brain parenchyma. Pericytes are in close contact with ECs and share the same*

basement membrane. Astrocytic endfeet cover almost completely the basement membrane and separate the vessel from the brain parenchyma. Right) ECs express highly specialized intercellular TJs and adherens junctions that prevent the paracellular diffusion of ions and hydrophilic molecules. Abbreviations: EC: endothelial cell, TJs: tight junctions, ZO: zonula occludens, JAM: junctional adhesion molecule. Source Kadry et al. Fluids Barriers CNS (2020), CC BY 4.0 DEED, https://creativecommons.org/licenses/by/4.0/.

1.3.1 Cellular components of the BBB

Endothelial cells

The ECs of the brain microvasculature have unique characteristics that enable them to precisely control the paracellular and transcellular movement of molecules. Gas exchange (O_2 and carbon dioxide, CO_2) occurs freely through the EC monolayer and some small lipophilic molecules, like many CNS permeable drugs, penetrate the BBB with passive diffusion (Fischer et al., 1998). However, the intercellular tight junctions (TJs) that form between neighboring ECs prevent the paracellular diffusion of ions and hydrophilic molecules. The barrier properties of the brain microvascular ECs are supplemented with the lack of fenestrae, the limited transcytosis, and the presence of specialized transporters on the luminal and abluminal side of the vascular wall that control molecules traffic to and from the brain parenchyma (Daneman & Prat, 2015; Kadry et al., 2020; Worzfeld & Schwaninger, 2016).

Pericytes

Pericytes share the same basement membrane with ECs in the microvascular bed (Figure 1). Pericytes and ECs exchange ions, metabolites, second messengers, and ribonucleic acids through peg-and-socket intercellular contacts (Ornelas et al., 2021). Numerous *in vitro* and *in vivo* studies have shown that pericytes play a significant role in the development and structural integrity of the BBB (Daneman et al., 2010b). Pericytes contribute to BBB properties by suppressing the transcytosis in brain ECs and leukocyte adhesion molecule expression (Daneman & Prat, 2015; Tietz & Engelhardt, 2015). Some studies have indicated that loss of pericytes results in BBB dysfunction and negatively affects capillary blood flow dynamics and these effects are exacerbated in the aged brain BBB (Bell et al., 2010; Berthiaume et al., 2022; Hall et al., 2014; Hartmann et al., 2021; Ornelas et al., 2021).

Astrocytes

The astrocyte-polarized cellular processes (glia limitans) ensheath blood vessels in the CNS. Due to their position, they provide a link between neurons and ECs. *In vitro* and *in vivo* studies have shown that astrocyte-secreted factors, including Sonic hedgehog, angiotensin, wingless-related integration site (Wnt), and basic fibroblast growth factor, are involved in BBB properties (Guérit et al., 2021; Profaci et al., 2020). However, during embryogenesis in rodents, astrogliogenesis and ensheathment of vasculature occur after the formation of the BBB, and laser ablation of endfeet in adult mice does not lead to BBB leakage (Daneman et al., 2010b; Kubotera et al., 2019). These findings point to the dispensable role of close astrocyte-endothelial interaction for the formation of BBB during embryogenesis and maintenance during adulthood. Perhaps astrocytes in the adult brain are more relevant for repairing and modulating BBB under specific stimuli (Bush et al., 1999; Profaci et al., 2020).

1.3.2 Molecular structure of the BBB

1.3.2.1 Junctional molecules of the BBB

As described above (section 1.3.1) ECs express highly specialized TJs which are a crucial characteristic of the BBB. The TJs form the interendothelial junctions, along with adherens junctions, between neighboring membranes of different cells or the same cell, creating a high electrical resistance barrier to ions and hydrophilic molecules (Kadry et al., 2020; Profaci et al., 2020; Tietz & Engelhardt, 2015). The TJs also restrict the free movement of integral membrane molecules, thus leading to the polarized phenotype of brain ECs to apical and basolateral sides (Daneman & Prat, 2015; Worzfeld & Schwaninger, 2016). The TJs' most critical and studied members in the CNS are the integral transmembrane proteins claudins, occludin and junctional adhesion molecules (JAMs) (Daneman & Prat, 2015; Kadry et al., 2020) (Figure 1). Furthermore, the members of the zonula occludens family (ZO-1, ZO-2, ZO-3) and cingulin are some of the intracellular supporting proteins that contribute to the formation of the barrier. They bind to the intracellular part of the TJs and link them to the actin cytoskeleton, adherens junctions and polarity complexes. (Figure 1) (Daneman & Prat, 2015; Kadry et al., 2020; Tietz & Engelhardt, 2015).

Claudins

The most significant member of the family is claudin-5, which has been shown to be specifically highly expressed and essential for the BBB's integrity. Claudin-5-deficient mice show BBB leakage to molecules smaller than 800 Daltons and die shortly after birth (Nitta et al., 2003). Other claudin proteins that have been studied *in vitro* or *in vivo* in relevance to the BBB are the claudin-1,-2,-3,-5,-11,-12 (Daneman & Prat, 2015; Kadry et al., 2020; Profaci et al., 2020; Sweeney et al., 2019; Tietz & Engelhardt, 2015).

Occludin

Occludin is a transmembrane protein highly expressed on the TJs of the CNS ECs. Occludin-deficient mice are viable and have intact CNS barriers, suggesting that occludin is not crucial for paracellular permeability. However, the deletion of occludin in these mice, similar to human diseases resulting from mutations in the occludin gene, leads to CNS calcification, pointing to the role of occludin in calcium homeostasis in the brain (Saitou et al., 2000; Zhao et al., 2015).

JAMs

JAM-A, JAM-B, and JAM-C are membrane proteins localized at TJs in epithelial cells and ECs. JAMs have been shown to regulate leukocyte extravasation and junctional tightness at the BBB (Garrido-Urbani et al., 2014; Lamagna et al., 2005).

Zonnula occludens

ZO-1, ZO-2, and ZO-3 are important cytoplasmic proteins localized in the TJs of the BBB. They link the membrane TJ proteins (claudins, occludin, JAMs) to the actin and vinculin-based cytoskeletal proteins, stabilizing the transmembrane elements and provide structural support to the ECs. (Itoh et al., 1999; Kadry et al., 2020; Tietz & Engelhardt, 2015).

Other BBB junctional molecules

Essential for the vascular physiology of the BBB is also the interaction of TJs with the adherens junctions, cadherin-5 (CDH5) and platelet endothelial cell adhesion molecule 1 (PECAM1 or cluster of differentiation 31, CD31) (Taddei et al., 2008). These transmembrane proteins are present in all ECs and are responsible for establishing connections between neighboring cells (Carmeliet et al., 1999). Finally, the proteins tricellulin (MARVEL domain containing 2, MARVELD2) and lipoprotein stimulated receptor (LSR), that are expressed in the contacts of three neighboring ECs and form the tricellular junctions, may be critical to the barrier formation and function (Daneman et al., 2010a; Tietz & Engelhardt, 2015).

1.3.2.2 BBB transporters

The transportation of molecules through the microvascular brain ECs is a tightly regulated process that protects the brain from toxic circulating substances and maintains water homeostasis, ions, glucose, and nutrients optimal for neuronal function. Although passive diffusion occurs through the EC membrane for small lipophilic molecules and gases, active transportation is the principal way of conveying nutrients through the vessel wall. The active transportation through the endothelial membrane is mediated by efflux transporters, carrier-mediated transport (CMT), transcytosis, transporters of the major facilitator superfamily, and ion transporters (Kadry et al., 2020).

Efflux transporters

These membrane proteins have an adenosine 5’-triphosphate (ATP)-binding cassette (ABC). They are efflux pumps that hydrolyze ATP and transport primarily xenobiotics and endogenous metabolites up their concentration gradient, mainly from endothelium to blood. The most abundant efflux transporters of the BBB are the P-glycoprotein (P-gp), the multidrug resistance-associated proteins

(MRP1/2/3/4/5), and breast cancer resistance protein (BCRP) (Kadry et al., 2020; Profaci et al., 2020; Sweeney et al., 2019).

CMT

The membrane transporters of this category are encoded genes within the solute carrier (SLC) transporter gene family. This family consists of more than 300 transporter genes. SLC transporters facilitate the transcellular movement of amino acids, carbohydrates, monocarboxylic acids, fatty acids, hormones, nucleotides, organic anions and cations, amines, choline, and vitamins. (Kadry et al., 2020; Sweeney et al., 2019; Worzfeld & Schwaninger, 2016).

Transcytosis

The transportation of larger molecules like specific neuroactive peptides, regulatory proteins, hormones, and growth factors through the BBB is facilitated by the transcytotic mechanisms receptor-mediated transcytosis (RMT) and adsorptive-mediated transcytosis (AMT) (Figure 2). Examples of RMT include transcytosis of insulin and transferrin (Tf), the transcytosis of immunoglobulin G (IgG) via fragment crystallizable receptor (FcR) from brain parenchyma to the blood, or only endocytosis into the brain capillary endothelium of acetyl low-density lipoprotein (LDL) from the blood into the BBB endothelium. (Kadry et al., 2020; Sweeney et al., 2019; Worzfeld & Schwaninger, 2016).

Major facilitator superfamily

The endothelial major facilitator superfamily domain-containing protein 2a (MFSD2a) is essential for transporting omega-3 fatty acids, like docosahexaenoic acid (DHA), into the brain parenchyma. Mice that do not express the MFSD2a on the brain endothelium show brain DHA deficits and a compromised BBB (Ben-Zvi et al., 2014; Nguyen et al., 2014).

Ion transportation

The ion homeostasis is achieved through various membrane proteins, including abluminal sodium pumps, the luminal sodium potassium chloride co-transporter 1 (Na^+ K^+ Cl^- co-transporter 1 or NKCC1), calcium transporters, and potassium channels. (Sweeney et al., 2019; Worzfeld & Schwaninger, 2016).

Immune cell movement across the BBB

Under physiological conditions in the adult brain, there is limited infiltration of immune cells into the CNS. However, during pathological states, ECs upregulate the expression of vascular cell adhesion molecule 1 (VCAM-1) and intercellular adhesion molecule 1 (ICAM-1), leading to the arrest and infiltration of circulating immune cells into the parenchyma (Abadier et al., 2015; Engelhardt & Ransohoff, 2012).

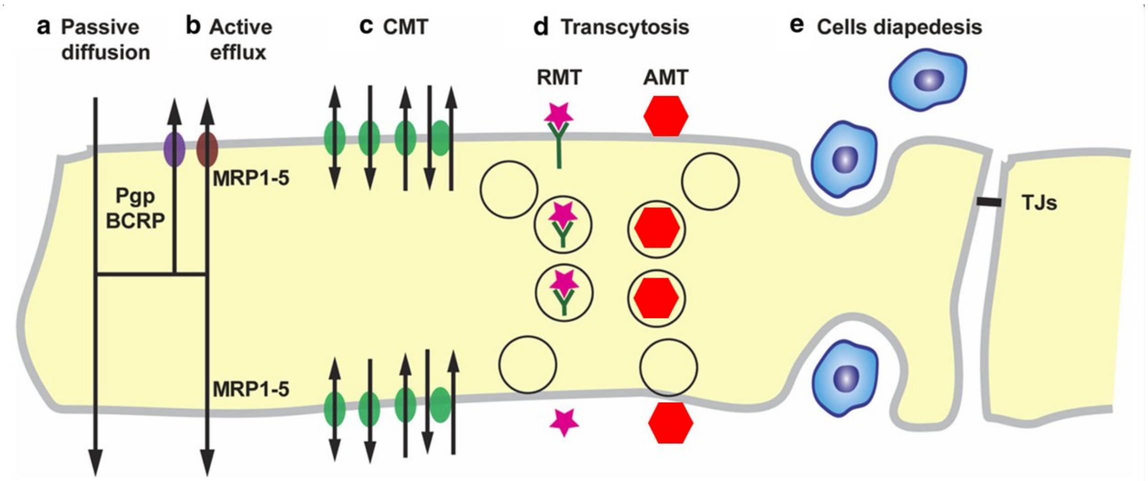

Figure 2: ***Transportation through the BBB:*** *Graphical depiction of the main transportation mechanisms through the BBB. Passive diffusion occurs mainly for small lipophilic molecules and gases. Larger molecules move through the endothelial plasma membrane via active efflux, CMT and transcytotic mechanisms. Immune cell movement across the BBB occurs through cell diapedesis. Abbreviations: P-gp: P-glycoprotein, BCRP: breast cancer resistance protein, MRP: multidrug resistance-associated protein, CMT: carrier-mediated transport, RMT: receptor-mediated transcytosis, AMT: adsorptive-mediated transcytosis, TJs: tight junctions Source Kadry et al. Fluids Barriers CNS (2020), CC BY 4.0 DEED, https://creativecommons.org/licenses/by/4.0/.*

1.4 Brain endothelial molecular pathways in health and disease

As part of the NVU and a building block of BBB, brain ECs interact with neurons, glial and mural cells to control cerebral blood flow and meet the metabolic demands of the brain with high spatiotemporal accuracy. By detecting chemical and mechanical cues originating from both sides of the vascular wall, ECs are able to respond to systemic and parenchymal signals and maintain brain homeostasis. This part will detail how ECs perceive mechanical and chemical forces through the activation of specific signaling pathways in physiological and pathological conditions.

1.4.1 Shear Stress

The strategic position of ECs in the vascular wall subjects them to blood-borne chemical stimuli as well as to highly dynamic biomechanical forces like shear stress. Shear stress is the mechanical frictional force exerted on ECs due to the blood flow. The ability of ECs to sense and adapt their functions to shear stress is essential for several developmental and physiological vascular processes as well as for the initiation and progression of pathological conditions.

Types of shear stress

The hemodynamic forces show great variation along the vascular segments and determine the mechanical responses evoked by ECs. For example, shear stress of large vessels like the human inferior vena cava and the abdominal aorta has been estimated at around 3.5 dyn/cm^2 (Cheng et al., 2003), in the human common carotid artery at 10-14 dyn/cm^2 (Reneman et al., 2006), while in smaller arterioles shear stress is significantly higher and estimated at 47.1 dyn/cm^2 (Lipowsky et al., 1978). However, it is of interest that shear stress at the vascular segments may differ between organs (Koutsiaris et al., 2007, 2013; Roux et al., 2020) and more research is needed to clarify this.

The vessel architecture and/or pathological conditions can significantly influence the type of flow. First of all, shear stress types can be roughly divided into two categories, the undisturbed laminar flow and the disturbed laminar flow (Chatzizisis et al., 2007; Dessalles et al., 2021). More specifically, in straight parts of mainly large vessels, shear stress is characterized as undisturbed laminar flow since the blood flow is smoothed and streamlined (Chatzizisis et al., 2007). Undisturbed laminar shear stress has protective effects on the blood vessels which result from the down-regulation of pro-inflammatory cytokines and adhesion molecules (Albarrán-Juárez et al., 2018; Tzima et al., 2005; Walpola et al., 1995). On the other hand, disturbed laminar flow is characterized by flow recirculation, separation, and reattachment to forward flow (Chatzizisis et al., 2007). Disturbed laminar flow can occur during pathological states like arterial stenosis or physiologically in the branching regions of the vasculature. In contrast to undisturbed laminar shear stress, disturbed shear stress can result in atherogenic processes (Albarrán-Juárez et al., 2018; Ku et al., 1985; Tzima et al., 2005; Walpola et al., 1995). Finally, a third type of shear stress, the pulsatile flow, describes the periodic changes in shear stress during the cardiac cycle. It is important to note that *in vivo* the types of flow can be more complicated and a combination of the aforementioned types of flow may act in a spatiotemporal manner on the vasculature (Chatzizisis et al., 2007).

Mechanosignaling in ECs

Many *in vitro* and *in vivo* studies have revealed candidate mechanisms through which ECs can sense shear stress and convert mechanical forces to biochemical signals. The localization of the mechanosensors and the mechanotransduction molecules can be found in different cell compartments. For example, the vascular endothelial growth factor receptors (VEGFRs), VEGFR2 (or else kinase insert domain receptor KDR) and VEGFR3, which are transmembrane tyrosine kinases are activated by shear stress in a ligand-independent way and form a mechanosensory complex that includes the junctional molecules PECAM1 and CDH5 (Coon et al., 2015; Tzima et al., 2005). Similar to VEGFRs, the Tie2 receptor, a cell membrane protein, has been shown to be activated by shear stress in a ligand-independent manner (Jong Lee & Young Koh, 2003). Furthermore, the guanine nucleotide-binding protein (G protein) coupled receptor 68 (GPR68) and the cation permeable ion channel Piezo1, have been identified as mechanosensors expressed in the EC membrane and necessary for shear stress sensing (Coste et al., 2010; Xu et al., 2018). Also, the glycocalyx, caveolae, and primary cilia are located on the apical side of the cell membrane and seem to play a role in shear stress mechanotransduction (Ando & Yamamoto, 2013; Fels & Kusche-Vihrog, 2020). In addition, mechanotransduction signaling may lead downstream to activation of the intracellular G protein subunits alpha q/11 ($G\alpha_{q/11}$) and adhesion molecules expressed in the basolateral side (Albarrán-Juárez et al., 2018). Finally, cytoskeleton reorganization as a result of the shear stress response can be mediated by focal adhesion sites, cellular junctional molecules and integrins (Fels & Kusche-Vihrog, 2020; Tzima et al., 2005).

ECs responses to shear stress are diverse and depend on many factors. Among others, it is well known that shear stress leads to nitric oxide (NO) and prostacyclin release which diffuse to adjacent SMCs and result in vessel dilation, a phenomenon called flow-dependent dilation (Frangos et al., 1985; Joannides et al., 1995). Also, it is important to note that shear stress effects on cytoskeletal reorganization is the formation of actin stress fibers or cell polarization through microtubules (Hayakawa et al., 2011b; Tzima et al., 2003, 2005).

Shear stress in health and disease

Shear stress controls vascular morphogenesis and remodeling, angiogenesis, and vascular tone (Dajnowiec & Langille, 2007; Joannides et al., 1995; Kamiya & Togawa, 1980). Additionally, diseases like hypertension, atherosclerosis, thrombosis, and aneurysms develop when ECs fail to respond to shear stress (Ando & Yamamoto, 2013).

It is known that in cerebrovascular and neurological diseases, like stroke, Alzheimer's disease (AD), and hypertension, as well as during normal aging, the blood flow is compromised, with devastating effects on neuronal function (Cortes-Canteli & Iadecola, 2020). How the brain vasculature responds to the changes in blood flow is still not well known, and given the unique properties of the ECs along the brain vasculature tree, more research is needed to elucidate the mechanosensory mechanisms.

Shear stress and BBB

Most studies related to shear stress have focused on the vasculature of the periphery. Little is known about its effect on the biology of brain ECs. Studies in some *in vitro* models of BBB have shown that shear stress induces upregulation of TJs and adherens junctions, some membrane transporters, receptors like THBD, and higher trans-endothelial electrical resistance (TEER) (Cucullo et al., 2011; Garcia-Polite et al., 2017; Rochfort & Cummins, 2015). On the other hand, these findings were not always confirmed, showing the discrepancies between the current *in vitro* models of BBB (Choublier et al., 2022; DeStefano et al., 2017). Other studies have revealed that the small guanosine 5'-triphosphate (GTP)-binding proteins with intrinsic hydrolase activity (GTPases) like the rat sarcoma (RAS) homolog family member A (RHOA), the cell division cycle 42 (CDC42), and the rat sarcoma-related C3 botulinum toxin substrate 1 (RAC1), whose expression can be induced by shear stress (Liu et al., 2014; Tzima et al., 2003; Wojciak-Stothard & Ridley, 2003), control the brain EC polarization and affect the BBB properties (Worzfeld & Schwaninger, 2016).

1.4.2 Aging brain and endothelium

With aging, several systemic and CNS-originating factors lead to endothelium changes that affect its physiological role in supplying the brain with blood. Vascular aging has been linked to the initiation and progression of CNS-related diseases, among which AD and Stroke are today leading causes of death worldwide (WHO, *Global Health Estimates* 2020). Several characteristic phenotypic changes mark the vasculature during normal aging, which, even without common risk factors, leads to a disease-prone state (Yang et al., 2017).

Atherosclerosis has been characterized as a critical feature of vascular aging (Cortes-Canteli & Iadecola, 2020). Atherosclerosis is characterized by the deposition of atherosclerotic plaques in the vessel wall leading to the narrowing of the vascular lumen, chronic cerebral hypoperfusion, ischemia and eventually cognitive impairments and dementia (Huang et al., 2021). Atherosclerotic lesions found in the arteries of the circle of Willis and the pial arteries have been correlated by some studies to characteristic features of AD pathology such as plaques and tangle load, and cognitive performance (Arvanitakis et al., 2016; Roher et al., 2003).

Another characteristic of vascular aging is arterial stiffness (Cortes-Canteli & Iadecola, 2020; Yang et al., 2017). Arterial stiffness of cerebrovascular and systemic arteries leads to increased pulse pressure and velocity (Schnerr et al., 2017), which may negatively impact the susceptible cerebral microcirculation. Also, arterial stiffness may profoundly affect the brain by decreasing cerebral blood flow (Jefferson et al., 2018) and is considered a risk factor for cerebrovascular disease and dementia (Poels et al., 2007). Finally, factors like the increased advanced glycation products and upregulation of the renin-angiotensin system which increases with aging, may contribute to arterial wall stiffness (Semba et al., 2015; Wang et al., 2005).

Moreover, vascular aging is characterized by increased oxidative stress and inflammation. Increased oxidative stress leads to the inactivation of NO, affecting the vasodilation and the atheroprotective effects of this mediator (Förstermann & Münzel, 2006). Furthermore, during aging, pro-inflammatory cytokines production, such as tumor necrosis factor (TNF), interleukin (IL)-6, and IL-1β, is elevated and promotes vascular dysfunction and endothelial apoptosis (Bruunsgaard et al., 2000; Miles et al., 2008).

BBB disruption is also a pathological mark of normal aging (Farrall & Wardlaw, 2009; Montagne et al., 2015). In healthy aging individuals, BBB permeability is increased and comorbid pathologies such as AD, leukoaraiosis and stroke result in a more severe BBB dysfunction (Yang et al., 2017). The main mechanisms causing BBB dysfunction during aging are chronic hypoxia and inflammation, which result in activating matrix metalloproteinases.

Microvascular rarefaction and increased endothelial apoptosis during aging may contribute to neuronal and oligodendrocyte malfunction by reduction in the secretion of growth factors (Riddle et al., 2003; Yang et al., 2017). In adults, brain derived neurotrophic factor (BDNF) is essential for guiding neuroblasts along the blood vessels (Snapyan et al., 2009) and for the proliferation and survival of oligodendrocytes (Arai & Lo, 2009). In addition to the neuronal BDNF, some studies have demonstrated that ECs may be an important source of BDNF in the brain (Monnier et al., 2017; Nakahashi et al., 2000). Furthermore, the vascular endothelial growth factor (VEGF) has been shown to have a substantial influence on various neuronal cell functions like dendritogenesis (Licht et al., 2010), axon guidance (Ruiz de Almodovar et al., 2011), neurogenesis (Jin et al., 2002) and oligodendrocyte precursor cell migration (Hayakawa et al., 2011a). Therefore, brain EC loss during normal aging and the subsequent reduction of the aforementioned growth factors have been proposed to contribute to neuronal and oligodendrocyte malfunction.

A further risk factor that develops with age is hypertension. Hypertension is a risk factor for dementia (Gottesman et al., 2017) and stroke (Benjamin et al., 2018) and is linked to AD (Kivipelto et al., 2001). This condition damages cerebral vessels structurally and functionally through vascular oxidative stress (Faraco & Iadecola, 2013). Furthermore, hypertension promotes atherosclerosis, reduces resting cerebral blood flow, leads to BBB leakage, and alters all the major factors regulating cerebral circulation (Hollander et al., 1993; Iadecola & Gottesman, 2019; Jennings et al., 2005).

1.4.3 String vessels and capillary rarefaction

So-called string vessels have been described as a histological finding in mammalian and avian tissue located, but not restricted, to the CNS microvasculature (Brown, 2010; Kamba et al., 2006). The structure of string vessels under the microscope is a characteristic thin connective tissue strand (string) composed of endothelial basement membrane components (collagen, laminin, and heparan sulfate) lacking ECs (Brown, 2010). String vessels are not perfused and research from the previous century has already focused on their formation and role during health and disease (Brown, 2010; Kohner & Henkind, 1970; Venecia et al., 1976). A prominent theory suggests that string vessels form after EC destruction, which leads to vessel collapse and manifests with the characteristic empty basement membrane tubes and capillary loss. However, string vessels could potentially precede the formation of new capillaries by providing a structural scaffold for the new vessel to grow (Kamba et al., 2006). Finally, it was recently demonstrated that in the brain exist structures named interpericyte tunneling nanotubes, which are essential for pericytic functions. These structures connect two bona fide pericytes in neighboring capillaries and have the characteristic structure of string vessels (Alarcon-Martinez et al., 2020).

String vessels are increased in CNS-related pathological conditions but they can also be found in the normal human brain at all life stages (Challa et al., 2002, 2004; Forsberg et al., 2018). Furthermore, string vessels might provide evidence of capillary loss and many studies have shown reduced cerebral microvascular density in the aging brain (Abernethy et al., 1993; Amenta et al., 1995; Brown, 2010; Reeson et al., 2018; Riddle et al., 2003). This could be explained by changes occurring during normal aging, like the loss of pro-angiogenic signals, oxidative damage of the endothelium, and lack of responsiveness to VEGF and hypoxia-inducible factor-1 alpha (HIF-1α) (Frenkel-Denkberg et al., 1999; Reeson et al., 2018; Rivard et al., 2000; Watanabe et al., 2020).

String vessels and microvascular rarefaction are associated with age-dependent cognitive decline and AD (Brown, 2010; Watanabe et al., 2020). In AD, it has been shown that more string vessels form compared to age-matched controls (Challa et al., 2004). Microvascular rarefaction occurs in 90 % of AD brains and, among others, is attributed to the toxicity of amyloid-β plaques (Aβ) to vascular cells (Cortes-Canteli & Iadecola, 2020).

Finally, string vessels are a histopathological hallmark of the genetic disease incontinentia pigmenti. In incontinentia pigmenti, the nuclear factor "kappa-light-chain-enhancer" of activated B-cells (NF-κB) signaling pathway is disrupted, leading to severe neurological symptoms. In a mouse model of incontinentia pigmenti, Ridder and colleagues have shown a brain endothelial-specific manner of the canonical NF-κB signaling pathway disruption, linked with significant upregulation of string vessels, leading to characteristic disease-related neurological symptoms (Ridder et al., 2015). These results point to the significance of the NF-κB signaling pathway and its regulation in the brain endothelium, which is further discussed below (see section 1.4.7).

1.4.4 G protein-coupled receptors

Among the wide variety of membrane proteins expressed in brain ECs, G protein-coupled receptors (GPCRs) have been shown to play an essential role in their function. In the human organism, GPCRs are the largest superfamily of integral membrane proteins, with more than 800 genes identified (Isberg et al., 2016). The GPCRs can be activated from various stimuli and transduce signals through diverse signaling pathways, controlling many physiological processes. The diversity of GPCRs positions them as an attractive pharmacological target, and currently, 20-30 % of marketed drugs target GPCRs (Pluimer et al., 2020).

The GPCRs have a common tertiary structure. It is comprised of an extracellular part (N-terminus and three extracellular loops), a transmembrane part (7 α-helices) and an intracellular part (C-terminus, three intracellular loops, amphiphatic helix). Upon ligand binding on the extracellular part, the intracellular region undergoes a conformational change and acts as a guanine nucleotide exchange factor (GEF). GEF exchanges guanosine diphosphate (GDP) for GTP and downstream signaling mediators are affected through phosphorylation/activation, including the heterotrimeric G proteins, kinases, and arrestins (Pluimer et al., 2020). The GPCRs of the human genome are divided into four classes: class A (rhodopsin), class B (subfamily B1 secretin and B2 adhesion), class C (glutamate) and class F (Frizzled). All four mammalian superfamilies are expressed in the BBB endothelium and some have been identified as essential for the BBB function and maintenance in developing and adult brain vasculature (Pluimer et al., 2020; Wootten et al., 2018; Yang et al., 2021).

1.4.5 The heterotrimeric G proteins

As discussed already above (section 1.4.4) one of the downstream signaling pathways of the GPCR activation involves the heterotrimeric G proteins. The heterotrimeric G proteins are formed by the G protein subunits G alpha (Gα), beta (Gβ) and gamma (Gγ). The human genome has 16 Gα, 5 Gβ and 13 Gγ subunits. When the GEF part of the GPCR leads to an exchange of GDP to GTP at the Gα subunit, it causes dissociation of it from the Gβγ proteins. Then, the Gα subunits signal independently, and the Gβ and Gγ subunits function as a single unit (Gβγ). The signaling is terminated by the intrinsic GTPase activity of the Gα subunit, which hydrolyzes the GTP to GDP. This process can be accelerated by GTPase activating proteins (GAPs) that bind to the Gα subunit (Pluimer et al., 2020; Syrovatkina et al., 2016).

The G proteins are classified according to Gα subunits into four major families ($G\alpha_s$, $G\alpha_{i/o}$, $G\alpha_{q/11}$ and $G\alpha_{12/13}$) based on the sequence and functional similarities. The $G\alpha_s$ and $G\alpha_{i/o}$ family, according to their well-defined G protein signaling pathway, regulate downstream the levels of cyclic adenosine monophosphate (cAMP) by stimulating or inhibiting adenylyl cyclase, respectively (Figure 3). The $G\alpha_{q/11}$ proteins' signaling pathway regulates the levels of inositol 1,4,5-trisphosphate (IP_3) and diacylglycerol (DAG) by activating the phospholipase C beta (PLC-β) (Figure 3). Finally, the $G\alpha_{12/13}$ signaling pathway involves the activation of small GTPases in the Rho family (Syrovatkina et al., 2016) (Figure 3). Nowadays, it is known that different GPCRs are coupled to the same Gα proteins and vice versa. Gβγ subunits have both regulatory and signaling functions, such as scaffolds for receptor kinases and as modulators of ion channels (Wootten et al., 2018).

G$\alpha_{q/11}$ family

In humans, the Gα_q family consists of Gα_q, Gα_{11}, Gα_{14} and Gα_{16} (the mouse equivalent is Gα_{15}). Gα_q and Gα_{11} are ubiquitously expressed, while Gα_{14} is mainly found in the kidney, lung, and liver. G$\alpha_{15/16}$ is specifically expressed in hematopoietic cells (Syrovatkina et al., 2016).

Gα_q family G proteins activate the beta-isoforms of PLC (PLC-β1-4), which cleave phosphatidylinositol 4,5-bisphosphate (PIP$_2$) into IP$_3$ and membrane-bound DAG. IP$_3$ binds then to the calcium permeable IP$_3$ receptors (IP$_3$Rs) localized on the endoplasmic reticulum membrane, leading to Ca^{2+} release from the endoplasmic reticulum to the cytosol. DAG can activate protein kinase C or membrane-bound receptors like the transient receptor potential cation (TRPC) channels 3 and 6 (Guerra et al., 2018; Syrovatkina et al., 2016).

Interestingly, the importance of this signaling pathway for normal vessel function is highlighted by a rare human somatic genetic mutation in the *GNAQ* locus that encodes the Gα_q protein and causes capillary malformations (Bichsel & Bischoff, 2019). This mutation is enriched in ECs isolated from the brain, skin, and choroidal capillary malformations (Bichsel & Bischoff, 2019). The mutation leads to a constitutively active Gα_q protein by reducing the affinity of GDP and formation of the inactive complex GDP-Gαβγ (Bichsel & Bischoff, 2019). Whether the loss of function is also essential for EC function in humans remains to be answered. In animal models, it has been demonstrated that the G$\alpha_{q/11}$ is essential for the regulation of blood pressure and during atherosclerosis (Albarrán-Juárez et al., 2018; Wang et al., 2015). Finally, our group has recently demonstrated that the selective knockout of the G$\alpha_{q/11}$ proteins from the brain endothelium leads to impaired cerebrovascular reactivity and endothelial dysfunction (Wenzel et al., 2020a) but the molecular mechanisms that involve the endothelial G$\alpha_{q/11}$- Ca^{2+} signaling and the observed phenotype are still not clear.

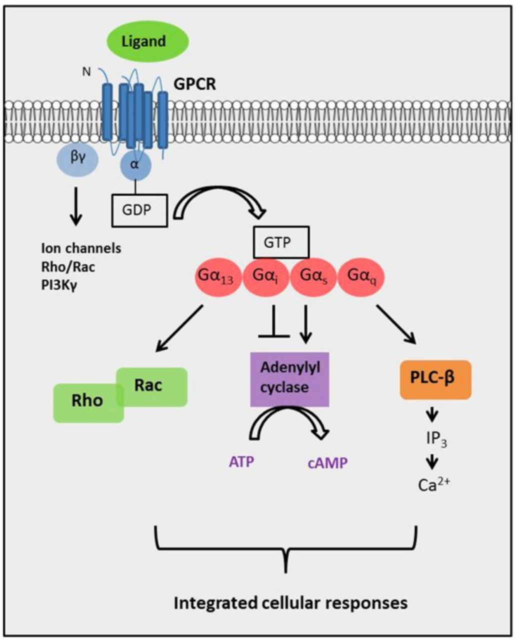

Figure 3: G protein-coupled receptor signaling. *Schematic presentation of the GPCR signaling upon activation through the four major families* $G\alpha_s$, $G\alpha_{i/o}$, $G\alpha_{q/11}$ *and* $G\alpha_{12/13}$ *and the Gβγ subunits. Abbreviations: GPCR: G protein-coupled receptor, GDP: guanosine diphosphate, GTP: guanosine triphosphate, Gα: G protein subunit alpha, Gβγ: G protein subunits beta gamma, PI3Kγ: phosphatidylinositol bisphosphate 3-kinase gamma, PLC-β: phospholipase C beta,* IP_3*: inositol triphosphate, ATP: adenosine triphosphate, cAMP: cyclic adenosine monophosphate, Rho: Ras homolog family, Rac: Ras-related C3 botulinum toxin substrate family. Source Lynch et al. Int. J. Mol. Sci. 2016, CC BY 4.0 DEED, https://creativecommons.org/licenses/by/4.0/.*

1.4.6 Calcium signaling in brain endothelial cells

ECs receive a myriad of chemical and physical stimuli originating from the luminal and abluminal side of the vessel that evoke changes in $[Ca^{2+}]_i$ concentrations. Dysregulation of the $[Ca^{2+}]_i$ signals has been implicated in the development of diseases like hypertension, atherosclerosis, type 2 diabetes, obesity, neurodegenerative disorders, and cancer (Lin et al., 2019; Moccia, 2018; Moccia et al., 2023; Peters et al., 2022). Indeed, endothelial $[Ca^{2+}]_i$ signals regulate vascular permeability (Tiruppathi et al., 2002), coagulation (Van Hinsbergh, 2012), leukocyte transmigration (Dalal et al., 2021) and neurovascular coupling (Hillman, 2014). However, the most widely investigated role of $[Ca^{2+}]_i$ is the regulation of vascular tone and angiogenesis. The synthesis and release of vasoactive molecules like NO and the endothelium-dependent hyperpolarization factor through the small/intermediate conductance Ca^{2+} activated K^+ channels (SKCA/IKCA) are two mechanisms that have been extensively investigated (Moccia et al., 2023). During angiogenesis, VEGF, the most important angiogenic factor, may influence$[Ca^{2+}]_i$ concentration through distinct pathways to finely tune the angiogenic process (Moccia et al., 2023; Sivaraj et al., 2015; Yokota et al., 2015). A wide range of mediators like acetylcholine, ATP, histamine, and bradykinin increases the cytosolic Ca^{2+} by binding to their respective GPCRs and through G$\alpha_{q/11}$ proteins. Also, angiopoietins and reactive oxygen species (ROS) induce Ca^{2+} signals, which are essential to exert their function (Negri et al., 2022; Pafumi et al., 2015).

Finally, $[Ca^{2+}]_i$ signals have been shown to mediate the pro- and anti-apoptotic effects of NF-κB in various cell types as well as in ECs (Lilienbaum & Israël, 2003; Sen et al., 1996; Thippegowda et al., 2010). In periphery ECs, it has been described that thrombin-induced Ca^{2+} influx through the TRPC1 results in the activation of NF-κB and subsequently expression of its target, the antiapoptotic protein A20 (Thippegowda et al., 2010). Also, it is of interest that the calcium-permeable mechanosensor Piezo1 and the G$\alpha_{q/11}$ proteins mediate the shear stress-induced pro-inflammatory effects of NF-κB in periphery ECs (Albarrán-Juárez et al., 2018; Wang et al., 2015, 2016). Whether the NF-κB pathway in brain ECs is also regulated by $[Ca^{2+}]_i$ signals is yet to be elucidated.

1.4.7 The NF-κB pathway

NF-κB is a transcription factor that was discovered in 1986 as a regulator of the expression of the immunoglobulin κ light chain in mature B cells and plasma cells (Sen & Baltimore, 1986). The NF-κB is a dimer complex and, depending on the subunits, can occur either as a homodimer or a heterodimer. NF-κB subunits belong to a family that consists of five members: p65 (RelA), RelB, c-Rel, p105/p50 (NF-κB1), and p100/p52 (NF-κB2). The most abundant combination, found in almost all cell types, is the heterodimer p65 and p50. The inactive NF-κB protein complex is secluded in the cytosol by inhibitory proteins, like the IκB family proteins (eg. the NF-κB inhibitor alpha, IκBα) or the precursor proteins p105 and p100, and upon activation translocates to the nucleus where it regulates the transcription of a variety of targets involved in inflammation, cell division, and cell survival (Brantley et al., 2001; Hayden & Ghosh, 2011). Two signaling pathways lead to the activation of the NF-κB, the canonical and the non-canonical. The canonical pathway can be initiated by cytokines, microbial antigens, growth factors, mitogens, stress agents, or high-energy radiation (Liu et al., 2017). This multitude of stimuli induces the activation of various receptors, like TNF receptor superfamily members, cytokine receptors, pattern-recognition receptors (PRRs), T lymphocyte cell receptor, B lymphocyte cell receptor, or other signaling pathways acting upstream of the NF-κB pathway and in turn lead to the activation of the transforming growth factor beta (TGFβ)-activated kinase 1 (TAK1) (Wenzel & Schwaninger, 2016). TAK1 phosphorylates and activates the IκB kinase (IKK) complex, which consists of two enzymatic subunits, IKK1 (IKKα) and IKK2 (IKKβ), and the regulatory NF-κB essential modulator subunit (NEMO, IKKγ). After the IKK complex is activated, it phosphorylates the IκBa protein, leading to dissociation from NF-κB. The IκBα subunit is tagged with ubiquitin and is directed to the proteasome for degradation. At the same time, the NF-κB dimer, consisting mainly of the dimer of p50/p65 and p50/c-Rel, can translocate to the nucleus (Karin & Delhase, 2000). In the non-canonical signaling pathway, the IKK complex consists of a homodimer of IKK1 and lacks NEMO while the NF-κB complex comprises p100 and RelB. In contrast to the canonical pathway, the NF-κB-inducing kinase (NIK) activates the IKK complex, which in turn phosphorylates the p100 subunit. This phosphorylation induces partial cleavage of p100, and the resulting product is p52. The complex of p52 and RelB is the active NF-κB complex that can translocate to the nucleus. Depending on the stimulation and cell type, both pathways can be simultaneously activated and interact or inhibit each other. The canonical pathway responds fast and has a short transient response, but the non-canonical pathway responds with a longer delay and has a persistent response (Liu et al., 2017; Wenzel & Schwaninger, 2016). The termination of the NF-κB activation may occur by different negative feedback pathways. For example, the expression of target genes of the NF-κB, like IκB and A20, results in the inhibition of NF-κB activity (Wenzel & Schwaninger, 2016).

In the brain, NF-κB plays an essential role in vascular and parenchymal cells' function and survival (Mattson & Meffert, 2006; Wenzel & Schwaninger, 2016). For example, during stroke, where the BBB is compromised due to the inflammatory response and reduced blood flow, NF-κB activation leads to neuronal cell death (Herrmann et al., 2005). Furthermore, activation of NF-κB in pericytes induces the opening of the BBB through secretion of matrix metalloproteinases (Bell et al., 2012), while in astrocytes, a constitutively active NF-κB signaling through IκBα deletion results in the opening of the BBB through inflammatory responses (Manu et al., 2023). Finally, the NF-κB pathway can induce TJ disruption in ECs if sufficiently activated (Aveleira et al., 2010).

On the other hand, it has been shown that the basal activity of NF-κB is necessary for EC survival. In a mouse model, where the regulatory subunit NEMO is not expressed in the brain endothelium, resulting in the inactivation of the canonical NF-κB signaling pathway, brain vessel density was decreased (Ridder et al., 2015; Wenzel et al., 2021). The decreased vessel density is presumably due to increased EC death indicated by the increased string vessel structures. Noteworthy, the BBB function was also compromised, as serum proteins, as well as smaller molecules extravasation into the brain parenchyma was increased. Furthermore, investigations on TJ expression showed decreased occludin but not claudin-5 and ZO-1 levels compared to a control group.

The absence of NEMO in the brain endothelium provokes inflammatory reactions probably induced by astrocytes and most likely caused by increased extravasation of serum proteins (Ridder et al., 2015). In addition, neuronal dysfunction manifested in epilepsy was observed in animals with brain endothelial deletion of genes encoding NEMO. In some cases, the epileptic phenotype led to death (Ridder et al., 2015). The phenotype of mice with brain endothelial deletion of genes encoding NEMO reflects the symptoms of an X-chromosome-linked genetic disease called incontinentia pigmenti. In humans, this rare genetic disease manifests with skin lesions, epileptic seizures, and other neurological disorders (Meuwissen & Mancini, 2012; Poziomczyk et al., 2014). In the brain endothelium, the NF-κB signaling pathway regulates the BBB function and EC survival in physiologic and pathologic conditions. It has been proposed that a bell-shaped graph can describe the NF-κB and BBB integrity activity (Wenzel & Schwaninger, 2016). EC survival is affected when NF-κB activity is lower than the basal activity in physiological states. In contrast, excess NF-κB activity leads to higher BBB permeability and neurological and glial dysfunction. Regulation of the activity of NF-κB in brain ECs could be exploited for potential disease-modifying therapies during cerebrovascular and neurological diseases where the brain endothelial function is affected.

1.5 Aims of the study

Cerebrovascular and neurological diseases have a big impact on the global death toll and share pathological characteristics attributed to vascular aging (WHO, *Global Health Estimates* 2020; T. Yang et al., 2017). The current therapeutic options are limited and there is a great urge for new pharmacological targets. The brain vasculature could be exploited for this purpose due to its unique characteristics and significant involvement in the initiation and progression of the aforementioned pathological conditions.

Our group has previously demonstrated that the $G\alpha_{q/11}$ signaling pathway is important for endothelial function as it leads to impaired cerebrovascular reactivity and endothelial dysfunction (Wenzel et al., 2020a). Although it has been demonstrated that the memory function was not affected by the deletion of $G\alpha_{q/11}$ in young mice, it was not tested whether this signaling pathway is important for the cognitive function in aging mice. Furthermore, $G\alpha_{q/11}$ proteins act downstream of a variety of GPCRs and are involved in the regulation of important endothelial responses through $[Ca^{2+}]_i$ signals. However, the exact upstream and downstream molecular cues are not well known.

More specifically in this thesis, I aimed to:

1) investigate the significance of $G\alpha_{q/11}$ in brain ECs in cognitive function during aging.
2) identify molecular pathways significant for survival and function with a focus on GPCRs, mechanosensors, and NF-κB related pathways.

2 Materials

2.1 Chemicals

Name	Vendor (Catalog number, Cat. Nr)
(2-Hydroxypropyl)-β-cyclodextrin	Sigma-Aldrich (H107-5G)
10X DreamTaq (thermus aquaticus) Green Buffer (includes 20 mM $MgCl_2$)	Thermo Fisher Scientific
2-(aminomethyl)imidazole	Provided by Prof. Bernd Wollscheid, ETH, Zürich, Switzerland
2,2,2-Tribromoethanol (Avertin)	Sigma-Aldrich (T48402)
2-Methylbutane	Carl Roth GmbH &Co. KG(3927.1)
4′,6-diamidino-2-phenylindole (DAPI)	Thermo Fisher Scientific, USA
Adenosin-5′-0-(2-thiodiphosphat) trilithiumsalt (ADP-β-S)	Sigma-Aldrich (A8016)
Antibiotic/Antimycotic (penicillin 10,000 U/mL, streptomycin 10,000 µg/mL, amphotericin B 25 µg/mL)	Thermo Fisher Scientific, Gibco^{TM} (15240-062)
ATP	Sigma Aldrich (A26209)
Biocytin	Pitsch Nucleic Acids, Switzerland (Provided by Prof. Bernd Wollscheid, ETH, Zürich, Switzerland)
Bovine serum albumin (BSA) fraction V	Carl Roth GmbH &Co. KG (8076.4)
Calcium chloride ($CaCl_2$)	Merck KGaA
Collagenase/Dispase®	Roche (11097113001)
D(+)-Glucose monohydrate	Merck KGaA (1.08342.100)
D(+)-Saccharose	Carl Roth GmbH &Co. KG (9286.1)
Deoxyribonuclease I (DNase I)	Roche (11284932001) or PanReacApplichem (A3778)
Dextran MW 60,000-90,000 Da	Thermo Scientific (J144495.A1)
Dimethyl sulfoxide (DMSO)	Sigma-Aldrich (D8418)
Endothelial cell growth supplement (ECGS)	Sigma-Aldrich (E2759)
Ethanol 100 % (absolute)	Carl Roth GmbH &Co. KG (9065.2) or other
Ethanol 70 % (denaturated)	Th. Geyer GmbH & Co. KG (Renningen, Germany) or other
Ethidium bromide (EtBr)	Carl Roth GmbH &Co. KG (2218.1)
Ethylenediaminetetraacetic acid (EDTA)	Carl Roth GmbH &Co. KG (8043.2)
Fluo-4 acetoxymethyl ester (AM)	Thermo Fisher Scientific, Invitrogen (F14217)
Fluorescence mounting medium	Dako (Glostrup, Denmark)

Formaldehyde solution (Formalin) ≥37 %	Carl Roth GmbH &Co. KG (7398.1)
FR900359	Provided by Prof. Evi Kostenis, Institute of Pharmaceutical Biology, University of Bonn, Bonn, Germany.
Glycerol	Carl Roth GmbH &Co. KG (7530.1)
Heparin-sodium-25,000 I.U.(international units)/5 mL	Ratiopharm® or Rotexmedica
Hydrochloric acid (HCl)	Merck KGaA (1003132500)
Isoflurane	Baxter (Deerfield, USA)
Ketamine 100 mg/mL	Bela-pharm GmbH & Co. KG Dr. (Vechta, Germany) or other
L-Glutamine	Thermo Fisher Scientific, Gibco™ (25030-024)
Magnesium chlori de ($MgCl_2$)	Sigma-Aldrich (M-8266)
Miglyol® 812	Caelo (3274)
Mouse collagen IV	Fisher Scientific, Corning™ (354233)
Murine IL-1β	PeproTech (211-11B)
N-α-tosyl-L-lysine chloromethyl ketone hydrochloride (TLCK)	Sigma-Aldrich (90182)
Objective immersion oils type F and type G	Leica Microsystems AG (11513859 and 11513910)
Penicillin 10,000 U/mL / Streptomycin 10,000 µg/mL	Biochrom (A2213) or PanReacApplichem (A8943)
Plasma derived bovine serum (PDS)	First Link (UK) Ltd. (60-00-850)
Pluronic™	Thermo Fisher Scientific, Invitrogen (F-127, P3000MP)
Potassium chloride (KCl)	Merck KGaA (1.04936.1000)
Potassium dihydrogen phosphate (KH_2PO_4)	Merck KGaA
Probenecid	Thermo Fisher Scientific, Invitrogen (P36400)
Protease inhibitor cocktail	Thermo Fisher Scientific (78415)
Proteinase K 20 mg/mL, for genotyping	Carl Roth GmbH &Co. KG (7528.3 or 3719.2)
Puromycin dihydrochloride	Sigma-Aldrich (P8833)
Rat collagen I	Sigma-Aldrich (C3867-1)
Ringer’s solution	Berlin-Chemie AG (Berlin, Germany)
Sodium azide (NaN_3)	Sigma-Aldrich (S8032)
Sodium bicarbonate ($NaHCO_3$)	Carl Roth GmbH &Co. KG (6885.1)
Sodium chloride (NaCl)	J.T. Baker Avantor Materials (7647-14-5)
Sodium deoxycholate	Sigma-Aldrich
Sodium dodecyl sulphate (SDS)	Carl Roth GmbH &Co. KG (2326.2)
Sodium periodate ($NaIO_4$)	Provided by Prof. Bernd Wollscheid, Eidgenössische

	technische hochschule, ETH, Zürich, Switzerland
Sodium phosphate dibasic dihydrate (Na_2HPO_4 x $2H_2O$)	Sigma-Aldrich
Sodium phosphate monobasic monohydrate ($NaH_2PO_4.H_2O$)	Applichem (A1047)
Tamoxifen	Sigma-Aldrich (T-5648)
Thrombin Bovine	Merck Millipore (605157-1KU)
Tris-(hydroxymethyl)-aminomethane hydrochloride (Tris-HCl)	Carl Roth GmbH &Co. KG (4855.2)
Triton X-100	Merck Millipore (9036-19-5)
Trypsin/EDTA 0.05 %/0.02 %	PAN-Biotech (P10-023100)
Tween-20	Sigma-Aldrich (P2287) or other
Xylazine 20 mg/mL	WDT (Garbsen, Germany) or other
Yoda1	Tocris Bioscience (5586)

2.2 Consumables

Name	Type	Vendor
Agarose gel chambers	SUB-CELL®GT	BIO-RAD
Cell culture plates	6-, 12-, 24-, 48-, 96-wells)	Greiner AG (Kremsmünster, Austria)
Culture flask	Cellstar® (T25, T75)	Cellstar, Greiner Bio-one (Austria)
Falcon tubes	15 mL, 50 mL	Greiner AG (Kremsmünster, Austria)
Fatty pen	DAKO	Agilent Technologies, Santa Clara (USA)
Glass coverslips	24x40 mm, 24x50 mm, 24x60 mm, ⌀ 12 mm	Th. Geyer GmbH & Co. KG (Renningen, Germany) or other
Ibidi perfusion sets	White perfusion set (Cat. Nr. 10963), Yellow-Green perfusion set (Cat. Nr. 10964)	ibidi GmbH (Gräfelfing, Germany)
Needles	20 G, 21 G, 22 G, 23 G Microlance™	Becton Dickinson (New Jersey, USA)
Pasteur pipettes	Labsolute® 150 mm, 230 mm	Th. Geyer (Hamburg, Germany)
Petri dishes	35, 60, 100 mm	Schott Duran (Wertheim, Germany)
Pipette tips	10 µL, 200 µL, 1000 µL, transparent	Sarstedt AG & Co KG (Nümbrecht, Germany)
Reaction (Eppendorf) tubes	0.2 mL, 0.5 mL , 1.5 mL, 2 mL	Eppendorf AG (Hamburg, Germany)
Scalpel	Feather™ disposable scalpel No 10, 11, 22	Electron Microscopy Sciences (Hatfield, USA)
Serial connectors for µ-slides	~60 mm wide, self-assembled from silicon tubing (Cat. Nr 10842) and	ibidi GmbH (Gräfelfing, Germany)

	luer male connectors (Cat. Nr. 10824)	
Serological pipettes	Cellstar® (1 mL, 10 mL, 25 mL, 50 mL)	Greiner AG (Kremsmünster, Austria)
Syringes	1 mL, Luer 2 mL, 5 mL, 10 mL, 20 mL DiscarditTM II	Becton Dickinson (New Jersey, USA)
Whatman® cellulose chromatography paper	3 MM Chr	Cytiva Global Life Sciences Solutions Operations UK Ltd. (Amersham, UK)
µ-slides	Ibidi µ-slide I Luer, 0.6 mm (Cat. Nr 80186) Ibidi µ-slide VI, 0.4 mm (Cat. Nr 80606)	ibidi GmbH (Gräfelfing, Germany)

2.3 Buffers and solutions

Name	Preparation
Artificial cerebrospinal fluid (aCSF)	• NaCl (130 mM) • KCl (3 mM) • $MgCl_2$ (2 mM) • NaH_2PO_4 (1.25 mM) • $NaHCO_3$ (26.5 mM) • $CaCl_2$ (2 mM) • D(+) Glucose (10 mM)
Dextran Solution (for MPBECs isolation)	• DPBS • Dextran (18 % w/v) • Penicillin (100 U/mL) • Streptomycin (100 µg/mL) • L-Glutamine (2 mM)
Digestion Medium (for MPBECs isolation)	• DMEM, no glucose • Penicillin (100 U/mL) • Streptomycin (100 µg/mL) • Collagenase/Dispase (1 mg/mL) • TLCK (0.147 µg/mL) DNase I (4 µg/mL)
Dulbecco's PBS	Biowest (L0615)
Fluo-4 staining solution	• aCSF (gassed with 95 % CO_2 and 5 % O_2) till final volume • Fluo-4 (2 µM) • Probenecid (2.5 mM) • Pluronic (0.02 %)
Full medium for MPBECs	• DMEM/F12 without glutamine • PDS (20 %)

	• Antibiotic / Antimycotic (Penicillin 100 U/mL, Streptomycin 100 µg/mL, Amphotericin B 0.25 µg/mL) • L-Glutamine (2 mM) • Heparin (15 I.U./mL) • ECGS (30 µg/mL)
Heparin/Ringers for perfusion	• 250 mL ringers solution • 0.1 mL heparin (25,000 I.U./5 mL)
Ketamine/Xylazine solution	• 0.7 mL ketamine (100 mg/mL) • 0.7 mL xylazine (20 mg/mL) • 100 mL NaCl 0.9 %
Labeling buffer (LB)	• PBS with pH = 6.5 adjusted with HCl
Lysis buffer for cell surface proteomics	• Tris – HCl (100 mM) • Sodium deoxycholate (0.5 %) • Protease inhibitor cocktail 1x • Adjust pH = 8.0-8.5
Lysis buffer for genomic deoxyribonucleic acid (gDNA) extraction	• Tris-HCl (20 mM), pH = 8.0 • EDTA (5 mM), pH = 8.0 • NaCl (400 mM) • SDS (1 %) • Proteinase K (400 µg/mL)
Mouse collagen IV for coating	• Dilution with sterile 0.05 N HCl to final concetration 50 µg/mL
Phosphate buffer saline (PBS) 10x	• 1.37 M NaCl • 27 mM KCl • 100 mM Na_2HPO_4 • 18 mM KH_2PO_4 • Aqua bidest.
PBS 1x	• 1:10 dilution from 10x solution and pH adjustment to 7.4 with 1 N HCl
Rat collagen I for coating	Dilution with sterile PBS to final concentration 25 µg/mL
Reaction mix for polymerase chain reaction (PCR) for genotyping	• Deoxynucleotide triphosphate, dNTP (0.23 mM) • 1x Dream Taq Green Buffer (including $MgCl_2$ 2.27 mM) • $MgCl_2$ (1.71 mM) • Primer (0.34 µM) • Dream Taq DNA Polymerase (1 U) • Diethyl pyrocarbonate (DEPC) water
Shear stress medium for MPBECs	• DMEM/F12 with glutamine, with phenol red or DMEM/F12 with glutamine without phenol red (for calcium imaging experiments) • PDS (10 %)

	• Antibiotic / Antimycotic (Penicillin 100 U/mL, Streptomycin 100 µg/mL, Amphotericin B 0.25 µg/mL) • Heparin (15 I.U./mL) • ECGS (30 µg/mL)
Starvation medium for MPBECs	• DMEM/F12 without glutamine • PDS (0.5 %) • Antibiotic / Antimycotic (Penicillin 100 U/mL, Streptomycin 100 µg/mL, Amphotericin B 0.25 µg/mL) • L-Glutamine (2 mM) • Heparin (15 I.U./mL) • ECGS (30 µg/mL)
Tamoxifen for i.p. injections	• Tamoxifen (20 mg/mL) • Ethanol (10 % v/v) • Miglyol® 812 (90 % v/v)
Tribromoethanol 2.5 %	• 2.5 mL of 100 % Tribromoethanol in 2-Methyl-butan-2-ol • 100 mL NaCl 0.9 %
Tris-acetate-EDTA buffer 30x (TAE)	• Tris-base 1.2 M • EDTA 30 mM • pH=8.3 with acetic acid
Washing solution (for calcium imaging)	• aCSF (gassed with 95 % CO_2 and 5 % O_2) • Probenecid (2.5 mM)
Working Medium (for cell isolation)	• Dulbecco's Modified Eagle Medium/Nutrient Mixture F-12 (DMEM/F12) without glutamine • Penicillin (100 U/mL) • Streptomycin (100 µg/mL) • L-Glutamine (2 mM)
Yoda1	• Stock 20 mM in 100 % DMSO • For NF-κB translocation: diluted with cell medium till final volume • For calcium imaging experiments: first mixed 1:2 with cyclodextrin solution (20 % in PBS) and then added aCSF till final volume

2.4 Cell culture media

Name	Vendor (Cat. Number)
DMEM/F12, no glutamine	Thermo Fisher Scientific, Gibco™ (21331-020)

DMEM, no glucose	Thermo Fisher Scientific, Gibco™ (11966-025)
DMEM/F12, with glutamine, with phenol red	Thermo Fisher Scientific, Gibco™ (11320-074)
DMEM/F12, with glutamine, without phenol red	Thermo Fisher Scientific, Gibco™ (21041-025)
EndoGRO-MV Complete Media Kit	Merck Millipore (SCME004)

2.5 Cell lines

Name	Vendor (Cat. Number)
Human cerebral microvascular endothelial cell line D3 (hCMEC/D3)	Sigma-Aldrich (Cat. Nr SC0066)

2.6 Kits, enzymes

Name	Vendor (Cat. Number)
Click-iT™ EdU (ethynyl-2'-deoxyuridine) imaging kit	Thermo Fischer Scientific Invitrogen (C10340)
iST preomics kit	Preomics (P.O.00001)

2.7 Devices, instruments

Name	Type	Vendor
Animal cage change station	ARIA	Tecniplast S.p.A., Milan/Italy
Autoclave	Systec V-65	Systec GmbH (Linden, Germany)
Barnes maze apparatus	Diameter 91 cm, height 90 cm, 20 holes, hole diameter 5 cm (Cat. Nr 60170)	Stoelting Co (Wood Dale, USA)
Cell culture Aspirator Vacuum Pump	N86 KN.18	KNF Laboport Neuberger, Freiburg, Germany
Cell culture hood	Safe 2020	Thermo Fisher Scientific, Waltham/USA
Cell culture hypoxia workstation	InvivO2	Baker Ruskinn, Sanford
Centrifuges	Universal 320R or Micro220R or Micro200R 5415R	Andreas Hettich GmbH & Co. KG (Tuttlingen, Germany) Eppendorf AG (Hamburg, Germany)
Chemical fume hood	Waldner Scala 1200	WALDNER Laboreinrichtungen GmbH & Co.KG, Wangen im Allgäu/Germany
CLARIOstar® Microplate reader	CLARIOstar®	BMG LABTECH GmbH (Ortenberg, Germany)

Confocal Laser Scanning Microscopes	Leica TCS SP5 or Stellaris 5	Leica Microsystems AG (Wetzlar, Germany)
Cryostat	CM3050	Leica Biosystems GmbH (Nussloch, Germany)
Digital camera for recordings (during OPR and Barnes maze)		Logitech (Lausanne, Switzerland) or other
Dounce tissue grinder	Glass, 15 mL, Cat. Nr. D9938	Sigma-Aldrich (St. Louis, USA)
Drying Oven/Sterilizer	DL 56 Prime	VWR International bvba, Leuven/Belgium
Freezer-20 °C	LGex 3410-22A 001	Liebherr Hausgeräte Lienz GmbH (Germany)
Freezer-80 °C	Hera Freeze HFU T Series	Thermo Fisher Scientific (Waltham, USA) or other
Fridge 4 °C	LKUexv 1610-23A-001 Coldroom	Liebherr Hausgeräte Lienz GmbH (Germany) Viessmann Refrigeration Solutions GmbH (Allendorf, Germany)
Handling box for OPR	Empty green line cage GM500 or other	Tecniplast S.p.A. (Italy)
Hemocytometer Neubauer	0.100 mm x 0.0025mm^2	Labor Optik Ltd (Lancing, England)
Ibidi pump system	Cat. Nr 10902	ibidi GmbH (Gräfelfing, Germany)
Ice machine	AF-10	Intercontinentale Ziegra Eismaschinen GmbH (Isernhagen, Germany)
Inverted fluorescence microscope	Leica DMI6000 B	Leica Microsystems AG (Wetzlar, Germany)
Inverted Light Microscope for cell culture	Leica DMi1	Leica Microsystems AG (Wetzlar, Germany)
Mammal cell culture incubator	CB210	BINDER GmbH, Tuttlingen/Germany
Object place recognition (OPR) apparatus	Square open field with opaque walls (35 x 35 cm, PVC material)	Self-assembled
Objects for OPR	6-7 pairs of glass bottles, different shapes and sizes, filled with different coloured sand	Self assembled
Peristaltic pump	505S	Watson-Marlow (Cornwall, United Kingdom)
PipetBoy	Pipetus®	Hirschman Laborgeräte GmbH & CO. KG, Eberstadt Germany
Pipettes	Variable volume air displacement single-channel	Eppendorf AG (Hamburg, Germany) or Gilson (Middleton, USA) or other

Programmable Infusion syringe pump	TSE 540100	TSE Systems GmbH & CO KG (Tuttlingen, Germany)
Programmable syringe pump (infusion pump)	540100	TSE GmbH (Bad Homburg, Germany)
Rocker Shaker	Drs-12	neoLab®Line (Heidelberg/Germany)
Sonicator pico	Bioruptor® pico	Diagenode (Seraing, Belgium)
Surgery tools	Scissors, tweezers etc.	Fine Science Tools (Heidelberg, Germany)
Thermocycler	2720 Thermal Cycler Analytikjena Flexcycler or TGradient or TADVANCED	Thermo Fisher Scientific (Waltham, USA) Biometra GmbH (Göttingen, Germany)
Thermomixer	Compact or 5436	Eppendorf AG (Hamburg, Germany)
Transportation box for OPR	Empty green line cage GM500	Tecniplast S.p.A. (Italy)
Vacuum evaporator	Savant SpeedVac SPD111V	Thermo Fisher Scientific (Waltham, USA)
Vibratome	VT 1200S	Leica Microsystems AG (Wetzlar, Germany)
Vortex	REAX 200	Heidolph Instruments (Schwabach, Germany)

2.8 Software

Software	Version	Vendor
ANY-maze	Version 7.1 or 4.72	Stoelting Co (Wood Dale, USA)
CLARIOstar® reader control	Version 6	BMG LABTECH GmbH (Ortenberg, Germany)
Fiji	v1.54f	Platform for the open-source software ImageJ (Schindelin et al., 2012)
Grammarly	v.1.2.94.1468	Grammarly (San Francisco, USA)
Graphpad Prism	Version 8	Dotmatics (Boston, USA)
Ibidi	1.5.4 or later	ibidi GmbH (Gräfelfing, Germany)
Leica application suite advanced fluorescence software	2.5.0.6735	Leica Microsystems AG (Wetzlar, Germany)
Leica application suite advanced fluoresence software	2.5.1.6757	Leica Microsystems AG (Wetzlar, Germany)
Leica Application Suite X software	Stellaris 5	Leica Microsystems AG (Wetzlar, Germany)
Mendeley	1.19.8	Elsevier (Amsterdam, The Netherlands)

Molecular signatures database (MSigDB) online software, https://www.gsea-msigdb.org/gsea/msigdb/mouse/annotate.jsp, (Castanza et al., 2023; Liberzon et al., 2011; Subramanian et al., 2005)	Broad Institute, Inc., Massachusetts Institute of Technology, and Regents of the University of California (USA)

2.9 Antibodies

2.9.1 Primary antibodies

Target	Host	Vendor (Cat. Nr)	Dilution (from manufacturer's stock solution)	Type	Research resource identifier (RRID)	Application
Bassoon	Chicken	Synaptic systems (141016)	1:500	Poly-clonal	AB_2661779	Cryosections
Caveolin-1	Rabbit	Cell signaling Technology (3267)	1:400	Mono-clonal	AB_2275453	Cryosections
CD31	Rat	Bio-Rad (MCA2388)	1:200	Mono-clonal	AB_2161026	MPBECs
CD31	Rat	BD Biosciences (553370)	1:200	Mono-clonal	AB_394816	MPBECs
Collagen IV	Goat	Bio-Rad (134001)	1:200	Poly-clonal	AB_2082646	Cryosections
Glial fibrillary acidic protein (GFAP)	Chicken	Millipore (AB5541)	1:400	Poly-clonal	AB_177521	Cryosections
Green fluorescent protein (GFP)	Chicken	Abcam (ab13970)	1:2000	Poly-clonal	AB_300798	MPBECs
Ionized calcium-binding adaptor molecule 1 (Iba1)	Rabbit	FUJIFILM Wako Shibayagi (019-19741)	1:400	Poly-clonal	AB_839504	Cryosections
Microtubule associated	Mouse	Thermo Fischer	1:500	Mono-clonal	AB_794874	Cryosections

protein 2 (MAP2)		Scientific (MA1-25044)				
Myelin basic protein (MBP)	Rat	Millipore (MAB386)	1:250	Mono-clonal	AB_94975	Cryosections
Neuronal nuclei (NeuN)	Mouse	Millipore (MAB377)	1:500	Mono-clonal	AB_2298772	Cryosections
NF-κB p65 (F-6)	Mouse	Santa Cruz Bio-technology (sc-8008)	1:200	Mono-clonal	AB_628017	MPBECs
Shank2	Guinea Pig	Synaptic systems (162204)	1:500	Poly-clonal	AB_2619861	Cryosections

2.9.2 Secondary antibodies

Target-conjugated fluorophore	Host	Vendor (Cat. Nr)	Dilution (from manufacturer's stock solution)	Type	RRID	Application
Chicken IgY-Alexa Fluor 488	donkey	Jackson ImmunoResearch (703-545-155)	1:400	Poly-clonal	AB_2340375	PBCEs
Chicken IgY-Alexa Fluor 488	goat	Abcam (ab150169)	1:200	Poly-clonal	AB_2636803	cryosections
Goat IgG-Alexa Fluor 555	donkey	Thermo Fisher Scientific (A-21432)	1:400	Poly-clonal	AB_2535853	cryosections
Goat IgG-Alexa Fluor 488	donkey	Thermo Fisher Scientific (A-11055)	1:200	Poly-clonal	AB_2534102	cryosections
Guinea Pig IgG- Alexa Fluor 633	goat	Thermo Fisher Scientific (A-21105)	1:400	Poly-clonal	AB_2535757	cryosections
Mouse IgG-Cyanine 3 (Cy3)	donkey	Jackson ImmunoResearch Labs (715-165-151)	1:400	Poly-clonal	AB_2315777	PBCEs

Mouse IgG fragment antigen-binding (Fab) fragments	goat	Jackson ImmunoResearch Labs (115-007-003)	1:50 to 1:100	Polyclonal	AB_2338476	cryosections
Mouse IgG-Alexa Fluor 555	goat	Thermo Fisher Scientific (A-21422)	1:400	Poly-clonal	AB_2535844	cryosections
Rabbit IgG-Alexa Fluor 647	donkey	Thermo Fisher scientific (A31573)	1:400	Poly-clonal	AB_2536183	PBCEs
Rabbit IgG-Alexa Fluor 488	donkey	Thermo Fisher scientific (A21206)	1:400	Poly-clonal	AB_2535792	PBCEs
Rabbit IgG-Alexa Fluor 750	goat	Thermo Fisher Scientific (A-21039)	1:400	Poly-clonal	AB_2535710	cryosections
Rat IgG-Alexa Fluor 488	donkey	Thermo Fischer Scientific (A21208)	1:400	Poly-clonal	AB_2535794	MPBECs
Rat IgG Alexa Fluor 555	donkey	Abcam (ab150154)	1:400	Poly-clonal	AB_2813834	PBCEs
Rat IgG-Alexa Fluor 647	donkey	Abcam, (ab150155)	1:400	Poly-clonal	AB_2813835	PBCEs and cryosections
Rat IgG- Cy3	donkey	Jackson ImmunoResearch Labs (712-165-150)	1:400	Poly-clonal	AB_2340666	PBCEs

3 Methods

3.1 Cell culture under static conditions

3.1.1 MPBECs

MPBECs cultures were performed as previously described (Assmann et al., 2017). For all experiments, mouse collagen IV was used to coat cell culture surfaces before cell seeding for at least 1 h at room temperature (RT), on a rocker shaker at 25 rpm, unless otherwise stated.

Mice were placed in a custom-built chamber under a fume hood and deeply anesthetized with an overdose of isoflurane. The mice were transferred to a clean working bench and quickly decapitated with sterile scissors. The head was thoroughly sprayed with 70 % ethanol, and the skin was removed to expose the skull. Incisions were made on the base of the cranium in the foramen magnum and on the frontal cranial bone in order to expose brain tissue. The brain was transferred in cold sterile DBPS in a 50 mL Falcon tube till all brains were collected. Next, under sterile conditions at the cell culture hood olfactory bulbs, cerebellum and brainstem were grossly dissected with a scalpel from the rest of the brain and discarded. The brains were rolled over sterilized cellulose chromatography paper to remove the meninges and the big vessels on the brain's surface. All brains were transferred into the glass dounce tissue homogenizer, which contained 5 mL working medium at 4 ^{o}C. For every tissue homogenizer, a maximum of 10 brains were used. The tissue was homogenized by using two pestles, large clearance pestle A and small clearance pestle B. Thirty strokes with pestle A served for the breakdown of the tissue into smaller pieces, and 25 strokes with pestle B served for further mechanical disruption and completion of the homogenization. The homogenized tissue was transferred to a new precooled 50 mL Falcon tube; the tissue homogenizer was washed with 5 mL of working medium and collected on the same tube. The tube was centrifuged at 1350 *g* for 5 min at 4 ^{o}C. The supernatant was carefully removed with a cell culture aspirator; the pellet was resuspended in 15 mL cold dextran solution and subsequently vortexed for 2 min. The tissue homogenate was centrifuged at 7080 *g* for 10 min at 4 ^{o}C. The myelin layer on the top of the supernatant was carefully aspirated and the precipitated vessel fragment layer was resuspended in 10 mL digestion medium. The vessel homogenate was incubated at 37 ^{o}C in a water bath for 1 h and 15 min and gently shaken by hand every 10-15 min. After digestion, the cell suspension was centrifuged at 1350 *g* for 5 min at RT, the supernatant was removed and the pellet was gently resuspended in 10 mL DBPS. The cell suspension was centrifuged at 1350 *g* for 5 min at RT and the supernatant was aspirated. Cells were resuspended in full medium for MPBECs (2 mL per mouse brain) containing puromycin (at final concentration 8 µg/mL), seeded on cell culture plates according to the experimental conditions and placed inside the incubator. After 24 h, the supernatant was aspirated, the cells were washed two times with DPBS and fresh full medium for MPBECs with puromycin was added. The next day, the supernatant was aspirated and replaced with fresh full medium for MPBECs without puromycin. The cells were let inside the incubator for five days, and afterward, the medium was changed every 2-3 days till the cells became confluent. In all experiments, MPBECs were used only at passage 0 (P0).

3.1.2 hCMEC/D3 cells

The commercially available hCMEC/D3 cell line was expanded and cryopreserved in liquid nitrogen (N_2) from P1 to P3. Before cell seeding, T25 flasks or other cell culture surfaces were coated with rat collagen I for 1 h at 37 ^{o}C and washed once with DPBS. Cells were thawed up, resuspended in 40 mL DPBS and subsequently centrifuged at 110 *g*, 5 min, RT. The pellet was resuspended in 10 mL EndoGro-MV complete medium and the complete cell suspension was seeded in a T25 flask and let for 24 h inside the incubator. The next day, the supernatant was aspirated, the cells were washed once with DPBS and harvested with 1 mL of 0.05 % trypsin at RT for 3 min. After the cells detached, 5 mL of EndoGro-MV complete medium was added to the flask to deactivate the trypsin. Next, 50-100 µL of cell suspension was diluted in 5 mL of EndoGro-MV and seeded to a new T25 flask. The cells were let grow till confluency and passaged once per week. In all experiments, cells were used between P4 and P20.

3.2 Cell culture under flow

The commercially available ibidi pump was used to cultivate cells under shear stress. The handling of all components of the system and the consumables was performed according to the instructions of the manufacturer unless otherwise stated.

3.2.1 Simple seeding of MPBECs on ibidi µ-slides

A protocol was developed and optimized to habituate and cultivate MPBECs under shear stress. Before cell seeding, the µ-slides were filled with mouse collagen IV and placed inside the incubator for 1-2 h for coating. Afterward, the slides were washed twice with sterile DPBS and kept inside the incubator till seeding. The MPBECs were isolated, as described previously in section 3.1.1, with minor modifications after the isolation of the final cell pellet. More specifically, the precipitate isolated per one mouse brain was resuspended in 750 µL of full medium for MPBECs with puromycin to ensure appropriate vessel density for cell growth. Then, a volume of cell suspension equal to the volume of the µ-slide channel (150 µL for µ-slides I, 30 µL for µ-slides VI) was seeded, and the vessels were let for 3 h to attach to the bottom surface of the channel inside the incubator. Afterward, 60 µL of the cell medium was added gently to each of the reservoirs of the channel. The next day, the channels of the µ-slides were washed twice with warm DPBS, and fresh full medium for MPBECs with puromycin was added to the µ-slides. After 24 h, the medium was completely replaced with fresh warm full medium for MPBECs without puromycin. Finally, the medium was replaced every 2-3 days with shear stress medium till the cells reached the desired confluency.

3.2.2 'Sandwich' seeding of MPBECs on ibidi µ-slides

For the proteomic experiments, the MPBECs were seeded on the top and bottom surfaces of the channel of the ibidi µ-slides I ('sandwich seeding') to ensure enough protein material would be retrieved for mass spectrometry analysis. In this case, the protocol described in section 3.2.1 was modified. More specifically, the µ-slides were coated with mouse collagen IV and let inside the incubator for 1-2 h in an inverted position to ensure the coating of the top surface of the channel. Afterward, the µ-slides were let for 1 h in a normal position to ensure the coating of the bottom surface of the channel. Next, the µ-slides were washed twice with DPBS and let inside the incubator till seeding of the vessel pellet. The vessel pellet was seeded on the channels of the µ-slides as described above in section 3.2.1. The µ-slides were transferred then to the incubator and let for 24 h in an inverted position so that the vessel fragments attach to the top surface of the channel. The next day, a second MPBEC isolation was prepared to seed the bottom surface of the µ-slides. The µ-slides were turned back to the upright position, washed twice with DPBS, and seeded with the new vessel suspension. Then the µ-slides were transferred back to the incubator on the normal upright position and let for 3 h so that the vessel fragments attach to the bottom surface of the channel. Afterward, the reservoirs of the channels were filled with 60 µL of full medium for MPBECs with puromycin. The following day, the µ-slides were washed twice with DPBS and filled with fresh full medium for MPBECs with puromycin. After 24 h, the medium was replaced with fresh full medium for MPBECs without puromycin. Afterward, the medium was replaced every 2-3 days with shear stress medium till the cells reached the desired confluency.

3.2.3 Short- and long-term treatment of MPBECs with shear stress

When the cells became 80-90 % confluent, the µ-slides were carefully connected to the ibidi perfusion set under sterile conditions and the system was recalibrated according to the manufacturer's instructions. For every perfusion set, either 1 to 4 µ-slides I serially (or one single µ-slide VI) were connected. Next, the fluidic unit was placed inside the incubator for at least 30 min to let the cells recover from handling. Afterward, depending on the purpose of the experiment, the cells were either treated directly with shear stress 1.7 dyn/cm^2 (see section 3.7.1.2 below) or were cultured for long-term under flow.

For the long-term treatment, habituation to flow for 24 h preceded the final application of shear stress of 1.7 dyn/cm^2 to the cells. More specifically, cells were treated with a non-continuous unidirectional laminar flow loop cycle (1 min shear stress 0.26 dyn/cm^2 → 5 min no shear stress, 0 dyn/cm^2) for 8 h. Afterward, the protocol was changed to apply constant flow and the desired flow pattern (unidirectional or oscillatory at 1 Hz) for 8 h at 0.26 dyn/cm^2, followed by 8 h at 1.0 dyn/cm^2. The final shear stress value of 1.7 dyn/cm^2 was applied for 72 h. Finally, for the cells that served as static control a partial medium change was performed every 12 hours to ensure proper growth of the cells (120 µl fresh shear stress medium was added to each µ-slide I).

3.3 Mass spectrometry

3.3.1 Sample preparation for whole cell proteomics

MPBECs were isolated and seeded in µ-slides I, 0.6 mm as described in section 3.2.2 and cultivated for 72 h at shear stress 1.7 dyn/cm^2 as described in section 3.2.3. Afterward, the µ-slides were washed twice with DPBS and then lysed with the lysis buffer provided from the kit (1x protease inhibitors cocktail was added to the lysis buffer to prevent protein degradation from proteases). The collected lysed material was further processed according to the manufacturer's instructions of the commercially available Preomics iST kit till the collection of the dry pellet. The reaction tubes containing the dry pellet were sealed with parafilm and stored at -20 °C. Finally, the samples were transported in dry ice to the proteotyping site (Wollscheid lab, ETH, Zürich, Switzerland) for the final processing and analysis (Hammer, 2024).

3.3.2 Sample preparation for cell surface proteomics

For the cell surface proteomic analysis of MPBECs, a previously described protocol of cell surface capture (CSC) (van Oostrum et al., 2019) was utilized and adapted for µ-slides I or 100 mm petri dishes. Briefly, cells were isolated and cultivated under shear stress in µ-slides I, 0.6 mm for 72 h as described in sections 3.2.2 and 3.2.3 or in 100 mm petri dishes till they reached confluency. Afterward, cells were washed twice with DPBS and gently oxidized at 4 °C with 3 mM $NaIO_4$ diluted in LB to oxidize the surface glycans. Then, the cells were washed twice with LB and subsequently treated with 5 mM biocytin and 50 mM 2-(Aminomethyl)imidazole for 1 h at 4 °C. Afterward, cells were washed twice with ice cold DPBS before being lysed. The lysed samples were collected in reaction tubes and heated at 100 °C for 5 min. Finally, the samples were cooled down to RT and stored at -80 °C till they were transported in dry ice to the proteotyping site (Wollscheid lab, ETH, Zürich, Switzerland) for the final processing and analysis (Hammer, 2024).

3.4 Scratch assay on MPBECs

The scratch assay was performed on confluent monolayers of MPBECs cultures adapted from Liang et al 2007 (reference). Shortly, MPBECs were isolated as described above in section 3.1.1 and plated on 24- or 48-well plates. When the cells reached 100 % confluency, the medium was aspirated and replaced with starvation medium for MPBECs. After 24 h, a scratch was made along the middle of the well on the cell monolayer with a 20 µL pipette tip. The supernatant was removed, the cells were washed once with DPBS, and fresh full medium for MPBECs without PDS was added to the wells. Next, well plates were transferred either to the cell culture workstation InvivO2 for hypoxic conditions (1 % O_2, 5 % CO_2, 37 °C, 70 % humidity) or to a regular incubator for normoxic conditions (21 % O_2, 5 % CO_2, 37 °C, 90 % humidity). Two different pictures of the scratch were acquired per well with a 2x objective of the inverted light microscope Leica Dmi1 at different time points. The surface of the scratch was calculated with the ImageJ plugin 'MRI Wound Healing Tool', and the percent of wound closure was calculated according to the following formula:

$$Wound\ Closure\ \% = \left[\frac{A_{t\,=\,0\,h} - A_{t\,=\,\Delta h}}{A_{t\,=\,0\,h}}\right] \times 100\ \%$$

$$A_{t\,=\,0\,h}\ is\ the\ area\ of\ the\ wound\ measured\ directly\ after\ scratch$$

$$A_{t\,=\,\Delta h}\ is\ the\ area\ of\ the\ wound\ measured\ at\ h\ hours\ after\ the\ scratch$$

After the end of the experiment, the supernatant was collected, snap-frozen in liquid N_2 and stored at-80 °C. The cells were washed once with DPBS, snap-frozen in liquid N_2 and stored at-80 °C.

3.5 Proliferation assay on MPBECs

For the measurement of proliferation on MPBECs, the commercially available EdU kit was used according to the manufacturer's instructions. Briefly, MPBECs were isolated according to the protocol described above in section 3.1.1 and plated on 48-well plates. When the cells reached a 50-70 % confluency, the supernatant was aspirated and replaced with starvation medium for MPBECs. After 24 h, half of the volume of the supernatant was aspirated and discarded, and an equal volume of fresh starvation medium for MPBECs containing a 2x working solution of EdU was added to each well. The cells were incubated for 24 h at a final concentration of EdU of 5 µM. Afterward, the medium was removed, and the cells were washed once with DPBS and fixed with 3.7 % formalin for 15 min at RT. The following steps of EdU detection was performed according to the manufacturer's instructions. After the end of the staining procedure, the wells were stored at 4 °C till imaging. Tile scan images of the whole wells were taken with the 10x dry objective of the inverted fluorescence microscope. The number of EdU-positive cells was semi-automatically calculated with the ImageJ software. The DAPI channel was used to calculate each well's total number of cells.

3.6 Measurement of NF-κB activation in MPBECs

MPBECs from control and $G\alpha_{q/11}^{beKO}$ animals were isolated as described in section 3.1.1 and plated on 24- or 48-well plates. When the cells reached confluency more than 90 %, the supernatant was aspirated and replaced with starvation medium for MPBECs. After 1 h, the tested substances Yoda1 (50 µM), vehicle of Yoda1 (DMSO 0.25 %) and IL-1β (0.2 µg/ml), were added directly to the wells, and the cells were incubated for 1 h. Next, the supernatant was removed, and the cells were fixed as described in section 3.8 and stained for the EC marker CD31 to assess cell surface and the p65 protein. DAPI was used to visualize nuclei. After staining, the wells were kept at 4 °C till imaging. Images were analyzed as described in section 3.10.2.

For the shear stress experiments, the µ-slides were plated with MPBECs isolated from the mouse line that expresses the GFP-Calmodulin-M13 peptide fusion protein calcium indicator (GCAMP8) as described in section 3.2.1 and assembled on the ibidi pump system as described in section 3.2.3. Then, the respective type of flow (unidirectional or pulsatile flow at 1 Hz) was applied to the cells for 30 min at 1.7 dyn/cm^2. Afterward, the µ-slides were disassembled from the ibidi pump system, washed 2x with PBS, fixed as described in section 3.8 and stained for GFP to assess whole cell surface and the p65 protein. DAPI was used to visualize nuclei. After staining, the wells were kept at 4 °C till imaging. Images were analyzed as described in section 3.10.2.

3.7 Calcium imaging

3.7.1 Ibidi µ-slides

3.7.1.1 hCMEC/D3 cells

The cells were passaged as described in section 3.1.2 and counted with the hemocytometer Neubauer. To achieve 90-95 % confluency, 300,000 cells were plated in a 35 mm petri dish. If more cells were necessary, adjustments were made to the size of the petri dish and the number of cells plated. The following day, the cells were harvested with 0.05 % trypsin, then diluted to 1:4 volume of EndoGro-MV medium and subsequently centrifuged at 110 *g*, 5 min, RT. The pellet was resuspended in EndoGro medium and seeded in µ-slides VI to a final confluency of 95-100 %. After 24 h, cells were washed 1x with gassed aCSF and then treated with the Fluo-4 staining solution for 30 min at RT. Afterward, the Fluo-4 staining solution was replaced by the washing solution and cells were treated with it for 30 min more. Then the cells were washed 1x with fresh gassed aCSF and mounted on the ibidi pump system according to the manufacturer’s instructions. Afterward, the cells were recorded for 2 min without flow as a baseline, then 4 min with 1.7 dyn/cm^2 shear stress and the respective flow type (unidirectional flow, oscillatory flow at 1 Hz and pulsatile flow at 1 Hz) as stimulation according to the manufacturer's instructions. The videos were analyzed with ImageJ by measuring the fluorescence signal from the whole field of view.

3.7.1.2 MPBECs from GCaMP8 mice

Calcium imaging on MPBECs isolated from the mouse line *Cdh5*-GCaMP8 was conducted before the habituation of the cells to the flow and/or 96 h after the start of the flow. For the calcium imaging before the habituation of the cells to the flow, the µ-slides I were assembled to the fluidic unit and the cells were left inside the incubator for 30 min to recover. Next, the fluidic unit was carefully transported next to the inverted fluorescence microscope, and the µ-slides were mounted on the stage of the microscope. The cells were recorded for 3 min without flow as a baseline, then 5 min with 1.7 dyn/cm^2 shear stress and the respective flow type as stimulation, and 3 min after the flow stopped. Three different flow types were tested: the unidirectional flow, the oscillatory flow at 1 Hz and the pulsatile flow at 1 Hz. The acquired videos were analyzed with ImageJ by calculating the fluorescence signal of the whole field of view.

For the experiments that involved the inhibition of the $G\alpha_{q/11}$ pathway, first the solutions of the inhibitor FR900359 (10 µM) and the DMSO control (0.1 %) were prepared in shear stress medium. Afterward, cells were treated with the solutions for 30 min inside the incubator, washed 2x carefully with fresh shear stress medium and finally connected to the ibidi system and treated with shear stress as described in the previous paragraph.

For the calcium imaging 96 h after the start of the flow at 1.7 dyn/cm^2 shear stress, the fluidic unit was carefully transported to the fluorescence microscope and the cells were recorded for 3 min with the respective type of flow, 5 min with no flow and 3 min after flow started again. Two different types of flow were tested: the unidirectional flow and the oscillatory flow at 1 Hz. The acquired videos were analyzed with ImageJ by calculating the fluorescence signal of the whole field of view.

3.7.2 Microplate reader

The microplate reader CLARIOstar® was used to stimulate MPBECs with different substances and measure the $[Ca^{2+}]_i$ responses. MPBECs were isolated from the *Cdh5*-GCaMP8 mouse line and plated in 96-well plates either with black or transparent walls and clear bottoms. The cells were isolated and cultivated till they became confluent, as described in section 3.1.1. Next, the supernatant was aspirated and the wells were filled with gassed aCSF. The well plate was placed inside the plate reader, the appropriate solutions were loaded on the injectors according to the manufacturer's instructions, and the environmental conditions were set at 25-37 °C and 5 % CO_2. In order to achieve the desired final concentrations of the substances during stimulation (Yoda1 47.61 µM or 25 µM, vehicle DMSO) the injected volume varied from 5 to 15 µL, and the initial volume of each well before the injection was from 90-100 µL. Most wells were stimulated once. ATP (100 µM) was used as a positive control of the $[Ca^{2+}]_i$ increase. Finally, each well's average fluorescence signal values were obtained by scanning the whole well or multiple points with acquisition rate ≤5 Hz. The relative fluorescence response was calculated by the ratio F/F_0, where F refers to the fluorescence signal measured and F_0 refers to the average fluorescence signal before the injection of the stimulus (baseline).

For the experiments that involved the inhibition of the $G\alpha_{q/11}$ pathway, first the solutions of the inhibitor FR900359 (10 µM) and the DMSO control (0.1 %) were prepared in gassed aCSF. Afterward, cells were treated with the solutions for 30 min inside the incubator. Finally, the supernatant was aspirated and wells were loaded with fresh gassed aCSF and the measurement was performed as described in the previous paragraph. Stimulation with ADP-β-S (10 µM) was used as a positive control of the $[Ca^{2+}]_i$ increase and inhibition of the $G\alpha_{q/11}$ pathway.

3.8 Fixation and staining of cells

This protocol was followed for all cell experiments unless otherwise stated. Cells were washed carefully twice with DPBS and subsequently fixed with 3.7 % formalin for 15-20 min at RT. Afterward, cells were permeabilized with 0.3 % Triton X-100 solution in PBS for 10 min at RT. The permeabilization solution was removed and cells were blocked with 5 % BSA in 0.3 % Triton X-100 solution in PBS for 30 min. Afterward, the blocking solution was removed and cells were incubated with primary antibodies diluted in the blocking solution overnight at 4 °C. Next, the supernatant was removed, and wells were washed three times with PBS for 5 min at RT and incubated for 1 h at RT with secondary antibodies and DAPI diluted in the blocking solution protected from light. Finally, wells were washed thrice with PBS for 5 min at RT and stored at 4 °C until image acquisition. For long-term storage, 0.02 % sodium azide (NaN_3) in PBS was used.

3.9 Animals

In house-bred mouse lines and animals obtained from external providers were taken care of by the animal facility of the University of Lübeck "Gemeinsame Tierhaltung der Universität Lübeck" (GTH). Mice were housed by sex (maximum five animals per group) in individually ventilated green line cages (500 cm^2) with dust-free wooden bedding under a 12 h light/dark cycle (artificial light, lights on at 7:00 a.m.). The mice were fed an autoclaved-pelleted mouse diet (#1314, Altromin Spezialfutter GmbH & Co. KG) and had free access to tap water *ad libitum*. Home cages were enriched with nesting material and in some cases, an additional enrichment with transparent plastic mouse tunnels was used. The mice used in the behavioral studies as well as the mice used in the THBD experiments did not receive the plastic tunnel in their home cages. Once a week or more often, if necessary, the home cages were cleaned and equipped with new bedding.

All studies followed the German Animal Welfare Act and the corresponding regulations. Breeding, husbandry, and the execution of experimental procedures were approved by the local animal ethics committee (Ministerium für Energiewende, Landwirtschaft, Umwelt, Natur und Digitalisierung, Kiel, Germany).

Mouse lines

All mice used were established on the C57BL/6 background. The mice were age and sex-matched between experimental groups unless otherwise stated. The age of the mice varied between 2 and 22 months of age.

For the proteomic study, male C57BL/6 mice were purchased from Charles River and used in the age between 8 and 16 weeks. For the generation of brain endothelial-specific knockout (beKO) animals of $G\alpha_{q/11}$ and *Thbd*, we utilized the bacterial artificial chromosome (BAC)-transgenic *Slco1c1-CreER*^{T2} (Cre fused to a mutant estrogen ligand-binding domain (ERctT2)) strain (Ridder et al., 2011), which expresses the tamoxifen-inducible CreER^{T2} recombinase under the control of the mouse *Slco1c1* regulatory sequences in brain ECs, in epithelial cells of the choroid plexus and to a small extent in cortical astrocytes. Mice from this strain were crossed with mice carrying the respective loxP-flanked alleles. More specifically, mice that carried floxed (fl) *Gnaq* alleles (*Gnaq*$^{fl/fl}$) and were $G\alpha_{11}$ - deficient (*Gna11*$^{-/-}$)(*Gnaq*$^{fl/fl}$::*Gna11*$^{-/-}$) (Wettschureck et al 2001) were used to delete the expression of both *Gnaq* and *Gna11* in brain ECs and were termed $G\alpha_{q/11}{}^{beKO}$. Littermates lacking the cyclisation recombinase (*cre)* transgene and were heterozygous for *Gna11* (*Gnaq*$^{fl/fl}$ :: *Gna11*$^{-/+}$) were used as controls. Similarly, the *Thbd*$^{fl/fl}$ mice (Isermann et al., 2001) were crossed with the *Slco1c1-CreER*^{T2} strain to generate the *Thbd*^{beKO} mice and littermates lacking the *cre* transgene were used as control and termed *Thbd*^{fl}. Finally, controls of both lines received tamoxifen in parallel to knockout groups.

The *Cdh5*-GCaMP8 mouse line that expresses the calcium biosensor GCaMP8 under the endothelial promoter *Cdh5* was used for calcium imaging experiments unless otherwise stated and has been described before (Lee et al., 2021; Longden et al., 2021). The line was provided by the Michael Kotlikoff lab.

Mouse line	Nomenclature	MGI number
***Cdh5*-GCaMP8**	B6;SJL-Tg(*Cdh5*-GCaMP8)B20-6Mik/J	6294077
Gna11$^{-/-}$	129S7/SvEvBrd-Gna11^{tm1Soff}	2151589
Gnaq$^{fl/fl}$	129P2/OlaHsd-Gnaq^{tm2Soff}	2446355
Slco1c1-CreER^{T2}	B6.D/2-Tg(Slco1c1-icre/ERT2)1Mrks	5301361
Thbd$^{fl/fl}$	129S2/SvPas-Thbd^{tm2Wlr}	2158819

***Table 1**: List of used mouse lines with laboratory name, nomenclature and mouse genome informatics (MGI) number.*

3.9.1 OPR

The OPR was performed with appropriate adaptations as described before (Binder et al., 2012). Mice from both genders were evenly distributed into two cohorts of 10 animals per group. Animals were either single-housed or in a maximum of 4 per cage when possible. Briefly, a handling period of 5 days preceded the OPR test, when all animals were handled either under the cage change station or inside the behavioral room for at least 5 min daily. The handling involved tail or cup handling and transportation to an empty handling box with high transparent walls to get accustomed to human contact and procedures related to the OPR test. Two days after the handling period, the mice underwent the habituation phase of the OPR test for 3 consecutive days. During the habituation, the mice were placed in the center of a dimly lit (approximately 20 lux) open field apparatus and left for 10 min to freely explore it before they were transported back to their home cages. One day after the last habituation day, the sample trial and the test trial of the OPR test took place. In the sample trial, two identical objects were placed in the corners of the apparatus, and the mice were allowed for 10 min to explore the apparatus and the objects freely. Afterward, the mice were transported back to their home cage for 60 min before the test trial began. During the test trial, the mice were placed in the open field apparatus and allowed for 5 min to explore the previously presented objects with the difference that one object was displaced. The apparatus and the objects were cleaned thoroughly with 70 % ethanol solution between trials and between animals. A visual clue attached to the wall of the apparatus was used for the spatial orientation of the mice (Murai et al. 2006) The animals' behavior during the habituation and the OPR test was recorded with a digital camera installed over the open field apparatus. The scoring was conducted using the software ANY-maze. For calculating the preference index for the displaced object, the time spent exploring the two objects was measured manually, and the following equation was used:

$$Preference\ Index = \frac{Time_{exploration\ of\ displaced\ object}}{Time_{exploration\ of\ displaced\ object} + Time_{exploration\ of\ stationary\ object}}$$

3.9.2 Barnes maze

The Barnes maze behavioral test was performed as described before (Binder et al., 2019) with minor adaptations. Mouse cages were transported into the behavioral room for at least one and a half hours before any procedure. The Barnes maze apparatus comprised an elevated circular platform with 20 holes. Under one hole, an escape box is placed, while the others are closed with false escape boxes. During the Barnes maze, mice were trained to find the escape box based on visual cues placed on the surrounding environment. During the experimental procedure, the lux intensity was set at approximately 350 lux and served as an aversive stimulus for the mice to find the escape box. Mice underwent five days of acquisition and probe trials took place on days 6 and 17.

During day 1 of acquisition, each mouse underwent an adaptation step first and then immediately after the acquisition trial. For the adaptation step, the mouse was placed in the middle of the apparatus and gently guided to the escape hole. The mouse was left inside the escape box for 2 min. For the acquisition trials, the mouse was placed in the middle of the apparatus and left to find the escape box for 3 min. If the mouse failed to find or enter the escape hole in this period, it was gently guided and placed inside the escape box. The mouse was left inside the escape box for 1 min before being transported back to the home cage. Every mouse received 4 acquisition trials daily with an inter-trial interval of 15 min. On days 6 and 17, the escape box was removed, the hole was closed with a false escape box, and the apparatus was turned by 180^o to exclude the influence of intra-maze cues. Then, mice were placed in the middle of the apparatus and allowed to explore it for 90 seconds before being transported back to their home cage. The mice were recorded during acquisition and probe trials, and the videos were analyzed offline. Distance and latency were calculated semiautomatically with the ANY-maze software, while pokes into holes and strategy were manually scored.

3.9.3 Animal perfusion and organ collection

Animals were deeply anesthetized dependent on their weight until no reaction was observed after toe pinching with tweezers. If needed, an additional half of the initial anesthetic dose was administered. Afterward, the mouse was fixed so the abdominal area was facing upwards. The thorax and abdominal area were sprayed with 70 % ethanol, and a longitudinal incision on the skin along the midline was made to expose the underneath muscle wall. Then an incision on the muscle wall was made to expose the internal organs, and the rib cage was carefully cut to expose the heart. A needle connected to a syringe with heparin (2 I.U./mL)/Ringer’s solution was inserted on the left ventricle of the heart, an incision was made on the right atrium to allow outflow of blood from circulation, and the mouse was manually perfused with 20 mL of heparin (2 I.U./mL)/Ringer’s. Afterwards, the head was cut and incisions on the skull were made in order to remove the brain. The olfactory bulbs were dissected and discarded, the brain was weighted, and with a cut in the middle alongside the hemispheres, it was separated into two equal parts. One part was snap-frozen in liquid N_2 and stored at-80 °C; the other was post-fixed overnight with 3.7 % formalin at 4 °C. After post-fixation, the brains were washed twice with PBS and left for 48 h in a 30 % saccharose solution. Finally, brains were gently rolled over tissue paper to remove extra saccharose, frozen with 2-methyl-butane at-30 °C and kept at-80 °C till cryosectioning.

3.9.4 Cryosections and staining

The frozen brain tissue was cut with a cryotome at-25 °C at a thickness of 20 µm. First, the half brains were cut at sagittal planes until 20 sections were collected on glass slides and stored at -20 °C. Afterward, the tissue orientation was shifted, and coronal sections (20 µm) were cut and collected in 1:1 glycerol/PBS solution from the anterior part of the prefrontal cortex. From the anterior part of the hippocampus, 10 sections were collected in 1:1 glycerol/PBS solution, and the rest were mounted on glass slides. The sections were kept at-20 °C before further processing.

For staining on the glass slides, the cryosections were encircled with a fatty pen and left at RT for 20 min. Afterwards, the sections were washed 2-3 times with PBS, permeabilized with 0.3 % Triton-X 100 for 15-30 min and then blocked with 3-5 % BSA in 0.3 % Triton-X 100 for 30-75 min at RT. Then, sections were incubated with the primary antibody diluted in a blocking solution at 4 °C overnight. The sections were washed 3 times with PBS for 5-10 min at RT and incubated with the respective secondary antibodies for 1 h at RT, protected from light. Finally, the sections were washed 3 times with PBS, mounted with glass coverslips and mounting medium and stored at 4 °C till imaging.

For collagen IV, caveolin-1, shank2, MAP2 and bassoon stainings, the cryosections mounted on a glass slide were boiled first at 95 °C with a 10 mM tri-sodium citrate, pH = 6.0, for 20 min. Then, they were left to cool down and the staining procedure followed as described in the previous paragraph.

Finally, for the MAP2 staining, a Fab fragment solution was added to the blocking solution to reduce the nonspecific binding of the primary antibody.

Beate Lembrich performed the stainings for shank2, MAP2 and bassoon as well as part of the stainings for collagen IV, caveolin-1, IgG, GFAP, Iba1, NeuN and MBP.

3.10 Microscopy

3.10.1 Phase contrast microscopy

Cell orientation

For analysis of the cell orientation, phase contrast images were taken with the inverted microscope Leica DMI6000 B and the 10x objective. A script on ImageJ adapted from (Reinitz et al., 2015) was used to measure the major axis, minor axis and orientation of the cells (θ° in respect to the flow direction). The inverse aspect ratio (IAR) was calculated by dividing the length of minor axis by the length major axis (Figure 16 A).

3.10.2 Fluorescence microscopy

Images of fixed stained cells and tissue as well as live calcium imaging of cells cultivated under shear stress were acquired with the fluorescence microscope Leica DMI6000 B equipped with a DFC360FX camera. The LAS software was used for appropriate settings. The filter cubes were chosen depending on the excitation and emission wavelength of the fluorochrome dye.The 10x and 20x dry objectives were used for tile scans or single images.

Cell counting

In-house scripts on ImageJ were developed to determine cell numbers in sections of NeuN and Iba1 stainings for the respective cell types. For the proliferation assay, the EdU and DAPI stainings were used to calculate the ratio of proliferating PBCEs with a semi-automatically cell counting function in ImageJ.

NF-κB/p65 translocation

The fluorescence intensity ratio of p65 in nuclei to the cytoplasm was used to measure the activation of the NF-κB signaling pathway semi-automatically with ImageJ. A mask of the cell surface was created using the CD31 staining to exclude areas not covered by cells. The nuclei area was masked using the DAPI channel, and the cytoplasm area was determined by subtracting the nuclei area from the whole cell surface area. The fluorescence intensity of p65 on the masked areas of nuclei and cytoplasm was calculated. Four pictures per well were acquired with the 10x objective and analyzed semi-automatically with ImageJ.

In shear stress experiments, tile scans of part of the µ-slide I were acquired with the 10x objective. Images were analyzed semi-automatically with ImageJ as described in the previous paragraph. A mask of the cell surface was created using the GFP staining.

String vessel analysis

String vessels were identified as structures positively stained for the basement membrane component collagen IV and negatively stained for caveolin-1 as an endothelial marker. They were manually measured on ImageJ. Beate Lembrich was involved in analyzing the string vessel length on the sagittal sections of the cortex. The total vessel length was automatically calculated with an in-house custom-built script on ImageJ using the caveolin-1 staining. For each animal, 4 pictures in total were acquired and analyzed, either 2 pictures from 2 sagittal sections or 1 picture from 4 coronal sections.

IgG extravasation

IgG extravasation was calculated on sagittal cryosections by masking and excluding the vessel area and calculating the fluorescence signal outside the vessels (Figure 10 A). An in-house custom-built script on ImageJ was used to identify the area of the vessels.

3.10.3 Laser scanning confocal microscopy

After establishing the staining protocols, images were taken and analysis was performed with help from Beate Lembrich and PD. Dr. Jan Wenzel. Immunostaining images were taken with the Stellaris 5 confocal microscope, and the Leica Application Suite X software was used for the appropriate settings. The fluorescence intensity in images was analyzed using ImageJ.

3.11 Genotyping

Genomic DNA (gDNA) was isolated from tails, ears, or other tissue for identification of the genotype after birth or sacrifice of mice. Wiebke Brandt genotyped the mouse lines $G\alpha_{q/11}^{beKO}$, $Thbd^{beKO}$, and the majority of the *Cdh5*-GCaMP8 mice. The tissue was collected in clean 1.5 mL reaction tubes and incubated with 400 µL lysis buffer overnight at 56 °C. The next day, the samples were vortexed and centrifuged (16,000 *g*, 3 min, RT). 300 µL from the supernatant were transferred to a new 1.5 mL reaction tube and cooled to 4 °C for 10 min. Afterward, 600 µL of 100 % ice-cold ethanol was added to each tube and thoroughly mixed by shaking by hand. The samples were centrifuged (16,000 *g*, 8 min, 4 °C), the supernatant was discarded and 500 µL of ice cold 70 % ethanol was added and mixed thoroughly by hand shaking. Afterwards, the samples were centrifuged (16,000 *g*, 8 min, 4 °C), the supernatant was discarded, and the pellet was dried at 56 °C for 10 min. Finally, the pellet was resuspended in 200 µL sterile ddH_2O. Next, 2 µL from the gDNA sample solution was mixed with 20 µL of the reaction mix for PCR for genotyping in a reaction tube, and the samples were spun down before being loaded on a PCR thermocycler. The following table describes the PCR protocols followed for each gene.

	Cdh5-GCaMP8	*Gna11$^{-/-}$*	*Gnaq$^{fl/fl}$*	*Slco1c1-CreER^{T2}*	*Thbd$^{fl/fl}$*
Start	4 °C	4 °C	4 °C	4 °C	4 °C
Initialisation	94 °C, 5 min	94 °C, 5 min	94 °C, 5 min	94 °C, 5 min	94 °C, 5 min
Denaturation	94 °C, 30 s	94 °C, 30 s	94 °C, 30 s	94 °C, 30 s	94 °C, 30 s
Annealing	65 °C, 30 s	60 °C, 30 s	65 °C, 30 s	60 °C, 30 s	65 °C, 30 s
Extension/Elongation	72 °C, 45 s	72 °C, 45 s	72 °C, 45 s	72 °C, 45 s	72 °C, 45 s
No of cycles	35x	35x	35x	30x	35x
Final Elongation	72 °C, 10 min	72 °C, 10 min	72 °C, 10 min	72 °C, 10 min	72 °C, 10 min
Final Hold	4 °C	4 °C	4 °C	4 °C	4 °C

Table 2: PCR steps for mouse gDNA amplification for the identification of each mouse line's genotype.

The PCR products were analyzed with gel electrophoresis using a 100-base pair (bp) marker. Briefly, 2 % agarose gel was prepared by heating the appropriate agarose weight with 1x TAE buffer till it dissolved. Afterwards, EtBr was added to the liquid gel at a concentration of 0.2 µg/mL and mixed thoroughly. The liquid was poured into an agarose tracer and led solidify. The solidified gel was transferred to an electrophoresis chamber, and the PCR products and the 100-bp marker were loaded on the gel. The gel was run for 45 min with adjusted voltage depending on the length of the gel (10 V per cm).

Mouse line	Direction	Sequence
Cdh5-GCaMP8	Forward Reverse	5’-AAG GGC GAG GAG CTG TTC A-3’ 5’-CGA TCT GCT CTT CAG TCA GTT GGT-3’
Il2 internal positive control for *Cdh5*-GCaMP8 and *Slco1c1-CreER*^{T2} *mouse lines genotyping*	Forward Reverse	5’-CTA GGC CAC AGA ATT GAA AGA TCT-3’ 5’-GTA GGT GGA AAT TCT AGC ATC ATC C-3’
Gna11$^{-/-}$	Forward	5’-GACTAGTGAGACGTGCTACTTCC-3’
	Reverse	5’-CAGGGGTAGGTGATGATTGTGC-3’
	Forward	5’-AGCATGCTGTAAGACCGTAG-3’
	Reverse	5’-GCCCCTTGTACAGATGGCAG-3’
Gnaq$^{fl/fl}$	Reverse	5’-AGCTTAGTCTGGTGACAGAGGC-3’
	Forward	5’-GCATGCGTGTCCTTTATGTGAG-3’
Slco1c1-CreER^{T2}	Forward	5’-GCT ATT CAT GTC TTG GAA GCC-3’
	Reverse	5’-CAG GTT CTT CCT GAC TTC ATC-3’
Thbd$^{fl/fl}$	Forward	5’-AGGTTGTGATAGAGGCTAGCTGCTGTC-3’
	Reverse	5’-GGCCCTAAATCCATACTGCTCT-3’
	Reverse	5’-ATGTGCTGCAAGGCGATTAAGTTGG-3’

Table 3: *Mouse line laboratory name and the respective primers used for the gDNA amplification and identification of each genotype.*

3.12 Statistical analysis

Data were analyzed blinded. Statistics and data visualization were performed using GraphPad Prism 8 and are specified in the figure legends. All datasets were tested for distribution, and parametric or non-parametric statistics were used accordingly. All data were analyzed without an outlier test. Graphs show data with the standard error of the mean (SEM) or standard deviation (SD) when no statistical analysis was performed due to a low number of replicates. Significance was considered if $p < 0.05$ unless stated otherwise. In all experiments, animals were randomly assigned to treatment groups and were age- and sex-matched. The experimenter was blinded to the genotype.

4 Results

4.1 Brain endothelial G$\alpha_{q/11}$ signaling affects the cognitive function of aged mice

In a recent work of our group, it was demonstrated that deleting the genes encoding G$\alpha_{q/11}$ proteins from the brain endothelium leads to altered cerebrovascular responses after stimulation with CO_2 (Wenzel et al., 2020a). A battery of behavioral experiments showed that the brain endothelial G$\alpha_{q/11}$ signaling affects anxiety but not memory function in young mice (Wenzel et al., 2020a). In addition, reports from human studies have demonstrated that with aging cerebrovascular reactivity declines (McKetton et al., 2018; Miller et al., 2019; Peng et al., 2018) but whether the chronic deletion of the genes encoding the G$\alpha_{q/11}$ proteins plays a role in age-related cerebrovascular changes has not been investigated so far. Therefore, we hypothesized that the brain endothelial G$\alpha_{q/11}$ signaling plays a role in cognitive function during aging.

We probed the effect of *Gnaq* and *Gna11* brain endothelial deletion on the cognitive function of control and $G\alpha_{q/11}^{beKO}$ mice during their lifespan. First, mice were subjected to the behavioral experiment OPR as described before (Binder et al., 2012; Jiang et al., 2021), at two months old, before the tamoxifen treatment, to estimate if basal differences exist between the two groups. After the induction of the deletion of the *Gnaq* and *Gna11,* we subjected the mice to OPR test at three, six, twelve, and eighteen months old. The OPR is a hippocampus-dependent spatial memory formation task that relies on the intricate behavior of rodents to explore objects in novel locations (Assini et al., 2009; Binder et al., 2012). The advantage of OPR is that it does not rely on the physical activity of the mice and induces less anxiety compared to other behavioral testing procedures like the Barnes or Morris water maze (Sharma et al., 2010). In the OPR task, the memory function of the mice was assessed by calculating the preference index (see section 3.9.1). Here, we found that the mice at all time points showed no difference between genotypes on the preference index (Figure 4 A) and had similar explorative behavior as shown by the total exploration time of both objects (Figure 4 B). These results confirm the findings previously reported by Wenzel and colleagues using the novel object recognition test on young mice (Wenzel et al., 2020a). However, the $G\alpha_{q/11}^{beKO}$ group failed to discriminate against the displaced object at two time points (three and eighteen months old), as shown by the statistical testing against the chance level of 0.5 (Figure 4 A). Also, we looked on the total distance traveled during the test trial and we found that the $G\alpha_{q/11}^{beKO}$ group had significantly lower traveling distance compared to the control group (Figure 4 C). Finally, we observed that at two months old, the $G\alpha_{q/11}^{beKO}$ spent less time exploring the two objects and traveled less during the test phase but there was no difference between the two groups regarding the preference index (Supplementary Figure 1 A- C).

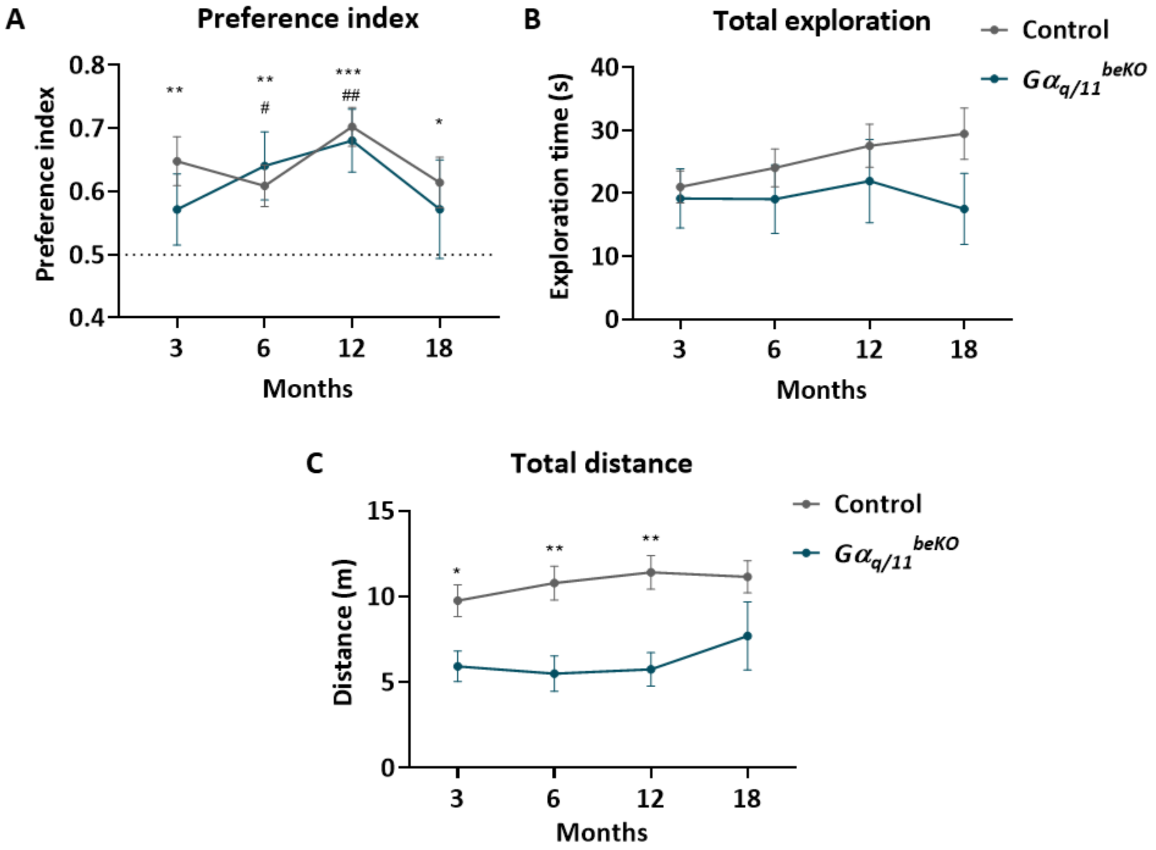

***Figure 4. Performance of control and $G\alpha_{q/11}^{beKO}$ mice on the OPR test across a lifespan**. Mice were tested at different time points during their lifespan for recognition memory deficits with the OPR test. **A)** The preference index between groups was not different at all time points. However, the $G\alpha_{q/11}^{beKO}$ group did not prefer the displaced object at 3 and 18 months time points. Data are shown as mean ± SEM. Statistical analysis: Mixed-effects analysis for repeated measurements with Geisser-Greenhouse correction ($\varepsilon = 0.9577$): genotype [$F(1, 34) = 0.6866$, $p = 0.7442$]; time [$F(2.873, 75.66) = 1.801$, $p = 0.1650$]; time x genotype [$F(3, 79)=0.5005$, $p = 0.4875$]. N = 10-18 animals per group. One sample t-test of each group to 0.5 chance level: 3 months old [control $t(16) = 3.798$, $p = 0.0016$; $G\alpha_{q/11}^{beKO}$ $t(13) = 1.267$, $p = 0.2275$]; 6 months old [control $t(17) = 3.315$, $p = 0.0041$; $G\alpha_{q/11}^{beKO}$ $t(12) = 2.597$, $p = 0.0233$]; 12 months old [control $t(17) = 6.565$, $p < 0.0001$; $G\alpha_{q/11}^{beKO}$ $t(13) = 3.627$, $p = 0.0031$]; 18 months old [control $t(17) = 0.6142$, $p = 0.0115$; $G\alpha_{q/11}^{beKO}$ $t(9) = 0.9197$, $p = 0.3817$]. **B)** There was no difference between groups regarding the total exploration time of the objects during the test trial, which indicated similar explorative behavior. Data are shown as mean ± SEM. Statistical analysis: Mixed-effects analysis for repeated measurements with Geisser-Greenhouse correction ($\varepsilon = 0.8073$): genotype [$F(1, 34) = 2.499$, $p = 0.1232$]; time [$F(2.422, 63.78) = 1.754$, $p = 0.1746$]; time x genotype [$F(3, 79) = 1.194$, $p = 0.3176$]. N = 10-18 animals per group. **C)** A significant difference between the $G\alpha_{q/11}^{beKO}$ and the control group was observed in the total distance during the test trial for the 3, 6 and 12 months time points. Data are shown as mean ± SEM. Statistical analysis: Mixed-effects analysis for repeated measurements with Geisser-Greenhouse correction ($\varepsilon = 0.8273$) and a Sidak's posthoc test. Genotype [$F(1, 34) = 16.07$, $p = 0.0003$]; time [$F(2.482, 65.36) = 2.875$, $p = 0.0524$]; time x genotype [$F(3, 79) = 1.199$, $p = 0.3155$]. N = 10-18 animals per group. * $p < 0.05$; ** $p < 0.01$, *** $p < 0.001$. * shows a significant difference between the control group and 0.5 chance level. # shows a*

significant difference of the $G\alpha_{q/11}{}^{beKO}$ to 0.5 chance level. Abbreviations: $G\alpha_{q/11}$: G protein subunit alpha q/11, beKO: brain endothelial knockout.

At the age of 19-21 months, the mice from both cohorts were subjected to the Barnes maze test to assess their cognitive function as described before (Binder et al., 2019). Barnes maze offers the advantage of assessing both hippocampus-dependent spatial learning and memory (Barnes et al., 1980; Sharma et al., 2010). Although it has been characterized as more stressful than the OPR test, it is still considered less stressful than other spatial memory tests like Water Maze (Sharma et al., 2010). Since mice tend to explore the maze after the initial identification of the target hole, primary measurements were used as more sensitive parameters for assessing spatial learning and memory (Binder et al., 2019; Sunyer et al., 2007). However, total measurements were calculated, too, and provided as supplementary information (Supplementary Figure 2 E- G and Supplementary Figure 3 E - F).

We found that both groups had similar learning curves, as shown by the significant reduction of primary errors, distance and latency from day 1 to day 5 and that no significant differences between groups were observed for primary errors and distance (Figure 5 A- C). Furthermore, the fact that no differences in the primary distance were found, points that both groups had similar locomotor activity (Figure 5 C). However, there was a significant genotype effect on the primary latency between groups (Figure 5 B). Furthermore, we assessed the learning strategies of the mice as previously described (Binder et al., 2019; Harrison et al., 2006). More specifically, the direct strategy was defined as the strategy where mice either reach the escape hole directly or one of the adjacent holes and subsequently the escape hole (Figure 5 D, green line). Mice that use this type of strategy use the extra maze spatial cues to solve the task; therefore, it is considered a spatial learning strategy. The serial strategy was defined as the strategy where mice first travel to a hole that is at least 2 adjacent holes away from the target hole and solve the task by visiting every adjacent hole either clockwise or counterclockwise until they reach the target hole (Figure 5 D, orange line). Finally, the mixed strategy was defined as a non-spatial learning strategy where mice do not follow one of the other two strategies and solve the task by randomly visiting the holes of the maze (Figure 5 D, black line). In this study, we found that both groups showed a significant increase in the use of the direct strategy during the acquisition days and a decrease in the use of the mixed strategy (Figure 5 E- F). Statistical analysis showed a significant genotype effect on day 4 and day 5 of acquisition days (Supplementary Figure 2 A). More specifically, the control group significantly decreased the use of the non-spatial learning strategies over time and increased the use of direct strategies (Figure 5 E and Supplementary Figure 2 A- D). However, although the *$G\alpha_{q/11}{}^{beKO}$* significantly decreased the use of mixed strategy and increased the use of direct strategy, the serial strategy was not changed over time (Figure 5 F and Supplementary Figure 2 A- D). Furthermore, there was a significant difference between the two groups in the use of serial strategy on day 4 and a tendency in the use of direct strategy on day 5 (Supplementary Figure 2 A- C). All in all, these results showed that the $G\alpha_{q/11}^{beKO}$ group could mainly learn and solve the task with a non-spatial learning strategy, indicating deficits in the spatial learning procedure.

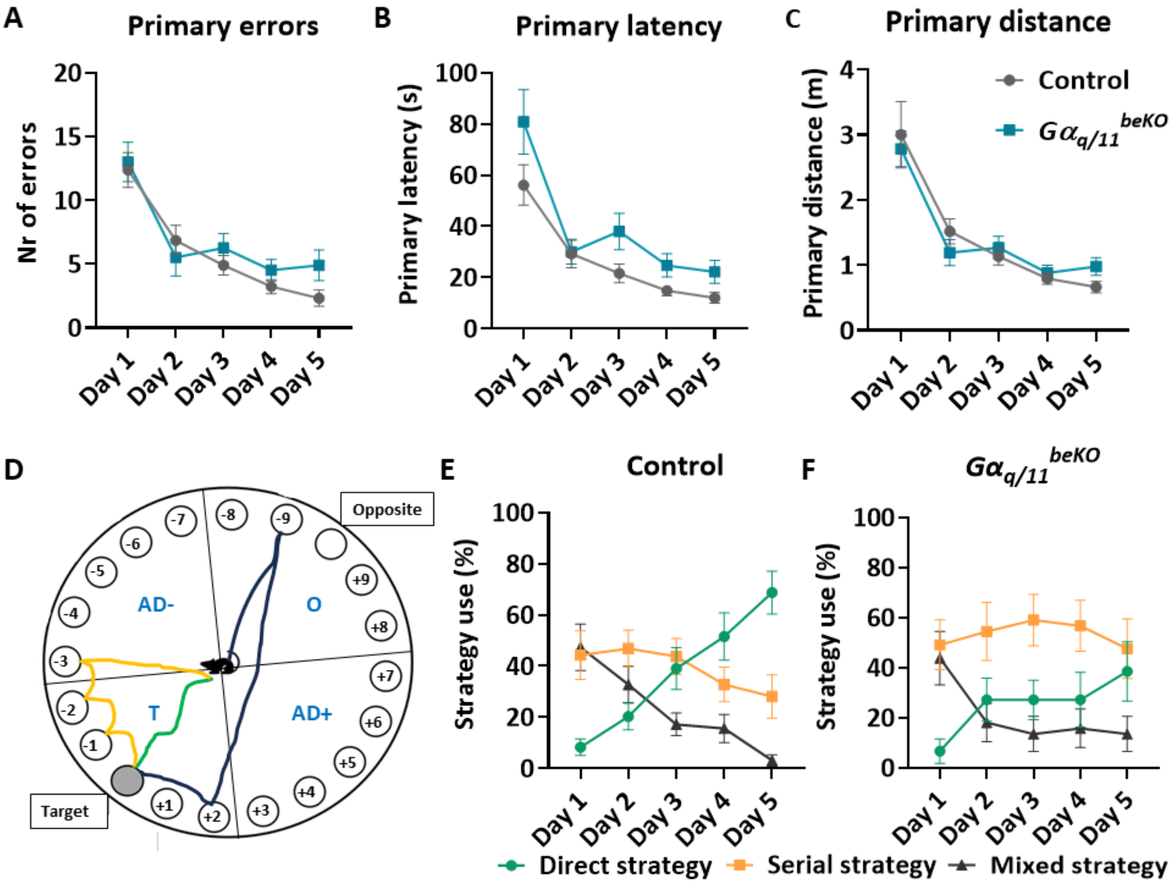

Figure 5. $G\alpha_{q/11}^{beKO}$ mice and control mice have similar learning processes but different learning strategies in the Barnes maze test. A-C) *Primary errors, distance, and latency significantly decline over time for both groups during the acquisition days, indicating no differences in the learning process. However, a significant genotype effect on primary latency was observed. Data are shown as mean ± SEM of four trials per day. Statistical analysis: two-way repeated measurements analysis of variance (ANOVA) with Sidak's posthoc test. Primary errors: genotype [F(1, 25) = 0.7738, p = 0.3874]; time [F(2.194, 54.85) = 32.42, p < 0.0001]; interaction [F(4, 100) = 1.227, p = 0.3044]; subject [F(25, 100) = 3.161, p < 0.0001]. Primary distance: genotype [F(1, 25) = 0.0001125, p = 0.9916]; time [F(1.420, 35.49) = 26.68, p < 0.0001]; interaction [F(4, 100) = 0.6317, p = 0.6410]; subject [F(25, 100) = 1.479, p = 0.09]. Primary latency: genotype [F(1, 25) = 4.542, p = 0.0431]; time [F(1.692, 42.31) = 37.59, p < 0.0001]; interaction [F(4, 100) = 1.726, p = 0.1501]; subject [F(25, 100) = 3.718, p < 0.0001]. N = 11-16 animals per group* ***D)*** *Schematic presentation of the Barnes maze. Colored lines indicate the different learning strategies: green (direct), orange (serial), and black (mixed). The quadrants are indicated with the capital letters T: target quadrant, AD+: right adjacent quadrant, AD-: left adjacent quadrant, O: opposite quadrant. Holes on the right side adjacent to the target hole are indicated with a positive charge and those on the left side with a negative.* ***E, F)*** *Percent use of strategies in control and $G\alpha_{q/11}^{beKO}$ mice during the acquisition days 1-5 from a total of four intertrials per mouse per day. Control mice showed a significant increase over time in using the direct spatial strategy and a decrease in the non-spatial spatial strategies. The $G\alpha_{q/11}^{beKO}$ mice showed a significant increase in the use of the direct strategy and a decrease in the mixed strategy. However, the non-spatial serial strategy did not change over time; it was the main strategy used during the acquisition days,*

*indicating a deficit in spatial learning. Data are shown as mean ± SEM of four trials per day. Statistical analysis: nonparametric, repeated measurements Friedman test. Control: direct strategy $p < 0.0001$; serial strategy $p = 0.0013$; mixed strategy $p < 0.0001$. $G\alpha_{q/11}^{beKO}$: direct strategy $p = 0.0123$; serial strategy $p = 0.4612$; mixed strategy $p < 0.0001$. N = 11-16 animals per group. * $p < 0.05$. Abbreviations: $G\alpha_{q/11}$: G protein subunit alpha q/11, beKO: brain endothelial knockout.*

Next, the assessment of short- and long-term spatial reference memory of the mice was based on the day 6 and day 17 probe trials, respectively (Sunyer et al., 2007). Similar to the acquisition days, we looked at the primary parameters of error, latency, and distance (Figure 6 A- C). We found that the $G\alpha_{q/11}^{beKO}$ group made significantly more primary errors and required more time to reach the target hole compared to the control group on day 6 (Figure 6 A- B), but did not find a difference between the groups on day 17 in all primary parameters (Figure 6 A- C). These data indicate that the $G\alpha_{q/11}^{beKO}$ group has a significant short-term memory deficit compared to the control group. However, long-term memory seemed not to be different between the groups. Finally, there was no difference in the primary distance between the two groups, pointing to similar locomotion activity (Figure 6 C).

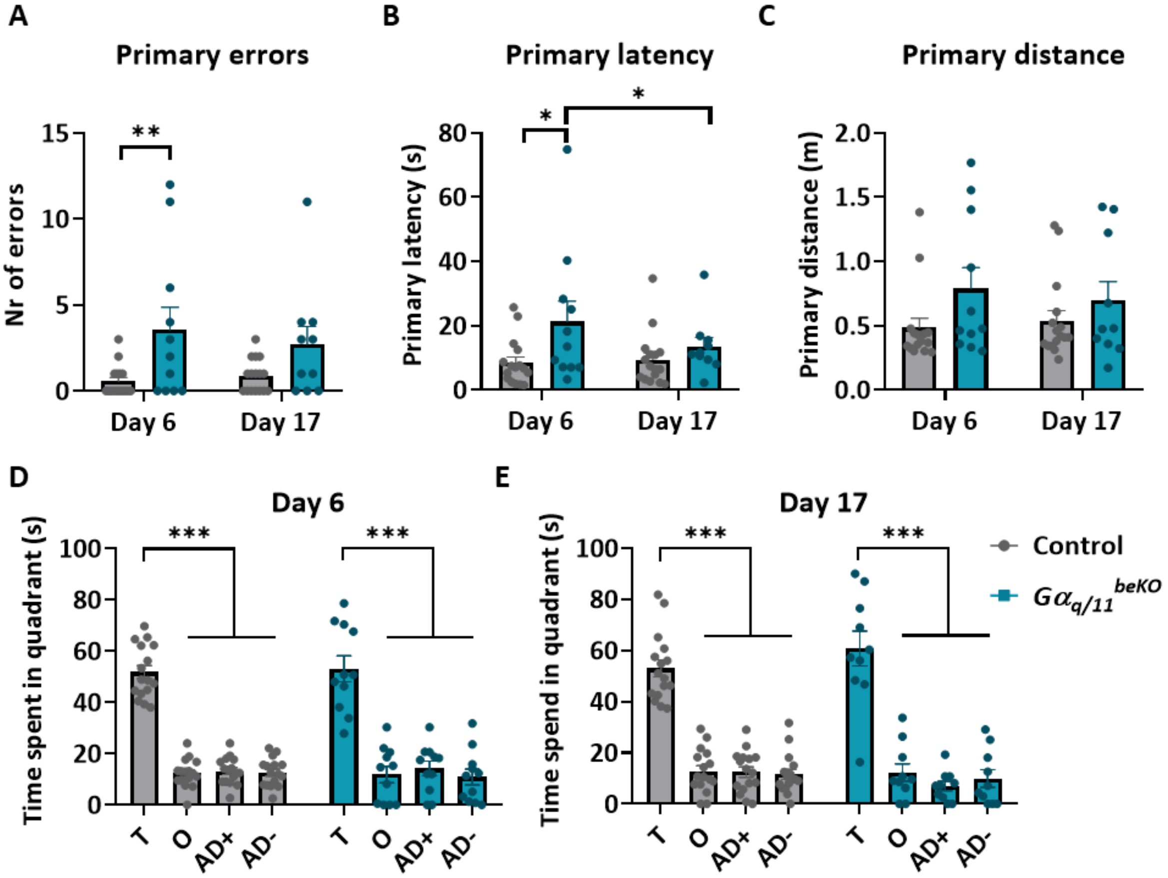

Figure 6: $G\alpha_{q/11}^{beKO}$ mice show impaired short-term spatial memory compared to control mice. A) *The number of primary errors between control and $G\alpha_{q/11}^{beKO}$ mice significantly differed on day 6 but not on day 17. Data are shown as mean ± SEM. Statistical analysis: Mixed effect analysis for repeated measurements and a Sidak's posthoc test. Genotype [F(1, 25) = 6.823, p = 0.0150]; time [F(1, 24) = 0.4399, p = 0.5135]; time x genotype [F(1, 24) = 2.227, p = 0.1486]. N = 11-16 animals per group* ***B)*** *Primary latency was significantly different higher between groups during day 6 but not during day 17. Data are shown as mean ± SEM. Statistical analysis: Mixed effect analysis for repeated measurements with a Sidak's posthoc test. Genotype [F(1, 25) = 3.448, p = 0.0752]; time [F(1, 24) = 3.903, p = 0.0598];*

time x genotype [F(1, 24) = 6.2, p = 0.0201]. N = 11-16 animals per group ***C)*** *Primary distance was not different between groups on both day 6 and day 17. Data are shown as mean ± SEM. Statistical analysis: Mixed effect analysis for repeated measurements. Genotype [F(1, 25) = 2.610, p = 0.1187]; time [F(1, 24) = 0.1289, p = 0.7228]; time x genotype [F(1, 24) = 1.142, p = 0.2959]. N = 11-16 animals per group.* ***D, E)*** *Both groups spent significantly more time on the target quadrant compared to all other quadrants on both day 6 and day 17, indicating the ability to distinguish it once they reached the target hole. Data are shown as mean ± SEM. Statistical analysis: two-way ANOVA with Sidak's posthoc test. Day 6: genotype [F(1, 100) = 0.000, p > 0.9999]; quadrant [F(3, 100) = 118.5, p < 0.0001]; interaction [F(3, 100) = 0.1458, p = 0.99321]. Day 17: genotype [F(1, 96) = 4.66e-007, p = 0.9995]; quadrant [F(3, 96) = 101.0, p < 0.0001]; interaction [F(3, 96) = 1.492, p = 0.2217]. N = 10-16 animals per group; * p < 0.05, ** p < 0.01, *** p < 0.001. Abbreviations:* $G\alpha_{q/11}$*: G protein subunit alpha q/11, beKO: brain endothelial knockout, T: target quadrant, AD+: right adjacent quadrant, AD-: left adjacent quadrant, O: opposite quadrant.*

In addition, we found that both groups spent significantly more time in the target quadrant compared to the other quadrants (Figure 6 D- E) and visited the target hole and its adjacent holes more often compared to all the other holes in both day 6 and day 17 (Supplementary Figure 3 A- B). These data indicate that mice of both groups were able to remember the position of the target hole after they reached it as well as that there were no visual impairments between groups.

We also assessed the general locomotor activity of the mice by looking at the total distance traveled on day 6 and day 17 (Supplementary Figure 3 E). We found a strong genotype effect and differences between genotypes on day 6 but not on day 17. These results point that the $G\alpha_{q/11}^{beKO}$ mice were less explorative after finding the target hole compared to the control group, which is also supported by the total number of errors (Supplementary Figure 3 F). Finally, looking at the use of strategies on day 6 and day 17 we found that 80 % of mice used spatial strategy and less than 20 % the non-spatial strategies to solve the task on both probe trials. However, mice from the $G\alpha_{q/11}^{beKO}$ group used spatial and non-spatial strategies to an almost even degree on both probe trials (Supplementary Figure 3 C - D).

4.2 Aged $G\alpha_{q/11}^{beKO}$ mice show higher string vessel formation but no major brain histopathological differences

Based on the previous findings, we were prompted to search for the underlying mechanisms that led to the worse performance of aged $G\alpha_{q/11}^{beKO}$ compared to control mice. The OPR and Barnes maze are two behavioral experiments that assess spatial memory and are dependent on the function of the hippocampus, which has also been shown to be critical for age-dependent cognitive deficits (Assini et al., 2009; Barnes et al., 1980; Sharma et al., 2010). Therefore, we looked first at the vessel density and structure in the hippocampus region. We stained coronal cryosections from control and $G\alpha_{q/11}^{beKO}$ mice for collagen IV and caveolin-1. Collagen IV is a basement membrane marker while caveolin-1 was used as an EC marker. We assessed the formation of string vessels in the hippocampus region by manually measuring structures that were positively stained for collagen IV and negative for caveolin-1 (Figure 7 A). We found that in the $G\alpha_{q/11}^{beKO}$ group, there was a significant increase in the formation of string vessels compared to the control group (Figure 7 B). However, there was no difference between the groups regarding the total vessel length (Figure 7 C). These results indicate that the vessel density is not different between groups, but substantial differences in the formation of collapsed vessels could be a reason for the observed cognitive deficits (Brown, 2010; Jiang et al., 2021).

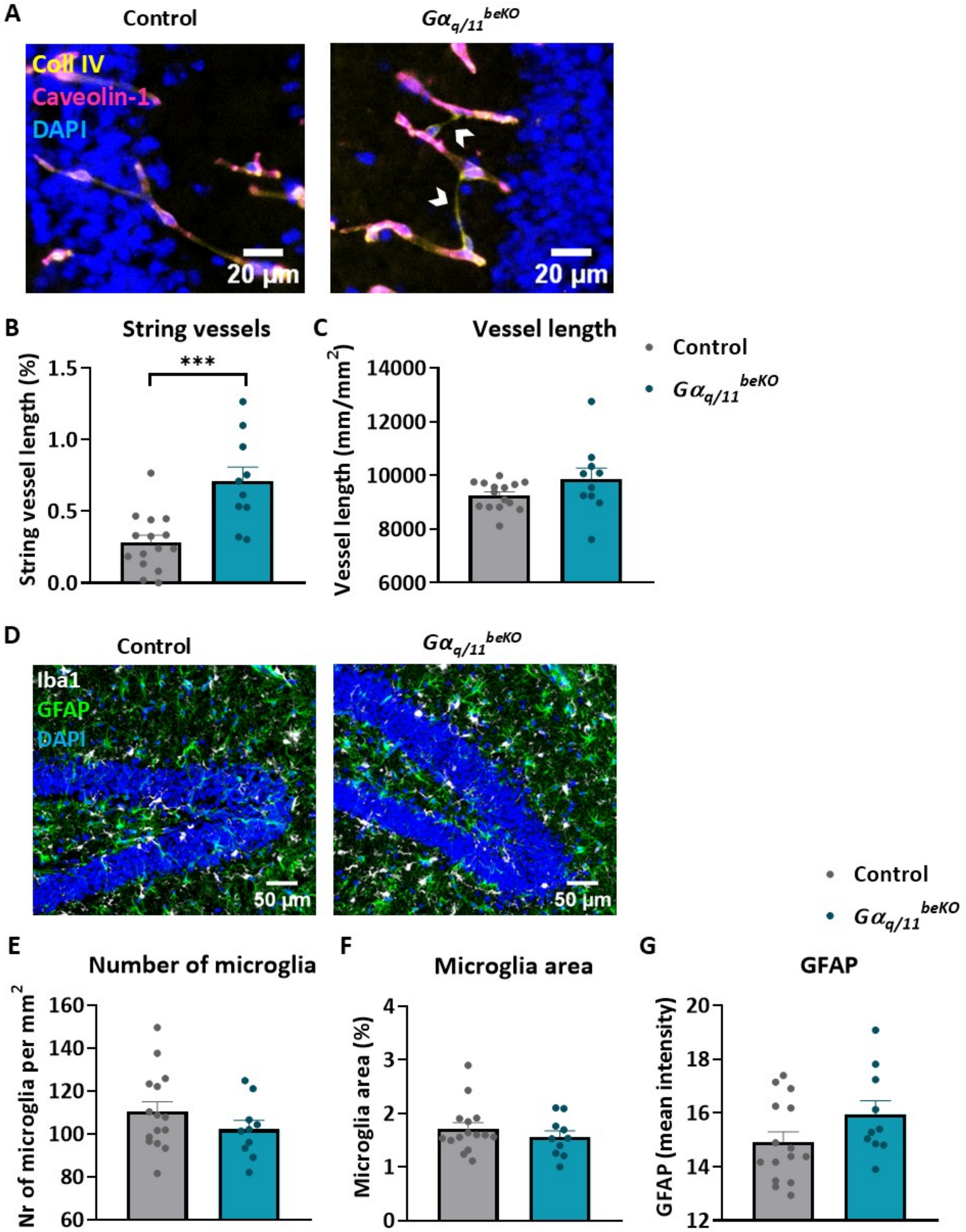

Figure 7: $G\alpha_{q/11}^{beKO}$ mice show increased string vessel formation in the hippocampus but no differences in neuroinflammation markers. A-C) *Coronal cryosections from control and $G\alpha_{q/11}^{beKO}$ mice were stained for the basement membrane marker collagen IV and the endothelial protein caveolin-1 (A). String vessels (white arrowheads) were manually quantified as structures positively stained for collagen IV and negative for caveolin-1. DAPI was used to visualize nuclei. (B) String vessels were normalized to total vessel length. The total vessel length was calculated based on the collagen IV-positively stained structures. Data are shown as mean ± SEM. Statistical analysis: string vessels: unpaired t-test [t(23) = 4.137, p = 0.0004]; vessel length Mann-Whitney U-test, p = 0.1289. N = 10-15 animals/group.* ***D-G)*** *Coronal cryosections from control and $G\alpha_{q/11}^{beKO}$ were stained for the astrocytic*

marker GFAP and the microglial marker Iba1 (D). The intensity of GFAP was calculated as a measure of activated astrocytes. Microglia activation was estimated by calculating the relative area of Iba1-positive structures to the total area. No differences were detected between the control and G$\alpha_{q/11}^{beKO}$ *regarding the number of microglia (E), the microglia area (F) and the mean fluorescence intensity of GFAP immunoreactivity (G). Data are shown as mean ± SEM. Statistical analysis: number of microglia: unpaired t-test [t(23) = 1.223, p = 0.2339]; microglia area: unpaired t-test [t(23) = 8791, p = 0.3885]; GFAP mean intensity: Mann-Whitney U-test p = 0.091. N = 10-15 animals/group. *** p < 0.001. Abbreviations: G*$\alpha_{q/11}$*: G protein subunit alpha q/11, beKO: brain endothelial knockout, coll IV: collagen IV, DAPI: diamidino-2-phenylindole, Iba1: ionized calcium-binding adaptor molecule 1, GFAP: glial fibrillary acidic protein, Nr: number.*

We also looked for signs of neuroinflammation that could affect neuronal function and lead to a cognitive decline in aged mice (Clarke et al., 2018; Yang et al., 2017). We stained coronal cryosections for the microglia marker Iba1 and for the marker for reactive astrocytes GFAP (Figure 7 D). Our results showed no difference in the relative area and the number of microglia between the two groups (Figure 7 E- F). Also, we did not find differences in the mean intensity of GFAP (Figure 7 G). These results indicate that the brain endothelial G$\alpha_{q/11}$ signaling does not significantly affect neuroinflammation in aged mice.

Since cognitive impairment is characterized by neuronal changes, ranging from altered neuronal function to neuronal degeneration and death, we were prompted to investigate some of these parameters (Burke & Barnes, 2006). First, we assessed neuronal density in the region of the hippocampus by a gross measurement of the thickness of the stratum pyrimidale layer in cornu ammonis region 1 (CA1), CA3, and dentate gyrus regions between the groups by using the mouse brain atlas and the DAPI stain (Supplementary Figure 4 A). We found no difference in the thickness of any of the regions of interest between groups (Supplementary Figure 4 B- D), which would be expected based on the mild cognitive deficits that the behavioral tests showed and previous studies that showed that no significant neuronal loss in the hippocampus occurs during normal aging (Burke & Barnes, 2006). Afterwards, we looked into more specific structures like neuronal synapses, neuronal somata, and dendrites. We stained coronal sections for the pre- and post-synaptic markers bassoon and shank2, respectively, as well as for the neuronal marker MAP2, which shows immunoreactivity against the neuronal microtubules in the soma and dendrites (Figure 8 A). Our results showed no differences between groups in the mean intensity on the pre- and post-synaptic markers and the neuronal marker MAP2 (Figure 8 B - J). These results point towards another mechanism that affects neuronal function unrelated to the number of synapses and neuronal integrity.

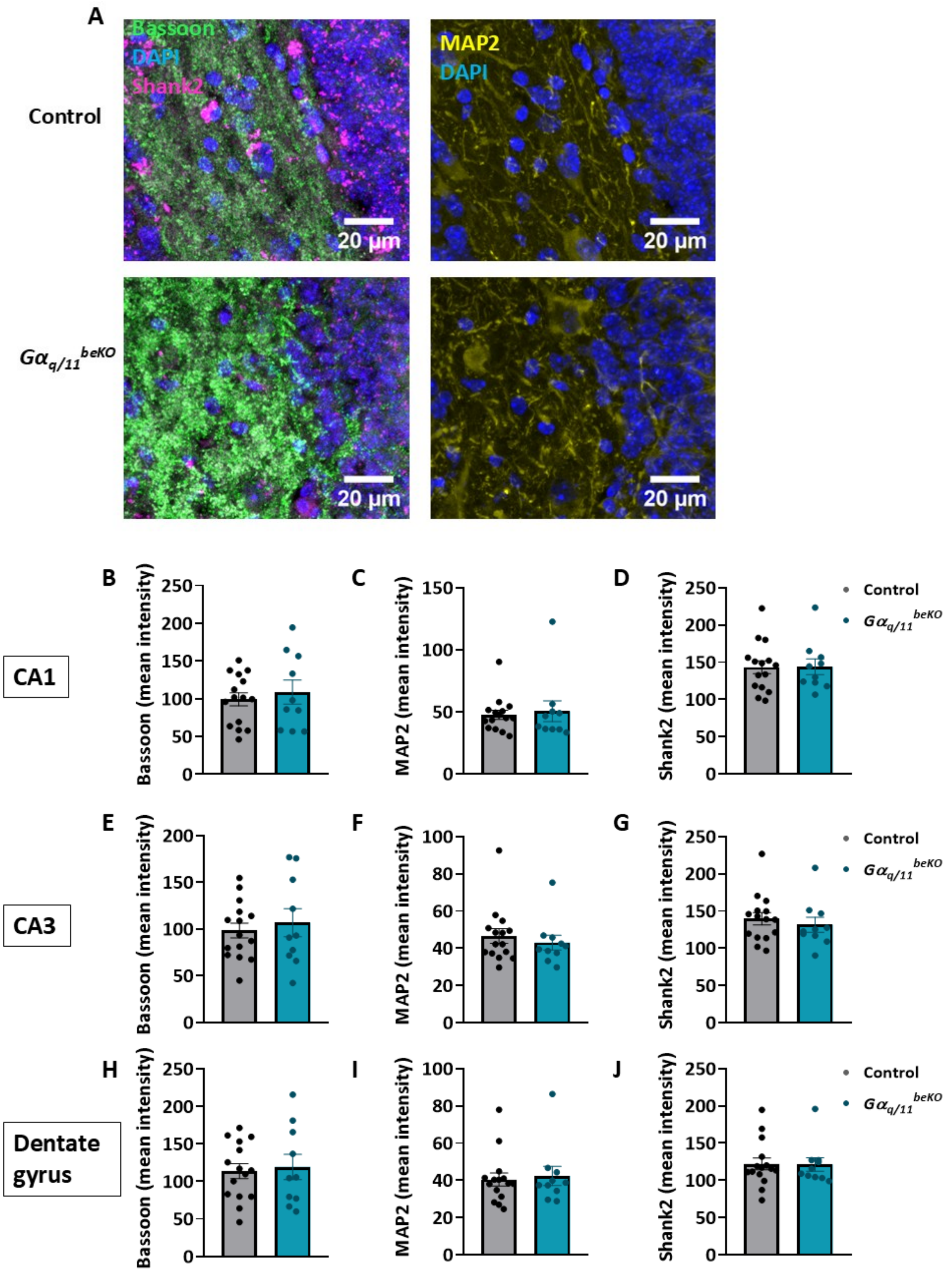

Figure 8: $G\alpha_{q/11}^{beKO}$ and control mice do not show differences in neuronal and synaptic markers. A) *Representative pictures of immunoreactivity of the presynaptic marker bassoon, the postsynaptic marker shank2 and the neuronal marker MAP2 in the dentate gyrus region on cryosections from control and $G\alpha_{q/11}^{beKO}$ mice. DAPI was used to visualize nuclei.* ***B-J)****: Quantification of the mean intensity of the fluorescence immunoreactivity of bassoon, MAP2 and shank2 in CA1, CA3 and dentate gyrus of hippocampus. No significant differences were observed between control and $G\alpha_{q/11}^{beKO}$ in any marker. Data are shown as mean ± SEM. Statistical analysis: CA1 region-bassoon: unpaired t-test*

[t(23) = 0.5859, p = 0.5637]; CA1 region-MAP2: Mann-Whitney U-test (p = 0.683); CA1 region-shank2: unpaired t-test [t(23) = 0.04081, p = 0.9678]; CA3 region-bassoon: unpaired t-test [t(23) = 0.5337, p = 0.5987]; CA3 region-MAP2: Mann-Whitney U-test (p = 0.4952); CA3 region-shank2: Mann-Whitney U-test (p = 0.5671); dentate gyrus region-bassoon: unpaired t-test [t(23) = 0.2959, p = 0.77]; dentate gyrus region-MAP2: Mann-Whitney U-test (p = 0.9783); dentate gyrus region shank2: Mann-Whitney U-test (p = 0.8065). N = 10-15 animals/group. Abbreviations: $G\alpha_{q/11}$*: G protein subunit alpha q/11, beKO: brain endothelial knockout, DAPI: diamidino-2-phenylindole, MAP2: microtubule associated protein 2, CA: cornu ammonis.*

Memory consolidation is a process that involves the coordination between the hippocampus and cortical regions in order to store new information (Squire et al., 2015). Therefore, we looked for structural differences in the neocortex, too. We stained sagittal cryosections of both groups with collagen IV and caveolin-1 and assessed the vessel structures (Figure 9 A). We found that, similarly to the hippocampus, there was a significant increase in the formation of string vessels in the $G\alpha_{q/11}{}^{beKO}$ group compared to the control group and no differences in total vessel length (Figure 9 B and C). Furthermore, we looked for signs of neuroinflammation by staining for the microglia marker Iba1 and for the astrocytic marker GFAP (Figure 9 D). Similar to the hippocampus, we did not observe any differences in the mean intensity of GFAP, the number of microglia, and their morphology between the two groups (Figure 9 E-G).

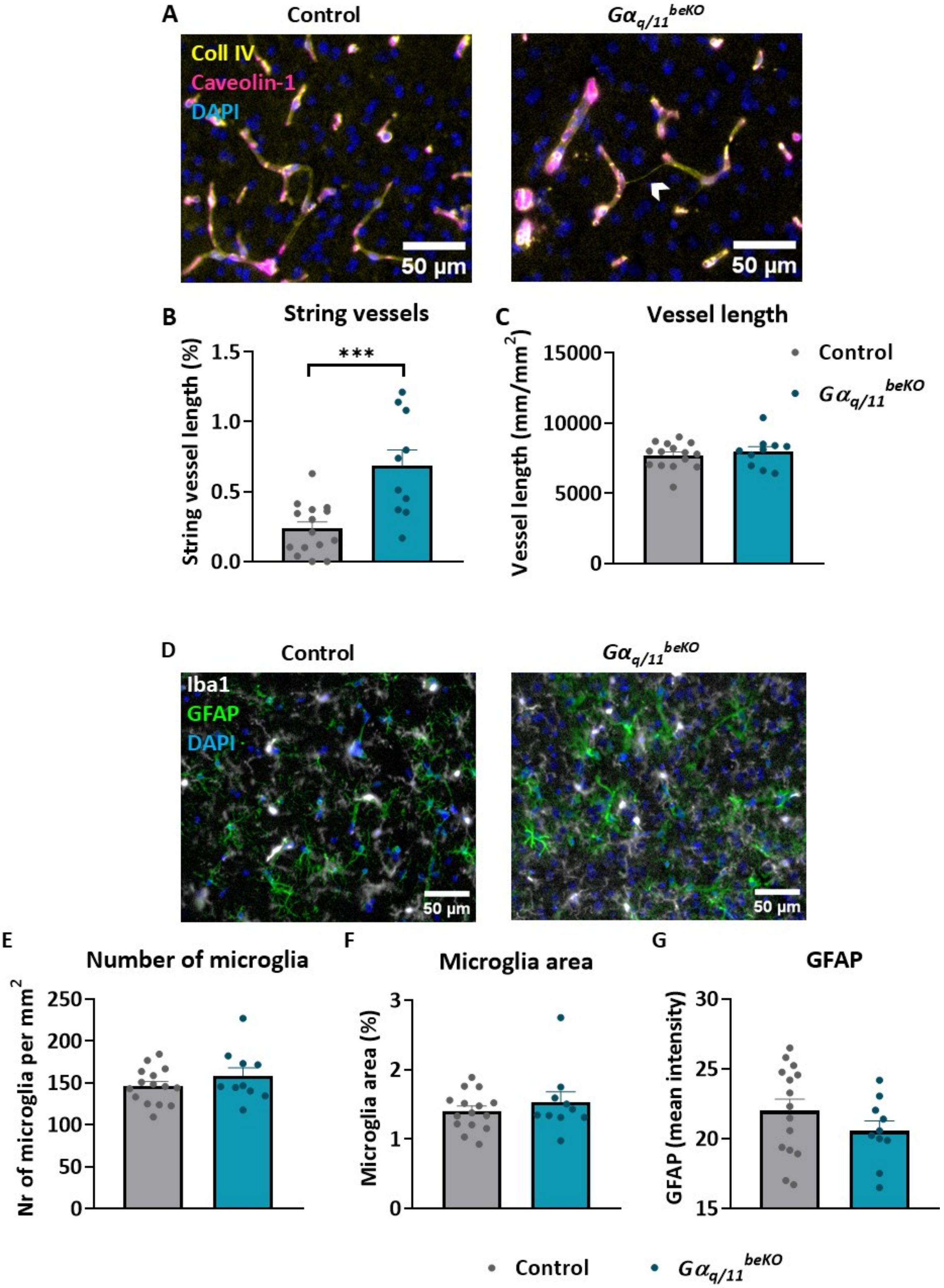

Figure 9: ***$G\alpha_{q/11}^{beKO}$ mice show increased string vessel formation in the cortex but no differences in neuroinflammation markers. A-C)*** *Sagittal cryosections from control and $G\alpha_{q/11}^{beKO}$ mice were stained for the basement membrane marker collagen IV and the endothelial marker caveolin-1 (A). String vessels (white arrowheads) were manually quantified as structures positively stained for collagen IV and negatively stained for caveolin-1 and were normalized to total vessel length (B). DAPI was used to visualize nuclei. The total vessel length was calculated using the collagen IV positively stained structures (C). Data are shown as mean ± SEM. Statistical analysis: unpaired t-test [t(23) = 4.043, p =*

0.0005]; total vessel length: unpaired t-test [t(23) = 0.6206, p = 0.5410]. N = 10-15 animals/group. Inlet magnification of string vessel area. Arrows indicate string vessel structures. ***D)*** *Sagittal cryosections from control and $G\alpha_{q/11}^{beKO}$ were stained for the astrocytic marker GFAP and the microglial marker Iba1. The intensity of GFAP was calculated as a measure of activated astrocytes. Microglia activation was estimated by calculating the relative area of Iba1-positive structures to the total area. No differences were detected between the control and $G\alpha_{q/11}^{beKO}$ mice regarding the number of microglia (E), the relative microglia area (F) and the mean fluorescence intensity of GFAP immunoreactivity (G). Data are shown as mean ± SEM. Statistical analysis: number of microglia: unpaired t-test [t(23) = 1.137, p = 0.2674]; relative microglia area: Mann-Whitney U-test (p = 0.7647); GFAP intensity: unpaired t-test [t(23) = 1.227, p = 0.2321]. N = 10-15 animals/group. *** p < 0.001. Abbreviations: $G\alpha_{q/11}$: G protein subunit alpha q/11, beKO: brain endothelial knockout, coll IV: collagen IV, DAPI: diamidino-2-phenylindole, Iba1: ionized calcium-binding adaptor molecule 1, GFAP: glial fibrillary acidic protein, Nr: number.*

Another parameter that we looked at afterward, was the BBB integrity. The leaky BBB has been demonstrated to be a characteristic of normal aging and can contribute to memory decline since blood-borne molecules can lead to inflammation (Yang et al., 2020, 2017). Therefore, we examined the IgG extravasation in the cortex. For this reason, we masked the vessel structures by using the caveolin-1 staining to exclude the vessel regions and assessed the IgG extravasation by measuring the mean intensity of IgG immunoreactivity in the brain parenchyma (Figure 10 A). However, we found no differences between the two groups (Figure 10 B).

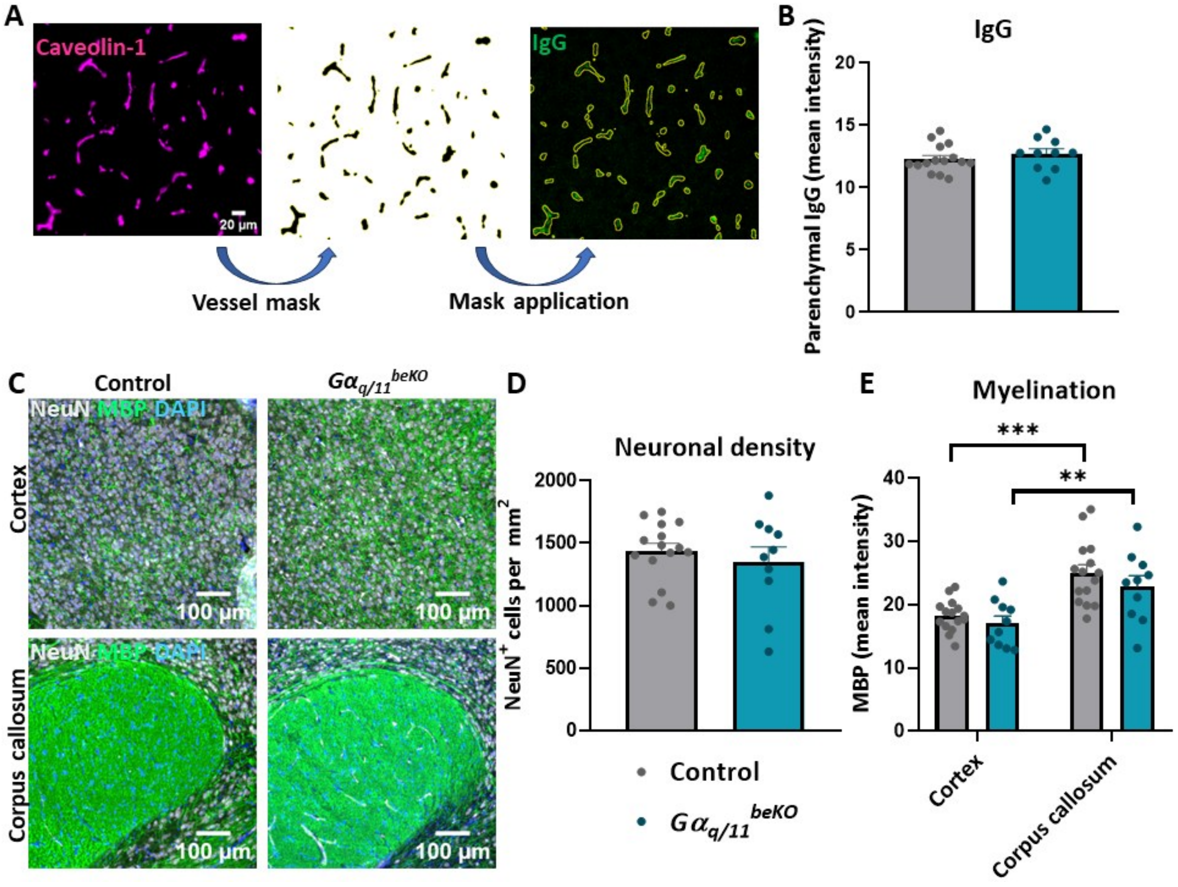

Figure 10: $G\alpha_{q/11}^{beKO}$ mice do not show differences in IgG extravasation, neuronal density and myelination compared to control mice. A) *Schematic representation of the calculation of immunofluorescence intensity of IgG in parenchyma. Caveolin-1 staining was used for the creation of*

the vessel mask which subsequently was applied to the IgG-stained images to exclude the vessel structures and calculate the immunoreactivity of IgG in the parenchyma. ***B)*** *Quantification of the IgG immunoreactivity in the brain parenchyma was not different between the two genotypes. Data are shown as mean ± SEM. Statistical analysis: unpaired t-test [t(23) = 0.8706, p = 0.393].* ***C)*** *Representative pictures of sagittal cryosections from control and* $G\alpha_{q/11}^{beKO}$ *mice stained for the neuronal marker NeuN and MBP in two different regions, cortex and corpus callosum.* ***D)*** *Quantification of the number of* $NeuN^{+}$ *cells in the cortex showed no difference between the two groups. Data are shown as mean ± SEM. Statistical analysis: unpaired t-test [t(23) = 0.7254, p = 0.4755]. N = 10-15 animals/group.* ***E)*** *Quantification of the mean intensity of the myelin basic protein in cortex and corpus callosum was not different between genotypes. Data are shown as mean ± SEM. Statistical analysis: two-way ANOVA with Sidak's posthoc test: genotype [F(1, 46) = 1.870, p = 0.1781]; brain region [F(1, 46) = 26.09, p < 0.0001]; interaction [F(1, 46) = 0.1424, p = 0.7077]. N = 10-15 animals/group. ** p < 0.01, *** p < 0.001. Abbreviations:* $G\alpha_{q/11}$*: G protein subunit alpha q/11, beKO: brain endothelial knockout, DAPI: diamidino-2-phenylindole, IgG: immunoglobulin G, NeuN: neuronal nuclei.*

Finally, we looked for neuronal density and myelination in the cortex and corpus callosum by staining sagittal cryosections for the neuronal marker NeuN and the MBP, a structural protein of the CNS myelin (Figure 10 C). However, we did not detect differences between the two groups for both markers in cortex and corpus callosum (Figure 10 D and E).

4.3 Brain endothelial $G\alpha_{q/11}$ affects the mortality of mice

As part of the general assessment of the $G\alpha_{q/11}^{beKO}$ line we calculated the survival rate based on data from all mice that participated in the current study. Strikingly, we found that the $G\alpha_{q/11}^{beKO}$ group showed a significant drop in survival curves compared to the control group (Figure 11 A, E – F)). It is of interest that the reasons for earlier termination from the study were either unexpected death or mice had to be terminated due to severe skin injuries (Figure 11 C). Finally, either additionally or separately the reasons for death were statistically significant between groups (Figure 11 B and D). Whether there is a connection between the brain endothelial-specific deletion of the *Gnaq* and *Gna11* genes and skin injuries is not clear, and further studies are needed to investigate this. Furthermore, regarding spontaneous deaths, a possible reason could be seizures. Therefore, we looked for spontaneous seizures in the home cage, but we did not observe differences. However, this notion should be further explored with more sensitive methods that could identify seizure activity more accurately than macroscopic observation of the mouse behavior.

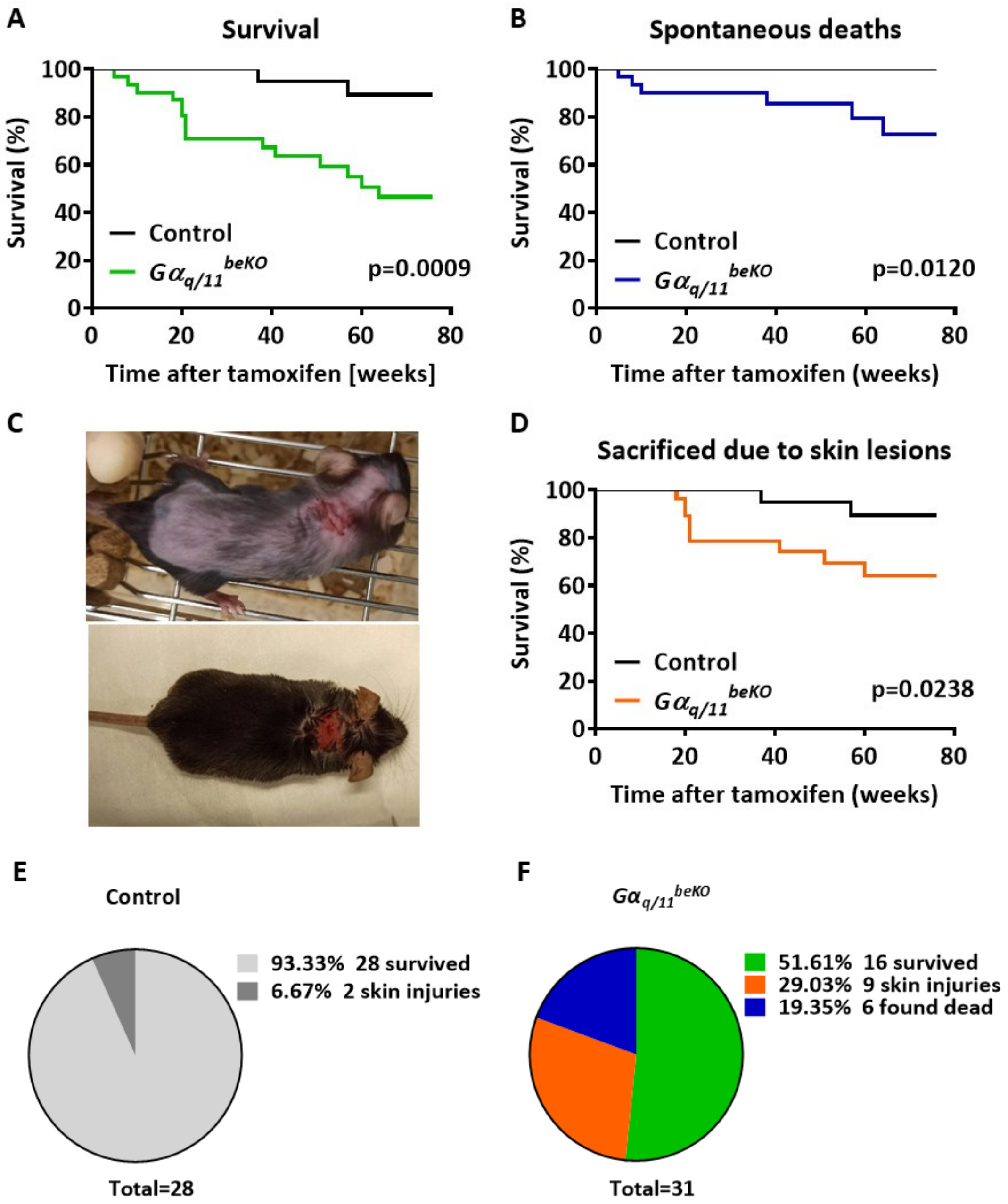

Figure 11: Brain endothelial deletion of $G\alpha_{q/11}$ leads to higher mortality. A) *Survival curves of all control and $G\alpha_{q/11}^{beKO}$ mice used in the current study. $G\alpha_{q/11}^{beKO}$ mice have significantly lower survival than the control littermates. Mantel-Cox test; $\chi^2(1) = 11.01$; $p < 0.001$.* ***B)*** *Survival curves of $G\alpha_{q/11}^{beKO}$ and control mice regarding only spontaneous deaths as a cause for termination. Statistical analysis Mantel-Cox test [$\chi^2(1) = 6.312$, $p = 0.012$].* ***C)*** *Representative pictures of the severe skin lesions that lead to the sacrifice of mice.* ***D)*** *Survival curves of $G\alpha_{q/11}^{beKO}$ and control mice regarding only severe skin lesions as a cause for termination. Statistical analysis Mantel-Cox test [$\chi^2(1) = 5.106$, $p = 0.0238$].* ***E, F)*** *Pie charts showing the percentage of mice that died due to severe skin injuries or spontaneously during this study. Abbreviations: $G\alpha_{q/11}$: G protein subunit alpha q/11, beKO: brain endothelial knockout.*

4.4 MPBECs respond to shear stress through $[Ca^{2+}]_i$ increase and NF-κB activation independent of $G\alpha_{q/11}$

Based on the immunohistochemical data that showed increased string vessel formation in the $G\alpha_{q/11}^{beKO}$ mice compared to control mice, we prompted the molecular mechanisms that involve the $G\alpha_{q/11}$ signaling and age-related alterations in the brain vasculature. It is known that with normal aging, several changes in the vasculature render the brain to a predisposition to neurological and cerebrovascular diseases (Watanabe et al., 2020). Among others, vascular stiffness and narrowing of the vascular lumen due to atherosclerosis (large arteries) and arteriolosclerosis (small vessels) lead to changes in cerebral blood flow (Yang et al., 2017). Furthermore, string vessels and vessel rarefaction have been associated with normal aging and the development of vascular cognitive impairment (Riddle et al., 2003; Yang et al., 2017). Also, unpublished data from our group have pointed out that GPCRs that act upstream of $G\alpha_{q/11}$ proteins and have been characterized as a part of the mechanosensory complex of ECs in the peripheral vasculature (Wang et al., 2015, 2016; Xu et al., 2018), have a significant effect in the mouse brain microvasculature and their absence leads to increased string vessel formation. Therefore, we hypothesized that shear stress, the mechanical force exerted on the endothelium due to the blood flow, could be an essential factor contributing to the increased string vessel formation in aged $G\alpha_{q/11}^{beKO}$ mice.

In order to investigate this, we prompted shear stress *in vitro* in MPBECs. Based on literature research we focused on Piezo1, which is one of the most important and well-characterized mechanosensory proteins expressed in ECs (Murthy et al., 2017). It has been proposed that Piezo1 activation in the periphery leads to the activation of $G\alpha_{q/11}$ pathway and downstream affects the NF-κB signaling (Albarrán-Juárez et al., 2018). However, whether this sequence of molecular functions is also present in the brain vasculature is not clear. Therefore, we isolated MPBECs from control and $G\alpha_{q/11}^{beKO}$ mice and treated them with a selective activator of Piezo1, Yoda1. Since during the activation of the canonical pathway of NF-κB, the NF-κB complex translocates from the cytoplasm to the nucleus (Liu et al., 2017), we estimated the NF-κB signaling activation by calculating the intensity of NF-κB in the cytoplasm compared to nuclei. As a positive control of the activation of the NF-κB signaling pathway we stimulated MPBECs with IL-1β. We found that Yoda1 leads to a significant increase in the activation of the NF-κB signaling pathway compared to vehicle, but there was no effect of $G\alpha_{q/11}$ proteins (Figure 12).

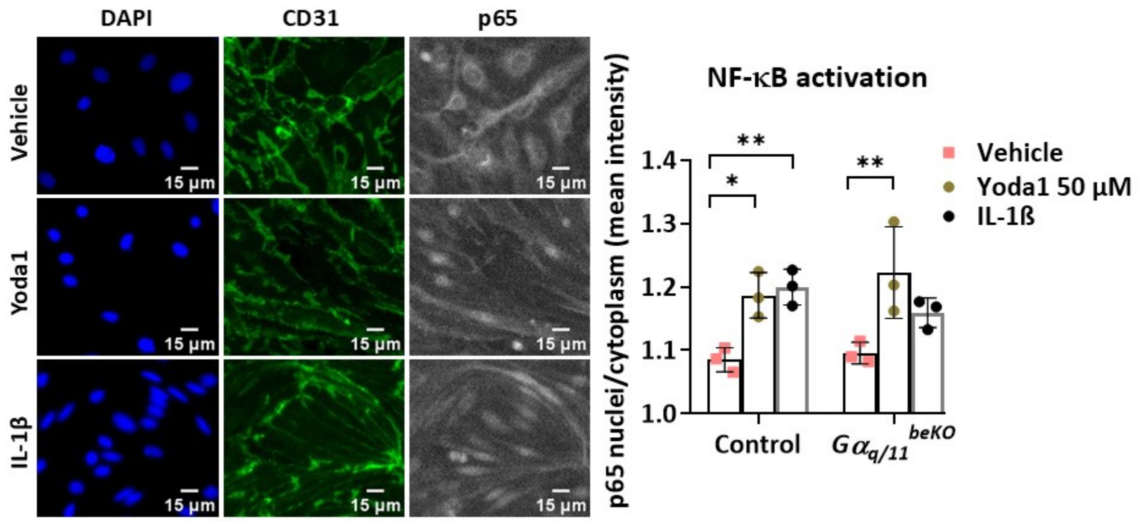

Figure 12: Yoda1 leads to activation of NF-κB signaling pathway independent of Gα$_{q/11}$. *Left: Representative immunofluorescence images of MPBECs isolated from control and Gα$_{q/11}^{beKO}$ mice showing immunoreactivity against the EC marker CD31 and the p65 component of the NF-κB complex. DAPI was used for nuclei visualization. Cells were treated with Yoda1, IL-1ß and respective controls for 1 h before fixation. Right: Quantification of the relative mean intensity of p65 immunoreactivity in nuclei and cytoplasm to estimate the translocation of p65 and activation of the NF-κB pathway. Yoda1 leads to a significantly higher ratio of p65 intensity in nuclei to cytoplasm than vehicle, but no genotype effect was detected. IL-1ß was used as a positive control of the activation of the canonical pathway of NF-κB. Data are shown mean ± SEM. Statistical analysis: two-way ANOVA with Sidak's posthoc test: genotype [F(1, 12) = 0.01309, p = 0.9108]; treatment [F(2, 12) = 15.25, p = 0.0005]; interaction [F(2, 12) = 1.579, p = 0.2462]. N = 3 independent experiments. * $p < 0.05$, ** $p < 0.01$. Abbreviations: Gα$_{q/11}$: G protein subunit alpha q/11, beKO: brain endothelial knockout, DAPI: diamidino-2-phenylindole, CD31: cluster of differentiation 31, NF-κB: Nuclear factor "kappa-light-chain-enhancer" of activated B-cells, IL-1ß: interleukin-1 beta.*

Afterward, we prompted the effect of Yoda1 on [Ca^{2+}]$_i$ responses of MPBECs as others have shown for ECs of the periphery (Wang et al., 2016). We isolated MPBECs from the mouse line *Cdh5*-GCaMP8, which expresses the fusion protein calcium sensor GCaMP8. We plated the MPBECs in 96-well plates and measured their [Ca^{2+}]$_i$ responses to different concentrations of Yoda1 on the microplate reader CLARIOstar® (Figure 13 A). In our experimental approach ATP or ADP-β-S were used as positive controls of [Ca^{2+}]$_i$ increase as they are known to activate the Gα$_{q/11}$ pathway through purinergic GPCRs (Lohman et al., 2012) (Figure 13). First, we could show that both concentrations of Yoda1 tested and the positive control lead to a significant increase in the [Ca^{2+}]$_i$ compared to the vehicle (Figure 13 B). In the next step, we explored further the effect of Yoda1 on [Ca^{2+}]$_i$ responses and we looked at whether the Gα$_{q/11}$ signaling pathway is activated after Piezo1 activation as has been proposed before for peripheral ECs (Wang et al., 2016). For this reason, we treated MPBECs with the Gα$_{q/11}$ inhibitor FR900359 (Schrage et al., 2015) as described in section 3.7.2 and then stimulated the cells with Yoda1 (Figure 13 C - D). These experiments showed no difference between the cells treated with the inhibitor FR900359 and the vehicle of FR900359 in the [Ca^{2+}]$_i$ responses after stimulation with Yoda1

(Figure 13 E) Cumulative, our results showed that MPBECs express a functional form of Piezo1, which upon activation leads to [Ca^{2+}]$_i$ increase independent of G$\alpha_{q/11}$ proteins.

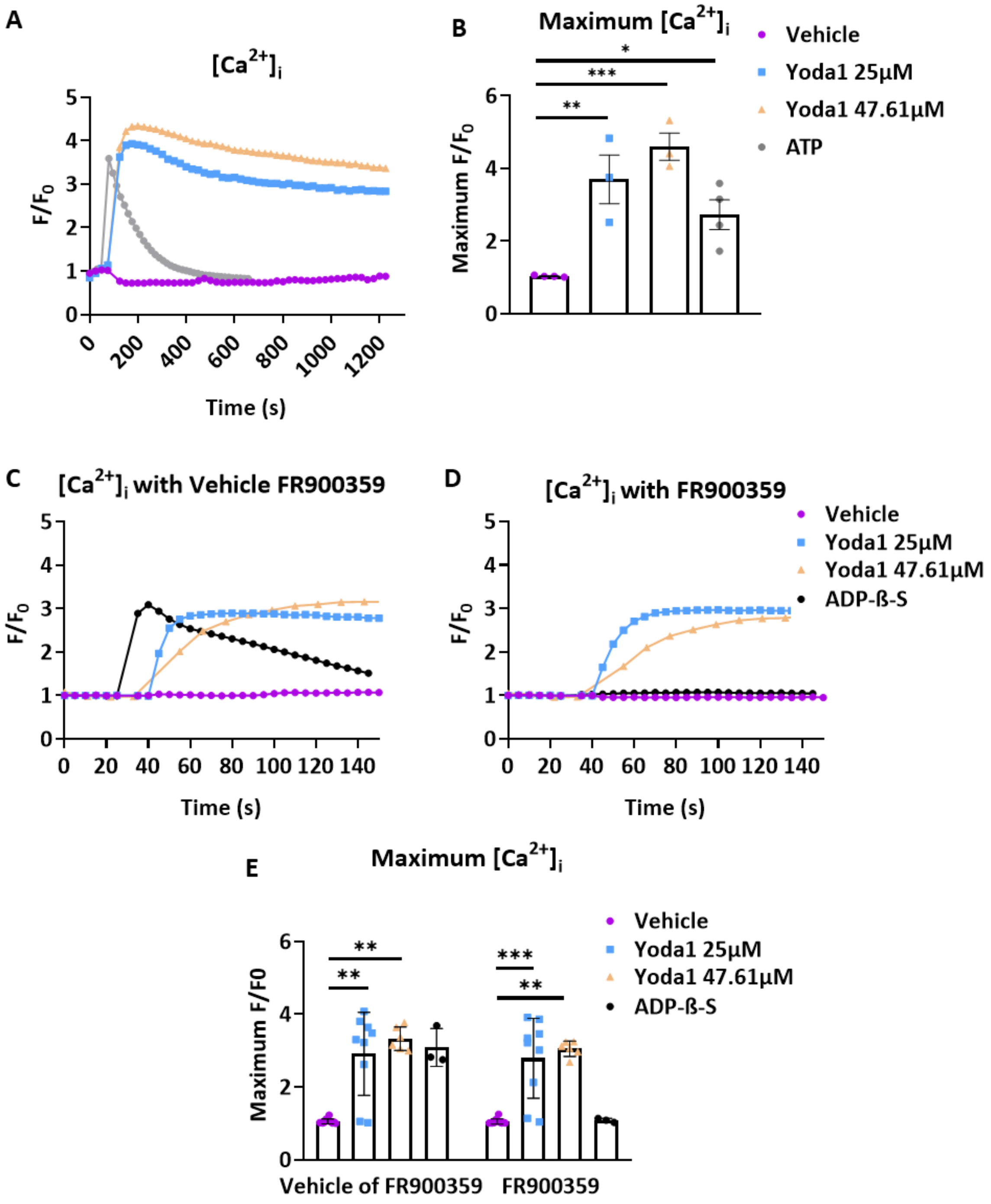

Figure 13:Yoda1 leads to [Ca^{2+}]$_i$ increase independent of the G$\alpha_{q/11}$ signaling pathway. A) *Representative curves of the relative fluorescence of [Ca^{2+}]$_i$ of MPBECs isolated from Cdh5-GCaMP8 mice stimulated with different Yoda1 (25 and 47.61 µM), vehicle of Yoda1 and ATP 100 µM. The fluorescence signal from whole wells of 96-well plates was measured in the microplate reader CLARIOstar®.* ***B)*** *Quantification of the maximum relative fluorescence response (F/F$_0$) showed a significant increase in the [Ca^{2+}]$_i$. ATP was used as a positive control to induce [Ca^{2+}]$_i$ increase. Data are shown as mean ± SEM. Statistical analysis ordinary one-way ANOVA with a Sidak's posthoc test; treatment [F(3, 10) = 14, p = 0.0005], N = 3-4 independent EC preparations.* ***C,D)*** *Representative curves*

of the relative fluorescence of [Ca^{2+}]$_i$ of MPBECs treated with the inhibitor FR900359 or its vehicle and stimulated with different concentrations of Yoda1 (25 and 47.61 µM), vehicle of Yoda1 and ADP-β-S (10 µM). ***E)*** *Quantification of the maximum relative fluorescence response (F/F$_0$) showed that the inhibitor FR900359 does not affect the Yoda1-induced [Ca^{2+}]$_i$ responses on MPBECs. ADP-β-S was used as a positive control of the [Ca^{2+}]$_i$ increase and inhibition of the Gα$_{q/11}$ signaling from FR900359. Data are shown as mean ± SD. Statistical analysis Kruskal-Wallis test followed by Dunn's posthoc test: vehicle FR900359 [$\chi^2(3) = 15.85$, $p = 0.0012$]; FR900359 [$\chi^2(3) = 19.41$, $p = 0.0002$]. n = 3-11 replicates from 1-5 independent EC preparations per group * $p < 0.05$, ** $p < 0.01$, *** $p < 0.001$. Abbreviations: EC: endothelial cell, [Ca^{2+}]$_i$: intracellular calcium, F: fluorescence intensity, ATP: adenosine triphosphate, ADP-β-S: Adenosine 5'-[β-thio]diphosphate.*

Whether MPBECs respond to shear stress and if Gα$_{q/11}$ proteins play a role in this response has not been investigated before. Therefore we established a protocol for cultivating MPBECs under flow using the Ibidi pump system and looked at the [Ca^{2+}]$_i$ responses of MPBECs isolated from *Cdh5*-GCaMP8 mice. Specifically, we looked at how cells cultivated under static conditions responded to stimulation with 1.7 dyn/cm^2 shear stress and if we could detect differences between the flow types, unidirectional and oscillatory flow at 1 Hz. The unidirectional flow type has been previously used to simulate the flow type in peripheral linear parts of bigger arteries. In contrast, the oscillatory flow type has been used to model *in vitro* the disturbed flow, which occurs in branching points of the vasculature and obstructed vessels due to atherosclerotic plaques (Albarrán-Juárez et al., 2018; Chatzizisis et al., 2007). Our results showed that both types of flow induce a prominent increase in the [Ca^{2+}]$_i$ responses and to a similar extent as shown by the quantification (Figure 14 A- E).

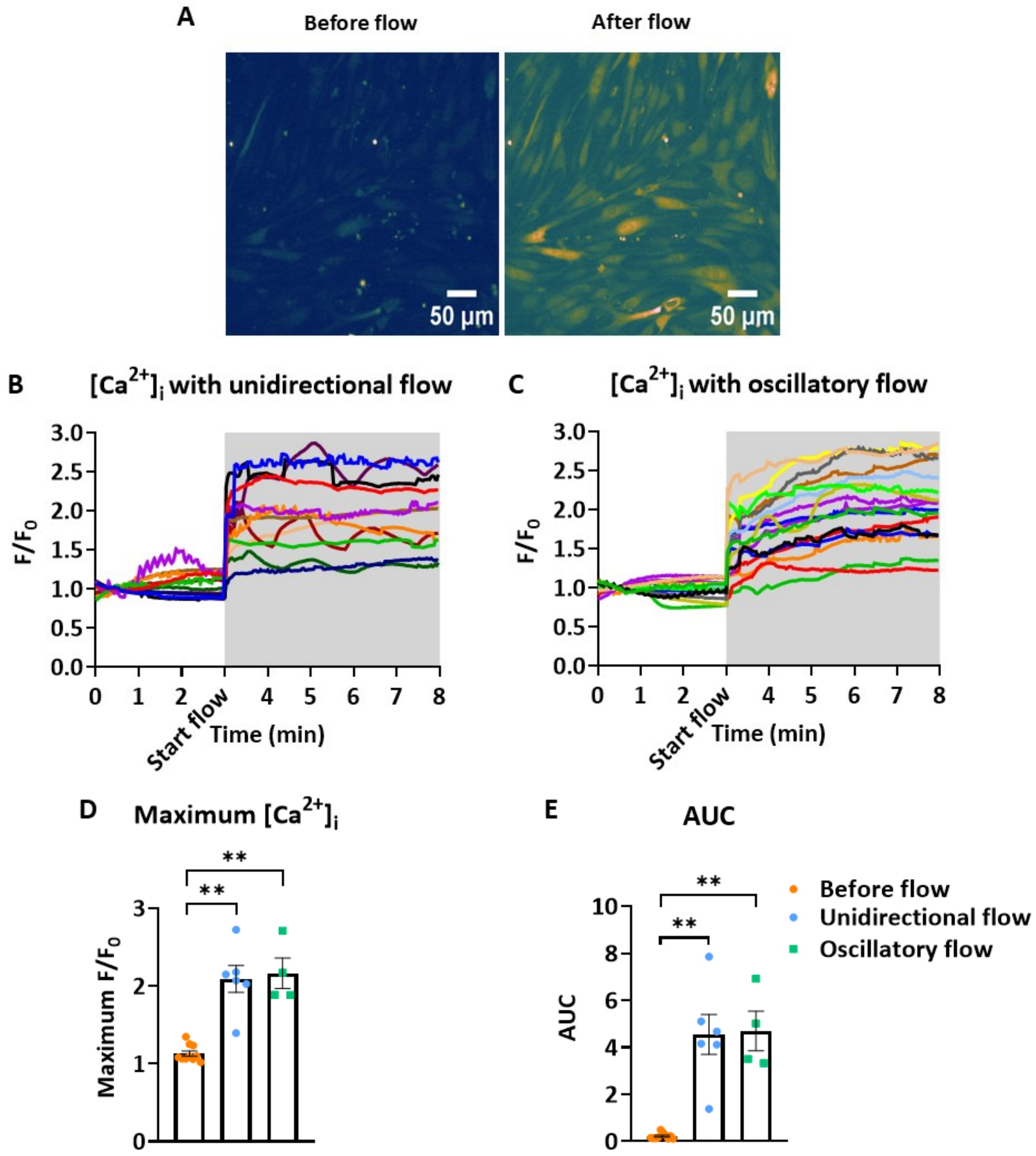

Figure 14: Shear stress leads to $[Ca^{2+}]_i$ increase in MPBECs independent of the flow type. A) *Representative images of MPBECs isolated from the Cdh5-GCaMP8 mice showing the increase in the fluorescence of $[Ca^{2+}]_i$ signal before and after applying shear stress 1.7 dyn/cm^2.* ***B, C)*** *Curves of the relative fluorescence of $[Ca^{2+}]_i$ signal of MPBECs expressing the calcium indicator GCaMP8 under unidirectional and oscillatory (1 Hz) types of flow at 1.7 dyn/cm^2. The curves were calculated from the whole field of view of time-lapse videos recorded with a 10x objective. Grey-shaded area indicates the application of shear stress* ***D, E)*** *Quantification of the maximum relative fluorescence response (F/F_0) and the AUC showed a significant increase of $[Ca^{2+}]_i$ signal after the application of shear stress in MPBECs. No differences between the unidirectional and oscillatory types of flow were observed. Data are shown as mean ± SEM. Statistical analysis Kruskal-Wallis test followed by Dunn's posthoc test: $\chi^2(2) = 14.31$, $p < 0.0001$. N = 4-6 independent EC preparations per group. Abbreviations: $[Ca^{2+}]_i$: intracellular calcium, F: fluorescence intensity, AUC: area under the curve.*

Furthermore, pretreatment of the cells with the $G\alpha_{q/11}$ inhibitor FR900359 showed that cells responded similarly to both flow types, indicating that the flow-dependent $[Ca^{2+}]_i$ responses are not $G\alpha_{q/11}$ dependent (Figure 15 A- F). Furthermore, with the ibidi pump system, we looked at the responses of MPBECs after stimulation with the pulsatile type of flow, which is used to simulate the blood flow fluctuations due to heartbeat. Our preliminary results show that pulsatile flow at 1.7 dyn/cm^2 and 1 Hz frequency leads to prominent $[Ca^{2+}]_i$ responses which are not $G\alpha_{q/11}$-mediated (Supplementary Figure 5).

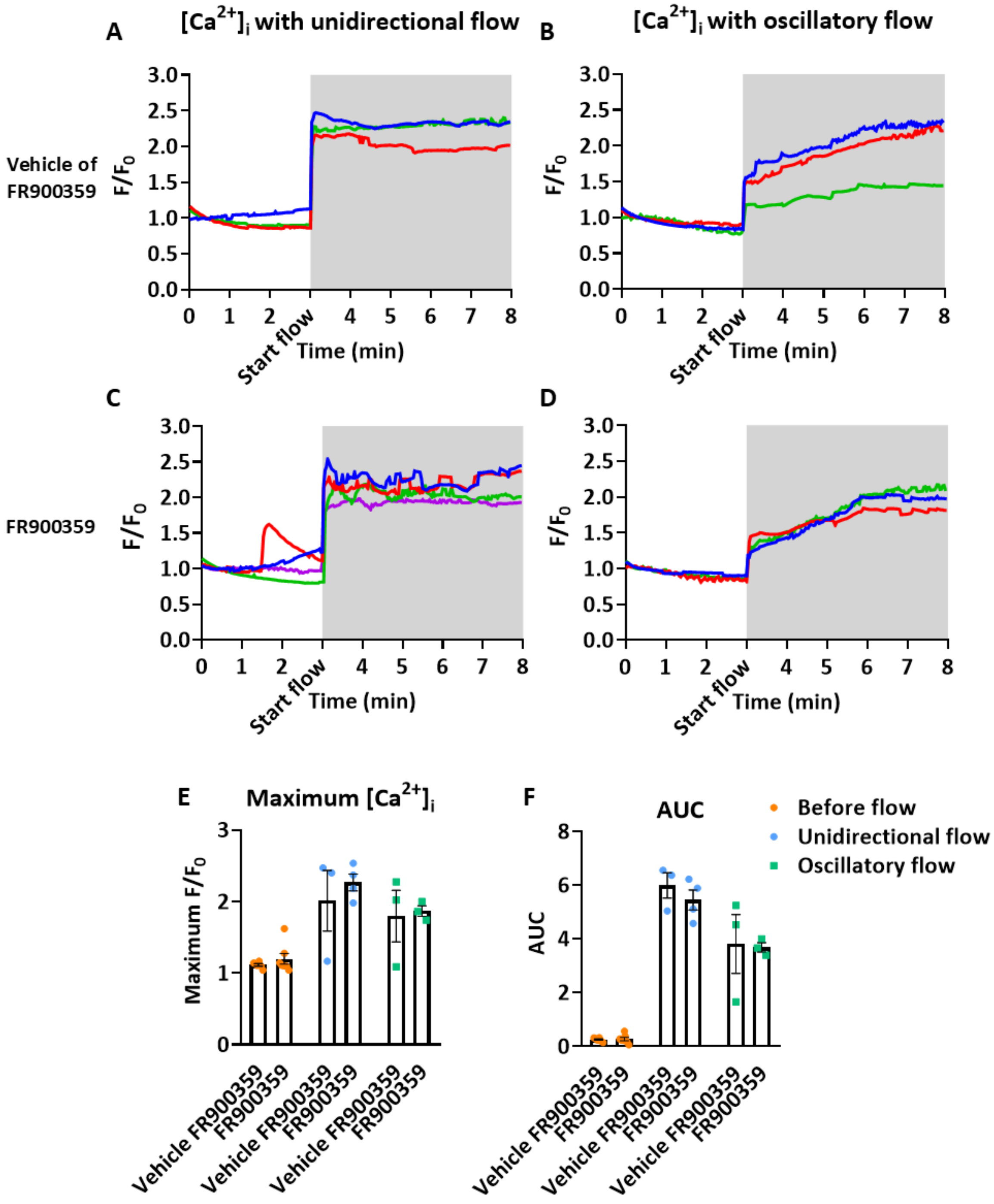

*Figure 15: **G$\alpha_{q/11}$ signaling pathway is not involved in the shear stress [Ca^{2+}]$_i$ increase induced by different types of flows. A-D)** Curves of the relative fluorescence of [Ca^{2+}]$_i$ signal of MPBECs isolated from Cdh5-GCaMP8 mice, treated with the inhibitor of the G$\alpha_{q/11}$ proteins (FR900359) and unidirectional or oscillatory (1 Hz) types of flow at 1.7 dyn/cm^2. The curves were calculated from the whole field of view of time-lapse videos recorded with a 10x objective. **E, F)** Quantification of the maximum relative fluorescence response (F/F$_0$) and AUC showed that the inhibitor FR900359 does not affect the shear stress-induced [Ca^{2+}]$_i$ responses on MPBECs. Data are shown as mean ± SD from 3-7 measurements from N = 1-2 independent experiments per group. Abbreviations: [Ca^{2+}]$_i$: intracellular calcium, F: fluorescence intensity, AUC: area under the curve.*

Interestingly, we also observed that the effect of shear stress on $[Ca^{2+}]_i$ responses of MPBECs that were not habituated to flow is reversible. Specifically, there was a gradient decline in the $[Ca^{2+}]_i$ fluorescence after the flow was stopped (Supplementary Figure 6 A- B). In a similar manner, we examined whether cells habituated and cultured under shear stress for 96 h, show $[Ca^{2+}]_i$ changes when the flow is disrupted. Interestingly, when we stopped the flow for a short term, we observed a gradient decline in the $[Ca^{2+}]_i$ fluorescence signal, which was reversed when the shear stress was restored (Supplementary Figure 6 C- D).

We also prompted the effect of shear stress on the human brain endothelial hCMEC/D3 cell line to confirm the reproducibility of the setup and to test if other cells can respond to shear stress in a similar or different way compared to MPBECs. Therefore, we stained hCMEC/D3 cells with the calcium indicator Fluo-4 and measured the $[Ca^{2+}]_i$ responses to shear stress under unidirectional, oscillatory, and pulsatile types of flow. Our observations indicate that hCMEC/D3 cells, similarly to the MPBECs, respond to acute stimulation with shear stress by $[Ca^{2+}]_i$ increase (Supplementary Figure 7).

Finally, based on the results of the effect of Yoda1 on the activation of the NF-κB signaling pathway we prompted the effect of different types of flow on the activation of the afore-mentioned pathway. Therefore, we treated MPBECs with unidirectional, oscillatory, and pulsatile types of flow and subjected them to shear stress of 1.7 dyn/cm^2 for 30 min. After quantifying the intensity of p65 on the nucleus and cytoplasm as described in section 3.10.2, our preliminary results showed no difference between the different types of flow and the control static conditions (Supplementary Figure 8).

4.5 Shear stress effect on morphology and proteomic profile of MPBECs *in vitro*

It has been shown that peripheral ECs develop a pro-inflammatory phenotype when they fail to align to the flow direction, while alignment is linked to an atheroprotective phenotype (Baeyens et al., 2014). However, many studies based on human BBB models have shown that brain ECs do not align with the flow direction (Choublier et al., 2022; DeStefano et al., 2017; Reinitz et al., 2015) in contrast to peripheral ECs. Whether mouse MPBECs can adapt to the direction of the flow after long-term cultivation has not been investigated before. Based on phase-contrast images that were taken during a 96 h time course of flow-treated cells and an ImageJ custom script adapted from (Reinitz et al. 2015), we calculated the orientation of MPBECs upon flow (Figure 16 A- B). We found that MPBECs under unidirectional flow show a significantly higher orientation to the flow direction than MPBECs under oscillatory flow type and static control (Figure 16 D- F). We also calculated the inverse aspect ratio (IAR) of the cells treated with different types of flow and in static control conditions.

Interestingly, we found that in both flow conditions, there is a significant decrease in the IAR compared to static conditions (Figure 16 C). All in all, these data provide strong evidence that unidirectional flow leads to a significantly higher cell alignment to flow direction than static and oscillatory flow and that both types of flow induce significant changes to the cell shape, leading to an elongated spindle-like morphology.

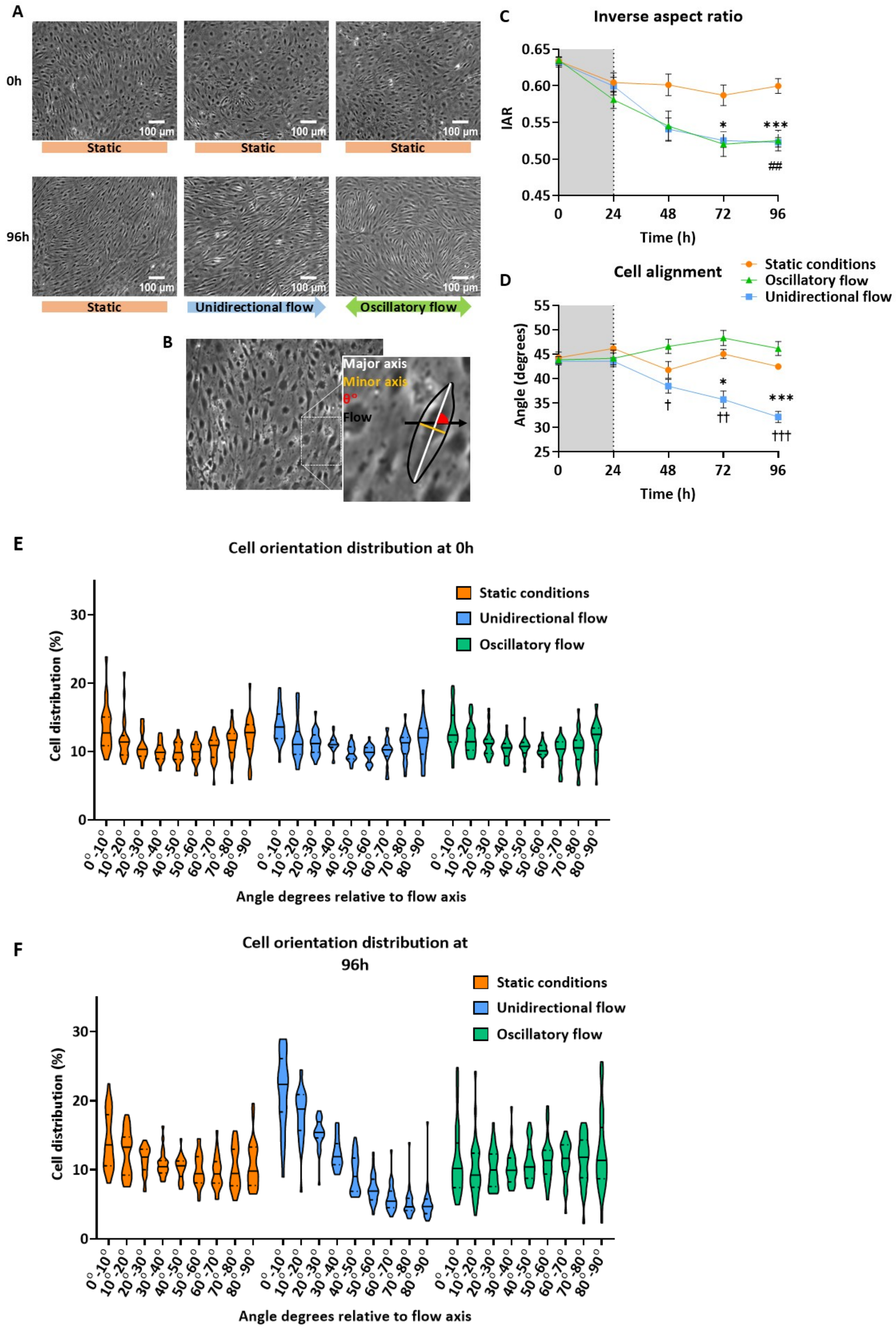

Figure 16: Shear stress leads to phenotypic changes in MPBECs. A) *Representative bright field pictures showing the cell appearance before and after applying shear stress of 1.7 dyn/cm^2 for 96 h.* ***B)*** *Schematic presentation of the parameters measured during image analysis and used for the*

calculation of the cell orientation (ϑ °, 0 °- 90 °) and the IAR. The major axis (white lane) and minor axis (yellow line) were measured based on the designated cell borders, the cell angle was calculated from the angle between the major axis and the flow direction (black arrow, x-axis) and IAR was measured by dividing the length of the minor axis by the length of the major axis. ***C)*** *Comparison of the IAR over time under different types of flow and during static culture showed that flow induces a significant change in cell morphology to a spindle-like shape. Data are shown as mean ± SEM. Statistical analysis mixed effects analysis for repeated measurements with Geisser-Greenhouse correction (ε = 0.5292): type of flow [F(2, 18) = 5.444, p = 0.0142]; time [F(2.117, 21.70) = 98.49, p < 0.0001]; time x type of flow [F(8, 41) = 9.925, p < 0.0001]. N = 4-8 independent experiments. The grey shade indicates the habituation period to flow before the final shear stress of 1.7 dyn/cm^2.* ***D)*** *Comparison of the cell alignment to the flow axis between the different types of flow and static control. Only under the unidirectional flow type did MPBECs show significant alignment over time, as indicated by the reduction in angle. No differences were detected between oscillatory flow and static conditions over time. Data are shown as mean ± SEM. Statistical analysis mixed effects analysis for repeated measurements with Geisser-Greenhouse correction (ε = 0.8061): type of flow [F(2, 59) = 43.94, p < 0.0001]; time [F(3.224, 47.56) = 6.533, p = 0.0007]; time x type of flow [F(8, 59) = 8.396, p < 0.0001]. N = 4-8 independent experiments. The grey shade indicates the habituation period to flow before the final shear stress of 1.7 dyn/cm^2.* ***E, F)*** *Violin plots depicting the distribution of cell orientation angle in the range of 0 ° to 90 ° at time points 0 h and 96 h. Before flow application, the distribution of cell orientation angles is even, showing no differences at the baseline level. At the 96 h time point, the distribution of cell orientation angles in the unidirectional type of flow shifts to lower values, while in static and oscillatory flow, the cell population is evenly distributed to all angles.* * indicates a significant difference between unidirectional flow and static control. # indicates a significant difference between oscillatory flow and static control. † indicates the difference between the unidirectional and oscillatory types of flow. * p < 0.05, *** p < 0.001, ## p < 0.01, † p < 0.05, †† p < 0.01, ††† p < 0.001. Abbreviations: IAR: inverse aspect ratio.*

The phenotypic changes and $[Ca^{2+}]_i$ responses observed in MPBECs under flow prompted us to look for protein expression changes related to flow. We first looked for the protein profile expression of whole cells after long-term cultivation under shear stress 1.7 dyn/cm^2. The cell culture preparation was performed as described in section 3.3.1 in our lab in Lübeck, and the samples were sent for analysis to our collaborators Prof. Bernd Wollscheid and Jacqueline Hammer at the ETH, Zürich for protein identification, mass spectrometry analysis, and partial data visualization (Hammer, 2024). With our approach, we could identify around 5700 proteins and reveal stark differences in protein expression between flow and static control conditions, as visualized by the significant number of upregulated and downregulated proteins in the volcano plots (Figure 17 A- B). More specifically, in the comparison of oscillatory flow vs static conditions, from the total number of 5711 identified proteins, 533 were significantly regulated (280 up-regulated and 253 down-regulated). In the comparison of unidirectional flow vs static conditions, from the total number of 5708 identified proteins, 699 proteins were significantly regulated (370 up-regulated and 329 down-regulated). However, no stark differences were found between the two flow conditions, as shown by the volcano plot (Figure 17 C). In the comparison of oscillatory flow vs unidirectional flow, from the total number of 5718 identified proteins only three proteins were found to be significantly regulated: angiopoietin-2 (ANGPT2), heme oxygenase 1 (HMOX1) and ABI gene family member 3 (ABI3)(Figure 17 C).

Furthermore, the heatmap of all measured samples with unsupervised clustering (Figure 17 D) showed that the samples of flow conditions did not cluster apart pointing further that the effect of the different types of flow on the whole cell protein expression profile is similar and more prominent against static conditions. Therefore, we looked then on the commonly up- and down-regulated proteins that we found on the comparisons of both oscillatory flow and unidirectional flow vs static conditions (Figure 17 E and Supplementary Figure 9 A). Using the commonly regulated protein dataset, we performed pathway enrichment analysis utilizing the MsigDB and the built-in mouse hallmark and gene ontology (GO) gene sets to identify the top 10 pathways that are up- or down-regulated due to shear stress (Figure 17 F- G, Supplementary Figure 9 B- C) (Castanza et al., 2023; Liberzon et al., 2011; Subramanian et al., 2005).

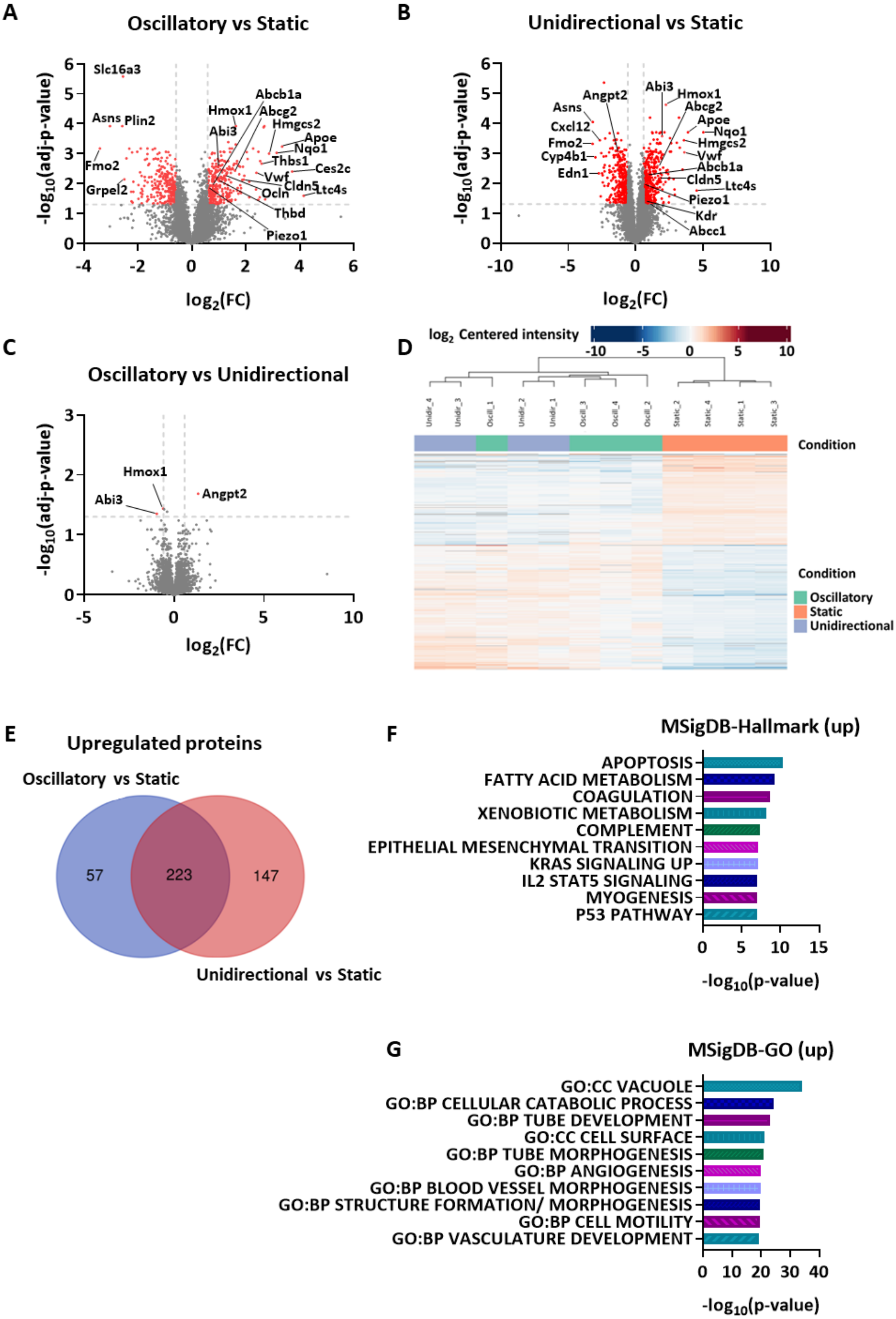

Figure 17: Proteotyping of the whole proteome of MPBECs under flow. A-C) *Volcano plots of the whole cell proteotyping representing the significantly upregulated (red dots, right side) and downregulated (red dots, left side) hits in the comparisons of oscillatory flow against static control (A), unidirectional*

flow against static control (B), and oscillatory flow against unidirectional flow (C). The top 5 upregulated and downregulated proteins as well as selective candidates of biological interest are indicated by their corresponding gene symbols. The grey dotted lines on the x and y axes indicate the significant thresholds |fold-change| > $\log_2(1.5)$ and adjusted p-value < 0.05 corrected for multiple testing respectively. ***D)*** *Heatmap of all measured samples with unsupervised clustering. Graph produced and adapted from Hammer, Jacqueline "Spatially Resolved Surfaceome Analysis using Light-activated Lipid-anchored Probes", DISS. ETH NO. 30247.* ***E)*** *Venn diagram depicting the number of shared upregulated proteins of the comparisons of oscillatory and unidirectional flow against static control from the whole cell lysate proteotyping.* ***F)*** *Graphical depiction of the top ten enriched biological processes based on the annotation of the shared upregulated proteins in flow conditions against static control using the MSigDB and the built-in mouse hallmark gene set.* ***G)*** *Graphical depiction of the top ten enriched GO terms based on the annotation of the shared upregulated proteins in flow conditions against static control using the MSigDB and the built-in mouse ontology gene set. Abbreviations: adj: adjusted, Slc16a3: solute carrier family 16 member 3, Asns: asparagine synthetase, Plin2: perilipin-2, Fmo2: flavin-containing monooxygenase 2, Grpel2: gro-P like protein E protein homolog 2, Abi3: ABI gene family member 3, Hmox1: heme oxygenase 1, Abc (eg Abc1ba): ATP-binding cassette, Hmgcs2: hydroxymethylglutaryl-CoA synthase 2, Apoe: apolipoprotein E, Nqo1: NAD(P)H dehydrogenase [quinone] 1, Thbs1: thrombospondin-1, Ces2c: carboxylesterase 2C, Vwf: von Willebrand factor, Cldn5: claudin-5, Ltc4s: leukotriene C4 synthase, Ocln: occludin, Angpt2: angiopoietin-2, Cxcl12: C-X-C motif chemokine ligand 12, Cyp4b1: cytochrome P450 4B1, Edn1: endothelin-1, Kdr: kinase insert domain receptor (Vegfr2), MsigDB: molecular signature database, GO: gene ontology, CC: cellular component, BP: biological process, FC: fold change. KRAS: kirsten rat sarcoma virus, IL-2: interleukin-2, STAT5: signal transducer and activator of transcription 5.*

The surprising result that almost no differences could be detected between the two flow types and the fact that endothelial mechanosensory complexes show primarily spatial organization on the cell membrane, (Aitken et al., 2023) led us to prompt the cell surface proteotyping on MPBECs. We used a previously described CSC protocol to identify cell surface-expressed proteins (van Oostrum et al., 2019). Sample preparation and CSC were performed in Lübeck as described in section 3.3.2, while the protein identification, mass spectrometry analysis, and part of data visualization were performed at the ETH Zürich (Hammer, 2024). Our approach resulted in a unique cell surface protein dataset of around 500 proteins from MPBECs, which not only revealed differences between the oscillatory and unidirectional flow vs static conditions but also between the two flow types (Figure 18 A- C). More specifically, in the comparison of oscillatory flow vs static conditions, from the total number of 502 identified proteins, 167 were significantly regulated (68 up-regulated and 99 down-regulated). In the comparison of unidirectional flow vs static conditions, from the total number of 499 identified proteins, 189 proteins were significantly regulated (85 up-regulated and 104 down-regulated). In the comparison of oscillatory flow vs unidirectional flow, from the total number of 500 identified proteins, 22 proteins were significantly regulated (8 up-regulated and 14 down-regulated). Furthermore, the heatmap of all measured samples with unsupervised clustering, in contrast to the whole cell proteomics, revealed the separate clustering of the flow types compared to static control conditions pointing to the differential effect of flow types on the cell surface protein expression profile (Figure 18 D). Finally, we performed pathway enrichment analysis on the commonly regulated proteins (Figure 18 E and Supplementary Figure 10 A) from the comparisons of oscillatory flow vs static control and unidirectional flow vs static conditions. Similarly to the whole cell proteomics, the MsigDB and the built-in mouse hallmark and GO gene sets (Castanza et al., 2023; Liberzon et al., 2011; Subramanian et al., 2005) enabled us to identify the top 10 pathways that are up- and down-regulated due to shear stress (Figure 18 F- G, Supplementary Figure 10 B- C).

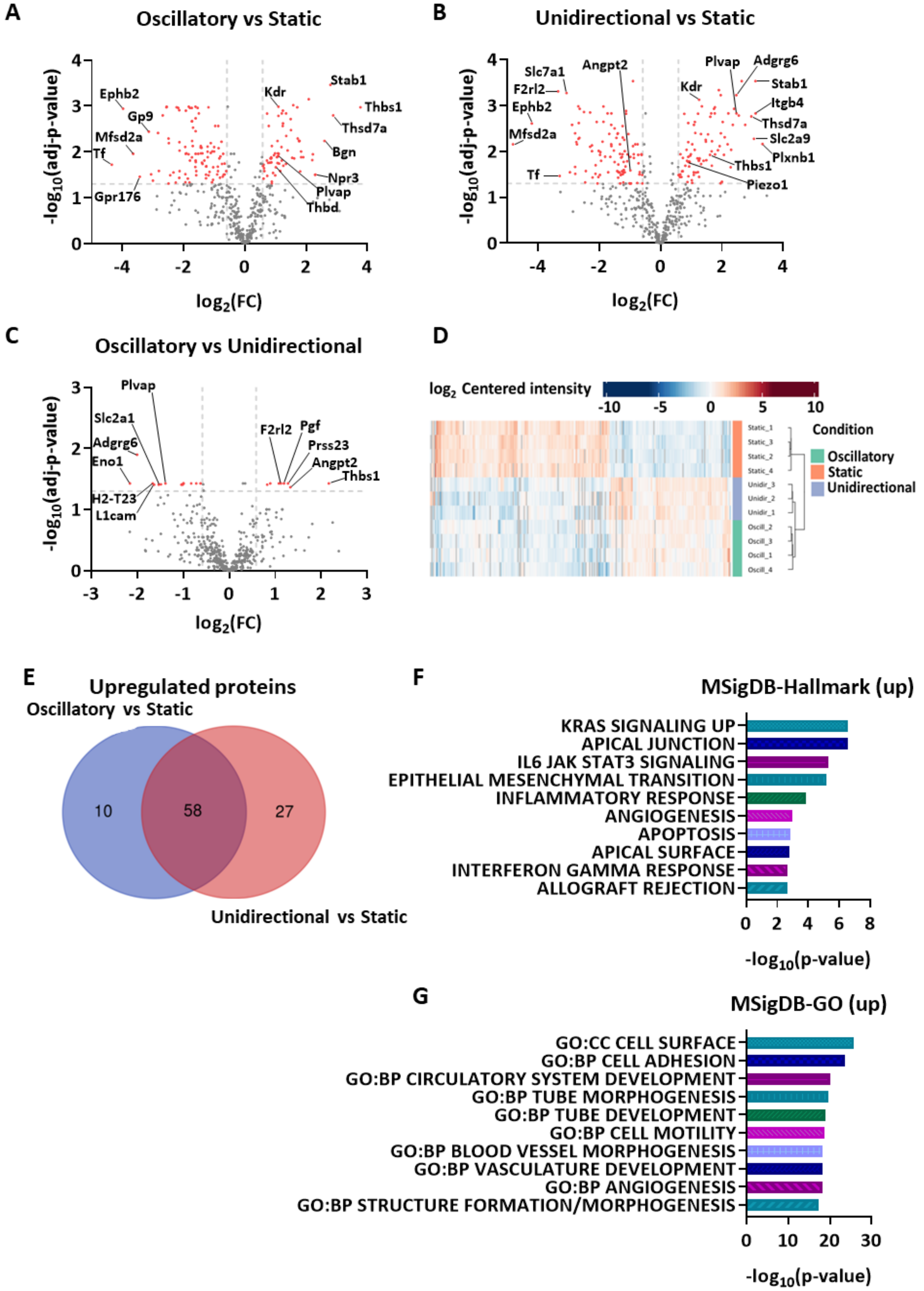

Figure 18: Proteotyping of the cell surface of MPBECs under flow. A-C) *Volcano plots of the cell surface proteotyping representing the significantly upregulated (red dots, right side) and downregulated (red dots, left side) hits in the comparisons of oscillatory flow against static control (A), unidirectional flow against static control (B), and oscillatory flow against the unidirectional flow (C). The top 5*

upregulated and downregulated proteins as well as selective candidates of biological interest are indicated by their corresponding gene symbols. The grey dotted lines on the x and y axes indicate the significant thresholds |fold-change| > $\log_2(1.5)$ and adjusted p-value < 0.05 corrected for multiple testing respectively. ***D)*** *Heatmap of all measured samples with unsupervised clustering. Graph produced and adapted from Hammer, Jacqueline "Spatially Resolved Surfaceome Analysis using Light-activated Lipid-anchored Probes", DISS. ETH NO. 30247.* ***E)*** *Venn diagram depicting the number of shared upregulated proteins of the comparisons of oscillatory and unidirectional flow against static control from the cell surface proteotyping.* ***F)*** *Graphical depiction of the top ten enriched biological processes based on the annotation of the shared upregulated proteins in flow conditions against static control using the MSigDB and the built-in mouse hallmark gene set.* ***G)*** *Graphical depiction of the top ten enriched GO terms based on the annotation of the shared upregulated proteins in flow conditions against static control using the MSigDB and the built-in mouse ontology gene set. Abbreviations: adj: adjusted, Ephb2: ephrin type-B receptor 2, Gp9: platelet glycoprotein IX, Mfsd2a: major facilitator superfamily domain-containing protein 2a, Tf: transferrin, Gpr176: G protein-coupled receptor 176, Kdr: kinase insert domain receptor (Vegfr2), Stab1: stabilin-1, Thbs1: thrombospondin-1, Thsd7a: thrombospondin type-1 domain-containing protein 7A, Bgn: biglycan, Npr3: atrial natriuretic peptide receptor 3, Plvap: plasmalemma vesicle associated protein, Thbd: thrombomodulin, Slc (eg Slc7a1): solute carrier, Angpt2: angiopoietin-2, F2rl2: coagulation factor II (thrombin) receptor-like 2, Adgrg6: adhesion G protein-coupled receptor g6, Itgb4: integrin beta-4, Plxnb1: plexin-b1, Eno1: enolase 1, H2-T23: histocompatibility 2, T region locus 23, L1cam: neural cell adhesion molecule L1, Pgf: placenta growth factor, Prss23: serine protease 23, MsigDB: molecular signature database, GO: gene ontology, CC: cellular component, BP: biological process, FC: fold change. KRAS: kirsten rat sarcoma virus, IL-6: interleukin-6, JAK: janus kinase, STAT3: signal transducer and activator of transcription 3.*

4.6 THBD and $G\alpha_{q/11}$ affect angiogenesis *in vitro*

One attractive candidate revealed from the whole cell and the cell surface proteotyping was THBD which was upregulated in the oscillatory shear stress condition. In addition, recent findings from our group showed that THBD has protective effects in a murine stroke model by affecting *in vivo* angiogenesis (Wenzel et al., 2020b). Therefore, we prompted how THBD affects the angiogenic properties in MPBECs in static conditions *in vitro*. We looked at THBD effects on EC migration by performing the scratch assay in confluent monolayers of MPBECs isolated from *Thbd*^{beKO} and control mice. The scratch assay was performed in normal and hypoxic conditions since the latter is a significant contributor to angiogenesis and a characteristic of ischemia due to blood flow cessation. We found that MPBECs from *Thbd*^{beKO} mice showed a significantly lower % of wound closure at 3 h compared to 6 h after the scratch and a significant genotype effect (Figure 19 A- B). However, the genotype effect was lost under hypoxic conditions, and posthoc analysis did not show differences between groups at 3 h or 6 h after the scratch (Figure 19 C- D).

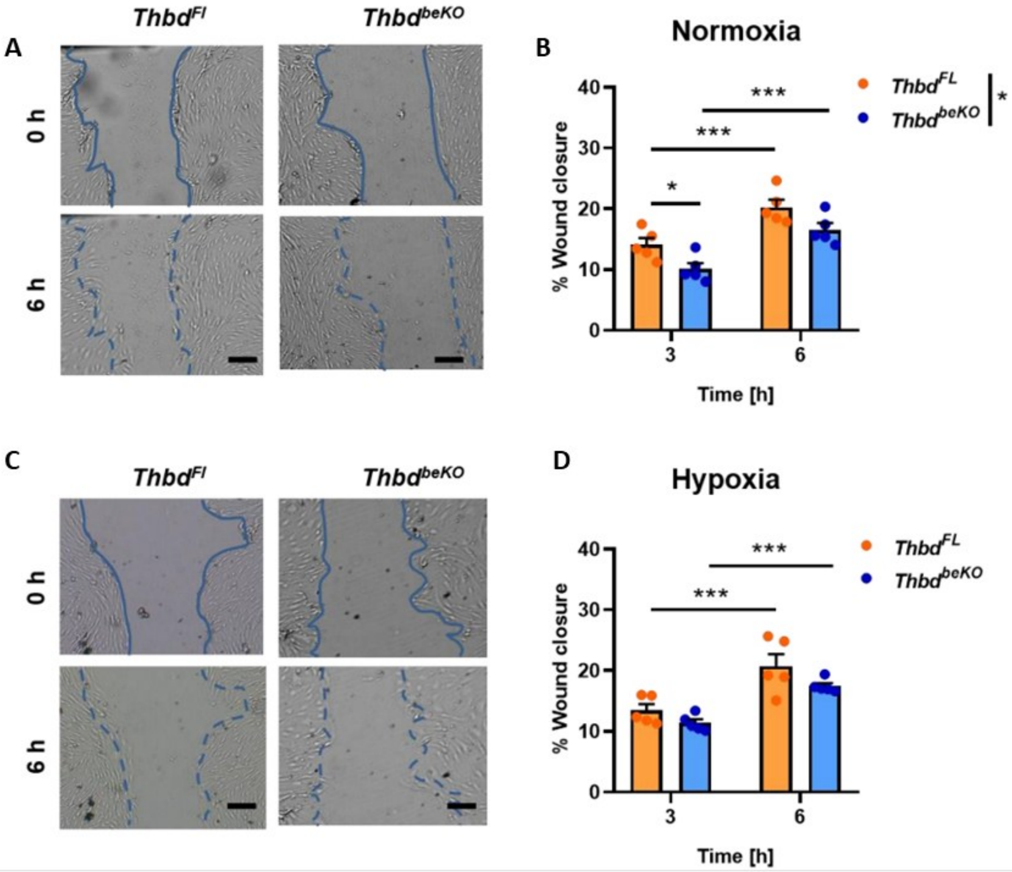

Figure 19: THBD affects the in vitro migration of MPBECs. ***A, B)*** *Exemplary images and quantification of a scratch assay performed on confluent MPBECs prepared from control (Thbd^{FL}) and Thbd^{beKO} mice under normoxic conditions. Data are shown as mean ± SEM. Statistical analysis: two-way ANOVA with Bonferroni´s posthoc test: genotype [F(1, 8) = 6.716, p = 0.032]; time [F(1, 8) = 189.2, p < 0.0001]; interaction [F(1, 8) = 0.06251, p = 0.8089], N = 5 independent preparations. Blue dotted lines in the lower part of the exemplary images show the scratch border at time point 0.* ***C, D)*** *Exemplary images and quantification of a scratch assay performed on confluent MPBECs prepared from control and Thbd^{beKO} mice under 1% hypoxic conditions. Statistical analysis two-way ANOVA with Bonferroni´s posthoc test: genotype [F(1, 8) = 2.962, p = 0.1235]; time [F(1, 8) = 130.9, p < 0.0001]; interaction [F(1, 8) = 1.046, p = 0.3363]. N = 5 independent preparations. Blue dotted lines in the lower part of the exemplary images show the scratch border at time point 0 h. * p < 0.05, ** p < 0.01, *** p < 0.001. Abbreviations: Thbd: thrombomodulin, beKO: brain endothelial knockout, FL: floxed. The figure has been published (Wenzel et al., 2020b).*

Finally, based on the pathway analysis (increased angiogenesis-related pathways) as well as on a previous report that G$\alpha_{q/11}$ proteins mediate the VEGFR2 signaling in endothelial cells (Sivaraj et al., 2015), we examined the proliferation of MPBECs from $G\alpha_{q/11}^{beKO}$ and control mice *in vitro*. By calculating the percent of proliferating cells (visualized by the incorporation of EdU), our findings showed a significant genotype effect. Although, there was no difference between $G\alpha_{q/11}^{beKO}$ and control cells under starvation and the 10 % serum (positive control treatment), only control cells showed a significant increase of proliferating cells in the 10 % serum (Figure 20). This suggests that the G$\alpha_{q/11}$ signaling pathway plays a role in the proliferation of MPBECs *in vitro*.

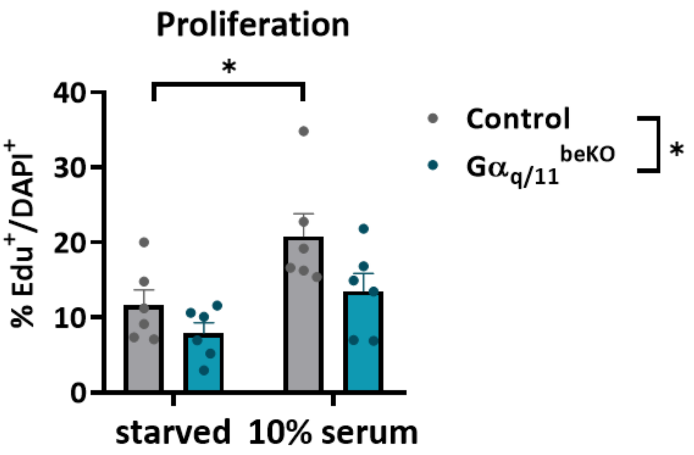

Figure 20: ***G$\alpha_{q/11}$*** ***affects the in vitro proliferation of MPBECs.*** *Low confluent cell cultures of MPBECs isolated from G$\alpha_{q/11}$^{beKO} and control mice were treated with starvation or 10 % serum-supplemented medium as a positive control for 24 h. A significant genotype difference was detected. MPBECs from control mice showed a significant increase during the 10 % serum treatment, but no difference in the number of proliferating MPBECs from G$\alpha_{q/11}$^{beKO} between the treatments was detected. Two-way ANOVA followed by Bonferroni's posthoc test: genotype [F(1, 20) = 5.891, p = 0.0248]; treatment [F(1, 20) = 10.59, p = 0.040]; interaction [F(1, 20) = 0.6420, p = 0.4324]. N = 6 independent experiments starved or treated with 10 % PDS to investigate their proliferation rate. Abbreviations: G$\alpha_{q/11}$: G protein subunit alpha q/11, beKO: brain endothelial knockout, Edu: ethynyl-2'-deoxyuridine, DAPI: diamidino-2-phenylindole.*

5 Discussion

5.1 Absence of brain endothelial G$\alpha_{q/11}$ pathway leads to string vessel formation and memory deficits in aged mice

Aged individuals currently account for a significant proportion of the population worldwide and this is expected to increase more in the next years (UN, World Population Prospects 2022). Elderly people have a higher risk for age-related diseases (stroke, neurodegenerative diseases), but even in the absence of other pathologies normal aging is characterized by a decline in cognitive function (Benjamin et al., 2018; Cortes-Canteli & Iadecola, 2020;). Age-dependent cognitive decline can severely affect the quality of life of aged people and could pose challenges for the healthcare and socioeconomic systems of the countries in the future. However, currently, there are no effective therapeutic options for age-dependent cognitive decline making it necessary to unravel new pharmacological targets that will pave the way for more effective therapies. In the forefront, as a promising field of research, stands brain vasculature, since strong evidence supports the association between vascular aging (systemic and cerebrovascular changes) and age-dependent cognitive decline (Cortes-Canteli & Iadecola, 2020; Sharma et al., 2010; Toth et al., 2017).

The current study, a continuation of our previous research, focused on brain endothelial G$\alpha_{q/11}$ signaling and its potential role in cognitive function during aging. Our earlier studies have shown that when *Gnaq* and *Gna11* alleles are deleted with high specificity from the brain endothelium, brain vessels do not respond with an increase in the cerebral blood flow after a CO_2 challenge (Wenzel et al., 2020a). This impaired cerebrovascular reactivity was associated with increased anxiety, longer apneic episodes, and reduced respiration in mice even without a CO_2 challenge. Furthermore, currently it is not clear whether aging affects cerebrovascular reactivity although some groups have reported that aged individuals show decline in cerebrovascular reactivity (McKetton et al., 2018; Miller et al., 2019; Peng et al., 2018). Therefore, our current study aimed to understand whether the effects of the brain endothelial deletion of *Gnaq* and *Gna11* alleles identified in young mice affect cognitive function during aging and potentially pave the way for new therapeutic strategies to combat age-dependent cognitive decline.

We formed the hypothesis that the G$\alpha_{q/11}$ pathway is involved in cognitive function during aging and we sought to investigate it by using $G\alpha_{q/11}^{beKO}$ and control mice. The mice were subjected to a longitudinal study with behavioral tests, which assess hippocampus-dependent memory formation. Spatial memory, part of declarative memory, is dependent on the normal function of the hippocampus and has been shown to decline with age in older humans and rodents (Barnes et al., 1980; Burke & Barnes, 2006; Newman & Kaszniak, 2000; Uttl & Graf, 1993) . Wenzel and colleagues had previously shown that the $G\alpha_{q/11}^{beKO}$ mice at approximately 4-8 months old did not show deficits in recognition memory on the novel object recognition test or in associative memory and learning on the conditioned taste aversion test (Wenzel et al., 2020a). In this study, we used the OPR test, which assesses the hippocampus-dependent spatial memory (Assini et al., 2009; Binder et al., 2012), and we could also confirm no differences in memory function between the $G\alpha_{q/11}^{beKO}$ and control groups on all time points investigated from 3- 18 months old (Figure 4 A). Despite that, we found that the $G\alpha_{q/11}^{beKO}$ group failed to discriminate between the displaced and the non-displaced objects at the time points of 3 and 18 months old and traveled significantly less at the time points 3, 6 and 12 months old (Figure 4 A and C). Lower locomotion and/or explorative behavior could be associated with the $G\alpha_{q/11}^{beKO}$ group´s failure to discriminate the location of the objects. For example, the genetic manipulation could have an effect on the motor sensory systems of the mice and therefore the aforementioned parameters are routinely investigated during the OPR test (Assini et al., 2009; Dere et al., 2007; Murai et al., 2007). However, analysis of the total exploration time in this study (Figure 4 B), along with previously published results on the explorative behavior and motor deficits in $G\alpha_{q/11}^{beKO}$ mice (Wenzel et al., 2020a), suggest no differences in the explorative behavior and that the locomotion differences observed in this study are not likely due to compromised ability to travel in the OPR apparatus. Even though the OPR test induces less anxiety in mice compared to other behavioral tasks (Sharma et al., 2010), it cannot be excluded that the decreased locomotion is due to this parameter, which has been previously shown to be the case for the $G\alpha_{q/11}^{beKO}$ group at baseline levels (Wenzel et al., 2020a). In this study, we did not analyze anxiety-related parameters, like freezing and immobility time, during the OPR test. However, it would be interesting to investigate by reanalyzing the acquired data and performing more sensitive behavioral tests to confirm previous findings from Wenzel and colleagues and reveal if older mice (18 months old) show the same behavior (Wenzel et al., 2020a). In conclusion, the longitudinal investigation of the effect of $\mathrm{G}\alpha_{\mathrm{q/11}}$ on memory did not reveal significant differences between $G\alpha_{q/11}^{beKO}$ and control mice at all times points investigated, confirming previous observations of our group.

It is worth mentioning that we observed differences in total exploration time and distance traveled between $G\alpha_{q/11}^{beKO}$ and the control group before the induction of the recombination (Supplementary Figure 1). These baseline differences could be attributed to our experimental strategy that involved global deletion of the expression of *Gna11.* Also, an other explanation could be due to the low recombination rate even without tamoxifen that has been previously reported by our lab on the *Slco1c1-CreER*^{T2} mouse line (Ridder et al., 2015).

At this point, it is essential to state that relating mouse age to human years only by considering the average lifespan of humans and laboratory mice is not regarded as accurate measurement since developmental stages are not uniform (Dutta & Sengupta, 2016). Based on the onset of senescence and the survival rate of C57BL/6J, the following chronological categories have been proposed for mice: young adults 3-6 months old, middle-aged 10-15 months old, and old 18-26 months old. These groups correspond to the human age equivalent of 20-30 years old, 38-47 years old, and 56-69 years old, respectively (Flurkey et al., 2007). However, a recent study employing a battery of behavioral tests on C57BL/6J mice showed that aging differentially affects mouse behavioral traits, and some aspects of cognitive decline could be observed from 12 months old on (Yanai & Endo, 2021). Furthermore, some groups have reported an age-dependent cognitive decline in the OPR test when comparing aged to young mice (Murai et al., 2007; Wimmer et al., 2012) but we could not confirm this with our current study neither in $G\alpha_{q/11}{}^{beKO}$ nor in the control group. These discrepancies could be possibly attributed to different experimental setups like testing young and aged mice in parallel instead of during the lifespan of the mice (Murai et al., 2007; Wimmer et al., 2012) or differences in the delay time between sample trial and test trial (Wimmer et al., 2012). Wimmer and colleagues demonstrated that 24 h after sample test, aged mice did not discriminate the displaced object compared to young mice but no differences between groups were observed when test trial was after 3 min after the sample test. The importance of the delay time between the sample and test trial was also shown by Murai and colleagues, who demonstrated that young healthy mice have best performance at 1 h delay and worst at 24 h (Murai et al., 2007).

A disadvantage of the OPR test is that it does not allow learning assessment (Sharma et al., 2010). Therefore, we were prompted to investigate spatial learning and memory with Barnes maze on our cohorts at the time point 20 months old, which has been successfully used in aged rodents (Barnes et al., 1980; Sharma et al., 2010; Shoji & Miyakawa, 2019; Yanai & Endo, 2021). The results of this study have shown that both groups had no differences in spatial learning, as indicated by the curves of primary errors, latency, and distance during the 5 acquisition days (Figure 5 A- C). However, a significant genotype effect between the groups was observed regarding the primary latency (Figure 5 B). While many studies are based on primary measurements as the most sensitive parameter to assess spatial learning and memory in Barnes maze, primary latency is considered the less sensitive parameter among them (Harrison et al., 2006; O'Leary & Brown, 2013). Furthermore, since the primary distance was not different between the groups, the difference in primary latency could be attributed to differences in locomotion and explorative behavior of aged mice, as also hypothesized for the OPR test in younger mice. To clarify this, we looked at the total distance and errors (Supplementary figure 2 E and G). These parameters did not differ between the two groups, pointing to no differences in locomotion and explorative behavior during the acquisition days. Also, Viney and colleagues during the analysis of the T-maze test on a transgenic mouse model that expresses pathological human Tau proteins, found no differences in spatial working memory but an increased delay of transgenic mice to initiate voluntary exploration (Viney et al., 2022). Whether the observed differences in primary latency between $G\alpha_{q/11}{}^{beKO}$ and control mice are also due to delayed initiation of voluntary exploration ,and whether, this could be attributed to increased freezing due to anxiety(Yanai & Endo, 2021) of the $G\alpha_{q/11}{}^{beKO}$ group has yet to be investigated by analyzing the acquired videos and performing ethological tests like open field or elevated plus maze on 20 months old mice.

We looked at the strategy the two groups employed to solve the maze. The learning strategies were categorized as spatial and non-spatial (Binder et al., 2019; Sunyer et al., 2007). In the current study, we found that both groups significantly decreased the use of the mixed strategy and increased the direct strategy over time, indicating that the learning process is not severely compromised between groups (Figure 5 E- F). However, the $G\alpha_{q/11}{}^{beKO}$ group did not show a decrease in the serial strategy over time in contrast to the control group (Supplementary Figure 2 C). The serial strategy was the primary strategy employed by the $G\alpha_{q/11}{}^{beKO}$ group to solve the task over time (Figure 5 F), pointing toward spatial learning deficits.

The short-term and long-term spatial memory references were assessed on the day 6 and day 17 probe trials (Binder et al., 2019; Sunyer et al., 2007). We found that the primary parameters significantly differed between the two groups, indicating memory deficits in the $G\alpha_{q/11}{}^{beKO}$ group. More specifically, primary errors and latency, but not distance, were markedly higher in the $G\alpha_{q/11}{}^{beKO}$ group compared to the control group on day 6 (Figure 6 A – C). These data indicate that the $G\alpha_{q/11}{}^{beKO}$ group had significant spatial memory deficits during the short-term reference memory test. However, we did not find differences in these parameters regarding the long-term reference memory test, similar to previous studies of other groups (Figure 6 A- C) (Binder et al., 2019; Sunyer et al., 2007). Memory trace stabilization involves fine-tuning between hippocampus and neocortical networks and is time-dependent. Maviel and colleagues showed that transient silencing of the dorsal hippocampus impairs recent memory retention (test after 1 day) but not remote memory retention (test after 30 days) (Maviel et al., 2004). Furthermore, analyzing the time spent in the target quadrant compared to all other quadrants, we found that both on days 6 and 17, the $G\alpha_{q/11}{}^{beKO}$ and the control group spent significantly more time in the target quadrant than all other quadrants (Figure 6 D- E). This result can be related to previous studies that suggested that in humans and rodents, different aspects of behavioral traits are affected during aging (Viney et al., 2022). Viney and colleagues showed in their study that spatial memory that requires less attention, like identifying the target quadrant in the Morris Water Maze, declines differently (in aged mice) compared to memory that requires high attention, like identifying the hidden platform (Viney et al., 2022). These observations could be relevant to our study since we observed that the $G\alpha_{q/11}^{beKO}$ group did not show differences in identifying the target quadrant and exploring the holes in it but rather showed differences in correctly locating the target hole for the first time, which requires greater attention. Furthermore, we observed that the $G\alpha_{q/11}^{beKO}$ group had less explorative behavior than the control group, as indicated by the total distance travelled, the total number of errors and the number of poke holes (Supplementary Figure 3 A- B, E- F). This could be due to increased anxiety of the $G\alpha_{q/11}^{beKO}$ group and ethological tests like open field or elevated plus maze would be needed to verify this (Shoji & Miyakawa, 2019; Yanai & Endo, 2021). Furthermore, other groups have shown that aged mice spent equal time around the target hole and the adjacent hole compared to younger mice during the analysis of probe trials (Shoji & Miyakawa, 2019), and this parameter further supported the spatial memory deficits. It would be interesting to quantify this parameter on the acquired videos of the current study and possibly identify differences between the $G\alpha_{q/11}^{beKO}$ and the control group. Finally, strategies to solve the maze during the probe trials align with the findings during the acquisition days. Most control mice used the spatial strategy to solve the task, while the $G\alpha_{q/11}^{beKO}$ showed an almost even use of direct and serial strategies to solve the task (Supplementary Figure 3 C- D).

Without visuospatial learning, normal mice can successfully solve the maze using the serial strategy (Harrison et al., 2006; O'Leary & Brown, 2013). This suggests that perhaps the $G\alpha_{q/11}^{beKO}$ group could not use the extra maze cues due to visual impairments. Although we did not test for visual impairments, this is less likely as the $G\alpha_{q/11}^{beKO}$ group, similarly to the control group, spent significantly more time in the target zone and visited the target hole and its adjacent holes significantly more compared to all other holes (Figure 6 D- E and Supplementary Figure 3 A- B). Therefore, our observations point to learning rather than visual deficits of the $G\alpha_{q/11}^{beKO}$ group. Finally, serial strategy, by definition, could contribute to the increased primary latency we observed in the $G\alpha_{q/11}^{beKO}$ group since mice explore more holes before reaching the target hole compared to direct strategy (Harrison et al., 2006).

It is long accepted that the hippocampus is the main brain structure involved in the formation of declarative memory in humans and rodents and is an especially vulnerable region not only during aging but also in neurodegenerative diseases that affect memory, like AD (Sharma et al., 2010; Sunyer et al., 2007). Furthermore, memory systems consolidation is a process that involves the communication of neocortical neuronal circuits and the hippocampus for remote memory consolidation and storage of long-lasting memories (Kitamura et al., 2017). Therefore, we focused on investigating structural differences between the $G\alpha_{q/11}^{beKO}$ and control mice in the region of the hippocampus and cortex, which were sacrificed at around 2 months after the last behavioral test (22 months old).

We identified a higher formation of string vessels but no differences in total vessel length in the hippocampus and cortex of $G\alpha_{q/11}^{beKO}$ mice (Figure 7 A – C and Figure 9 A – C). Higher formation of string vessels and vessel rarefaction has been shown in humans and rodents as a consequence of aging and may contribute to memory decline (Brown, 2010; Cortes-Canteli & Iadecola, 2020; Csiszar et al., 2017; Toth et al., 2017). Furthermore, our group has previously demonstrated that in a mouse model of the hereditary disease incontinentia pigmenti, the string vessel formation is a prominent structural finding that leads to increased hypoxia in the brain and memory deficits (Jiang et al., 2021). In addition to that, the hippocampus is a region more susceptible to hypoxia than the cortex due to its lower vascular density and oxygenation (Shaw et al., 2021). Therefore, the increased string vessels in the hippocampus could explain the recent memory and learning deficits identified during the Barnes maze.

Studies have shown that neuroinflammation can negatively affect cognitive function in the aging brain (Clarke et al., 2018; Sparkman & Johnson, 2008). However, we could not observe differences in the reactive astrocytic marker GFAP and the microglial marker of Iba1, neither in the hippocampus nor the cortex (Figure 7 D – G) and Figure 9 D – G). It is possible, though, that differences could be observed for other parameters, like the number of astrocytes or microglial morphology (Damani et al., 2011; Kim et al., 2021; Pao et al., 2020, 2023).

Neuronal damage and loss are a consequence of neurodegenerative diseases that affect memory, but during normal aging, the evidence suggests no significant loss of neurons (Brito et al., 2023; Riddle et al., 2003). Age-dependent cognitive decline instead occurs due to neuronal dysfunction such as loss of synaptic plasticity, axonal degeneration, or metabolic dysfunction (Brito et al., 2023; Burke & Barnes, 2006; Morrison & Baxter, 2012). Our data indicate no significant differences between aged mice of $G\alpha_{q/11}^{beKO}$ and the control group regarding neuronal density and synapses in brain regions necessary for memory formation (Figure 8, Figure 10 C – D and Supplementary Figure 4). It would be interesting for future studies to show if differences in, e.g., axonal transportation of BDNF, long-term potentiation impairment, mitochondria dysfunction, protein synthesis, or impaired neurogenesis, could be the reason for the observed memory deficits like others have shown before (Agasse et al., 2020; Arias-Aragón et al., 2023; Faraco et al., 2019; Pao et al., 2020, 2023; Yang et al., 2019). Finally, a recent study from Faraco and colleagues demonstrated a link between nitric oxide deficit in cerebral endothelial cells, accumulation of hyperphosphorylated tau and cognitive dysfunction (Faraco et al., 2019). Whether aged $G\alpha_{q/11}^{beKO}$ and control mice show differences in hyperphosphorylated tau, which is a hallmark of Alzheimer's disease and linked to vascular cognitive impairment (Cortes-Canteli & Iadecola, 2020), is not known and future studies could clarify this.

Decreased myelination has been shown to occur during normal aging in mice affecting their spatial memory (Wang et al., 2020). Furthermore, in humans, neurological and cerebrovascular pathologies lead to white matter hyperintensities, which are associated with memory decline, probably due to the vulnerability of the region to hypoxia (Cooper et al., 2016; Liu et al., 2016; Mutsaerts et al., 2011; Quick et al., 2021; Yang et al., 2017). Our study did not detect differences in the MBP protein expression in the corpus callosum and cortex (Figure 10 C and E), suggesting that the endothelial $G\alpha_{q/11}$ proteins do not affect myelination in aged mice.

The BBB permeability is an important factor that changes during normal aging (Montagne et al., 2015; Yang et al., 2020). Although BBB permeability is higher in aged humans than in young, healthy individuals, it increases in people with AD and vascular dementia (Farrall & Wardlaw, 2009). This study found no differences in IgG extravasation in the cortex (Figure 10 A and B), but we did not assess this parameter in the hippocampus. Furthermore, BBB integrity may be adequate to exclude molecules with high molecular weight like IgG but still compromised for smaller molecules (Stamatovic et al., 2019; Vázquez-Liébanas et al., 2024). Since conducting permeability assays *in vivo* is time and economically restricted, either *in vitro* studies or analysis of key TJs expression in the aged mice could reveal if BBB is compromised when $G\alpha_{q/11}$ proteins are not expressed in the aged brain endothelium (Stamatovic et al., 2019).

With aging, several factors change that can lead to cognitive dysfunction. As discussed above, the aged mice of the $G\alpha_{q/11}^{beKO}$ group may be affected by higher anxiety, a symptom associated with chronic stress. Studies in rodents have shown an age-dependent increase in anxiety (Lupien et al., 2009; Shoji & Miyakawa, 2019; Yanai & Endo, 2021), while others have shown that with aging, glucocorticoid levels increase and correlate with memory impairments (Garrido et al., 2012). In addition, chronic stress and high glucocorticoids in aged rodents can accelerate memory decline by reducing the ability of neurons to resist toxic or ordinary insults, like higher extracellular glutamate, and inhibit neurogenesis (Lupien et al., 2009; Mclay et al., 1998; Montaron et al., 2006; Shoji & Miyakawa, 2019). Whether this is true in the aged mice of this study is something that needs to be further investigated by looking at the plasma levels of corticosterone and/or the brain parenchyma (Garrido et al., 2012).

5.2 Mechanosensation in MPBECs involves Piezo1 and NF-κB but not G$\alpha_{q/11}$ proteins

How does the lack of endothelial G$\alpha_{q/11}$ signaling lead to string vessel formation? This question came up due to the immunohistochemical results, and we ventured to answer it on the molecular level. String vessels in the aging brain may arise due to increased capillary regression and decreased angiogenesis (Brown, 2010; Csiszar et al., 2017). A recent study showed that the microvascular rarefaction observed during normal aging could be rescued in the periphery by restoring VEGFA-VEGFR2 signaling (Grunewald et al.,2021). In addition, a study by Sivaraj and colleagues demonstrated that in human umbilical vein endothelial cells, the endothelial G$\alpha_{q/11}$ proteins mediate VEGF-induced angiogenesis (Sivaraj et al., 2015). The deletion of the genes expressing the G$\alpha_{q/11}$ proteins from the endothelium leads to decreased angiogenesis, proliferation, and increased apoptosis in the retinal vasculature in P6 mice (Sivaraj et al., 2015). Similarly to this report, MPBECs isolated from $G\alpha_{q/11}^{beKO}$ mice did not show increased proliferation to the angiogenic stimulus of 10 % serum (Figure 20). This indicates that brain endothelial G$\alpha_{q/11}$ proteins play a role in angiogenic signaling, which could affect string vessel formation in aged mice. However, further investigation would be necessary to dissect the exact angiogenic pathway which, similar to what has been shown for the periphery, could involve the VEGFR2 signaling by eg. stimulating cells with VEGFA and investigating the VEGFR2 activation (Sivaraj et al., 2015).

String vessels are non-perfused collapsed vessels that are prominent during development, normal aging, and AD (Brown, 2010). A proposed mechanism that could lead to increased string vessel formation and microvessel rarefaction in the brain during normal aging and in brain pathologies are the changes in blood flow and loss of shear stress (Brown, 2010; Cortes-Canteli & Iadecola, 2020; Csiszar et al., 2017). In the periphery, it has been shown that G$\alpha_{q/11}$ proteins could act downstream of mechanosensory activation and play an essential role in endothelial responses by activating nitric oxide synthase or NF-κB signaling, depending on the flow type (Albarrán-Juárez et al., 2018; Wang et al., 2015, 2016). Unpublished data from our group has shown that deleting the mechanosensory GPCRs GPR68 in the whole organism or P2Y$_2$ in brain ECs leads to increased string vessel formation. In addition, deletion of the genes that encode NEMO from brain endothelium also leads to a prominent increase in string vessel formation (Ridder et al., 2015; Wenzel et al., 2021). Therefore, we hypothesized that G$\alpha_{q/11}$ proteins are an essential part of a mechanosensing repertoire in the brain endothelium that senses the age-related blood flow changes in the brain and contributes to the EC fate with a molecular mechanism involving NF-κB.

Piezo1 is a bona fide mechanosensor expressed in ECs and can be specifically activated by the agonist Yoda1 (Coste et al., 2010; Syeda et al., 2015; Wang et al., 2016). In the periphery it has been proposed that shear stress activates Piezo1 and downstream, the $G\alpha_{q/11}$ and NF-κB in a flow-dependent manner (Albarrán-Juárez et al., 2018). In the current study, we demonstrated that *in vitro* treatment of MPBECs isolated from $G\alpha_{q/11}^{beKO}$ and control mice with Yoda1 led to a significant activation of NF-κB but without the involvement of the $G\alpha_{q/11}$ proteins (Figure 12). This result confirms previous findings showing that brain ECs express functional Piezo1 (Harraz et al., 2022) and that Yoda1 seems to induce responses that mimic the effect of shear stress (Albarrán-Juárez et al., 2018). However, our preliminary observations on the effect of different types of flow on NF-κB activation did not reveal differences between flow types probably due to the low number of experiments (Supplementary Figure 8).

In the current study, we observed, similarly to the ECs in the periphery, that activation of Piezo1 by Yoda1 leads to a prominent increase in $[Ca^{2+}]_i$, but $G\alpha_{q/11}$ proteins are not involved in this (Figure 13). This difference could be attributed to the differences between brain and peripheral ECs. Also, to our knowledge, no previous report links Yoda1 stimulation of ECs to NF-κB activation, pointing to differences between shear stress effects and specific activation of mechanosensors. Furthermore, the concentration used in this study is higher than what others have used before (Chuntharpursat-Bon et al., 2023; Harraz et al., 2022; Swain & Liddle, 2021; Wang et al., 2016), which suggests that in lower concentrations, the effect of Yoda1 may be different. A problem with Yoda1 solutions is the insolubility in higher concentrations (> 20 µM) (Syeda et al., 2015), which has also been observed by us. However, given that we solved this problem (see section 2.3), we probed high concentrations to ensure Yoda1 would elicit an effect. Whether lower concentrations of Yoda1 elicit the same responses on MPBECs would be interesting to be answered in future studies.

In this study, we established a protocol for cultivating MPBECs utilizing the ibidi pump system, which enabled us to investigate the effects of different types of shear stress on MPBECs. Our results showed that regardless of the type of shear stress, the initial calcium responses of MPBECs are similar and do not involve the $G\alpha_{q/11}$ proteins (Figure 14, Figure 15 and Supplementary Figure 5). These findings are in line with previous *in vivo* experiments showing that shear stress elicits $[Ca^{2+}]_i$ increases in the CNS vasculature through Piezo1 on *Cdh5*-GcaMP8 mice (Harraz et al., 2022). However, these results are in contrast to what has been shown for peripheral ECs pointing to substantial differences between the two cell types (Wang et al., 2016).

Interestingly, our initial observations on the effect of shear stress on the hCMEC/D3 line suggest similar calcium responses to different types of flow and validated our protocol applied to MPBECs (Supplementary Figure 7).

Shear stress reversibly affected $[Ca^{2+}]_i$ responses in naïve and sheared endothelial MPBECs (Supplementary Figure 6). The physiological relevance of these responses is not fully understood. It is known that ischemic stroke, during which the blood flow acutely stops, has deleterious effects on EC function. In an *in vitro* model of the BBB, consisting of primary ECs and astrocytes, cessation of flow for 1 h and subsequent reperfusion has been used to mimic stroke (Krizanac-Bengez et al., 2003, 2006). In their work, Krizanac and colleagues showed that flow cessation leads to the release of the inflammatory cytokines IL-1β and IL-6. However, BBB integrity was not compromised, presumably due to the protective effects of released NO (Krizanac-Bengez et al., 2003, 2006). Another study based on a monoculture of brain microvascular ECs of bovine and human origin showed that when cells are pre-conditioned to shear stress and subsequently a flow reduction occurs, BBB permeability increases due to TJ disruption (Walsh et al., 2011). Whether the endothelial mechanosensation and calcium responses observed in our study play a role in these events would be interesting to be further investigated.

The level of shear stress in our measurements was near the lower value that has been measured in the post-capillary venules and which many groups use to simulate *in vitro* immune cell infiltration through the endothelial monolayer (Hamminger et al., 2021; Koutsiaris et al., 2007; Wang et al., 2022). However, shear stress varies significantly along the vascular tree, dependent on the vessel diameter (Koutsiaris et al., 2007), as well as physiologically by factors that change blood flow like neurovascular coupling or hypercapnia (Schaeffer & Iadecola, 2021; Wenzel et al., 2020a). Whether MPBECs respond differently to higher shear stress, as other groups have shown for some BBB models (Choublier et al., 2022), would be interesting to investigate in future studies.

The current study found that MPBECs change their morphology to adapt to flow. MPBECs showed spindle morphology, elongated under shear stress, and could align to the flow direction when cultured under the unidirectional flow type (Figure 16). The elongated morphology of brain microvascular ECs under shear stress has also been shown by other groups (Choublier et al., 2022; Steiner et al., 2011), while others, similar to this study, have shown that they are able to align to flow (Garcia-Polite et al., 2017; Moya et al., 2020). However, our results are in contrast to some studies based on brain microvascular ECs, which showed a cobblestone morphology and resistance to alignment in the direction of flow (Choublier et al., 2022; DeStefano et al., 2017; Reinitz et al., 2015; Ye et al., 2014). Furthermore, the elongation and alignment to flow measured in this study were close to what has been calculated for non-CNS ECs (Reinitz et al., 2015). It has been proposed that resistance to elongation and alignment of BBB models is necessary for minimizing cell-cell contacts and preserving the BBB (DeStefano et al., 2017; Reinitz et al., 2015; Ye et al., 2014). Previous findings of our group have demonstrated the purity of our *in vitro* culture of MPBECs and the expression of the TJ proteins ZO-1 and claudin-5 (Assmann et al., 2017). Furthermore, *in vivo* data have shown that alignment is a characteristic of straight parts of big vessels, and failure to adapt to the flow direction is associated with the pro-inflammatory phenotype (Baeyens et al., 2014; Li et al., 2014). Whether ECs in the microvascular bed *in vivo* have distinct morphology is yet to be elucidated. All in all, our results show for the first time that mouse MPBECs show substantial differences compared to other BBB models in response to flow and mimic atheroprotective aspects of peripheral ECs. The discrepancies between our results and those previously published probably arise from the cell types used in terms of primary or immortalized cells or species, and experimental setup differences such as time and magnitude of shear stress, the setup itself or co-culture with other cell types.

5.3 Shear stress significantly affects the proteomic profile of MPBECs

The prominent morphological changes induced by shear stress prompted us to investigate the whole-cell and cell surface proteomics of MPBECs. Many *in vitro* studies have shown that shear stress has significant effects on gene and protein expression profiles (Bouhrira et al., 2022; Choublier et al., 2022; Cucullo et al., 2011; DeStefano et al., 2017; Garcia-Polite et al., 2017), but to our knowledge, there is no previous report regarding mouse MPBECs expression profile after long-term exposure to shear stress. Analysis of the proteomic data from whole cell preparations revealed significant differences between flow and static conditions but not between flow types (Figure 17). Interestingly we found that a large number of differentially regulated proteins were shared in the comparisons between the flow types and static control. We used the Gene Set Enrichment Analysis on the shared upregulated and downregulated proteins The pathway enrichment analysis using the MSigDB and hallmark gene set on the shared upregulated and downregulated candidates in flow conditions against the static control, showed that shear stress results in an upregulation of pathways related to apoptosis, fatty acid metabolism, and coagulation (Figure 17 F). On the other hand, based on the hallmark gene set we observed downregulation of pathways related to hypoxia, the mammalian target of rapamycin complex1 (mTORC1) and glycolysis (Supplementary Figure 9 B). Downregulation of glycolysis due to shear stress has been shown before by other groups on the transcription level and confirmed by measurement of lactate and glucose on supernatants, indicating that shear stress favors the shift of energy production from glycolysis to the more efficient aerobic respiration (Cucullo et al., 2011). Also, the increased fatty acid metabolism reflects the metabolic demands of the cells, as fatty acids are a source of ATP production (Mallick & Duttaroy, 2022). Increased expression of proteins involved in apoptosis has also been reported for the hCMEC/D3 cells under flow (Choublier et al., 2022). However, the measurement of apoptotic rates in induced pluripotent stemmcells (iPSCs) showed that they decreased under flow compared to static conditions (DeStefano et al., 2017).

Apoptosis and proliferation are in balance and tightly regulated in an *in vitro* cell system. Although our microscopic observations did not indicate increased apoptosis under shear stress, it would be interesting to investigate in the future. Finally, the pathway analysis with the gene ontology set revealed the upregulation of many pathways involved in vascular development (angiogenesis, vasculature and tube development, blood vessel morphogenesis) pointing to the angiogenic effects of shear stress (Figure 17 G). Regarding the downregulated pathways according to the gene ontology dataset, they involved mainly pathways in metabolic processes (small molecule, organic acid amino acid and amide metabolic process) (Supplementary Figure 9 C).

Interestingly, the whole lysate analysis revealed significant upregulation of proteins that are critical for BBB function under flow conditions compared to static control (Figure 17 A- B). First, we found an upregulation of the TJ proteins claudin-5 and occludin. These results are in line with previous studies on human and bovine brain microvascular ECs exposed to shear stress compared to static conditions (Cucullo et al., 2011; Garcia-Polite et al., 2017; Rochfort & Cummins, 2015; Walsh et al., 2011). However, in the immortalized human microvascular cell line hCMEC/D3 and a human iPSCs-derived BBB model, claudin-5 and occludin expression was not altered after exposure to shear stress (Choublier et al., 2022; DeStefano et al., 2017). Furthermore, we found upregulation of the efflux transporters P-gp (encoded by the gene *Abcb1a*) and BCRP (encoded by the gene *Abcg2*) as well as for MRP1 (encoded by the gene *Abcc1*) but only between unidirectional flow vs static conditions. These results align with those of other groups in the level of transcription or protein expression (Choublier et al., 2022; Garcia-Polite et al., 2017). However, in a BBB model derived from human iPSCs, gene expression of *ABCB1* (the human gene that encodes the P-gp) was found unchanged (DeStefano et al., 2017), and BCRP in hCMEC/D3 cells was found to decrease in shear stress compared to static conditions (Choublier et al., 2022). Cumulatively, our results show that shear stress induces the sealing of the BBB by upregulating key components of TJs and membrane transporters that tightly regulate the passage of molecules through the endothelial layer (Daneman & Prat, 2015; Kadry et al., 2020).

We did not find differences between flow conditions and static control on TJs JAM-A, ZO-1, and ZO-2 and the adherens junctions CDH5 and PECAM1. Furthermore, we could not detect some essential efflux transporters of the MRP family (MRP2/3/4/5). Some groups have reported upregulation of ZO-1, ZO-2, CDH5, and PECAM1 at the level of gene or protein expression after shear stress (Cucullo et al., 2011; Garcia-Polite et al., 2017; Rochfort et al., 2015; Rochfort & Cummins, 2015) while others have shown that shear stress induces localization of these components of TJs and adherens junctions in the intercellular connections leading to sealing and stabilization of the BBB (Bouhrira et al., 2021; Choublier et al., 2022; Garcia-Polite et al., 2017). DeStefano and colleagues showed that *CDH5* and tight junction protein 1 (*TJP1,* the gene that encodes ZO-1 protein) do not change upon shear stress stimulation compared to static conditions in the human BBB model derived from stem cells (DeStefano et al., 2017). Therefore, future work based on fluorescence microscopy could reveal, whether the aforementioned proteins play a role in establishing a steady-state barrier function and tightening of the BBB in mouse MPBECs by showing higher localization to cell-cell junctions (Tietz & Engelhardt, 2015). Finally, we saw upregulation of ICAM-1 under flow compared to static control, as others have shown before (Cucullo et al., 2011), but not for VCAM-1, which has been shown to be upregulated under the oscillatory type of flow in the periphery (Albarrán-Juárez et al., 2018).

It is of high interest that in our experimental approach, we found only three proteins to be differentially expressed between the two types of flow: HMOX1, ANGPT2 and ABI3. HMOX1 and ABI3 were found to be upregulated in both types of flow compared to static control and downregulated in the oscillatory type of flow compared to the unidirectional flow type (Figure 17 C). HMOX1 is a protein whose expression is induced by oxidative stress and vascular pathologies like stroke and exerts cytoprotective and antioxidant effects by catalyzing free heme and producing carbon monoxide (Ali et al., 2009; Callegari et al., 2023; Choublier et al., 2022). Our results are in line with observations on periphery ECs where the expression of *HMOX1* was significantly induced by both oscillatory flow and unidirectional flow, and this increase was higher in the latter (Ali et al., 2009). Furthermore, shear stress on hCMEC/D3 cells leads to a significant upregulation of HMOX1 expression (Choublier et al., 2022). Little is known about the role of ABI3 in ECs since it is not highly expressed in the brain endothelium but mostly in microglia (Ibanez et al., 2022; Vanlandewijck et al., 2018). Human gene variants of *ABI3* play a role in the innate immunity response to AD pathology (Sims et al., 2017). However, ABI3 is presumably a regulator of the actin cytoskeleton reorganization based on its similarity to the other members of the family (Sekino et al., 2015) and given the stark differences in the cell morphology observed between the flow types, this protein could be a potential novel endothelial shear stress-related protein for future research. Finally, ANGPT2, a molecule involved in angiogenic processes, was downregulated under unidirectional flow vs oscillatory flow and static control. Interestingly, a study on periphery ECs on oscillatory and unidirectional flow's role in angiogenesis showed that ANGPT2 was significantly higher under oscillatory flow and mediated the flow-induced angiogenesis. On the other hand, the unidirectional type of flow decreased the expression of ANGPT2 and inhibited angiogenesis *in vitro* (Tressel et al., 2007). ANGPT2 physiologically is a secreted protein that can act in an autocrine manner and antagonizes the ANGPT1 for binding to the Tie2 receptor and it was recently shown that is stored in the Weibel-Pallade bodies with VwF and interacts with it (Mobayen et al., 2023). Based on the cell surface proteomic data, that showed same expression profile to the whole cell proteomics (Figure 18 A – C), the increased ANGPT2 expression could be due to higher intracellular storage and/or increased interaction with its receptor.

Our cell surface proteotyping approach revealed substantial differences in the abundance of membrane proteins between static and flow conditions and between flow types (Figure 18). Interestingly, cell surface proteotyping showed, similarly to the whole proteomic analysis, prominent differences between flow types and static conditions and a substantial dataset of commonly upregulated and downregulated proteins under shear stress. Pathway analysis with the MSigDB and the hallmark and GO gene sets using the common differentially regulated proteins under both flow conditions compared to static control, revealed an upregulation on pathways that are involved in angiogenic and vascular development similarly to what the whole proteomic analysis revealed. Finally, as expected, the pathway analysis revealed upregulation and downregulation (Supplementary Figure 10) of gene sets related specifically to the cell surface (eg. apical junction, apical surface, cell surface, cell adhesion, plasma membrane region eth) confirming the high specificity of CSC for enrichment with cell surface proteins compared to the whole cell proteotyping.

We focused on identifying novel flow-specific candidates, which could also be essential for the morphological alterations observed between flow types. On the top significantly regulated candidates in the comparison between the two types of flow, the adhesion G protein-coupled receptor G6 (ADGRG6), the coagulation factor II (thrombin) receptor-like 2 (F2RL2), the disintegrin and metalloproteinase domain-containing protein 15 (ADAM15), the KIT proto-oncogene receptor tyrosine kinase (KIT), the ectonucleoside triphosphate diphosphohydrolase 1 (ENTPD1), the activated leukocyte cell adhesion molecule (ALCAM), and plasmalemma vesicle associated protein (PLVAP) showed specific differential expression in unidirectional flow vs oscillatory flow and static control conditions. Interestingly, some of these candidates, like ADGRG6, F2RL2, ENTPD1, ALCAM, and PLVAP, either were not detected in the whole proteomic dataset or were identified, but there were no differences between the conditions showing that cell surface proteotyping can reveal differences and complement the results obtained from the whole cell proteomic approach.

The ADGRG6 (or GPR126) was specifically upregulated under unidirectional flow. ADGRG6 is expressed in the mouse venous ECs and fibroblasts (Vanlandewijck et al., 2018), and little is known about its function. Members of the adhesion G protein-coupled receptor family have long extracellular parts that interact with other proteins or mediate cell adhesion (Pluimer et al., 2020). A study by Cui and colleagues provided substantial evidence that GPR126 is implicated in the angiogenic process and vascular development by modulating the VEGFR2 activity (Cui et al., 2014). Future work could reveal whether this protein is involved in the barrier genesis in the BBB like other members of the family, e.g., GPR124 and GPR116 (Pluimer et al., 2020).

The PLVAP upregulation was a characteristic of the unidirectional flow type. PLVAP expression did not differ in the whole lysate proteomic dataset, but the cell surface proteotyping revealed spatial differences. One study on human periphery ECs found that shear stress leads to upregulation of *PLVAP in vitro* (Wasserman et al., 2002). However, *in vivo*, PLVAP is essential for vesicle and fenestrae formation in vessels and increases vessel permeability. In the CNS endothelium, PLVAP is strongly downregulated during BBB formation and upregulated during pathological conditions like stroke (Callegari et al., 2023; Profaci et al., 2020; Vanlandewijck et al., 2018). Evidence suggests that PLVAP expression is associated with the VEGF-VEGFR2 signaling pathway and contributes to barrier loss in the retina-blood barrier (Wisniewska-Kruk et al., 2016). It is of interest that we found upregulation of VEGFR2 on both datasets of whole lysate and cell surface proteotyping in the comparison between flow conditions and static control but not between the flow types, suggesting that further investigation is necessary to reveal why PLVAP expression is specifically higher in the unidirectional type of flow and whether VEGFR2 signaling is involved. Furthermore, our preliminary microscopic observations showed that not all cells under the unidirectional flow type express the PLVAP but rather some distinct populations. This suggests that perhaps only cells that undergo proliferation transiently upregulate PLVAP. Finally, there is evidence in the literature that the orientation of the cells and the direction of flow affect the activation of inflammatory and anti-inflammatory pathways (Albarrán-Juárez et al., 2018; Wang et al., 2013). Since in the unidirectional flow type, a percentage of cells are not aligned to the flow direction; it would be interesting to investigate whether aligned cells overexpress PLVAP *in vitro*.

In our dataset, we identified an upregulation of Piezo1 in both whole lysate and CSC datasets. This upregulation is specific to flow vs static conditions; to our knowledge, it is the first time described *in vitro*. Piezo1 is essential for the *in vivo* alignment of ECs in cerebral arteries during embryogenesis as well as *in vitro* (Li et al., 2014). Based on our results and previous research on different types of flow, Piezo1 is vital for the initial steps of mechanosensation. However, downstream, distinct pathways are activated depending on the kind of flow, which may involve adhesion molecules, VEGFR2, GPCRs, or $G\alpha_{q/11}$ signaling, which affect actin cytoskeleton and finely tune the response of ECs to different types of flow (Albarrán-Juárez et al., 2018; Baeyens et al., 2014; Li et al., 2014). In our datasets, we did not find differences in the expression of the adhesion molecules PECAM1 and CDH5, but we found upregulation of VEGFR2 in both flow conditions compared to static control. These proteins have been shown to form a vital mechanotransduction complex to mediate shear stress-dependent cell alignment in peripheral ECs (Tzima et al., 2005). All in all, since no differences were found between flows for Piezo1 and VEGFR2, future studies could elucidate which downstream molecules are essential for the morphological changes observed between flow conditions. These could more likely involve signaling that affects adhesion and cytoskeleton reorganization and in that case, ADAM15 as well as ADGRG6 could be proven potent novel candidates.

An interesting candidate revealed from the cell surface proteotyping was THBD. This molecule was specifically upregulated only in oscillatory flow compared to static conditions in both whole cell and cell surface proteotyping. Also, THBD showed a tendency in the comparison between unidirectional and oscillatory types of flow. THBD has anti-inflammatory and barrier-stabilizing effects on the endothelium (Wenzel et al., 2014). A study on human brain microvascular ECs demonstrated that THBD protein levels increase after 24 h under laminar shear stress, and the mRNA expression was significantly higher after 72 h (Rochfort & Cummins, 2015). Since we did not find differences between unidirectional flow and static conditions in our proteomic analysis, discrepancies could probably be attributed to transcriptional or translational differences or experimental design, which would be interesting to be further investigated. Wenzel and colleagues generated a mouse line to specifically delete the expression of *Thbd* in brain ECs ($Thbd^{beKO}$) and showed that in the peri-infarct area, where blood flow is still present after stroke, $Thbd^{beKO}$ mice had lower vessel diameter, vessel length and angiogenesis compared to control mice (Wenzel et al., 2020b). Our demonstration that the expression of *Thbd* affects the migration of MPBECs *in vitro* under static conditions as well as that shear stress upregulates THBD and angiogenic related pathways is in line with the role of THBD in angiogenesis *in vivo* in a mouse stroke model (Wenzel et al., 2020b). In addition, some studies have shown that shear stress promotes migration of ECs *in vitro* (Urbich et al., 2002) but whether shear stress and THBD work synergistically during migration would be interesting to be further explored.

5.4 Summary, limitations and outlook

Alterations in the brain's blood flow supply during normal aging contribute to age-dependent cognitive decline. In the current study, we provide evidence that the $G\alpha_{q/11}$ signaling in brain endothelium affects the cognitive function of aged mice. Based on previous results of our group that brain endothelial $G\alpha_{q/11}$ signaling attenuates cerebrovascular reactivity in young mice (Wenzel et al., 2021) as well as evidence that cerebrovascular reactivity declines with aging (McKetton et al., 2018; Miller et al., 2019; Peng et al., 2018) we asked whether the vascular changes observed in young mice affect the cognitive function during aging. We investigated our hypothesis based on the behavioral tests OPR and Barnes maze during the life span of mice. We observed cognitive deficits in aged $G\alpha_{q/11}{}^{beKO}$ compared to control which could be attributed to the increased string vessel formation in the hippocampus and the presumably subsequent significant changes in blood supply, affecting neuronal function.

In our study, we used mice of both sexes, which, on one side, excludes sex biases, but on the other side, it leads to higher variability. The performance of female rodents is strongly affected by the estrous cycle, and there is evidence that female mice perform worse than males in OPR and Barnes maze (Frick & Gresack, 2003; Gresack et al., 2007; O'Leary & Brown, 2013). We did not include this parameter in our statistical analysis in the current study due to the low number of animals. Therefore, we cannot exclude that differences may not have been detected. Finally, we cannot exclude that aged mice similar to younger mice have increased anxiety-related behavior, which could also mask undetected differences.

As discussed above, the quantification of string vessels in this study was based on collagen IV and caveolin-1 staining. However, it has been shown that structures similar to what we name here, string vessels, have been characterized by other groups as interpericyte tunneling nanotubes that connect two bona fide pericytes in neighboring capillaries (Alarcon-Martinez et al., 2020). Alarcon-Martinez and colleagues have provided evidence that these structures are essential for neurovascular coupling (Alarcon-Martinez et al., 2020). Future work could shed light on what percentage of the string vessels quantified in this study belong to interpericyte tunneling nanotubes or arise after EC death.

The hippocampus is a brain region susceptible to hypoxia and severely affected during normal aging. It is possible that the increased string vessels observed in this study in aged mice could lead to increased hypoxia and, therefore, neuronal dysfunction (Jiang et al., 2021). In addition to that, it would be interesting to compare the histopathological findings of aged mice of this study to those of young mice to observe for age-related changes in the brain as well as for the degree of endothelial recombination of our model (Jiang et al., 2021). Finally, in the current study, we did not find evidence of altered neuronal function, which points out that neuronal integrity is preserved in aged mice. Still, axonal transportation, protein synthesis, or mitochondria function differences should be investigated.

Based on the *in vivo* results of this study and unpublished data of the group on the role of mechanosensors in the formation of string vessels in the mouse brain vasculature, we explored the hypothesis that $G\alpha_{q/11}$ proteins mediate mechanotransduction in the brain endothelium. Our *in vitro* approach has revealed that $G\alpha_{q/11}$ proteins in MPBECs, in contrast to the periphery, are not involved in the shear stress and Yoda1-induced $[Ca^{2+}]_i$ increase. The differences may arise due to the *in vitro* models and experimental design. Whether there is a dose-dependent effect of shear stress and Yoda1 is currently unclear. Finally, whether the $[Ca^{2+}]_i$ increase has an intracellular or extracellular origin has yet to be investigated. Still, evidence on the *Cdh5*-GCaMP8 mice indicates that the origin is rather extracellular, and the involvement of $G\alpha_{q/11}$ proteins in these events is dispensable (Harraz et al., 2022).

Shear stress induces significant changes in the proteome of MPBECs, both in whole and cell surface proteome. We have identified that shear stress induces the expression of proteins that promote the tightening of the BBB. However, we could not identify some prominent proteins expressed by the BBB ECs (eg. MRPs), which could be attributed to the technique limitations or possibly to decreased expression *in vitro*. Furthermore, the cell surface proteotyping identified candidates expressed explicitly on the surface of brain ECs that were not identified in the whole proteomic analysis (eg ADGRG6, F2RL2, JAM-B, ABCC5). This is an advantage of our approach to performing both proteomic analyses to complement each other and reveal novel proteins involved in mechanotransduction. A limitation of our *in vitro* approach is the lack of the different NVU or blood components that can substantially influence the response of ECs to shear stress. Also, our *in vitro* model may recapitulate characteristics of ECs from different compartments after shear stress and future analysis of the data of this study to publicly available RNA sequencing datasets could show which phenotype MPBECs acquire after exposure to shear stress (Vanlandewijck et al., 2018).

6 Supplementary

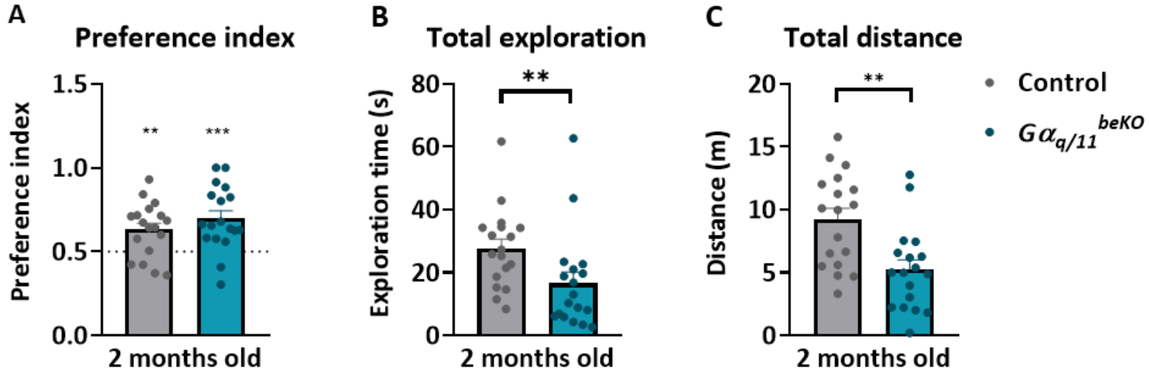

Supplementary Figure 1: Performance of mice in the OPR test before tamoxifen treatment: *Mice were assigned to control and* $G\alpha_{q/11}^{beKO}$ *groups according to their genotype and performed the OPR test before tamoxifen treatment.* ***A)*** *Preference index was significantly higher than the 0.5 chance level for both groups and no difference between groups was observed. Data are shown as mean ± SEM. Statistical analysis: unpaired T-test between groups [t(34) = 1.147, p = 0.2594]. N = 18 animals per group. One sample t-test of each group to 0.5 chance level: control group [t(17) = 3.428, p = 0.0032];* $G\alpha_{q/11}^{beKO}$ *group [t(17) = 4.442, p < 0.001]. One sample t-test of each group to 0.5 chance level: control [t(17) = 3.428, p = 0.0032];* $G\alpha_{q/11}^{beKO}$ *[t(17) = 4.442, p < 0.001]. * shows a significant difference to the 0.5 chance level.* ***B-C)*** *Analysis of the total exploration time of both objects and total distance travelled during the test trial revealed that the* $G\alpha_{q/11}^{beKO}$ *spent significantly less time exploring the two objects and had lower locomotion. Statistical analysis: total exploration: Mann-Whitney U-test, p = 0.0037; total distance: unpaired T-test [t(34) = 3.404, p = 0.0017]. N = 18 animals per group ** p < 0.01, *** p < 0.001. Abbreviations:* $G\alpha_{q/11}$*: G protein subunit alpha q/11, beKO: brain endothelial knockout.*

A

	Strategy	Control (%inter-trials)	$G\alpha_{q/11}^{beKO}$ (%inter-trials)	Statistics (chi-square)
Acquisition Day 1	Direct	8.06	5.56	
	Serial	45.16	50.00	$\chi^2(2)=0.3412, p=0.8431$
	Mixed	46.77	44.44	
Acquisition Day 2	Direct	20.31	27.27	
	Serial	46.88	54.55	$\chi^2(2)=2.931, p=0.231$
	Mixed	32.81	18.18	
Acquisition Day 3	Direct	39.06	27.91	
	Serial	43.75	58.14	$\chi^2(2)=2.17, p=0.3379$
	Mixed	17.19	13.95	
Acquisition Day 4	Direct	51.56	27.27	
	Serial	32.81	56.82	**$\chi^2(2)=7.221, p=0.027$**
	Mixed	15.63	15.91	
Acquisition Day 5	Direct	68.75	38.64	
	Serial	28.13	47.73	**$\chi^2(2)=10.85, p=0.0044$**
	Mixed	3.13	13.64	

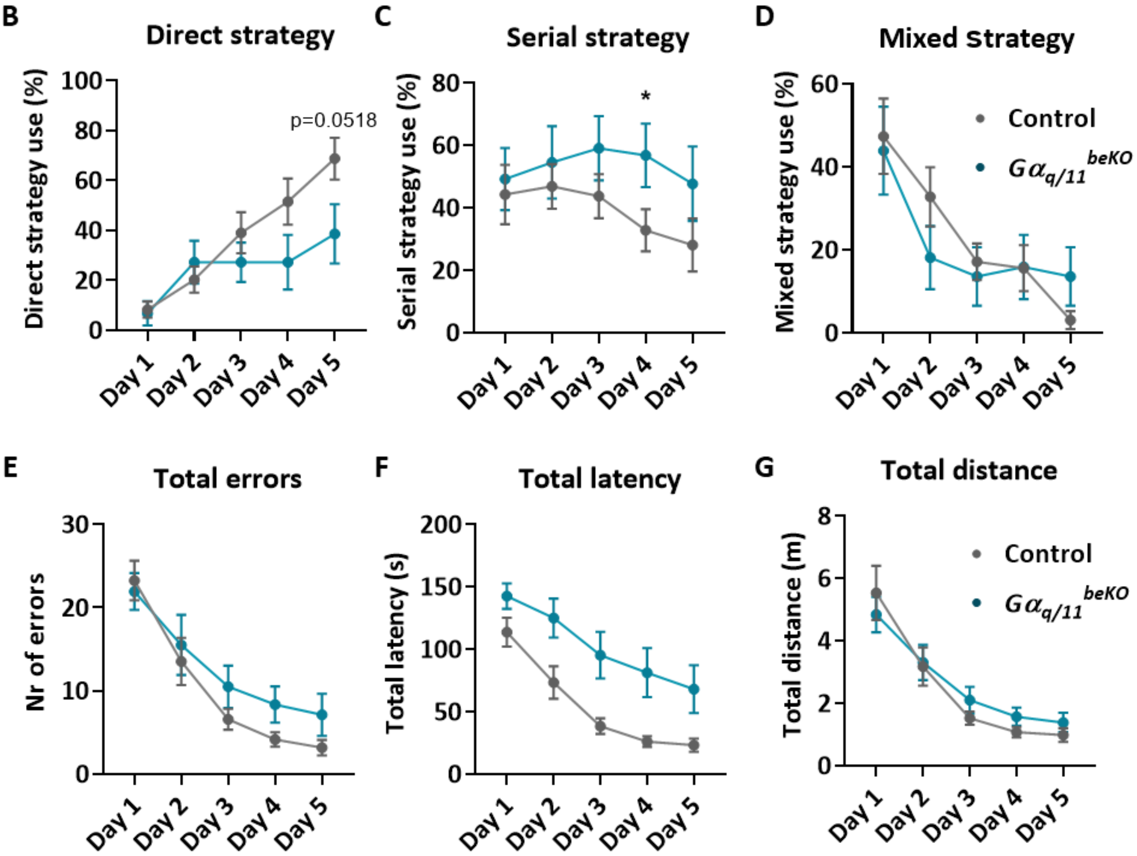

Supplementary Figure 2: Analysis of learning strategies during acquisition days 1 to 5 in Barnes maze test. A) *Percent of strategy use calculated from 4-intertrial sessions per mouse during acquisition days. On days 4 and 5, a statistically significant difference between the groups was observed in the use of the strategies. Statistical analysis: contingency table chi-square analysis. N = 11-16 animals per group* ***B-D)*** *Graphical depiction of the percent use of every strategy from 4-intertrial sessions per mouse over time. A strong tendency was found on day 5 on the use of direct strategy (B) and a significantly different use of serial strategy on day 4 (C) between genotypes. Data are shown as mean ± SEM. Statistical analysis Mann-Whitney U-test: direct strategy day 5, p = 0.0518; serial strategy day 4, p = 0.0456. N = 11-16 animals per group.* ***E-G)*** *Total errors (E), total latency (F) and total distance (G) significantly decline over time for both groups during the acquisition days, indicating no differences in the learning process. However, a significant genotype effect on total latency was observed. Data* *are shown as mean ± SEM of four trials per day. Statistical analysis two-way repeated measurements ANOVA with Sidak's posthoc test. Total errors: genotype [F(1, 25) = 1.135, p = 0.2969]; time [F(2.198, 54.94) = 41.15, p < 0.0001]; interaction [F(4, 100) = 1.073, p = 0.3737]; subject [F(25, 100) = 5.605, p < 0.0001]. Total latency: genotype [F(1, 25) = 10.36, p = 0.0036]; time [F(1.908, 47.71) = 41.52, p < 0.0001]; interaction [F(4, 100) = 1.135, p = 0.3445]; subject [F(25, 100) = 9.545 , p < 0.0001]. Total distance: genotype [F(1, 25) = 0.008228, p = 0.9284]; time [F(1.221, 30.53) = 19.06, p < 0.0001]; interaction [F(4, 100) = 0.9602, p = 0.4328]; subject [F(25, 100) = 2.321, p = 0.0017]. N = 11-16 animals per group * p < 0.05. Abbreviations: $G\alpha_{q/11}$: G protein subunit alpha q/11, beKO: brain endothelial knockout, Nr: number.*

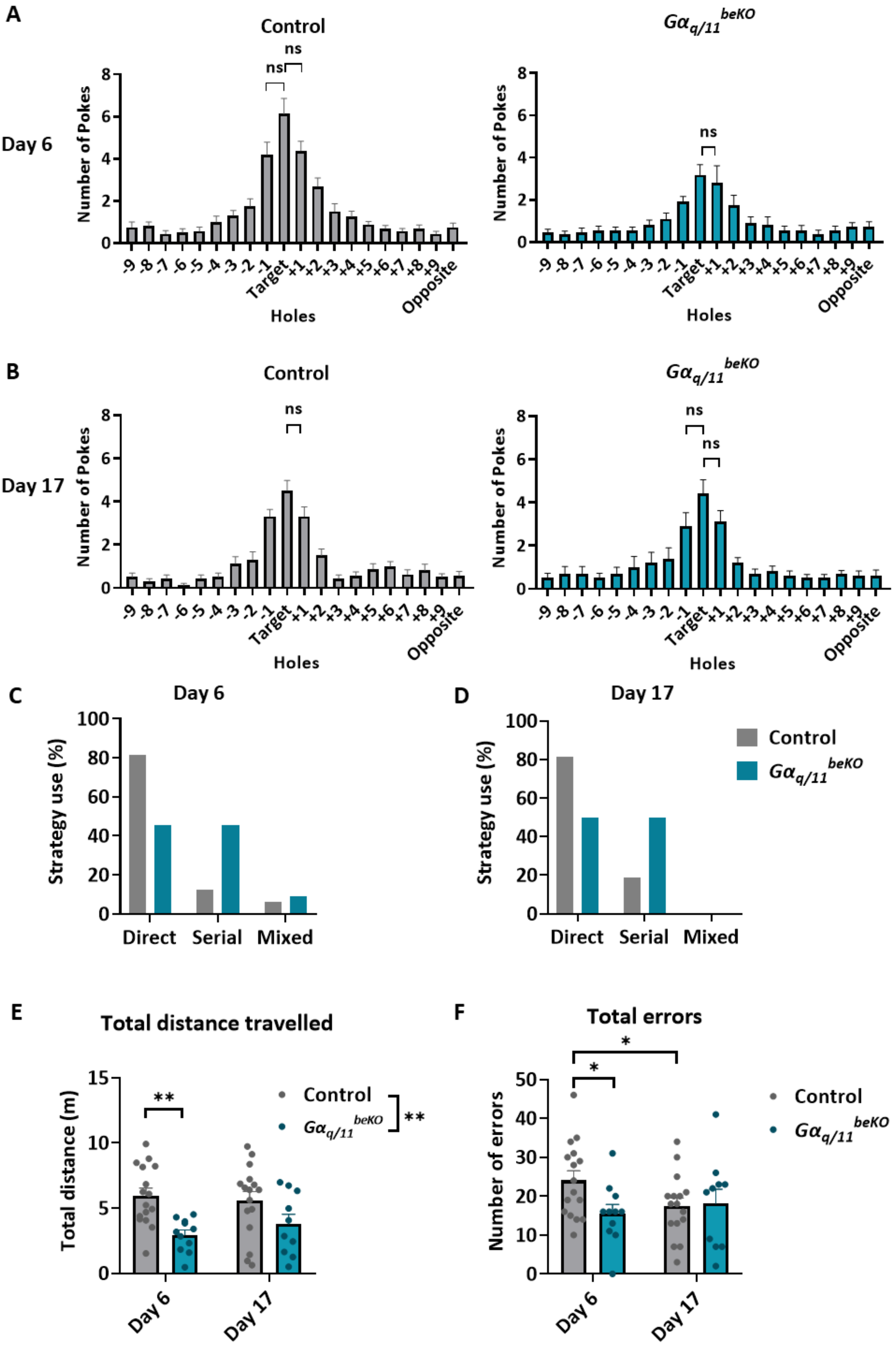

Supplementary Figure 3: Effect of Gα$_{q/11}$ on the exploratory behavior and strategy use during the probe trials in Barnes maze. A, B) Analysis of the number of pokes per hole and graphical depiction of the percent use of strategies (C,D) on days 6 and 17 of probe trials. Mice of both groups showed a significant preference for the target hole and its adjacent holes +1 and/or -1 on days 6 and 17. Data are shown as mean ± SEM. Statistical analysis student t-test of target hole against every other hole. Only non-significant differences (ns) are shown. N = 11-16 animals per group. **C,D)** Graphical depiction of the percent use of strategies on days 6 and 17 of probe trials. Control mice used mostly the direct strategy (around 80 %) on both probe trials while $G\alpha_{q/11}^{beKO}$ group used direct and serial strategy evenly (around 45 %) on both probe trials. **E, F)** Control and $G\alpha_{q/11}^{beKO}$ showed significant differences in the total distance traveled and the total number of errors during the probe trial day 6, indicating less explorative behavior in $G\alpha_{q/11}^{beKO}$ mice. Data are shown as mean ± SEM. Statistical analysis mixed-effects analysis for repeated measurements and a Sidak's posthoc test: Total distance: genotype [F(1, 25) = 8.382, $p = 0.0078$]; time [F(1, 24) = 0.5037, $p = 0.4847$]; time x genotype [F(1, 24) = 2.698, $p = 0.1135$]. Total errors: genotype F(1, 25) = 1.209, $p = 0.2819$; time F(1, 24) = 0.7733, $p = 0.3879$; time x genotype [F(1, 24) = 7.091, $p = 0.0136$]. N = 11-16 animals per group. * $p < 0.05$, ** $p < 0.01$. Abbreviations: $G\alpha_{q/11}$: G protein subunit alpha q/11, beKO: brain endothelial knockout.

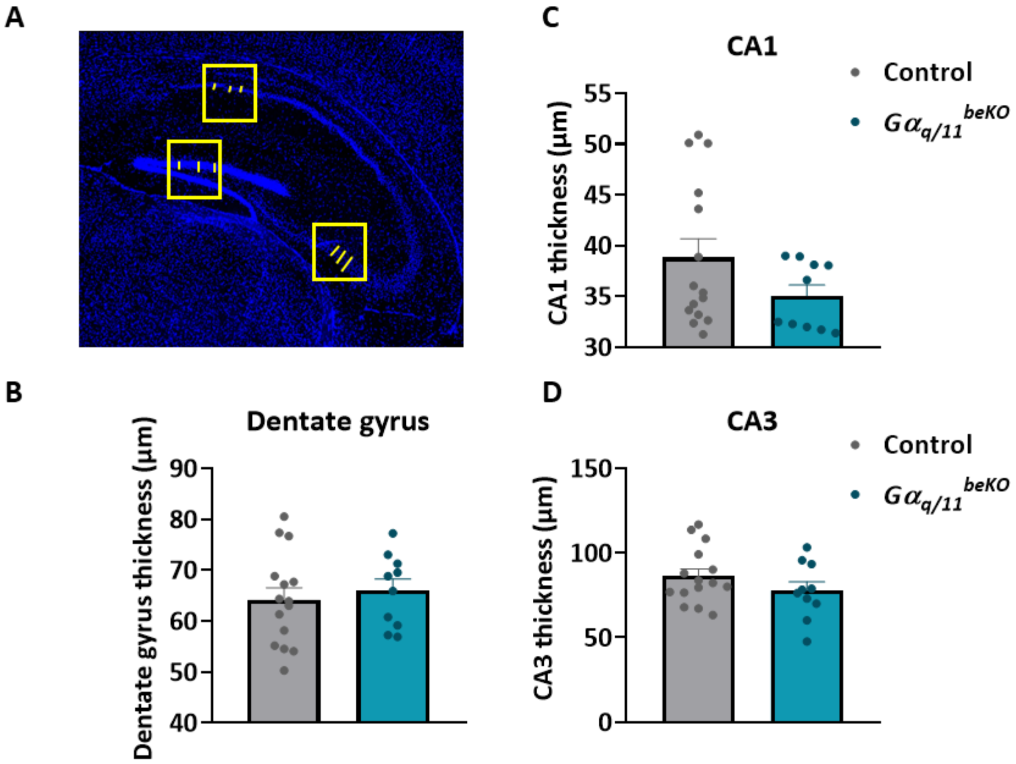

Supplementary Figure 4: $G\alpha_{q/11}^{beKO}$ mice show no differences in the thickness of CA1, CA3 and dentate gyrus regions of the hippocampus. A) *Representative fluorescence image of the hippocampus region showing the quantification of the thickness of the regions CA1, CA3 and dentate gyrus based on the visualization of stratum pyrimidale with the nuclear staining DAPI.* ***A-D)*** *Quantification of the thickness of every region based on the mean from 3 measurements per region. Data are shown as mean ± SEM. Statistical analysis: dentate gyrus unpaired t-test [t(23) = 0.5229, p = 0.606]; CA1 Mann-Whitney U-test (p = 0.2380); CA3 unpaired t-test [t(23) = 1.262, p = 0.2196]. N = 10-15 animals/group. Abbreviations: $G\alpha_{q/11}$: G protein subunit alpha q/11, beKO: brain endothelial knockout, CA: cornu ammonis.*

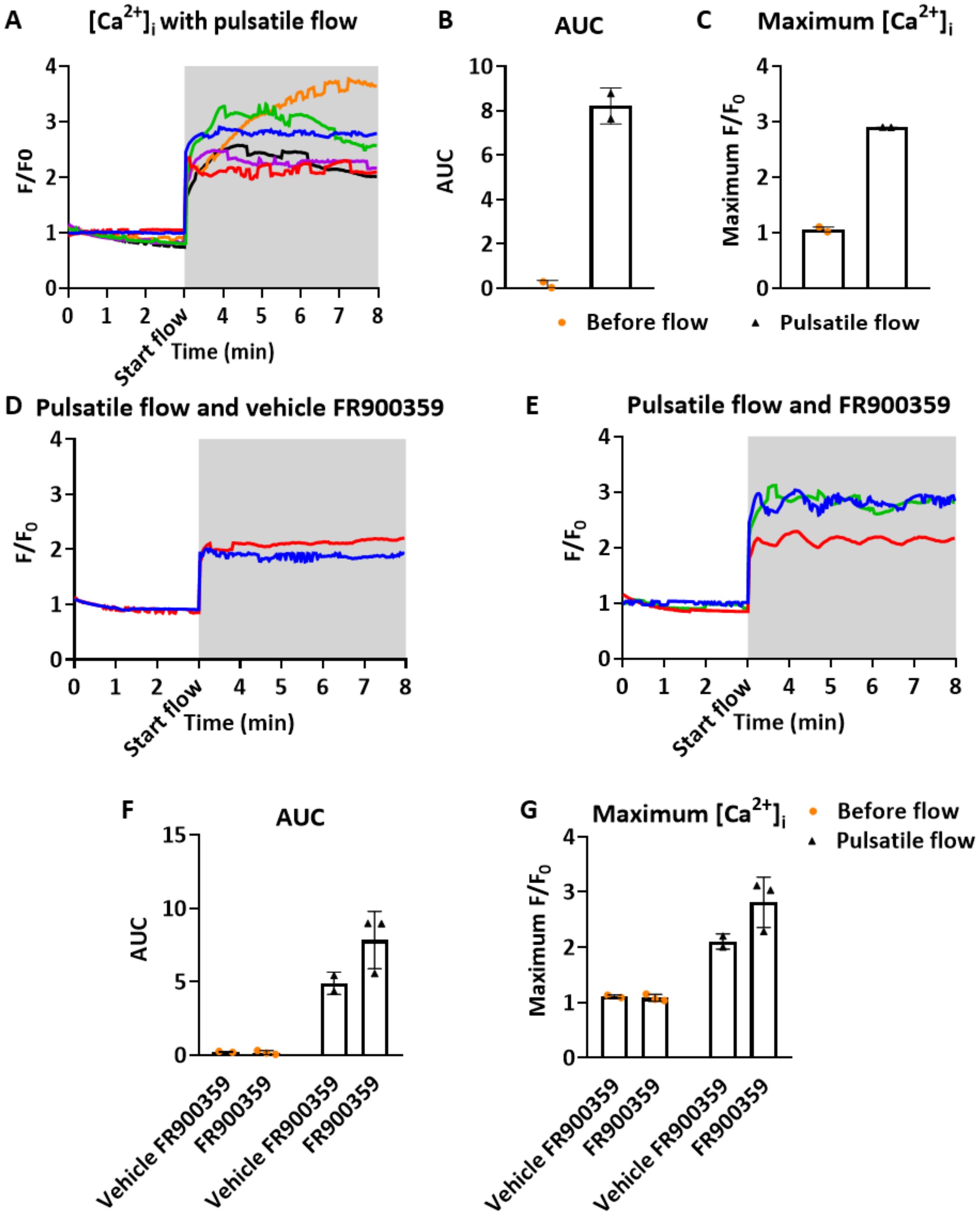

Supplementary Figure 5: Pulsatile flow leads to $[Ca^{2+}]_i$ increase independent of the $G\alpha_{q/11}$ signaling pathway. A) *Curves of the relative fluorescence of $[Ca^{2+}]_i$ signal of MPBECs expressing the calcium indicator GCaMP8 under pulsatile flow (1 Hz) at 1.7 dyn/cm^2. The curves were calculated from the whole field of view of time-lapse videos recorded with a 10x objective. Grey-shaded area indicates the application of shear stress.* ***B, C)*** *Quantification of the maximum relative fluorescence response (F/F_0) and the AUC before and after the application of pulsatile flow stress in MPBECs. Data are shown as mean ± SD from N = 2 independent experiments.* ***D, E)*** *Curves of the relative fluorescence of $[Ca^{2+}]_i$ signal of MPBECs isolated from Cdh5-GCaMP8 mice, treated with the inhibitor of the $G\alpha_{q/11}$ proteins (FR900359) and pulsatile flow (1 Hz) at 1.7 dyn/cm^2. The curves were calculated from the whole field of view of time-lapse videos recorded with a 10x objective.* ***F, G)*** *Quantification of the maximum relative F/F_0 and the AUC of the fluorescence curves shows no effect of the inhibitor FR900359. Data are shown as mean ± SD from N = 1 independent experiments. Relative fluorescence curves and their* *respective quantification of the intracellular calcium responses of MPBECs isolated from Cdh5-GCaMP8 mice under pulsatile (1 Hz) flow type at 1.7 dyn/cm^2. Grey shaded area indicates the application of shear stress. Data are shown as mean ± SEM.* ***D, F)*** *Relative fluorescence curves of the intracellular calcium responses of MPBECs isolated from Cdh5-GCaMP8 mice and treated with the inhibitor of the G$\alpha_{q/11}$ proteins FR900359 and pulsatile (1 Hz) type of flow at 1.7 dyn/cm^2.* ***F, G)*** *Quantification of the relative maximum F/F$_0$ and the AUC of the fluorescence curves points to the effect of the inhibitor FR900359. Data are shown as mean ± SD from N = 1 independent experiments. Abbreviations: [Ca^{2+}]$_i$: intracellular calcium, F: fluorescence intensity, AUC: area under the curve.*

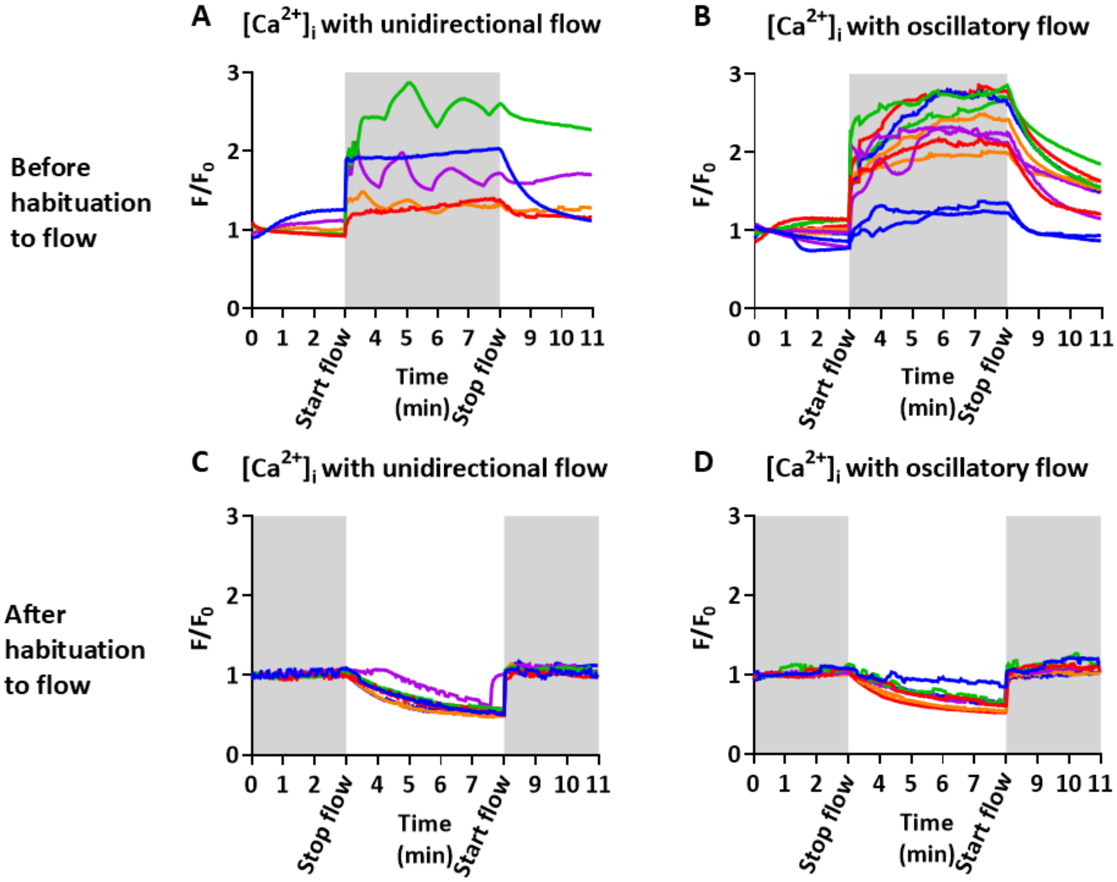

Supplementary Figure 6: Effect of shear stress on the [Ca^{2+}]$_i$ in MPBECs is reversible. A, B) Representative curves of the relative fluorescence response of MPBECs cultured under static conditions and stimulated with unidirectional and oscillatory (1 Hz) types of flow and shear stress at 1.7 dyn/cm^2. Stimulation with shear stress leads to an increase of [Ca^{2+}]$_i$ signal which gradually drops when the application of shear stress stops. Data from n = 2-8 measurements from N = 2 independent experiments. C, D) Representative curves of the relative fluorescence response of MPBECs cultured under shear stress 1.7 dyn/cm^2 and different flow conditions for 96 h. Short-term cessation of flow leads to a drop in [Ca^{2+}]$_i$ signal, which increases back to initial levels after the restoration of flow. Grey shade indicates flow treatment. Data from n = 3-4 measurements from N = 2 independent experiments. Abbreviations: F: fluorescence intensity.

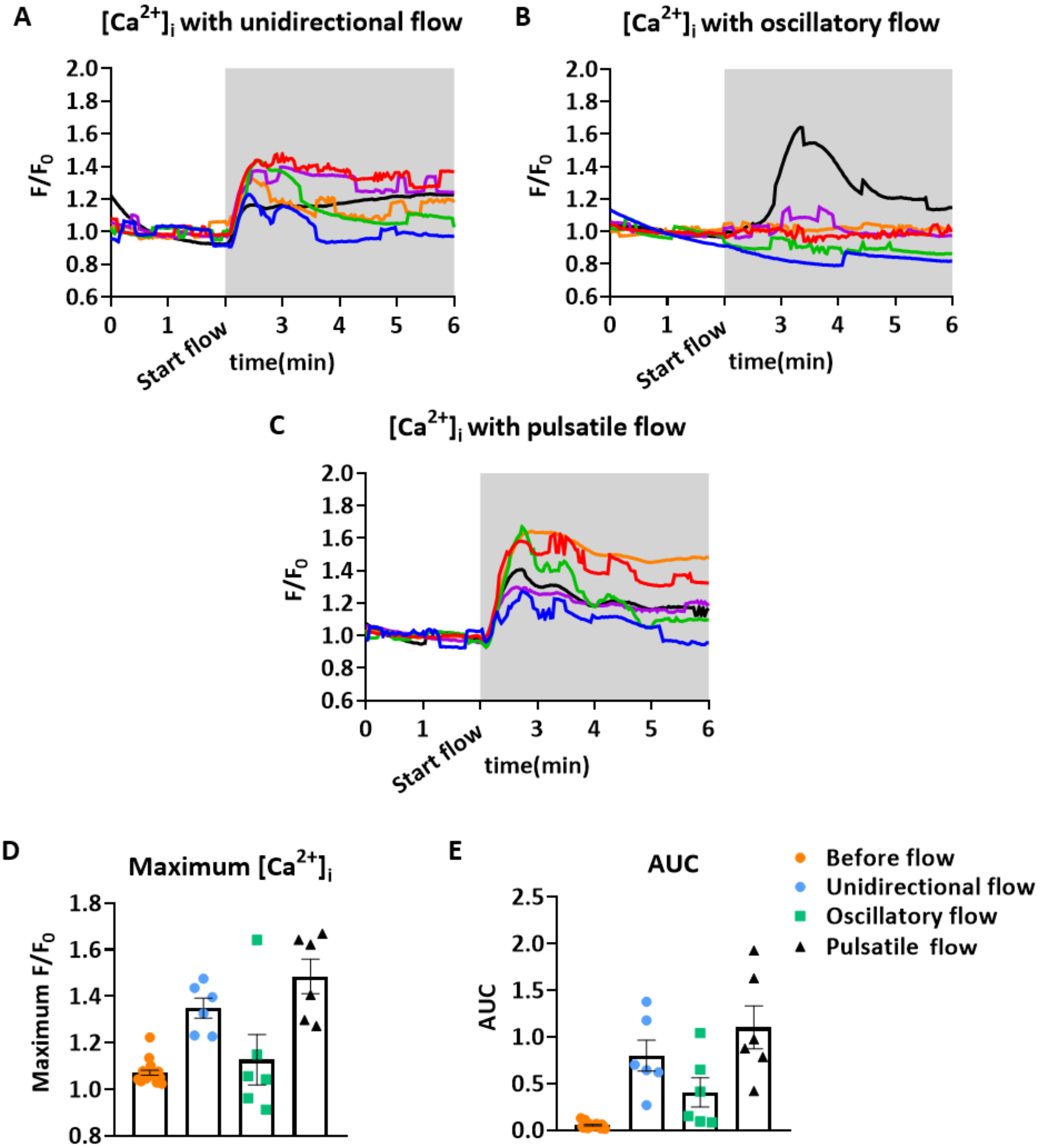

Supplementary Figure 7: Shear stress leads to $[Ca^{2+}]_i$ increase in hCMEC/D3 independent of the flow ***type.*** *Curves of the relative fluorescence of $[Ca^{2+}]_i$ signal of hCMEC/D3 cells stained with the calcium indicator Fluo-4 after stimulation with unidirectional, oscillatory (1 Hz) and pulsatile (1 Hz) type of flow and shear stress at 1.7 dyn/cm^2. The curves were calculated from the whole field of view of time-lapse videos recorded with a 10x objective. Grey-shaded area indicates the application of shear stress.* ***D, E)*** *Quantification of the maximum relative fluorescence response (F/F$_0$) and the AUC of the curves presented in graphs A-C point to shear stress induced $[Ca^{2+}]_i$ signals in hCMEC/D3. Data are shown as mean ± SD from 6 measurements from N = 1 experiment. Abbreviations: $[Ca^{2+}]_i$: intracellular calcium, F: fluorescence intensity, AUC: area under the curve.*

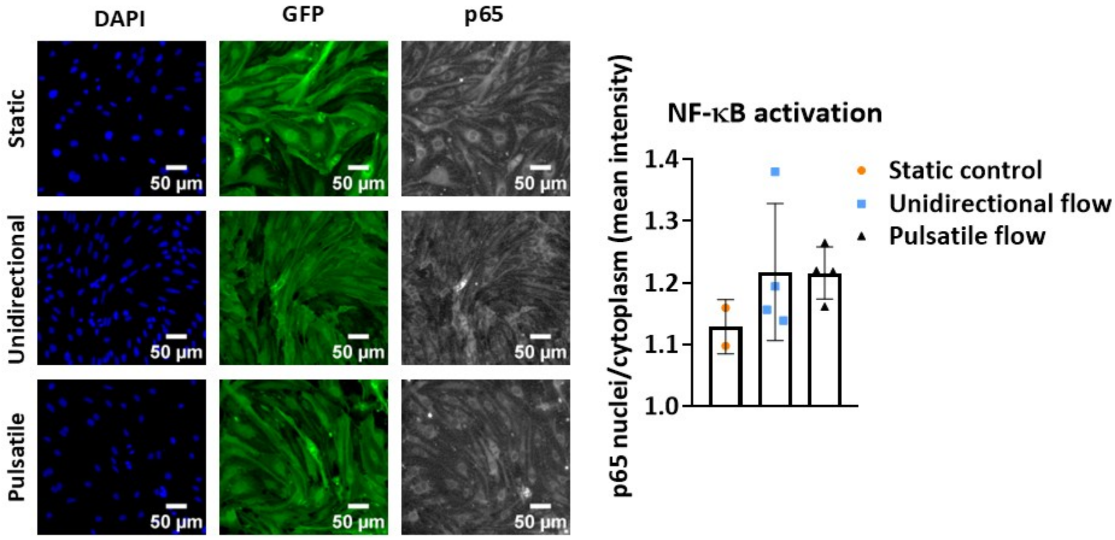

***Supplementary Figure 8: Effect of different types of shear stress on the activation of NF-κB pathway**. Left: Representative immunofluorescence images of MPBECs isolated from Cdh5-GCaMP8 mice showing immunoreactivity against the GFP protein and the p65 component of the NF-κB complex. DAPI was used for nuclei visualization. Cells were treated with unidirectional or pulsatile (1 Hz) types of flow at 1.7 dyn/cm^2 for 30 min before fixation. Cells not treated with shear stress served as static control. Right: Quantification of the relative mean intensity of p65 immunoreactivity in nuclei and cytoplasm to estimate the translocation of p65 and activation of the NF-κB pathway. Data are shown mean ± SD from N = 2 independent experiments. Abbreviations: DAPI: diamidino-2-phenylindole, GFP: green fluorescent protein, NF-κB: Nuclear factor "kappa-light-chain-enhancer" of activated B-cells, IL-1β: interleukin-1 beta.*

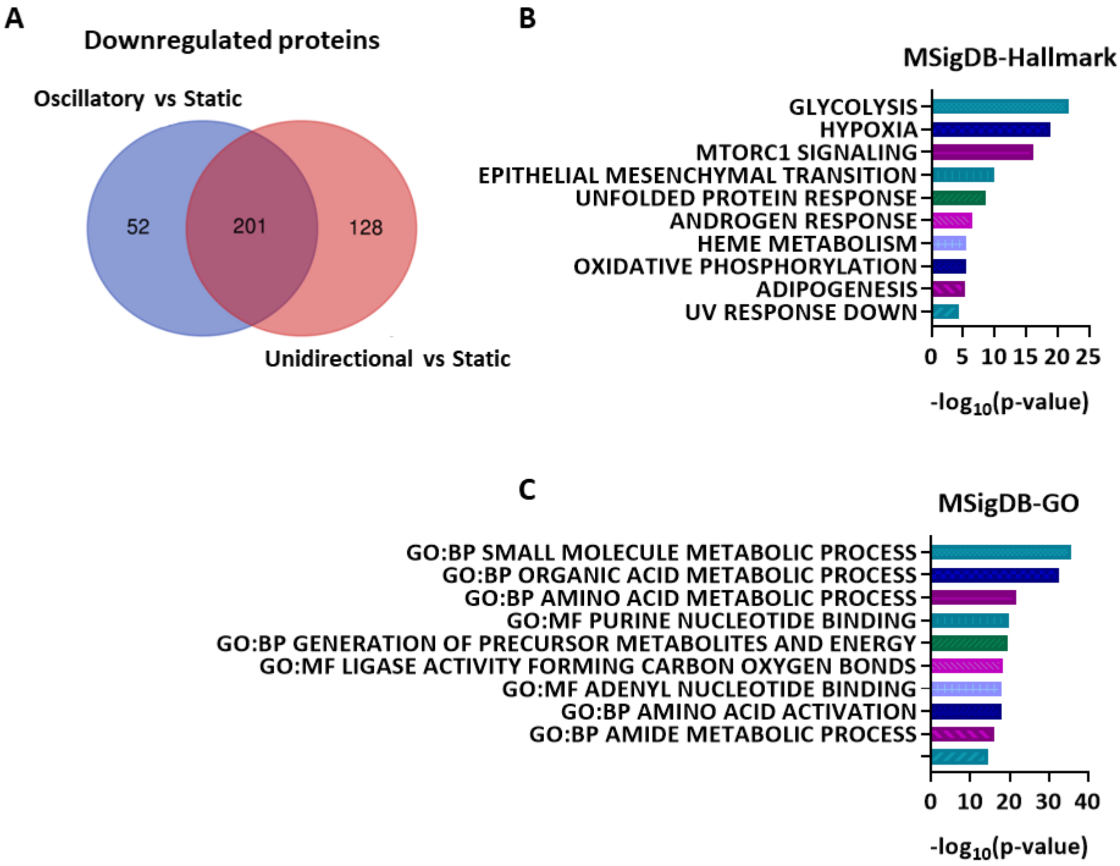

Supplementary Figure 9: Commonly downregulated proteins under flow from the whole proteome of MPBECs and pathway analysis. ***A)*** *Venn diagram depicting the number of shared downregulated proteins of the comparisons of oscillatory and unidirectional flow against static control from the whole cell lysate proteotyping.* ***B)*** *Graphical depiction of the top ten enriched biological processes based on the annotation of the shared downregulated proteins in flow conditions against static control using the MSigDB and the built-in mouse hallmark gene set.* ***C)*** *Graphical depiction of the top ten enriched GO terms based on the annotation of the shared downregulated proteins in flow conditions against static control using the MSigDB and the built-in mouse ontology gene set. Abbreviations: MTORC1: mammalian target of rapamycin complex 1, MsigDB: molecular signature database, GO: gene ontology, CC: cellular component, MF: molecular function, BP: biological process, FC: fold change.*

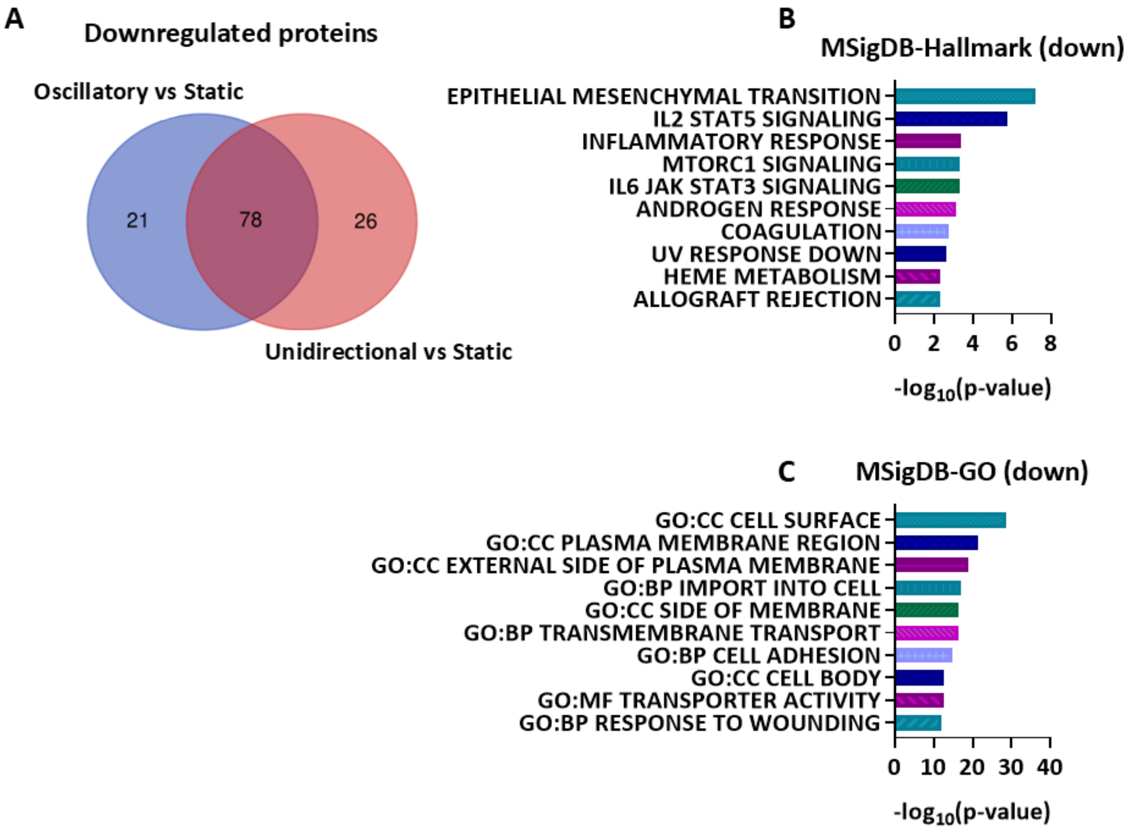

Supplementary Figure 10: Commonly downregulated proteins under flow from the cell surface proteome of MPBECs and pathway analysis. A) *Venn diagram depicting the number of shared downregulated proteins of the comparisons of oscillatory and unidirectional flow against static control from the cell surface proteotyping.* ***B)*** *Graphical depiction of the top ten enriched biological processes based on the annotation of the shared downregulated proteins in flow conditions against static control using the MSigDB and the built-in mouse hallmark gene set.* ***C)*** *Graphical depiction of the top ten enriched GO terms based on the annotation of the shared downregulated proteins in flow conditions against static control using the MSigDB and the built-in mouse ontology gene set. Abbreviations: IL (eg IL-2): interleukin, STAT (eg STAT5): signal transducer and activator of transcription , MTORC1: mammalian target of rapamycin complex 1, JAK: janus kinase. MsigDB: molecular signature database, GO: gene ontology, CC: cellular component, MF: molecular function, BP: biological process, FC: fold change.*

7 References

Abadier, M., Haghayegh Jahromi, N., Cardoso Alves, L., Boscacci, R., Vestweber, D., Barnum, S., Deutsch, U., Engelhardt, B., & Lyck, R. (2015). Cell surface levels of endothelial ICAM-1 influence the transcellular or paracellular T-cell diapedesis across the blood-brain barrier. *European Journal of Immunology*, *45*(4), 1043–1058. https://doi.org/10.1002/eji.201445125

Abernethy, W. B., Bell, M. A., Morris, M., & Moody, D. M. (1993). Microvascular density of the human paraventricular nucleus decreases with aging but not hypertension. *Experimental Neurology*, *121*(2), 270–274. https://doi.org/10.1006/exnr.1993.1095

Agasse, F., Mendez-David, I., Christaller, W., Carpentier, R., Braz, B. Y., David, D. J., Saudou, F., & Humbert, S. (2020). Chronic Corticosterone Elevation Suppresses Adult Hippocampal Neurogenesis by Hyperphosphorylating Huntingtin. *Cell Reports*, *32*(1). https://doi.org/10.1016/j.celrep.2020.107865

Aitken, C., Mehta, V., Schwartz, M. A., & Tzima, E. (2023). Mechanisms of endothelial flow sensing. In *Nature Cardiovascular Research* (Vol. 2, Issue 6, pp. 517–529). Nature Publishing Group. https://doi.org/10.1038/s44161-023-00276-0

Alarcon-Martinez, L., Villafranca-Baughman, D., Quintero, H., Kacerovsky, J. B., Dotigny, F., Murai, K. K., Prat, A., Drapeau, P., & Di Polo, A. (2020). Interpericyte tunnelling nanotubes regulate neurovascular coupling. *Nature*, *585*(7823), 91–95. https://doi.org/10.1038/s41586-020-2589-x

Albarrán-Juárez, J., Iring, A., Wang, S. P., Joseph, S., Grimm, M., Strilic, B., Wettschureck, N., Althoff, T. F., & Offermanns, S. (2018). Piezo1 and Gq/G11 promote endothelial inflammation depending on flow pattern and integrin activation. *Journal of Experimental Medicine*, *215*(10), 2655–2672. https://doi.org/10.1084/JEM.20180483

Ali, F., Zakkar, M., Karu, K., Lidington, E. A., Hamdulay, S. S., Boyle, J. J., Zloh, M., Bauer, A., Haskard, D. O., Evans, P. C., & Mason, J. C. (2009). Induction of the cytoprotective enzyme heme oxygenase-1 by statins is enhanced in vascular endothelium exposed to laminar shear stress and impaired by disturbed flow. *Journal of Biological Chemistry*, *284*(28), 18882–18892. https://doi.org/10.1074/jbc.M109.009886

Amenta, F., Cavallotti, D., Del Valle, M., Mancini, M., Naves, F. J., Vega, J., & Zeng, Y. C. (1995). Age-related changes in brain microanatomy: Sensitivity to treatment with the dihydropyridine calcium channel blocker darodipine (PY 108-068). *Brain Research Bulletin*, *36*(5), 453–460. https://doi.org/10.1016/0361-9230(94)00210-R

Ando, J., & Yamamoto, K. (2013). Flow detection and calcium signalling in vascular endothelial cells. In *Cardiovascular Research* (Vol. 99, Issue 2, pp. 260–268). https://doi.org/10.1093/cvr/cvt084

Arai, K., & Lo, E. H. (2009). An oligovascular niche: Cerebral endothelial cells promote the survival and proliferation of oligodendrocyte precursor cells. *Journal of Neuroscience*, *29*(14), 4351–4355. https://doi.org/10.1523/JNEUROSCI.0035-09.2009

Arias-Aragón, F., Tristán-Clavijo, E., Martínez-Gallego, I., Robles-Lanuza, E., Coatl-Cuaya, H., Martín-Cuevas, C., Sánchez-Hidalgo, A. C., Rodríguez-Moreno, A., Martinez-Mir, A., & Scholl, F. G. (2023). A Neuroligin-1 mutation associated with Alzheimer's disease produces memory and age-dependent impairments in hippocampal plasticity. *IScience*, *26*(6). https://doi.org/10.1016/j.isci.2023.106868

Arvanitakis, Z., Capuano, A. W., Leurgans, S. E., Bennett, D. A., & Schneider, J. A. (2016). Relation of cerebral vessel disease to Alzheimer's disease dementia and cognitive function in elderly people: a cross-sectional study. *The Lancet Neurology*, *15*(9), 934–943. https://doi.org/10.1016/S1474-4422(16)30029-1

Assini, F. L., Duzzioni, M., & Takahashi, R. N. (2009). Object location memory in mice: Pharmacological validation and further evidence of hippocampal CA1 participation. *Behavioural Brain Research*, *204*(1), 206–211. https://doi.org/10.1016/j.bbr.2009.06.005

Assmann, J., Müller, K., Wenzel, J., Walther, T., Brands, J., Thornton, P., Allan, S., & Schwaninger, M. (2017). Isolation and Cultivation of Primary Brain Endothelial Cells from Adult Mice. *BIO-PROTOCOL*, *7*(10). https://doi.org/10.21769/bioprotoc.2294

Aveleira, C. A., Lin, C. M., Abcouwer, S. F., Ambrósio, A. F., & Antonetti, D. A. (2010). TNF-α signals through PKCζ/NF-κB to alter the tight junction complex and increase retinal endothelial cell permeability. *Diabetes*, *59*(11), 2872–2882. https://doi.org/10.2337/db09-1606

Baeyens, N., Mulligan-Kehoe, M. J., Corti, F., Simon, D. D., Ross, T. D., Rhodes, J. M., Wang, T. Z., Mejean, C. O., Simons, M., Humphrey, J., & Schwartz, M. A. (2014). Syndecan 4 is required for endothelial alignment in flow and atheroprotective signaling. *Proceedings of the National Academy of Sciences of the United States of America*, *111*(48), 17308–17313. https://doi.org/10.1073/pnas.1413725111

Barnes, C. A., Nadel, L., & Honig, W. K. (1980). Spatial memory deficit in senescent rats. *Canadian Journal of Psychology*, *34*(1), 29–39. https://doi.org/10.1037/h0081022

Bell, R. D., Winkler, E. A., Sagare, A. P., Singh, I., LaRue, B., Deane, R., & Zlokovic, B. V. (2010). Pericytes Control Key Neurovascular Functions and Neuronal Phenotype in the Adult Brain and during Brain Aging. *Neuron*, *68*(3), 409–427. https://doi.org/10.1016/j.neuron.2010.09.043

Bell, R. D., Winkler, E. A., Singh, I., Sagare, A. P., Deane, R., Wu, Z., Holtzman, D. M., Betsholtz, C., Armulik, A., Sallstrom, J., Berk, B. C., & Zlokovic, B. V. (2012). Apolipoprotein E controls cerebrovascular integrity via cyclophilin A. *Nature*, *485*(7399), 512–516. https://doi.org/10.1038/nature11087

Ben-Zvi, A., Lacoste, B., Kur, E., Andreone, B. J., Mayshar, Y., Yan, H., & Gu, C. (2014). Mfsd2a is critical for the formation and function of the blood-brain barrier. *Nature*, *509*(7501), 507–511. https://doi.org/10.1038/nature13324

Benjamin, E. J., Virani, S. S., Callaway, C. W., Chamberlain, A. M., Chang, A. R., Cheng, S., Chiuve, S. E., Cushman, M., Delling, F. N., Deo, R., De Ferranti, S. D., Ferguson, J. F., Fornage, M., Gillespie, C., Isasi, C. R., Jiménez, M. C., Jordan, L. C., Judd, S. E., Lackland, D., … Muntner, P. (2018). Heart disease and stroke statistics - 2018 update: A report from the American Heart Association. *Circulation*, *137*(12), E67–E492. https://doi.org/10.1161/CIR.0000000000000558

Berthiaume, A. A., Schmid, F., Stamenkovic, S., Coelho-Santos, V., Nielson, C. D., Weber, B., Majesky, M. W., & Shih, A. Y. (2022). Pericyte remodeling is deficient in the aged brain and contributes to impaired capillary flow and structure. *Nature Communications*, *13*(1), 1–19. https://doi.org/10.1038/s41467-022-33464-w

Bichsel, C., & Bischoff, J. (2019). A somatic missense mutation in GNAQ causes capillary malformation. *Current Opinion in Hematology*, *26*(3), 179–184. https://doi.org/10.1097/MOH.0000000000000500

Binder, S., Baier, P. C., Mölle, M., Inostroza, M., Born, J., & Marshall, L. (2012). Sleep enhances memory consolidation in the hippocampus-dependent object-place recognition task in rats. *Neurobiology of Learning and Memory*, *97*(2), 213–219. https://doi.org/10.1016/j.nlm.2011.12.004

Binder, S., Mölle, M., Lippert, M., Bruder, R., Aksamaz, S., Ohl, F., Wiegert, J. S., & Marshall, L. (2019). Monosynaptic hippocampal-prefrontal projections contribute to spatial memory consolidation in mice. *Journal of Neuroscience*, *39*(35), 6978–6991. https://doi.org/10.1523/JNEUROSCI.2158-18.2019

Bouhrira, N., DeOre, B. J., & Galie, P. A. (2021). Implementation and characterization of a physiologically relevant flow waveform in a 3D microfluidic model of the blood–brain barrier. *Biotechnology and Bioengineering*, *118*(7), 2411–2421. https://doi.org/10.1002/bit.27719

Bouhrira, N., DeOre, B. J., Tran, K. A., & Galie, P. A. (2022). Transcriptomic analysis of a 3D blood–brain barrier model exposed to disturbed fluid flow. *Fluids and Barriers of the CNS*, *19*(1). https://doi.org/10.1186/s12987-022-00389-x

Brantley, D. M., Chen, C. L., Muraoka, R. S., Bushdid, P. B., Bradberry, J. L., Kittrell, F., Medina, D., Matrisian, L. M., Kerr, L. D., & Yull, F. E. (2001). Nuclear factor-κB (NF-κB) regulates proliferation and branching in mouse mammary epithelium. *Molecular Biology of the Cell*, *12*(5), 1445–1455. https://doi.org/10.1091/mbc.12.5.1445

Brito, D. V. C., Esteves, F., Rajado, A. T., Silva, N., Andrade, R., Apolónio, J., Calado, S., Faleiro, L., Matos, C., Marques, N., Marreiros, A., Nzwalo, H., Pais, S., Palmeirim, I., Roberto, V., Simão, S., Joaquim, N., Miranda, R., Pêgas, A., … Nóbrega, C. (2023). Assessing cognitive decline in the aging brain: lessons from rodent and human studies. In *NPJ Aging* (Vol. 9, Issue 1, pp. 1–11). Nature Publishing Group. https://doi.org/10.1038/s41514-023-00120-6

Brown, W. R. (2010). A review of string vessels or collapsed, empty basement membrane tubes. *Journal of Alzheimer's Disease*, *21*(3), 725–739. https://doi.org/10.3233/JAD-2010-100219

Bruunsgaard, H., Skinhøj, P., Pedersen, A. N., Schroll, M., & Pedersen, B. K. (2000). Ageing, tumour necrosis factor-alpha (TNF-α) and atherosclerosis. *Clinical and Experimental Immunology*, *121*(2), 255–260. https://doi.org/10.1046/j.1365-2249.2000.01281.x

Burke, S. N., & Barnes, C. A. (2006). Neural plasticity in the ageing brain. *Nature Reviews Neuroscience*, *7*(1), 30–40. https://doi.org/10.1038/nrn1809

Bush, T. G., Puvanachandra, N., Horner, C. H., Polito, A., Ostenfeld, T., Svendsen, C. N., Mucke, L., Johnson, M. H., & Sofroniew, M. V. (1999). Leukocyte infiltration, neuronal degeneration, and neurite outgrowth after ablation of scar-forming, reactive astrocytes in adult transgenic mice. *Neuron*, *23*(2), 297–308. https://doi.org/10.1016/S0896-6273(00)80781-3

Callegari, K., Dash, S., Uchida, H., Shingai, Y., Liu, C., Khodarkovskaya, A., Lee, Y., Ito, A., Lopez, A., Zhang, T., Xiang, J., Kluk, M. J., & Sanchez, T. (2023). Molecular profiling of the stroke-induced alterations in the cerebral microvasculature reveals promising therapeutic candidates. *Proceedings of the National Academy of Sciences of the United States of America*, *120*(16). https://doi.org/10.1073/pnas.2205786120

Carmeliet, P., Lampugnani, M. G., Moons, L., Breviario, F., Compernolle, V., Bono, F., Balconi, G., Spagnuolo, R., Oosthuyse, B., Dewerchin, M., Zanetti, A., Angellilo, A., Mattot, V., Nuyens, D., Lutgens, E., Clotman, F., De Ruiter, M. C., Groot, A. G. De, Poelmann, R., … Dejana, E. (1999). Targeted deficiency or cytosolic truncation of the VE-cadherin gene in mice impairs VEGF-mediated endothelial survival and angiogenesis. *Cell*, *98*(2), 147–157. https://doi.org/10.1016/S0092-8674(00)81010-7

Castanza, A. S., Recla, J. M., Eby, D., Thorvaldsdóttir, H., Bult, C. J., & Mesirov, J. P. (2023). Extending support for mouse data in the Molecular Signatures Database (MSigDB). In *Nature Methods* (Vol. 20, Issue 11, pp. 1619–1620). Nature Publishing Group. https://doi.org/10.1038/s41592-023-02014-7

Challa, V. R., Thore, C. R., Moody, D. M., Anstrom, J. A., & Brown, W. R. (2004). Increase of white matter string vessels in Alzheimer's disease. *Journal of Alzheimer's Disease*, *6*(4), 379–383. https://doi.org/10.3233/JAD-2004-6404

Challa, V. R., Thore, C. R., Moody, D. M., Brown, W. R., & Anstrom, J. A. (2002). A three-dimensional study of brain string vessels using celloidin sections stained with anti-collagen antibodies. *Journal of the Neurological Sciences*, *203–204*, 165–167. https://doi.org/10.1016/S0022-510X(02)00284-8

Chatzizisis, Y. S., Coskun, A. U., Jonas, M., Edelman, E. R., Feldman, C. L., & Stone, P. H. (2007). Role of Endothelial Shear Stress in the Natural History of Coronary Atherosclerosis and Vascular Remodeling. Molecular, Cellular, and Vascular Behavior. *Journal of the American College of Cardiology*, *49*(25), 2379–2393. https://doi.org/10.1016/j.jacc.2007.02.059

Cheng, C. P., Herfkens, R. J., & Taylor, C. A. (2003). Inferior vena caval hemodynamics quantified in vivo at rest and during cycling exercise using magnetic resonance imaging. *American Journal of Physiology - Heart and Circulatory Physiology*, *284*(4 53-4), 1161–1167. https://doi.org/10.1152/ajpheart.00641.2002

Choublier, N., Taghi, M., Menet, M. C., Le Gall, M., Bruce, J., Chafey, P., Guillonneau, F., Moreau, A., Denizot, C., Parmentier, Y., Nakib, S., Borderie, D., Bouzinba-Segard, H., Couraud, P. O., Bourdoulous, S., & Declèves, X. (2022). Exposure of human cerebral microvascular endothelial cells hCMEC/D3 to laminar shear stress induces vascular protective responses. *Fluids and Barriers of the CNS*, *19*(1). https://doi.org/10.1186/s12987-022-00344-w

Chuntharpursat-Bon, E., Povstyan, O. V., Ludlow, M. J., Carrier, D. J., Debant, M., Shi, J., Gaunt, H. J., Bauer, C. C., Curd, A., Simon Futers, T., Baxter, P. D., Peckham, M., Muench, S. P., Adamson, A., Humphreys, N., Tumova, S., Bon, R. S., Cubbon, R., Lichtenstein, L., & Beech, D. J. (2023). PIEZO1 and PECAM1 interact at cell-cell junctions and partner in endothelial force sensing. *Communications Biology*, *6*(1). https://doi.org/10.1038/s42003-023-04706-4

Cipolla, J. (2009). *The The Cerebral Cerebral Circulation Circulation*. Morgan et Claypool Life

Sciences. https://doi.org/10.4199/C00005ED1V01Y200912ISP002

Clarke, L. E., Liddelow, S. A., Chakraborty, C., Münch, A. E., Heiman, M., & Barres, B. A. (2018). Normal aging induces A1-like astrocyte reactivity. *Proceedings of the National Academy of Sciences of the United States of America*, *115*(8), E1896–E1905. https://doi.org/10.1073/pnas.1800165115

Coon, B. G., Baeyens, N., Han, J., Budatha, M., Ross, T. D., Fang, J. S., Yun, S., Thomas, J. L., & Schwartz, M. A. (2015). Intramembrane binding of VE-cadherin to VEGFR2 and VEGFR3 assembles the endothelial mechanosensory complex. *Journal of Cell Biology*, *208*(7), 975–986. https://doi.org/10.1083/JCB.201408103

Cooper, L. L., Woodard, T., Sigurdsson, S., Van Buchem, M. A., Torjesen, A. A., Inker, L. A., Aspelund, T., Eiriksdottir, G., Harris, T. B., Gudnason, V., Launer, L. J., & Mitchell, G. F. (2016). Cerebrovascular Damage Mediates Relations Between Aortic Stiffness and Memory. *Hypertension*, *67*(1), 176–182. https://doi.org/10.1161/HYPERTENSIONAHA.115.06398

Cortes-Canteli, M., & Iadecola, C. (2020). Alzheimer's Disease and Vascular Aging: JACC Focus Seminar. In *Journal of the American College of Cardiology* (Vol. 75, Issue 8, pp. 942–951). J Am Coll Cardiol. https://doi.org/10.1016/j.jacc.2019.10.062

Coste, B., Mathur, J., Schmidt, M., Earley, T. J., Ranade, S., Petrus, M. J., Dubin, A. E., & Patapoutian, A. (2010). Piezo1 and Piezo2 are essential components of distinct mechanically activated cation channels. *Science*, *330*(6000), 55–60. https://doi.org/10.1126/science.1193270

Csiszar, A., Tarantini, S., Fülöp, G. A., Kiss, T., Valcarcel-Ares, M. N., Galvan, V., Ungvari, Z., & Yabluchanskiy, A. (2017). Hypertension impairs neurovascular coupling and promotes microvascular injury: role in exacerbation of Alzheimer's disease. *GeroScience*, *39*(4), 359–372. https://doi.org/10.1007/s11357-017-9991-9

Cucullo, L., Hossain, M., Puvenna, V., Marchi, N., & Janigro, D. (2011). The role of shear stress in Blood-Brain Barrier endothelial physiology. *BMC Neuroscience*, *12*(1), 1–15. https://doi.org/10.1186/1471-2202-12-40

Cui, H., Wang, Y., Huang, H., Yu, W., Bai, M., Zhang, L., Bryan, B. A., Wang, Y., Luo, J., Li, D., Ma, Y., & Liu, M. (2014). GPR126 protein regulates developmental and pathological angiogenesis through modulation of VEGFR2 receptor signaling. *Journal of Biological Chemistry*, *289*(50), 34871–34885. https://doi.org/10.1074/jbc.M114.571000

Dajnowiec, D., & Langille, B. L. (2007). Arterial adaptations to chronic changes in haemodynamic function: Coupling vasomotor tone to structural remodelling. In *Clinical Science* (Vol. 113, Issues 1–2, pp. 15–23). Portland Press. https://doi.org/10.1042/CS20060337

Dalal, P. J., Sullivan, D. P., Weber, E. W., Sacks, D. B., Gunzer, M., Grumbach, I. M., Brown, J. H., & Muller, W. A. (2021). Spatiotemporal restriction of endothelial cell calcium signaling is required during leukocyte transmigration. *Journal of Experimental Medicine*, *218*(1). https://doi.org/10.1084/JEM.20192378

Damani, M. R., Zhao, L., Fontainhas, A. M., Amaral, J., Fariss, R. N., & Wong, W. T. (2011). Age-related alterations in the dynamic behavior of microglia. *Aging Cell*, *10*(2), 263–276. https://doi.org/10.1111/j.1474-9726.2010.00660.x

Daneman, R., & Prat, A. (2015). The blood–brain barrier. *Cold Spring Harbor Perspectives in Biology*, *7*(1). https://doi.org/10.1101/cshperspect.a020412

Daneman, R., Zhou, L., Agalliu, D., Cahoy, J. D., Kaushal, A., & Barres, B. A. (2010a). The mouse blood-brain barrier transcriptome: A new resource for understanding the development and function of brain endothelial cells. *PLoS ONE*, *5*(10), e13741. https://doi.org/10.1371/journal.pone.0013741

Daneman, R., Zhou, L., Kebede, A. A., & Barres, B. A. (2010b). Pericytes are required for blood-brain barrier integrity during embryogenesis. *Nature*, *468*(7323), 562–566. https://doi.org/10.1038/nature09513

Dere, E., Huston, J. P., & De Souza Silva, M. A. (2007). The pharmacology, neuroanatomy and neurogenetics of one-trial object recognition in rodents. In *Neuroscience and Biobehavioral Reviews* (Vol. 31, Issue 5, pp. 673–704). Pergamon. https://doi.org/10.1016/j.neubiorev.2007.01.005

Dessalles, C. A., Leclech, C., Castagnino, A., & Barakat, A. I. (2021). Integration of substrate- and flow-derived stresses in endothelial cell mechanobiology. In *Communications Biology* (Vol. 4, Issue 1). Nature Research. https://doi.org/10.1038/s42003-021-02285-w

DeStefano, J. G., Xu, Z. S., Williams, A. J., Yimam, N., & Searson, P. C. (2017). Effect of shear stress on iPSC-derived human brain microvascular endothelial cells (dhBMECs). *Fluids and Barriers of the CNS*, *14*(1). https://doi.org/10.1186/s12987-017-0068-z

Dutta, S., & Sengupta, P. (2016). Men and mice: Relating their ages. In *Life Sciences* (Vol. 152, pp. 244–248). Elsevier Inc. https://doi.org/10.1016/j.lfs.2015.10.025

Engelhardt, B., & Ransohoff, R. M. (2012). Capture, crawl, cross: The T cell code to breach the blood-brain barriers. In *Trends in Immunology* (Vol. 33, Issue 12, pp. 579–589). Elsevier. https://doi.org/10.1016/j.it.2012.07.004

Engelhardt, B., Vajkoczy, P., & Weller, R. O. (2017). The movers and shapers in immune privilege of the CNS. *Nature Immunology*, *18*(2), 123–131. https://doi.org/10.1038/ni.3666

Faraci, F. M., & Heistad, D. D. (1990). Regulation of large cerebral arteries and cerebral microsvascular pressure. In *Circulation Research* (Vol. 66, Issue 1, pp. 8–17). https://doi.org/10.1161/01.RES.66.1.8

Faraco, G., Hochrainer, K., Segarra, S. G., Schaeffer, S., Santisteban, M. M., Menon, A., Jiang, H., Holtzman, D. M., Anrather, J., & Iadecola, C. (2019). Dietary salt promotes cognitive impairment through tau phosphorylation. *Nature*, *574*(7780), 686–690. https://doi.org/10.1038/s41586-019-1688-z

Faraco, G., & Iadecola, C. (2013). Hypertension: A harbinger of stroke and dementia. In *Hypertension* (Vol. 62, Issue 5, pp. 810–817). https://doi.org/10.1161/HYPERTENSIONAHA.113.01063

Farrall, A. J., & Wardlaw, J. M. (2009). Blood-brain barrier: Ageing and microvascular disease - systematic review and meta-analysis. In *Neurobiology of Aging* (Vol. 30, Issue 3, pp. 337–352). Elsevier. https://doi.org/10.1016/j.neurobiolaging.2007.07.015

Fels, B., & Kusche-Vihrog, K. (2020). It takes more than two to tango: mechanosignaling of the endothelial surface. *Pflugers Archiv European Journal of Physiology*, *472*(4), 419–433. https://doi.org/10.1007/s00424-020-02369-2

Fischer, H., Gottschlich, R., & Seelig, A. (1998). Blood-brain barrier permeation: Molecular parameters governing passive diffusion. *Journal of Membrane Biology*, *165*(3), 201–211. https://doi.org/10.1007/s002329900434

Flurkey, K., Currer, J. M., & Harrison, D. E. (2007). Chapter 20 - Mouse Models in Aging Research. In *The Mouse in Biomedical Research* (Vol. 3, pp. 637–672). https://doi.org/10.1016/B978-012369454-6/50074-1

Forsberg, K. M. E., Zhang, Y., Reiners, J., Ander, M., Niedermayer, A., Fang, L., Neugebauer, H., Kassubek, J., Katona, I., Weis, J., Ludolph, A. C., Del Tredici, K., Braak, H., & Yilmazer-Hanke, D. (2018). Endothelial damage, vascular bagging and remodeling of the microvascular bed in human microangiopathy with deep white matter lesions. *Acta Neuropathologica Communications*, *6*(1), 128. https://doi.org/10.1186/s40478-018-0632-z

Förstermann, U., & Münzel, T. (2006). Endothelial nitric oxide synthase in vascular disease: From marvel to menace. In *Circulation* (Vol. 113, Issue 13, pp. 1708–1714). Lippincott Williams & Wilkins. https://doi.org/10.1161/CIRCULATIONAHA.105.602532

Frangos, J. A., Eskin, S. G., McIntire, L. V., & Ives, C. L. (1985). Flow effects on prostacyclin production by cultured human endothelial cells. *Science*, *227*(4693), 1477–1479. https://doi.org/10.1126/science.3883488

Frenkel-Denkberg, G., Gershon, D., & Levy, A. P. (1999). The function of hypoxia-inducible factor 1 (HIF-1) is impaired in senescent mice. *FEBS Letters*, *462*(3), 341–344. https://doi.org/10.1016/S0014-5793(99)01552-5

Frick, K. M., & Gresack, J. E. (2003). Sex Differences in the Behavioral Response to Spatial and Object Novelty in Adult C57BL/6 Mice. *Behavioral Neuroscience*, *117*(6), 1283–1291. https://doi.org/10.1037/0735-7044.117.6.1283

Garcia-Polite, F., Martorell, J., Del Rey-Puech, P., Melgar-Lesmes, P., O'Brien, C. C., Roquer, J., Ois, A., Principe, A., Edelman, E. R., & Balcells, M. (2017). Pulsatility and high shear stress deteriorate barrier phenotype in brain microvascular endothelium. *Journal of Cerebral Blood Flow and Metabolism*, *37*(7), 2614–2625. https://doi.org/10.1177/0271678X16672482

Garrido-Urbani, S., Bradfield, P. F., & Imhof, B. A. (2014). Tight junction dynamics: The role of junctional adhesion molecules (JAMs). In *Cell and Tissue Research* (Vol. 355, Issue 3, pp. 701–715). Springer Verlag. https://doi.org/10.1007/s00441-014-1820-1

Garrido, P., de Blas, M., del Arco, A., Segovia, G., & Mora, F. (2012). Aging increases basal but not stress-induced levels of corticosterone in the brain of the awake rat. *Neurobiology of Aging*, *33*(2), 375–382. https://doi.org/10.1016/j.neurobiolaging.2010.02.015

Gibbs, E. L., Lennox, W. G., Nims, L. F., & Gibbs, F. A. (1942). ARTERIAL AND CEREBRAL VENOUS BLOOD. *Journal of Biological Chemistry*, *144*(2), 325–332. https://doi.org/10.1016/s0021-9258(18)72512-x

Gottesman, R. F., Albert, M. S., Alonso, A., Coker, L. H., Coresh, J., Davis, S. M., Deal, J. A., McKhann, G. M., Mosley, T. H., Sharrett, A. R., Schneider, A. L. C., Windham, B. G., Wruck, L. M., & Knopman, D. S. (2017). Associations between midlife vascular risk factors and 25-year incident dementia in the Atherosclerosis Risk in Communities (ARIC) cohort. *JAMA Neurology*, *74*(10), 1246–1254. https://doi.org/10.1001/jamaneurol.2017.1658

Gould, I. G., Tsai, P., Kleinfeld, D., & Linninger, A. (2017). The capillary bed offers the largest hemodynamic resistance to the cortical blood supply. *Journal of Cerebral Blood Flow and Metabolism*, *37*(1), 52–68. https://doi.org/10.1177/0271678X16671146

Gresack, J. E., Kerr, K. M., & Frick, K. M. (2007). Life-long environmental enrichment differentially affects the mnemonic response to estrogen in young, middle-aged, and aged female mice.

Neurobiology of Learning and Memory, *88*(4), 393–408. https://doi.org/10.1016/j.nlm.2007.07.015

Grunewald, M., Kumar, S., Sharife, H., Volinsky, E., Gileles-Hillel, A., Licht, T., Permyakova, A., Hinden, L., Azar, S., Friedmann, Y., Kupetz, P., Tzuberi, R., Anisimov, A., Alitalo, K., Horwitz, M., Leebhoff, S., Khoma, O. Z., Hlushchuk, R., Djonov, V., … Keshet, E. (2021). Counteracting age-related VEGF signaling insufficiency promotes healthy aging and extends life span. *Science*, *373*(6554). https://doi.org/10.1126/science.abc8479

Guérit, S., Fidan, E., Macas, J., Czupalla, C. J., Figueiredo, R., Vijikumar, A., Hasan Yalcin, B., Thom, S., Winter, P., Gerhardt, H., Devraj, K., Liebner, S., Yalcin, B. H., Thom, S., Winter, P., Gerhardt, H., Devraj, K., & Liebner, S. (2021). Astrocyte-derived Wnt growth factors are required for endothelial blood-brain barrier maintenance. *Progress in Neurobiology*, *199*, 101937. https://doi.org/10.1016/j.pneurobio.2020.101937

Guerra, G., Lucariello, A., Perna, A., Botta, L., De Luca, A., & Moccia, F. (2018). The role of endothelial Ca2+ signaling in neurovascular coupling: A view from the lumen. *International Journal of Molecular Sciences*, *19*(4). https://doi.org/10.3390/ijms19040938

Hall, C. N., Reynell, C., Gesslein, B., Hamilton, N. B., Mishra, A., Sutherland, B. A., Oâ Farrell, F. M., Buchan, A. M., Lauritzen, M., & Attwell, D. (2014). Capillary pericytes regulate cerebral blood flow in health and disease. *Nature*, *508*(1), 55–60. https://doi.org/10.1038/nature13165

Hammer, J. (2024). *Spatially Resolved Surfaceome Analysis using Light-activated Lipid-anchored Probes*. ETH Zurich DISS. ETH NO. 30247.

Hamminger, P., Marchetti, L., Preglej, T., Platzer, R., Zhu, C., Kamnev, A., Rica, R., Stolz, V., Sandner, L., Alteneder, M., Kaba, E., Waltenberger, D., Huppa, J. B., Trauner, M., Bock, C., Lyck, R., Bauer, J., Dupré, L., Seiser, C., … Ellmeier, W. (2021). Histone deacetylase 1 controls CD4+ T cell trafficking in autoinflammatory diseases. *Journal of Autoimmunity*, *119*. https://doi.org/10.1016/j.jaut.2021.102610

Harraz, O. F., Klug, N. R., Senatore, A. J., Hill-Eubanks, D. C., & Nelson, M. T. (2022). Piezo1 Is a Mechanosensor Channel in Central Nervous System Capillaries. *Circulation Research*, *130*(10), 1531–1546. https://doi.org/10.1161/CIRCRESAHA.122.320827

Harrison, F. E., Reiserer, R. S., Tomarken, A. J., & McDonald, M. P. (2006). Spatial and nonspatial escape strategies in the Barnes maze. *Learning and Memory*, *13*(6), 809–819. https://doi.org/10.1101/lm.334306

Hartmann, D. A., Berthiaume, A. A., Grant, R. I., Harrill, S. A., Koski, T., Tieu, T., McDowell, K. P., Faino, A. V., Kelly, A. L., & Shih, A. Y. (2021). Brain capillary pericytes exert a substantial but slow influence on blood flow. *Nature Neuroscience*, *24*(5), 633–645. https://doi.org/10.1038/s41593-020-00793-2

Hayakawa, K., Pham, L. D. D., Som, A. T., Lee, B. J., Guo, S., Lo, E. H., & Arai, K. (2011a). Vascular endothelial growth factor regulates the migration of oligodendrocyte precursor cells. *Journal of Neuroscience*, *31*(29), 10666–10670. https://doi.org/10.1523/JNEUROSCI.1944-11.2011

Hayakawa, K., Tatsumi, H., & Sokabe, M. (2011b). Actin filaments function as a tension sensor by tension-dependent binding of cofilin to the filament. *Journal of Cell Biology*, *195*(5), 721–727. https://doi.org/10.1083/jcb.201102039

Hayden, M. S., & Ghosh, S. (2011). NF-κB in immunobiology. In *Cell Research* (Vol. 21, Issue 2, pp. 223–244). Cell Res. https://doi.org/10.1038/cr.2011.13

Herrmann, O., Baumann, B., De Lorenzi, R., Muhammad, S., Zhang, W., Kleesiek, J., Malfertheiner, M., Köhrmann, M., Potrovita, I., Maegele, I., Beyer, C., Burke, J. R., Hasan, M. T., Bujard, H., Wirth, T., Pasparakis, M., & Schwaninger, M. (2005). IKK mediates ischemia-induced neuronal death. *Nature Medicine*, *11*(12), 1322–1329. https://doi.org/10.1038/nm1323

Hillman, E. M. C. (2014). Coupling mechanism and significance of the BOLD signal: A status report. In *Annual Review of Neuroscience* (Vol. 37, Issue Volume 37, 2014, pp. 161–181). Annual Reviews Inc. https://doi.org/10.1146/annurev-neuro-071013-014111

Hollander, W., Prusty, S., Kemper, T., Rosene, D. L., & Moss, M. B. (1993). The effects of hypertension on cerebral atherosclerosis in the cynomolgus monkey. *Stroke*, *24*(8), 1218–1226. https://doi.org/10.1161/01.STR.24.8.1218

Huang, Y. T., Hong, F. F., & Yang, S. L. (2021). Atherosclerosis: The Culprit and Co-victim of Vascular Dementia. In *Frontiers in Neuroscience* (Vol. 15, p. 673440). Frontiers Media S.A. https://doi.org/10.3389/fnins.2021.673440

Iadecola, C., & Gottesman, R. F. (2019). Neurovascular and Cognitive Dysfunction in Hypertension: Epidemiology, Pathobiology, and Treatment. *Circulation Research*, *124*(7), 1025–1044. https://doi.org/10.1161/CIRCRESAHA.118.313260

Ibanez, K. R., McFarland, K. N., Phillips, J., Allen, M., Lessard, C. B., Zobel, L., De La Cruz, E. G., Shah, S., Vo, Q., Wang, X., Quicksall, Z., Ryu, D., Funk, C., Ertekin-Taner, N., Prokop, S., Golde, T. E., & Chakrabarty, P. (2022). Deletion of Abi3/Gngt2 influences age-progressive amyloid β and tau pathologies in distinctive ways. *Alzheimer’s Research and Therapy*, *14*(1). https://doi.org/10.1186/s13195-022-01044-1

Ighodaro, E. T., Abner, E. L., Fardo, D. W., Lin, A. L., Katsumata, Y., Schmitt, F. A., Kryscio, R. J., Jicha, G. A., Neltner, J. H., Monsell, S. E., Kukull, W. A., Moser, D. K., Appiah, F., Bachstetter, A. D., Van Eldik, L. J., & Nelson, P. T. (2017). Risk factors and global cognitive status related to brain arteriolosclerosis in elderly individuals. *Journal of Cerebral Blood Flow and Metabolism*, *37*(1), 201–216. https://doi.org/10.1177/0271678X15621574

Isberg, V., Mordalski, S., Munk, C., Rataj, K., Harpsøe, K., Hauser, A. S., Vroling, B., Bojarski, A. J., Vriend, G., & Gloriam, D. E. (2016). GPCRdb: An information system for G protein-coupled receptors. *Nucleic Acids Research*, *44*(D1), D356–D364. https://doi.org/10.1093/nar/gkv1178

Isermann, B., Hendrickson, S. B., Zogg, M., Wing, M., Cummiskey, M., Kisanuki, Y. Y., Yanagisawa, M., & Weiler, H. (2001). Endothelium-specific loss of murine thrombomodulin disrupts the protein C anticoagulant pathway and causes juvenile-onset thrombosis. *Journal of Clinical Investigation*, *108*(4). https://doi.org/10.1172/JCI13077

Itoh, M., Furuse, M., Morita, K., Kubota, K., Saitou, M., & Tsukita, S. (1999). Direct binding of three tight junction-associated MAGUKs, ZO-1, ZO-2, and ZO-3, with the COOH termini of claudins. *Journal of Cell Biology*, *147*(6), 1351–1363. https://doi.org/10.1083/jcb.147.6.1351

Jefferson, A. L., Cambronero, F. E., Liu, D., Moore, E. E., Neal, J. E., Terry, J. G., Nair, S., Pechman, K. R., Rane, S., Davis, L. T., Gifford, K. A., Hohman, T. J., Bell, S. P., Wang, T. J., Beckman, J. A., & Carr, J. J. (2018). Higher aortic stiffness is related to lower cerebral blood flow and preserved cerebrovascular reactivity in older adults. *Circulation*, *138*(18), 1951–1962. https://doi.org/10.1161/CIRCULATIONAHA.118.032410

Jennings, J. R., Muldoon, M. F., Ryan, C., Price, J. C., Greer, P., Sutton-Tyrrell, K., Van Der Veen, F. M., & Meltzer, C. C. (2005). Reduced cerebral blood flow response and compensation among patients with untreated hypertension. *Neurology*, *64*(8), 1358–1365. https://doi.org/10.1212/01.WNL.0000158283.28251.3C

Jiang, Y., Müller, K., Khan, M. A., Assmann, J. C., Lampe, J., Kilau, K., Richter, M., Kleint, M., Ridder, D. A., Hübner, N., Schmidt-Supprian, M., Wenzel, J., & Schwaninger, M. (2021). Cerebral angiogenesis ameliorates pathological disorders in Nemo-deficient mice with small-vessel disease. *Journal of Cerebral Blood Flow and Metabolism*, *41*(2), 219–235. https://doi.org/10.1177/0271678X20910522

Jin, K., Zhu, Y., Sun, Y., Mao, X. O., Xie, L., & Greenberg, D. A. (2002). Vascular endothelial growth factor (VEGF) stimulates neurogenesis in vitro and in vivo. *Proceedings of the National Academy of Sciences of the United States of America*, *99*(18), 11946–11950. https://doi.org/10.1073/pnas.182296499

Joannides, R., Haefeli, W. E., Linder, L., Richard, V., Bakkali, E. H., Thuillez, C., & Lüscher, T. F. (1995). Nitric oxide is responsible for flow-dependent dilatation of human peripheral conduit arteries in vivo. *Circulation*, *91*(5), 1314–1319. https://doi.org/10.1161/01.CIR.91.5.1314

Jong Lee, H., & Young Koh, G. (2003). Shear stress activates Tie2 receptor tyrosine kinase in human endothelial cells. *Biochemical and Biophysical Research Communications*, *304*(2), 399–404. https://doi.org/10.1016/S0006-291X(03)00592-8

Kadry, H., Noorani, B., & Cucullo, L. (2020). A blood–brain barrier overview on structure, function, impairment, and biomarkers of integrity. *Fluids and Barriers of the CNS*, *17*(1), 1–24. https://doi.org/10.1186/s12987-020-00230-3

Kamba, T., Tam, B. Y. Y., Hashizume, H., Haskell, A., Sennino, B., Mancuso, M. R., Norberg, S. M., O'Brien, S. M., Davis, R. B., Gowen, L. C., Anderson, K. D., Thurston, G., Joho, S., Springer, M. L., Kuo, C. J., & McDonald, D. M. (2006). VEGF-dependent plasticity of fenestrated capillaries in the normal adult microvasculature. *American Journal of Physiology - Heart and Circulatory Physiology*, *290*(2), 560–576. https://doi.org/10.1152/ajpheart.00133.2005

Kamiya, A., & Togawa, T. (1980). Adaptive regulation of wall shear stress to flow change in the canine carotid artery. *American Journal of Physiology - Heart and Circulatory Physiology*, *8*(1), 14–21. https://doi.org/10.1152/ajpheart.1980.239.1.h14

Karin, M., & Delhase, M. (2000). The I kappa B kinase (IKK) and NF-kappa B: Key elements of proinflammatory signalling. *Seminars in Immunology*, *12*(1), 85–98. https://doi.org/10.1006/smim.2000.0210

Kety, S. S. (1957). THE GENERAL METABOLISM OF THE BRAIN IN VIVO. In *Metabolism of the Nervous System* (pp. 221–237). Pergamon. https://doi.org/10.1016/B978-0-08-009062-7.50026-6

Kim, E. C., Zhang, J., Tang, A. Y., Bolton, E. C., Rhodes, J. S., Christian-Hinman, C. A., & Chung, H. J. (2021). Spontaneous seizure and memory loss in mice expressing an epileptic encephalopathy variant in the calmodulin-binding domain of Kv7.2. *Proceedings of the National Academy of Sciences of the United States of America*, *118*(51). https://doi.org/10.1073/pnas.2021265118

Kitamura, T., Ogawa, S. K., Roy, D. S., Okuyama, T., Morrissey, M. D., Smith, L. M., Redondo, R. L., & Tonegawa, S. (2017). Engrams and circuits crucial for systems consolidation of a memory. *Science*, *356*(6333), 73–78. https://doi.org/10.1126/science.aam6808

Kivipelto, M., Helkala, E. L., Laakso, M. P., Hänninen, T., Hallikainen, M., Alhainen, K., Soininen, H., Tuomilehto, J., & Nissien, A. (2001). Midlife vascular risk factors and Alzheimer's disease in later life: Longitudinal, population based study. *British Medical Journal*, *322*(7300), 1447–

1451. https://doi.org/10.1136/bmj.322.7300.1447

Kohner, E. M., & Henkind, P. (1970). Correlation of fluorescein angiogram and retinal digest in diabetic retinopathy. *American Journal of Ophthalmology*, *69*(3), 403–414. https://doi.org/10.1016/0002-9394(70)92273-7

Koutsiaris, A. G., Tachmitzi, S. V., & Batis, N. (2013). Wall shear stress quantification in the human conjunctival pre-capillary arterioles in vivo. *Microvascular Research*, *85*(1), 34–39. https://doi.org/10.1016/j.mvr.2012.11.003

Koutsiaris, A. G., Tachmitzi, S. V., Batis, N., Kotoula, M. G., Karabatsas, C. H., Tsironi, E., & Chatzoulis, D. Z. (2007). Volume flow and wall shear stress quantification in the human conjunctival capillaries and post-capillary venules in vivo. In *Biorheology* (Vol. 44, Issues 5–6, pp. 375–386).

Krizanac-Bengez, L., Kapural, M., Parkinson, F., Cucullo, L., Hossain, M., Mayberg, M. R., & Janigro, D. (2003). Effects of transient loss of shear stress on blood-brain barrier endothelium: Role of nitric oxide and IL-6. *Brain Research*, *977*(2), 239–246. https://doi.org/10.1016/S0006-8993(03)02689-1

Krizanac-Bengez, L., Mayberg, M. R., Cunningham, E., Hossain, M., Ponnampalam, S., Parkinson, F. E., & Janigro, D. (2006). Loss of shear stress induces leukocyte-mediated cytokine release and blood-brain barrier failure in dynamic in vitro blood-brain barrier model. *Journal of Cellular Physiology*, *206*(1), 68–77. https://doi.org/10.1002/jcp.20429

Ku, D. N., Giddens, D. P., Zarins, C. K., & Glagov, S. (1985). Pulsatile flow and atherosclerosis in the human carotid bifurcation. Positive correlation between plaque location and low oscillating shear stress. *Arteriosclerosis*, *5*(3), 293–302. https://doi.org/10.1161/01.atv.5.3.293

Kubotera, H., Ikeshima-Kataoka, H., Hatashita, Y., Allegra Mascaro, A. L., Pavone, F. S., & Inoue, T. (2019). Astrocytic endfeet re-cover blood vessels after removal by laser ablation. *Scientific Reports*, *9*(1), 1–10. https://doi.org/10.1038/s41598-018-37419-4

Lamagna, C., Meda, P., Mandicourt, G., Brown, J., Gilbert, R. J. C., Jones, E. Y., Kiefer, F., Ruga, P., Imhof, B. A., & Aurrand-Lions, M. (2005). Dual interaction of JAM-C with JAM-B and αMβ2 Integrin: Function in junctional complexes and leukocyte adhesion. *Molecular Biology of the Cell*, *16*(10), 4992–5003. https://doi.org/10.1091/mbc.E05-04-0310

Lee, F. K., Lee, J. C., Shui, B., Reining, S., Jibilian, M., Small, D. M., Jones, J. S., Allan-Rahill, N. H., Lamont, M. R. E., Rizzo, M. A., Tajada, S., Navedo, M. F., Santana, L. F., Nishimura, N., & Kotlikoff, M. I. (2021). Genetically engineered mice for combinatorial cardiovascular optobiology. *ELife*, *10*. https://doi.org/10.7554/eLife.67858

Li, J., Hou, B., Tumova, S., Muraki, K., Bruns, A., Ludlow, M. J., Sedo, A., Hyman, A. J., McKeown, L., Young, R. S., Yuldasheva, N. Y., Majeed, Y., Wilson, L. A., Rode, B., Bailey, M. A., Kim, H. R., Fu, Z., Carter, D. A. L., Bilton, J., … Beech, D. J. (2014). Piezo1 integration of vascular architecture with physiological force. *Nature*, *515*(7526), 279–282. https://doi.org/10.1038/nature13701

Liberzon, A., Subramanian, A., Pinchback, R., Thorvaldsdóttir, H., Tamayo, P., & Mesirov, J. P. (2011). Molecular signatures database (MSigDB) 3.0. *Bioinformatics*, *27*(12), 1739–1740. https://doi.org/10.1093/bioinformatics/btr260

Licht, T., Eavri, R., Goshen, I., Shlomai, Y., Mizrahi, A., & Keshet, E. (2010). VEGF is required for dendritogenesis of newly born olfactory bulb interneurons. *Development*, *137*(2), 261–271. https://doi.org/https://doi.org/10.1242/dev.039636

Lilienbaum, A., & Israël, A. (2003). From Calcium to NF-κB Signaling Pathways in Neurons. *Molecular and Cellular Biology*, *23*(8), 2680–2698. https://doi.org/10.1128/mcb.23.8.2680-2698.2003

Lin, Q., Zhao, L., Jing, R., Trexler, C., Wang, H., Li, Y., Tang, H., Huang, F., Zhang, F., Fang, X., Liu, J., Jia, N., Chen, J., & Ouyang, K. (2019). Inositol 1,4,5-Trisphosphate receptors in endothelial cells play an essential role in vasodilation and blood pressure regulation. *Journal of the American Heart Association*, *8*(4). https://doi.org/10.1161/JAHA.118.011704

Lipowsky, H. H., Kovalcheck, S., & Zweifach, B. W. (1978). The distribution of blood rheological parameters in the microvasculature of cat mesentery. *Circulation Research*, *43*(5), 738–749. https://doi.org/10.1161/01.RES.43.5.738

Liu, B., Lu, S., Hu, Y. L., Liao, X., Ouyang, M., & Wang, Y. (2014). RhoA and membrane fluidity mediates the spatially polarized Src/FAK activation in response to shear stress. *Scientific Reports*, *4*(1), 1–8. https://doi.org/10.1038/srep07008

Liu, T., Zhang, L., Joo, D., & Sun, S.-C. (2017). NF-κB signaling in inflammation. In *Signal Transduction and Targeted Therapy* (Vol. 2). Springer Nature. https://doi.org/10.1038/sigtrans.2017.23

Liu, Z., Zhao, Y., Wang, X., Zhang, H., Cui, Y., Diao, Y., Xiu, J., Sun, X., & Jiang, G. (2016). Low carotid artery wall shear stress is independently associated with brain white-matter hyperintensities and cognitive impairment in older patients. *Atherosclerosis*, *247*, 78–86. https://doi.org/10.1016/j.atherosclerosis.2016.02.003

Lohman, A. W., Billaud, M., & Isakson, B. E. (2012). Mechanisms of ATP release and signalling in the blood vessel wall. In *Cardiovascular Research* (Vol. 95, Issue 3, pp. 269–280). Oxford Academic. https://doi.org/10.1093/cvr/cvs187

Longden, T. A., Mughal, A., Hennig, G. W., Harraz, O. F., Shui, B., Lee, F. K., Lee, J. C., Reining, S., Kotlikoff, M. I., König, G. M., Kostenis, E., Hill-Eubanks, D., & Nelson, M. T. (2021). Local IP3 receptor-mediated Ca2+ signals compound to direct blood flow in brain capillaries. *Science Advances*, *7*(30). https://doi.org/10.1126/sciadv.abh0101

Lupien, S. J., McEwen, B. S., Gunnar, M. R., & Heim, C. (2009). Effects of stress throughout the lifespan on the brain, behaviour and cognition. In *Nature Reviews Neuroscience* (Vol. 10, Issue 6, pp. 434–445). Nature Publishing Group. https://doi.org/10.1038/nrn2639

Mallick, R., & Duttaroy, A. K. (2022). Modulation of endothelium function by fatty acids. In *Molecular and Cellular Biochemistry* (Vol. 477, Issue 1, pp. 15–38). Springer. https://doi.org/10.1007/s11010-021-04260-9

Manu, D. R., Slevin, M., Barcutean, L., Forro, T., Boghitoiu, T., & Balasa, R. (2023). Astrocyte Involvement in Blood–Brain Barrier Function: A Critical Update Highlighting Novel, Complex, Neurovascular Interactions. In *International Journal of Molecular Sciences* (Vol. 24, Issue 24, p. 17146). Multidisciplinary Digital Publishing Institute. https://doi.org/10.3390/ijms242417146

Mattson, M. P., & Meffert, M. K. (2006). Roles for NF-κB in nerve cell survival, plasticity, and disease. In *Cell Death and Differentiation* (Vol. 13, Issue 5, pp. 852–860). Nature Publishing Group. https://doi.org/10.1038/sj.cdd.4401837

Maviel, T., Durkin, T. P., Menzaghi, F., & Bontempi, B. (2004). Sites of neocortical reorganization critical for remote spatial memory. *Science*, *305*(5680), 96–99. https://doi.org/10.1126/science.1098180

McKetton, L., Sobczyk, O., Duffin, J., Poublanc, J., Sam, K., Crawley, A. P., Venkatraghavan, L., Fisher, J. A., & Mikulis, D. J. (2018). The aging brain and cerebrovascular reactivity. *NeuroImage*, *181*, 132–141. https://doi.org/10.1016/j.neuroimage.2018.07.007

Mclay, R. N., Freeman, S. M., & Zadina, J. E. (1998). Chronic Corticosterone Impairs Memory Performance in the Barnes Maze. In *Physiology & Behavior* (Vol. 63, Issue 5). Elsevier. https://doi.org/10.1016/S0031-9384(97)00529-5

Meuwissen, M. E. C., & Mancini, G. M. S. (2012). Neurological findings in incontinentia pigmenti; a review. In *European Journal of Medical Genetics* (Vol. 55, Issue 5, pp. 323–331). Elsevier Masson. https://doi.org/10.1016/j.ejmg.2012.04.007

Miles, E. A., Rees, D., Banerjee, T., Cazzola, R., Lewis, S., Wood, R., Oates, R., Tallant, A., Cestaro, B., Yaqoob, P., Wahle, K. W. J., & Calder, P. C. (2008). Age-related increases in circulating inflammatory markers in men are independent of BMI, blood pressure and blood lipid concentrations. *Atherosclerosis*, *196*(1), 298–305. https://doi.org/10.1016/j.atherosclerosis.2006.11.002

Miller, K. B., Howery, A. J., Rivera-Rivera, L. A., Johnson, S. C., Rowley, H. A., Wieben, O., & Barnes, J. N. (2019). Age-Related Reductions in Cerebrovascular Reactivity Using 4D Flow MRI. *Frontiers in Aging Neuroscience*, *11*, 487045. https://doi.org/10.3389/fnagi.2019.00281

Mobayen, G., Smith, K., Ediriwickrema, K., Starke, R. D., Solomonidis, E. G., Laffan, M. A., Randi, A. M., & McKinnon, T. A. J. (2023). von Willebrand factor binds to angiopoietin-2 within endothelial cells and after release from Weibel–Palade bodies. *Journal of Thrombosis and Haemostasis*, *21*(7), 1802–1812. https://doi.org/10.1016/j.jtha.2023.03.027

Moccia, F. (2018). Endothelial Ca2+ signaling and the resistance to anticancer treatments: Partners in crime. In *International Journal of Molecular Sciences* (Vol. 19, Issue 1, p. 217). Multidisciplinary Digital Publishing Institute. https://doi.org/10.3390/ijms19010217

Moccia, F., Brunetti, V., Soda, T., Berra-Romani, R., & Scarpellino, G. (2023). Cracking the Endothelial Calcium (Ca2+) Code: A Matter of Timing and Spacing. *International Journal of Molecular Sciences*, *24*(23). https://doi.org/10.3390/ijms242316765

Monnier, A., Prigent-Tessier, A., Quirié, A., Bertrand, N., Savary, S., Gondcaille, C., Garnier, P., Demougeot, C., & Marie, C. (2017). Brain-derived neurotrophic factor of the cerebral microvasculature: a forgotten and nitric oxide-dependent contributor of brain-derived neurotrophic factor in the brain. *Acta Physiologica*, *219*(4), 790–802. https://doi.org/10.1111/apha.12743

Montagne, A., Barnes, S. R., Sweeney, M. D., Halliday, M. R., Sagare, A. P., Zhao, Z., Toga, A. W., Jacobs, R. E., Liu, C. Y., Amezcua, L., Harrington, M. G., Chui, H. C., Law, M., & Zlokovic, B. V. (2015). Blood-Brain barrier breakdown in the aging human hippocampus. *Neuron*, *85*(2), 296–302. https://doi.org/10.1016/j.neuron.2014.12.032

Montaron, M. F., Drapeau, E., Dupret, D., Kitchener, P., Aurousseau, C., Le Moal, M., Piazza, P. V., & Abrous, D. N. (2006). Lifelong corticosterone level determines age-related decline in neurogenesis and memory. *Neurobiology of Aging*, *27*(4), 645–654. https://doi.org/10.1016/j.neurobiolaging.2005.02.014

Morris, A. W. J., Sharp, M. M. G., Albargothy, N. J., Fernandes, R., Hawkes, C. A., Verma, A., Weller, R. O., & Carare, R. O. (2016). Vascular basement membranes as pathways for the passage of fluid into and out of the brain. *Acta Neuropathologica*, *131*(5), 725–736. https://doi.org/10.1007/s00401-016-1555-z

Morrison, J. H., & Baxter, M. G. (2012). The ageing cortical synapse: Hallmarks and implications for cognitive decline. In *Nature Reviews Neuroscience* (Vol. 13, Issue 4, pp. 240–250). Nat Rev Neurosci. https://doi.org/10.1038/nrn3200

Moya, M. L., Triplett, M., Simon, M., Alvarado, J., Booth, R., Osburn, J., Soscia, D., Qian, F., Fischer, N. O., Kulp, K., & Wheeler, E. K. (2020). A Reconfigurable In Vitro Model for Studying the Blood–Brain Barrier. *Annals of Biomedical Engineering*, *48*(2), 780–793. https://doi.org/10.1007/s10439-019-02405-y

Murai, T., Okuda, S., Tanaka, T., & Ohta, H. (2007). Characteristics of object location memory in mice: Behavioral and pharmacological studies. *Physiology and Behavior*, *90*(1), 116–124. https://doi.org/10.1016/j.physbeh.2006.09.013

Murthy, S. E., Dubin, A. E., & Patapoutian, A. (2017). Piezos thrive under pressure: Mechanically activated ion channels in health and disease. *Nature Reviews Molecular Cell Biology*, *18*(12), 771–783. https://doi.org/10.1038/nrm.2017.92

Mutsaerts, H. J. M. M., Palm-Meinders, I. H., De Craen, A. J. M., Reiber, J. H. C., Blauw, G. J., Van Buchem, M. A., Van Der Grond, J., & Box, F. M. A. (2011). Diastolic carotid artery wall shear stress is associated with cerebral infarcts and periventricular white matter lesions. *Stroke*, *42*(12), 3497–3501. https://doi.org/10.1161/STROKEAHA.111.614453

Nakahashi, T., Fujimura, H., Altar, C. A., Li, J., Kambayashi, J. I., Tandon, N. N., & Sun, B. (2000). Vascular endothelial cells synthesize and secrete brain-derived neurotrophic factor. *FEBS Letters*, *470*(2), 113–117. https://doi.org/10.1016/S0014-5793(00)01302-8

Nations, U. (2022). World Population Prospects 2022. In *United Nation* (Issue 9). www.un.org/development/ desa/pd/.

Negri, S., Faris, P., Tullii, G., Vismara, M., Pellegata, A. F., Lodola, F., Guidetti, G., Rosti, V., Antognazza, M. R., & Moccia, F. (2022). Conjugated polymers mediate intracellular Ca2+ signals in circulating endothelial colony forming cells through the reactive oxygen species-dependent activation of Transient Receptor Potential Vanilloid 1 (TRPV1). *Cell Calcium*, *101*, 102502. https://doi.org/10.1016/j.ceca.2021.102502

Newman, M. C., & Kaszniak, A. W. (2000). Spatial memory and aging: Performance on a human analog of the Morris water maze. *Aging, Neuropsychology, and Cognition*, *7*(2), 86–93. https://doi.org/https://doi.org/10.1076/1382-5585(200006)7:2;1-U;FT086

Nguyen, L. N., Ma, D., Shui, G., Wong, P., Cazenave-Gassiot, A., Zhang, X., Wenk, M. R., Goh, E. L. K., & Silver, D. L. (2014). Mfsd2a is a transporter for the essential omega-3 fatty acid docosahexaenoic acid. *Nature*, *509*(7501), 503–506. https://doi.org/10.1038/nature13241

Nitta, T., Hata, M., Gotoh, S., Seo, Y., Sasaki, H., Hashimoto, N., Furuse, M., & Tsukita, S. (2003). Size-selective loosening of the blood-brain barrier in claudin-5-deficient mice. *Journal of Cell Biology*, *161*(3), 653–660. https://doi.org/10.1083/jcb.200302070

O'Leary, T. P., & Brown, R. E. (2013). Optimization of apparatus design and behavioral measures for the assessment of visuo-spatial learning and memory of mice on the Barnes maze. *Learning and Memory*, *20*(2), 85–96. https://doi.org/10.1101/lm.028076.112

Ornelas, S., Berthiaume, A. A., Bonney, S. K., Coelho-Santos, V., Underly, R. G., Kremer, A., Guérin, C. J., Lippens, S., & Shih, A. Y. (2021). Three-dimensional ultrastructure of the brain pericyte-endothelial interface. *Journal of Cerebral Blood Flow and Metabolism*, *41*(9), 2185–2200. https://doi.org/10.1177/0271678X211012836

Pafumi, I., Favia, A., Gambara, G., Papacci, F., Ziparo, E., Palombi, F., & Filippini, A. (2015). Regulation of angiogenic functions by angiopoietins through calcium-dependent signaling pathways. *BioMed Research International*, *2015*. https://doi.org/10.1155/2015/965271

Pao, P. C., Patnaik, D., Watson, L. A., Gao, F., Pan, L., Wang, J., Adaikkan, C., Penney, J., Cam, H. P., Huang, W. C., Pantano, L., Lee, A., Nott, A., Phan, T. X., Gjoneska, E., Elmsaouri, S., Haggarty, S. J., & Tsai, L. H. (2020). HDAC1 modulates OGG1-initiated oxidative DNA damage repair in the aging brain and Alzheimer's disease. *Nature Communications*, *11*(1). https://doi.org/10.1038/s41467-020-16361-y

Pao, P. C., Seo, J., Lee, A., Kritskiy, O., Patnaik, D., Penney, J., Raju, R. M., Geigenmuller, U., Silva, M. C., Lucente, D. E., Gusella, J. F., Dickerson, B. C., Loon, A., Yu, M. X., Bula, M., Yu, M., Haggarty, S. J., & Tsai, L. H. (2023). A Cdk5-derived peptide inhibits Cdk5/p25 activity and improves neurodegenerative phenotypes. *Proceedings of the National Academy of Sciences of the United States of America*, *120*(16). https://doi.org/10.1073/pnas.2217864120

Peng, S. L., Chen, X., Li, Y., Rodrigue, K. M., Park, D. C., & Lu, H. (2018). Age-related changes in cerebrovascular reactivity and their relationship to cognition: A four-year longitudinal study. *NeuroImage*, *174*, 257–262. https://doi.org/10.1016/j.neuroimage.2018.03.033

Peters, E. C., Gee, M. T., Pawlowski, L. N., Kath, A. M., Polk, F. D., Vance, C. J., Sacoman, J. L., & Pires, P. W. (2022). Amyloid-β disrupts unitary calcium entry through endothelial NMDA receptors in mouse cerebral arteries. *Journal of Cerebral Blood Flow and Metabolism*, *42*(1), 145–161. https://doi.org/10.1177/0271678X211039592

Pluimer, B. R., Colt, M., & Zhao, Z. (2020). G Protein-Coupled Receptors in the Mammalian Blood-

Brain Barrier. In *Frontiers in Cellular Neuroscience* (Vol. 14). Frontiers Media S.A. https://doi.org/10.3389/fncel.2020.00139

Poels, M. M. F., Van Oijen, M., Mattace-Raso, F. U. S., Hofman, A., Koudstaal, P. J., Witteman, J. C. M., & Breteler, M. M. B. (2007). Arterial stiffness, cognitive decline, and risk of dementia: The Rotterdam study. *Stroke*, *38*(3), 888–892. https://doi.org/10.1161/01.STR.0000257998.33768.87

Poziomczyk, C. S., Maria, F. D. S., Freitas, A. M., Fiegenbaum, M., Bau, A. E. K., Recuero, J. K., Campos, C. W., Maahs, M. A. P., De Almeida, S. T., Bringhenti, L., Travi, G. M., Zen, P. R. G., & Bonamigo, R. R. (2014). Incontinentia pigmenti. *Anais Brasileiros de Dermatologia*, *89*(1), 26–36. https://doi.org/10.1590/abd1806-4841.20142584

Profaci, C. P., Munji, R. N., Pulido, R. S., & Daneman, R. (2020). The blood–brain barrier in health and disease: Important unanswered questions. *Journal of Experimental Medicine*, *217*(4), 1–16. https://doi.org/10.1084/jem.20190062

Quick, S., Moss, J., Rajani, R. M., & Williams, A. (2021). A Vessel for Change: Endothelial Dysfunction in Cerebral Small Vessel Disease. *Trends in Neurosciences*, *44*(4), 289–305. https://doi.org/10.1016/j.tins.2020.11.003

Reeson, P., Choi, K., & Brown, C. E. (2018). VEGF signaling regulates the fate of obstructed capillaries in mouse cortex. *ELife*, *7*. https://doi.org/10.7554/eLife.33670

Reinitz, A., DeStefano, J., Ye, M., Wong, A. D., & Searson, P. C. (2015). Human brain microvascular endothelial cells resist elongation due to shear stress. *Microvascular Research*, *99*, 8–18. https://doi.org/10.1016/j.mvr.2015.02.008

Reinmuth, O. M., Scheinberg, P., & Bourne, B. (1965). Total Cerebral Blood Flow And Metabolism: A New Method for the Repeated Serial Measurement of Total Cerbral Blood Flow Using Iodoantipyrine (1131) With a Report of Determination in Normal Human Beings of Blood Flow, Oxygen Consumption, Glucose Utilization. *Archives of Neurology*, *12*(1), 49–66. https://doi.org/10.1001/ARCHNEUR.1965.00460250053007

Reneman, R. S., Arts, T., & Hoeks, A. P. G. (2006). Wall shear stress - An important determinant of endothelial cell function and structure - In the arterial system in vivo: Discrepancies with theory. *Journal of Vascular Research*, *43*(3), 251–269. https://doi.org/10.1159/000091648

Ridder, D. A., Lang, M. F., Salinin, S., Röderer, J. P., Struss, M., Christiane, M. G., & Schwaninger, M. (2011). TAK1 in brain endothelial cells mediates fever and lethargy. *Journal of Experimental Medicine*, *208*(13), 2615–2623. https://doi.org/10.1084/jem.20110398

Ridder, D. A., Wenzel, J., Müller, K., Töllner, K., Tong, X. K., Assmann, J. C., Stroobants, S., Weber, T., Niturad, C., Fischer, L., Lembrich, B., Wolburg, H., Grand'Maison, M., Papadopoulos, P., Korpos, E., Truchetet, F., Rades, D., Sorokin, L. M., Schmidt-Supprian, M., … Schwaninger, M. (2015). Brain endothelial TAK1 and NEMO safeguard the neurovascular unit. *Journal of Experimental Medicine*, *212*(10), 1529–1549. https://doi.org/10.1084/jem.20150165

Riddle, D. R., Sonntag, W. E., & Lichtenwalner, R. J. (2003). Microvascular plasticity in aging. *Ageing Research Reviews*, *2*(2), 149–168. https://doi.org/10.1016/S1568-1637(02)00064-8

Rivard, A., Berthou-Soulie, L., Principe, N., Kearney, M., Curry, C., Branellec, D., Semenza, G. L., & Isner, J. M. (2000). Age-dependent defect in vascular endothelial growth factor expression is associated with reduced hypoxia-inducible factor 1 activity. *Journal of Biological Chemistry*, *275*(38), 29643–29647. https://doi.org/10.1074/jbc.M001029200

Rochfort, K. D., Collins, L. E., McLoughlin, A., & Cummins, P. M. (2015). Shear-dependent attenuation of cellular ROS levels can suppress proinflammatory cytokine injury to human brain microvascular endothelial barrier properties. *Journal of Cerebral Blood Flow and Metabolism*, *35*(10), 1648–1656. https://doi.org/10.1038/jcbfm.2015.102

Rochfort, K. D., & Cummins, P. M. (2015). Thrombomodulin regulation in human brain microvascular endothelial cells in vitro: Role of cytokines and shear stress. *Microvascular Research*, *97*, 1–5. https://doi.org/10.1016/j.mvr.2014.09.003

Roher, A. E., Esh, C., Kokjohn, T. A., Kalback, W., Luehrs, D. C., Seward, J. D., Sue, L. I., & Beach, T. G. (2003). Circle of Willis Atherosclerosis Is a Risk Factor for Sporadic Alzheimer's Disease. *Arteriosclerosis, Thrombosis, and Vascular Biology*, *23*(11), 2055–2062. https://doi.org/10.1161/01.ATV.0000095973.42032.44

Roux, E., Bougaran, P., Dufourcq, P., & Couffinhal, T. (2020). Fluid Shear Stress Sensing by the Endothelial Layer. In *Frontiers in Physiology* (Vol. 11). Frontiers Media S.A. https://doi.org/10.3389/fphys.2020.00861

Ruiz de Almodovar, C., Fabre, P. J., Knevels, E., Coulon, C., Segura, I., Haddick, P. C. G., Aerts, L., Delattin, N., Strasser, G., Oh, W. J., Lange, C., Vinckier, S., Haigh, J., Fouquet, C., Gu, C., Alitalo, K., Castellani, V., Tessier-Lavigne, M., Chedotal, A., … Carmeliet, P. (2011). VEGF Mediates Commissural Axon Chemoattraction through Its Receptor Flk1. *Neuron*, *70*(5), 966–978. https://doi.org/10.1016/j.neuron.2011.04.014

Saitou, M., Furuse, M., Sasaki, H., Schulzke, J. D., Fromm, M., Takano, H., Noda, T., & Tsukita, S. (2000). Complex phenotype of mice lacking occludin, a component of tight junction strands.

Molecular Biology of the Cell, *11*(12), 4131–4142. https://doi.org/10.1091/mbc.11.12.4131

Saunders, A., Macosko, E. Z., Wysoker, A., Goldman, M., Krienen, F. M., de Rivera, H., Bien, E., Baum, M., Bortolin, L., Wang, S., Goeva, A., Nemesh, J., Kamitaki, N., Brumbaugh, S., Kulp, D., & McCarroll, S. A. (2018). Molecular Diversity and Specializations among the Cells of the Adult Mouse Brain. *Cell*, *174*(4), 1015-1030.e16. https://doi.org/10.1016/j.cell.2018.07.028

Schaeffer, S., & Iadecola, C. (2021). Revisiting the neurovascular unit. *Nature Neuroscience*, *24*(9), 1198–1209. https://doi.org/10.1038/s41593-021-00904-7

Schindelin, J., Arganda-Carreras, I., Frise, E., Kaynig, V., Longair, M., Pietzsch, T., Preibisch, S., Rueden, C., Saalfeld, S., Schmid, B., Tinevez, J. Y., White, D. J., Hartenstein, V., Eliceiri, K., Tomancak, P., & Cardona, A. (2012). Fiji: An open-source platform for biological-image analysis. In *Nature Methods* (Vol. 9, Issue 7, pp. 676–682). Nature Publishing Group. https://doi.org/10.1038/nmeth.2019

Schnerr, R. S., Jansen, J. F. A., Uludag, K., Hofman, P. A. M., Wildberger, J. E., van Oostenbrugge, R. J., & Backes, W. H. (2017). Pulsatility of lenticulostriate arteries assessed by 7 Tesla flow MRI-Measurement, reproducibility, and applicability to aging effect. *Frontiers in Physiology*, *8*(NOV), 295639. https://doi.org/10.3389/fphys.2017.00961

Schrage, R., Schmitz, A. L., Gaffal, E., Annala, S., Kehraus, S., Wenzel, D., Büllesbach, K. M., Bald, T., Inoue, A., Shinjo, Y., Galandrin, S., Shridhar, N., Hesse, M., Grundmann, M., Merten, N., Charpentier, T. H., Martz, M., Butcher, A. J., Slodczyk, T., … Kostenis, E. (2015). The experimental power of FR900359 to study Gq-regulated biological processes. *Nature Communications*, *6*. https://doi.org/10.1038/ncomms10156

Sekino, S., Kashiwagi, Y., Kanazawa, H., Takada, K., Baba, T., Sato, S., Inoue, H., Kojima, M., & Tani, K. (2015). The NESH/Abi-3-based WAVE2 complex is functionally distinct from the Abi-1-based WAVE2 complex. *Cell Communication and Signaling*, *13*(1), 1–15. https://doi.org/10.1186/s12964-015-0119-5

Semba, R. D., Sun, K., Schwartz, A. V., Varadhan, R., Harris, T. B., Satterfield, S., Garcia, M., Ferrucci, L., & Newman, A. B. (2015). Serum carboxymethyl-lysine, an advanced glycation end product, is associatedwith arterial stiffness in older adults. *Journal of Hypertension*, *33*(4), 797–803. https://doi.org/10.1097/HJH.0000000000000460

Sen, C. K., Roy, S., & Packer, L. (1996). Involvement of intracellular Ca2+ in oxidant-induced NF-κB activation. *FEBS Letters*, *385*(1–2), 58–62. https://doi.org/10.1016/0014-5793(96)00346-8

Sen, R., & Baltimore, D. (1986). Multiple nuclear factors interact with the immunoglobulin enhancer sequences. *Cell*, *46*(5), 705–716. https://doi.org/10.1016/0092-8674(86)90346-6

Sharma, S., Rakoczy, S., & Brown-Borg, H. (2010). Assessment of spatial memory in mice. In *Life Sciences* (Vol. 87, Issues 17–18, pp. 521–536). https://doi.org/10.1016/j.lfs.2010.09.004

Shaw, K., Bell, L., Boyd, K., Grijseels, D. M., Clarke, D., Bonnar, O., Crombag, H. S., & Hall, C. N. (2021). Neurovascular coupling and oxygenation are decreased in hippocampus compared to neocortex because of microvascular differences. *Nature Communications*, *12*(1). https://doi.org/10.1038/s41467-021-23508-y

Shoji, H., & Miyakawa, T. (2019). Age-related behavioral changes from young to old age in male mice of a C57BL/6J strain maintained under a genetic stability program. *Neuropsychopharmacology Reports*, *39*(2), 100–118. https://doi.org/10.1002/npr2.12052

Sims, R., Van Der Lee, S. J., Naj, A. C., Bellenguez, C., Badarinarayan, N., Jakobsdottir, J., Kunkle, B. W., Boland, A., Raybould, R., Bis, J. C., Martin, E. R., Grenier-Boley, B., Heilmann-Heimbach, S., Chouraki, V., Kuzma, A. B., Sleegers, K., Vronskaya, M., Ruiz, A., Graham, R. R., … Schellenberg, G. D. (2017). Rare coding variants in PLCG2, ABI3, and TREM2 implicate microglial-mediated innate immunity in Alzheimer's disease. *Nature Genetics 2017 49:9*, *49*(9), 1373–1384. https://doi.org/10.1038/ng.3916

Sivaraj, K. K., Li, R., Albarran-Juarez, J., Wang, S., Tischner, D., Grimm, M., Swiercz, J. M., Offermanns, S., & Wettschureck, N. (2015). Endothelial Gαq/11 is required for VEGF-induced vascular permeability and angiogenesis. *Cardiovascular Research*, *108*(1), 171–180. https://doi.org/10.1093/cvr/cvv216

Snapyan, M., Lemasson, M., Brill, M. S., Blais, M., Massouh, M., Ninkovic, J., Gravel, C., Berthod, F., Götz, M., Barker, P. A., Parent, A., & Saghatelyan, A. (2009). Vasculature guides migrating neuronal precursors in the adult mammalian forebrain via brain-derived neurotrophic factor signaling. *Journal of Neuroscience*, *29*(13), 4172–4188. https://doi.org/10.1523/JNEUROSCI.4956-08.2009

Sparkman, N. L., & Johnson, R. W. (2008). Neuroinflammation associated with aging sensitizes the brain to the effects of infection or stress. In *NeuroImmunoModulation* (Vol. 15, Issues 4–6, pp. 323–330). Neuroimmunomodulation. https://doi.org/10.1159/000156474

Squire, L. R., Genzel, L., Wixted, J. T., & Morris, R. G. (2015). Memory consolidation. *Cold Spring Harbor Perspectives in Biology*, *7*(8). https://doi.org/10.1101/cshperspect.a021766

Stamatovic, S. M., Martinez-Revollar, G., Hu, A., Choi, J., Keep, R. F., & Andjelkovic, A. V. (2019). Decline in Sirtuin-1 expression and activity plays a critical role in blood-brain barrier permeability in aging. In *Neurobiology of Disease* (Vol. 126, pp. 105–116). Academic Press Inc. https://doi.org/10.1016/j.nbd.2018.09.006

Steiner, O., Coisne, C., Engelhardt, B., & Lyck, R. (2011). Comparison of immortalized bEnd5 and primary mouse brain microvascular endothelial cells as in vitro blood-κBrain barrier models for the study of T cell extravasation. *Journal of Cerebral Blood Flow and Metabolism*, *31*(1), 315–327. https://doi.org/10.1038/jcbfm.2010.96

Subramanian, A., Tamayo, P., Mootha, V. K., Mukherjee, S., Ebert, B. L., Gillette, M. A., Paulovich, A., Pomeroy, S. L., Golub, T. R., Lander, E. S., & Mesirov, J. P. (2005). Gene set enrichment analysis: A knowledge-based approach for interpreting genome-wide expression profiles. *Proceedings of the National Academy of Sciences of the United States of America*, *102*(43), 15545–15550. https://doi.org/10.1073/pnas.0506580102

Sunyer, B., Patil, S., Höger, H., & Luber, G. (2007). Barnes maze, a useful task to assess spatial reference memory in the mice. *Protocol Exchange*. https://doi.org/https://doi.org/10.1038/nprot.2007.390

Swain, S. M., & Liddle, R. A. (2021). Piezo1 acts upstream of TRPV4 to induce pathological changes in endothelial cells due to shear stress. *Journal of Biological Chemistry*, *296*. https://doi.org/10.1074/jbc.RA120.015059

Sweeney, M. D., Zhao, Z., Montagne, A., Nelson, A. R., & Zlokovic, B. V. (2019). Blood-brain barrier: From physiology to disease and back. In *Physiological Reviews* (Vol. 99, Issue 1, pp. 21–78). American Physiological Society. https://doi.org/10.1152/physrev.00050.2017

Syeda, R., Xu, J., Dubin, A. E., Coste, B., Mathur, J., Huynh, T., Matzen, J., Lao, J., Tully, D. C., Engels, I. H., Michael Petrassi, H., Schumacher, A. M., Montal, M., Bandell, M., & Patapoutian, A. (2015). Chemical activation of the mechanotransduction channel Piezo1. *ELife*, *4*(MAY). https://doi.org/10.7554/eLife.07369

Syrovatkina, V., Alegre, K. O., Dey, R., & Huang, X. Y. (2016). Regulation, Signaling, and Physiological Functions of G-Proteins. In *Journal of Molecular Biology* (Vol. 428, Issue 19, pp. 3850–3868). Academic Press. https://doi.org/10.1016/j.jmb.2016.08.002

Taddei, A., Giampietro, C., Conti, A., Orsenigo, F., Breviario, F., Pirazzoli, V., Potente, M., Daly, C., Dimmeler, S., & Dejana, E. (2008). Endothelial adherens junctions control tight junctions by VE-cadherin-mediated upregulation of claudin-5. *Nature Cell Biology*, *10*(8), 923–934. https://doi.org/10.1038/ncb1752

Thippegowda, P. B., Singh, V., Sundivakkam, P. C., Xue, J., Malik, A. B., & Tiruppathi, C. (2010). Ca2+

influx via TRPC channels induces NF-κB-dependent A20 expression to prevent thrombin-induced apoptosis in endothelial cells. *American Journal of Physiology - Cell Physiology*, *298*(3), 656–664. https://doi.org/10.1152/ajpcell.00456.2009

Tietz, S., & Engelhardt, B. (2015). Brain barriers: Crosstalk between complex tight junctions and adherens junctions. In *Journal of Cell Biology* (Vol. 209, Issue 4, pp. 493–506). J Cell Biol. https://doi.org/10.1083/jcb.201412147

Tiruppathi, C., Minshall, R. D., Paria, B. C., Vogel, S. M., & Malik, A. B. (2002). Role of Ca2+ signaling in the regulation of endothelial permeability. In *Vascular Pharmacology* (Vol. 39, Issues 4–5, pp. 173–185). Elsevier Inc. https://doi.org/10.1016/S1537-1891(03)00007-7

Toth, P., Tarantini, S., Csiszar, A., & Ungvari, Z. (2017). Functional vascular contributions to cognitive impairment and dementia: Mechanisms and consequences of cerebral autoregulatory dysfunction, endothelial impairment, and neurovascular uncoupling in aging. In *American Journal of Physiology - Heart and Circulatory Physiology* (Vol. 312, Issue 1, pp. H1–H20). American Physiological Society. https://doi.org/10.1152/ajpheart.00581.2016

Tressel, S. L., Huang, R. P., Tomsen, N., & Jo, H. (2007). Laminar shear inhibits tubule formation and migration of endothelial cells by an angiopoietin-2-dependent mechanism. *Arteriosclerosis, Thrombosis, and Vascular Biology*, *27*(10), 2150–2156. https://doi.org/10.1161/ATVBAHA.107.150920

Tzima, E., Irani-Tehrani, M., Kiosses, W. B., Dejana, E., Schultz, D. A., Engelhardt, B., Cao, G., DeLisser, H., & Schwartz, M. A. (2005). A mechanosensory complex that mediates the endothelial cell response to fluid shear stress. *Nature*, *437*(7057), 426–431. https://doi.org/10.1038/nature03952

Tzima, E., Kiosses, W. B., Del Pozo, M. A., & Schwartz, M. A. (2003). Localized Cdc42 activation, detected using a novel assay, mediates microtubule organizing center positioning in endothelial cells in response to fluid shear stress. *Journal of Biological Chemistry*, *278*(33), 31020–31023. https://doi.org/10.1074/jbc.M301179200

Urbich, C., Dernbach, E., Reissner, A., Vasa, M., Zeiher, A. M., & Dimmeler, S. (2002). Shear stress-induced endothelial cell migration involves integrin signaling via the fibronectin receptor subunits α5 and β1. *Arteriosclerosis, Thrombosis, and Vascular Biology*, *22*(1), 69–75. https://doi.org/10.1161/hq0102.101518

Uttl, B., & Graf, P. (1993). Episodic Spatial Memory in Adulthood. *Psychology and Aging*, *8*(2), 257–273. https://doi.org/10.1037/0882-7974.8.2.257

Van Hinsbergh, V. W. M. (2012). Endothelium - Role in regulation of coagulation and inflammation. In *Seminars in Immunopathology* (Vol. 34, Issue 1, pp. 93–106). Springer. https://doi.org/10.1007/s00281-011-0285-5

van Oostrum, M., Müller, M., Klein, F., Bruderer, R., Zhang, H., Pedrioli, P. G. A., Reiter, L., Tsapogas, P., Rolink, A., & Wollscheid, B. (2019). Classification of mouse B cell types using surfaceome proteotype maps. *Nature Communications*, *10*(1). https://doi.org/10.1038/s41467-019-13418-5

Vanlandewijck, M., He, L., Mäe, M. A., Andrae, J., Ando, K., Del Gaudio, F., Nahar, K., Lebouvier, T., Laviña, B., Gouveia, L., Sun, Y., Raschperger, E., Räsänen, M., Zarb, Y., Mochizuki, N., Keller, A., Lendahl, U., & Betsholtz, C. (2018). A molecular atlas of cell types and zonation in the brain vasculature. *Nature*, *554*(7693), 475–480. https://doi.org/10.1038/nature25739

Vázquez-Liébanas, E., Mocci, G., Li, W., Laviña, B., Reddy, A., O'Connor, C., Hudson, N., Elbeck, Z., Nikoloudis, I., Gaengel, K., Vanlandewijck, M., Campbell, M., Betsholtz, C., & Mäe, M. A. (2024). Mosaic deletion of claudin-5 reveals rapid non-cell-autonomous consequences of blood-brain barrier leakage. *Cell Reports*, *43*(3), 113911. https://doi.org/10.1016/j.celrep.2024.113911

Venecia, G., Davis, M., & Engerman, R. (1976). Clinicopathologic Correlations in Diabetic Retinopathy: I. Histology and Fluorescein Angiography of Microaneurysms. *Archives of Ophthalmology*, *94*(10), 1766–1773. https://doi.org/10.1001/archopht.1976.03910040540013

Viney, T. J., Sarkany, B., Ozdemir, A. T., Hartwich, K., Schweimer, J., Bannerman, D., & Somogyi, P. (2022). Spread of pathological human Tau from neurons to oligodendrocytes and loss of high-firing pyramidal neurons in aging mice. *Cell Reports*, *41*(7). https://doi.org/10.1016/j.celrep.2022.111646

Walpola, P. L., Gotlieb, A. I., Cybulsky, M. I., & Langille, B. L. (1995). Expression of ICAM-1 and VCAM-1 and monocyte adherence in arteries exposed to altered shear stress. *Arteriosclerosis, Thrombosis, and Vascular Biology*, *15*(1), 2–10. https://doi.org/10.1161/01.ATV.15.1.2

Walsh, T. G., Murphy, R. P., Fitzpatrick, P., Rochfort, K. D., Guinan, A. F., Murphy, A., & Cummins, P. M. (2011). Stabilization of brain microvascular endothelial barrier function by shear stress involves VE-cadherin signaling leading to modulation of pTyr-occludin levels. *Journal of Cellular Physiology*, *226*(11), 3053–3063. https://doi.org/10.1002/jcp.22655

Wang, C., Baker, B. M., Chen, C. S., & Schwartz, M. A. (2013). Endothelial cell sensing of flow direction. *Arteriosclerosis, Thrombosis, and Vascular Biology*, *33*(9), 2130–2136. https://doi.org/10.1161/ATVBAHA.113.301826

Wang, F., Ren, S. Y., Chen, J. F., Liu, K., Li, R. X., Li, Z. F., Hu, B., Niu, J. Q., Xiao, L., Chan, J. R., & Mei, F. (2020). Myelin degeneration and diminished myelin renewal contribute to age-related deficits in memory. *Nature Neuroscience*, *23*(4), 481–486. https://doi.org/10.1038/s41593-020-0588-8

Wang, M., Zhang, J., Spinetti, G., Jiang, L. Q., Monticone, R., Zhao, D., Cheng, L., Krawczyk, M., Talan, M., Pintus, G., & Lakatta, E. G. (2005). Angiotensin II activates matrix metalloproteinase type II and mimics age-associated carotid arterial remodeling in young rats. *American Journal of Pathology*, *167*(5), 1429–1442. https://doi.org/10.1016/S0002-9440(10)61229-1

Wang, S. P., Chennupati, R., Kaur, H., Iring, A., Wettschureck, N., & Offermanns, S. (2016). Endothelial cation channel PIEZO1 controls blood pressure by mediating flow-induced ATP release. *Journal of Clinical Investigation*, *126*(12), 4527–4536. https://doi.org/10.1172/JCI87343

Wang, S. P., Iring, A., Strilic, B., Juárez, J. A., Kaur, H., Troidl, K., Tonack, S., Burbiel, J. C., Müller, C. E., Fleming, I., Lundberg, J. O., Wettschureck, N., & Offermanns, S. (2015). P2Y2 and Gq/G11 control blood pressure by mediating endothelial mechanotransduction. *Journal of Clinical Investigation*, *125*(8), 3077–3086. https://doi.org/10.1172/JCI81067

Wang, S. P., Wang, B., Shi, Y., Möller, T., Stegmeyer, R. I., Strilic, B., Li, T., Yuan, Z., Wang, C., Wettschureck, N., Vestweber, D., & Offermanns, S. (2022). Mechanosensation by endothelial PIEZO1 is required for leukocyte diapedesis. *Blood*, *140*(3), 171–183. https://doi.org/10.1182/blood.2021014614

Wasserman, S. M., Mehraban, F., Komuves, L. G., Yang, R. B., Tomlinson, J. E., Zhang, Y., Spriggs, F., & Topper, J. N. (2002). Gene expression profile of human endothelial cells exposed to sustained fluid shear stress. *Physiological Genomics*, *12*(1), 13–23. https://doi.org/10.1152/physiolgenomics.00102.2002

Watanabe, C., Imaizumi, T., Kawai, H., Suda, K., Honma, Y., Ichihashi, M., Ema, M., & Mizutani, K. I. (2020). Aging of the Vascular System and Neural Diseases. In *Frontiers in Aging Neuroscience* (Vol. 12). Frontiers Media S.A. https://doi.org/10.3389/fnagi.2020.557384

Wenzel, J., Assmann, J. C., & Schwaninger, M. (2014). Thrombomodulin – A New Target for Treating Stroke at the Crossroad of Coagulation and Inflammation. *Current Medicinal Chemistry*, *21*(18), 2025–2034. https://doi.org/10.2174/0929867321666131228204839

Wenzel, J., Hansen, C. E., Bettoni, C., Vogt, M. A., Lembrich, B., Natsagdorj, R., Huber, G., Brands, J., Schmidt, K., Assmann, J. C., Stölting, I., Saar, K., Sedlacik, J., Fiehler, J., Ludewig, P., Wegmann, M., Feller, N., Richter, M., Müller-Fielitz, H., … Schwaninger, M. (2020a). Impaired endothelium-mediated cerebrovascular reactivity promotes anxiety and respiration disorders in mice. *Proceedings of the National Academy of Sciences of the United States of America*, *117*(3), 1753–1761. https://doi.org/10.1073/pnas.1907467117

Wenzel, J., Lampe, J., Müller-Fielitz, H., Schuster, R., Zille, M., Müller, K., Krohn, M., Körbelin, J., Zhang, L., Özorhan, Ü., Neve, V., Wagner, J. U. G., Bojkova, D., Shumliakivska, M., Jiang, Y., Fähnrich, A., Ott, F., Sencio, V., Robil, C., … Schwaninger, M. (2021). The SARS-CoV-2 main protease Mpro causes microvascular brain pathology by cleaving NEMO in brain endothelial cells. *Nature Neuroscience*, *24*(11), 1522–1533. https://doi.org/10.1038/s41593-021-00926-1

Wenzel, J., & Schwaninger, M. (2016). The blood–brain barrier and its regulation by NF-κB. *E-Neuroforum*, *22*(2), 23–30. https://doi.org/https://doi.org/10.1007/s13295-016-0022-6

Wenzel, J., Spyropoulos, D., Assmann, J. C., Khan, M. A., Stölting, I., Lembrich, B., Kreißig, S., Ridder, D. A., Isermann, B., & Schwaninger, M. (2020b). Endogenous THBD (Thrombomodulin) Mediates Angiogenesis in the Ischemic Brain - Brief Report. *Arteriosclerosis, Thrombosis, and Vascular Biology*, *40*(12), 2837–2844. https://doi.org/10.1161/ATVBAHA.120.315061

WHO. (2020). *Global Health Estimates 2020 Deaths by Cause, Age, Sex, by Country and by Region*. World Health Organization. https://www.who.int/data/gho/data/themes/mortality-and-global-health-estimates/ghe-leading-causes-of-death

Wimmer, M. E., Hernandez, P. J., Blackwell, J., & Abel, T. (2012). Aging impairs hippocampus-dependent long-term memory for object location in mice. *Neurobiology of Aging*, *33*(9), 2220–2224. https://doi.org/10.1016/j.neurobiolaging.2011.07.007

Wisniewska-Kruk, J., Van Der Wijk, A. E., Van Veen, H. A., Gorgels, T. G. M. F., Vogels, I. M. C., Versteeg, D., Van Noorden, C. J. F., Schlingemann, R. O., & Klaassen, I. (2016). Plasmalemma vesicle-associated protein has a key role in blood-retinal barrier loss. *American Journal of Pathology*, *186*(4), 1044–1054. https://doi.org/10.1016/j.ajpath.2015.11.019

Wojciak-Stothard, B., & Ridley, A. J. (2003). Shear stress–induced endothelial cell polarization is mediated by Rho and Rac but not Cdc42 or PI 3-kinases. *The Journal of Cell Biology*, *161*(2), 429–439. https://doi.org/10.1083/jcb.200210135

Wootten, D., Christopoulos, A., Marti-Solano, M., Babu, M. M., & Sexton, P. M. (2018). Mechanisms of signalling and biased agonism in G protein-coupled receptors. *Nature Reviews Molecular*

Cell Biology, *19*(10), 638–653. https://doi.org/10.1038/s41580-018-0049-3

Worzfeld, T., & Schwaninger, M. (2016). Apicobasal polarity of brain endothelial cells. *Journal of Cerebral Blood Flow and Metabolism*, *36*(2), 340–362. https://doi.org/10.1177/0271678X15608644

Xing, C. Y., Tarumi, T., Liu, J., Zhang, Y., Turner, M., Riley, J., Tinajero, C. D., Yuan, L. J., & Zhang, R. (2017). Distribution of cardiac output to the brain across the adult lifespan. *Journal of Cerebral Blood Flow and Metabolism*, *37*(8), 2848–2856. https://doi.org/10.1177/0271678X16676826

Xu, J., Mathur, J., Vessières, E., Hammack, S., Nonomura, K., Favre, J., Grimaud, L., Petrus, M., Francisco, A., Li, J., Lee, V., Xiang, F. li, Mainquist, J. K., Cahalan, S. M., Orth, A. P., Walker, J. R., Ma, S., Lukacs, V., Bordone, L., … Patapoutian, A. (2018). GPR68 Senses Flow and Is Essential for Vascular Physiology. *Cell*, *173*(3), 762-775.e16. https://doi.org/10.1016/j.cell.2018.03.076

Yanai, S., & Endo, S. (2021). Functional Aging in Male C57BL/6J Mice Across the Life-Span: A Systematic Behavioral Analysis of Motor, Emotional, and Memory Function to Define an Aging Phenotype. *Frontiers in Aging Neuroscience*, *13*. https://doi.org/10.3389/fnagi.2021.697621

Yang, A. C., Stevens, M. Y., Chen, M. B., Lee, D. P., Stähli, D., Gate, D., Contrepois, K., Chen, W., Iram, T., Zhang, L., Vest, R. T., Chaney, A., Lehallier, B., Olsson, N., du Bois, H., Hsieh, R., Cropper, H. C., Berdnik, D., Li, L., … Wyss-Coray, T. (2020). Physiological blood–brain transport is impaired with age by a shift in transcytosis. *Nature*, *583*(7816), 425–430. https://doi.org/10.1038/s41586-020-2453-z

Yang, D., Zhou, Q., Labroska, V., Qin, S., Darbalaei, S., Wu, Y., Yuliantie, E., Xie, L., Tao, H., Cheng, J., Liu, Q., Zhao, S., Shui, W., Jiang, Y., & Wang, M. W. (2021). G protein-coupled receptors: structure- and function-based drug discovery. *Signal Transduction and Targeted Therapy*, *6*(1). https://doi.org/10.1038/s41392-020-00435-w

Yang, T., Sun, Y., Lu, Z., Leak, R. K., & Zhang, F. (2017). The impact of cerebrovascular aging on vascular cognitive impairment and dementia. In *Ageing Research Reviews* (Vol. 34, pp. 15–29). Elsevier Ireland Ltd. https://doi.org/10.1016/j.arr.2016.09.007

Yang, W., Zhou, X., & Ma, T. (2019). Memory Decline and Behavioral Inflexibility in Aged Mice Are Correlated With Dysregulation of Protein Synthesis Capacity. *Frontiers in Aging Neuroscience*, *11*. https://doi.org/10.3389/fnagi.2019.00246

Ye, M., Sanchez, H. M., Hultz, M., Yang, Z., Bogorad, M., Wong, A. D., & Searson, P. C. (2014). Brain microvascular endothelial cells resist elongation due to curvature and shear stress. *Scientific Reports*, *4*. https://doi.org/10.1038/srep04681

Yokota, Y., Nakajima, H., Wakayama, Y., Muto, A., Kawakami, K., Fukuhara, S., & Mochizuki, N. (2015). Endothelial Ca2+ oscillations reflect VEGFR signaling-regulated angiogenic capacity in vivo. *ELife*, *4*(NOVEMBER2015). https://doi.org/10.7554/eLife.08817

Zhao, Z., Nelson, A. R., Betsholtz, C., & Zlokovic, B. V. (2015). Establishment and Dysfunction of the Blood-Brain Barrier. *Cell*, *163*(5), 1064–1078. https://doi.org/10.1016/j.cell.2015.10.067

Acknowledgments

First and foremost, I would like to thank my main supervisor PD. Dr. Jan Wenzel for his trust in me to pursue my PhD as part of his team. His profound knowledge of the field, guidance, encouragement and open communication throughout the research process was invaluable. Also, I would like to express my gratitude to my second supervisor and director of the Institute of Pharmacology Prof. Dr. med. Markus Schwaninger. His constructive feedback during our meetings and his guidance shaped the success of the current PhD project. Finally, I would like to thank Prof. Dr. Peter König and Prof. Dr. Stefan Taube for accepting to be part of the examination committee and for their insightful comments.

Additionally, I would like to acknowledge the financial support provided to my supervisors from the European Union´s Horizon 2020 research and innovation program under the Marie Skłodowska-Curie grant agreement (ENTRAIN) No. 813294 and the Deutsche Forschungsgemeinschaft (WE 6456/1-1). Without ENTRAIN, the collaboration on the proteomic study with Prof. Bernd Wollscheid and Dr. Jacqueline Hammer wouldn't have been possible, and I am grateful for their professionalism and cooperation.

A special thank you goes to all the PhD students of the Institute of Pharmacology whom I had the opportunity to meet and work with. I am glad for their great cooperation and assistance whenever I encountered problems. Our everyday interaction in the lunch breaks, corridors, labs, or after work, cheered me up during the difficult times of the coronavirus pandemic. Special thanks, to Dr. Josephine Lampe and Dr. Manon Rivagorda for their helpful comments while writing this dissertation as well as to Dr. Marius, Doro, Joanna and Franzesco for the great moments we shared in our office.

I also feel privileged to have been part of the ENTRAIN consortium, my second 'PhD family', from which I got invaluable input on my research project and established international connections.

I am particularly grateful for the support of the technical assistants of our lab. Bea, Ines, Wiebke, Frauke and Christine were always there for me when I needed help, shared their technical expertise, and supported me on my journey to improve my German language. Furthermore, I owe thanks to Dr. Helge Müller-Fielitz, Dr. Sonja Binder and Dr. Marietta Zille for their constant support during the organization and execution of my experiments.

In conclusion, the biggest gratitude for this journey goes to my parents, Christos and Eirini, my brothers Antonis, Margianna and Aggelos and my closest Greek friend Fotini. Their support gave me the courage to take the step to move to another country and pursue my dreams. Thank you for the advice and emotional support during the most challenging moments of this journey.